QCD TEST IN THREE-JET Z° DECAYS AT SLD AND DETECTOR DEVELOPMENT FOR $H^\circ \rightarrow \gamma\gamma$ SEARCHES IN HIGH ENERGY HADRON COLLIDERS

Hyun Hwang

SLAC-Report-453
August 1994

Prepared for the Department of Energy
under contract number DE-AC03-76SF00515

2/80

SLAC-453
UC-414
(M)

QCD TEST IN THREE-JET Z^0 DECAYS AT SLD AND DETECTOR DEVELOPMENT FOR $H^0 \rightarrow \gamma\gamma$ SEARCHES IN HIGH ENERGY HADRON COLLIDERS*

Hyun Hwang
Stanford Linear Accelerator Center
Stanford University, Stanford, CA 94309

August 1994

Prepared for the Department of Energy
under contract number DE-AC03-76SF00515

Printed in the United States of America. Available from the National Technical Information Service, U.S. Department of Commerce, 5285 Port Royal Road, Springfield, Virginia 22161.

*Ph.D. thesis, University of Oregon.

An Abstract of the Dissertation of

Hyun Hwang for the degree of Doctor of Philosophy

in the Department of Physics to be taken August 1994

Title: QCD TEST IN THREE-JET Z^0 DECAYS AT SLD AND DETECTOR DEVELOPMENT FOR $H^0 \rightarrow \gamma\gamma$ SEARCHES IN HIGH ENERGY HADRON COLLIDERS

Approved: _____
Dr. James E. Brau

Polarized Z^0 decays into three jets have been detected and measured in the SLAC Large Detector (SLD) experiment operating at the SLAC Linear Collider (SLC). The hadrons from the jets were detected in the SLD liquid argon calorimeter, providing a sensitivity over 98% of the solid angle. The spin of the gluon was tested by studying the scaled jet energies (x_1, x_2, x_3), the Ellis-Karliner angle ($cos\theta_{EK}$) and the parameters of event plane orientation (α, α_N, β). These measured variables are compared with quantum chromodynamics (QCD) and a scalar gluon model. Good agreement is found between data and the vector QCD model for the distributions of x_1, x_2, x_3 and $cos\theta_{EK}$.

Two detector prototypes for the GEM detector of the Superconducting Super Collider have been studied: a prototype silicon-tungsten preradiator and a liquid

argon hadron calorimeter. The silicon-tungsten preradiator was designed for the GEM detector to distinguish between single photons from Higgs decay and background photon pairs from π^0 decay. This preradiator was tested in a beam at Brookhaven National Laboratory in July, 1992. A lead glass array placed behind the silicon was used to determine energy resolution effects. The results from the test on spatial distributions and energy resolution, including correction for the energy deposited in the preradiator are presented, along with comparisons to EGS simulations. Data from a beam test of the liquid argon prototype was analyzed and compared to CALOR89 simulations. The studies concentrated on energy resolution optimization and electronic noise suppression.

ACKNOWLEDGMENTS

I personally appreciate my advisor, James Brau, for his guidance, encouragement and patience. I also wish to appreciate Raymond Frey and David Strom for their advice.

I would especially like to thank the members of the University of Oregon Luminosity Group: Koichiro Furuno, Kevin Pitts, Matt Langston, Anatoli Arodzero, Xiao Qing Yang, Hwanbae Park, J. Zhou and David Mason. I especially wish to thank for Kevin Pitts's help.

I also appreciate Phlip Burrows for his help as a QCD leader, C.G. Fan, QCD working groups and SLD collaborators. I wish to thank T.W. Reeves and A. Weidemann for the HERWIG5.7 MC installation to SLD.

My Ph.D thesis would never been completed without the financial and spiritual support of my parents, Young and Kwang Hwang. I will not forget your love forever. I thank my wife, Kee Hyun, for her support, prayers and patience. Thanks to my son's baseball and basketball entertainment.

TABLE OF CONTENTS

LIST OF TABLES

LIST OF FIGURES

CHAPTER I

INTRODUCTION

This thesis will present the analysis of a calorimetric measurement of three-jet events, which are sensitive to the spin of the gluon, in polarized Z^0 hadronic decays in the SLAC Large Detector (SLD) at the Stanford Linear Accelerator Center (SLAC) and tests of two detector prototypes (prototype silicon-tungsten preradiator and liquid argon hadron calorimeter) for the Gamma Electron Muon (GEM) detector of the Superconducting Super Collider (SSC).

SLD accumulated approximately 50,000 Z^0 hadronic decays with a typical electron beam polarization of 60-65% during the 1993 run. A calorimetric measurement of three-jet distributions is performed with 50,000 Z^0 hadronic decays accumulated in the Liquid Argon Calorimeter (LAC). Variables of the three-jet events which are sensitive to the spin of the gluon are studied: the scaled jet energies (x_1, x_2, x_3), the Ellis-Karliner angle ($cos\theta_{EK}$) and parameters (α, α_N, β) of event plane orientation.

The silicon-tungsten preradiator could be used to enhance the identification of photons and electrons at high energy hadron colliders. Specifically, it was designed for the GEM detector to distinguish between single photons from Higgs decay and background photon pairs from π^0 decay. This preradiator was tested in a beam at BNL in July 1992. A lead glass array placed behind the silicon was used to determine energy resolution effects. The results from the test on spatial distributions and energy resolution, including correction for the energy deposited in the preradiator are presented, along with comparisons to EGS simulations.

A liquid argon hadron calorimeter was tested in 1991 during the summer test beam run at the Brookhaven National Laboratory (BNL). Typically, the slow drift of charges in liquid argon calorimeters require relatively long integration times to fully collect charges and to minimize noise. The 16 ns period of the SSC demands a shorter integration time, increasing the electronic noise of a liquid argon calorimeter above an optimally low value. Through off-line analysis we have investigated decreasing the electronic noise, which can be important to reduce QCD background through an isolation cut (see chapter VI) and to get better energy resolution.

Chapter II will describe the theory of three-jet event distributions, including the cross section for three-jet events and the method of deriving equations of variables such as three-jet scaled energies, the Ellis-Karliner angle ($cos\theta_{EK}$), and event plane

orientation.

Chapter III will describe the experimental apparatus, the SLC and the SLD. The description of the accelerator will pay particular attention to the production and transport of a polarized electron beam, due to the unique capability of the SLC to produce and accelerate polarized electrons. The main subsystems of the SLD (calorimetry, tracking, particle identification and polarimetry) will be introduced and outlined. The SLD LAC, the detector module used for analysis of the three-jet events, will be presented with additional detail.

Event selection and preparation for hadronic Z^0 event will be presented in Chapter IV. This will include aspects of triggering and event selection, as well as corrections to the data due to detection inefficiencies in the region of the endcap calorimeter. Also, the improved results after LAC energy response correction are presented.

Chapter V will describe the procedure for reconstructing three-jet events, the rescaling three-jet energies by momentum conservation and corrections for hadronization and detector effects. The raw data are found to be in good agreement with the Monte Carlo simulations passing the same set of event selection cuts. The distributions of variables for three-jet events are done with a bin-to-bin correction to explain the effects of hadronization, detector acceptance and resolution. The corrected data was fitted to equations presented in Chapter II for event plane orientation, and parameters (α, α_N, β) associated with the equations are obtained. The corrected data is compared to the expected parton level distributions of variables for three-jet events simulated from the vector QCD model and a scalar gluon model respectively. Systematic errors, calculated for all the bins in these distributions, are obtained by comparing the results from different sets of event selection cuts and from different Monte Carlo programs installed with different hadronization models with those from the standard cut. Good agreement is found between data and the vector QCD model for the distributions of the scaled energies and $cos\theta_{EK}$.

The $H^0 \rightarrow \gamma\gamma$ decay of the intermediate Higgs boson, a potentially clean and distinctive signature, will be outlined in Chapter VI, with special attention given to the aspects of $H^0 \rightarrow \gamma\gamma$ production and background production. Also, the importance of the off-line analysis of the silicon-tungsten preradiator and a liquid argon hadron calorimeter will be discussed.

The analysis of the preradiator beam test data will be presented in Chapter VII, including pedestal correction of silicon strip detector, cut conditions for selecting good electron events, energy resolution and correction, and comparisons to EGS simulations. Chapter VIII will describe the off-line analysis of a liquid argon hadron calorimeter. The energy resolution is optimized through reduced electronic noise. A pion rejection study will also be presented. Comparisons to CALOR89 simulations play an important role in this analysis.

CHAPTER II

QUANTUM CHROMODYNAMICS AND THE THEORY OF THREE-JET EVENTS IN POLARIZED Z^0 HADRONIC DECAYS

Quantum Chromodynamics (QCD) is the theory of quarks and gluons and their interactions, called strong interactions and is a quantum gauge field theory. In this section the history of QCD will be explained briefly, covering the quark model of hadrons, the color degree of freedom, the QCD running coupling constant and three-jet events. The gluon in QCD theory is a self-interacting gauge boson and has one unit of spin. A scalar gluon would have spin 0. Several groups at PETRA([1]-[3]) measured three-jet event distributions sensitive to the gluon spin, but the effect of gluon spin was smaller at energies around 30 GeV than at Z^0 resonance energy of LEP due to lower statistics and larger hadronization corrections.

The SLAC Linear Collider (SLC) result in better jet definition, allow for smaller hadronization corrections and yield higher statistics at the Z^0 resonance than at energies around 30 GeV of PETRA. This permits the selection of distributions of three-jet scaled energies (x_1,x_2,x_3) and the cosine of the Ellis-Karliner angle ($cos\theta_{EK}$) with clear discrimination between scalar and vector gluon theory. Similar analyses have also been done by L3[4] and OPAL at the Z^0 resonance[5]. Also, the three-jet event plane orientation (θ,θ_N,χ) gives us an another probe of the spin of the gluon. Here θ is the polar angle of the electron relative to the most energetic jet, and χ is the angle between the most energetic jet-electron plane (production plane) and the three-jet event plane. θ_N is the polar angle of the normal to the event plane with respect to the electron beam. Such an analysis has been done by DELPHI[6].

This chapter will describe briefly the cross section for production of three-jet events[7]. According to the cross section of three-jet events, it would be possible to measure distributions of the three-jet event plane orientation whose shapes depends on the degree of longitudinal polarization of the electron beam with tagging of the jet originality(q, $\overline{q}$, or g). Since it is not possible to identify the jet origin through the calorimeter type experiment used in this analysis, this analysis uses distributions of three-jet event plane orientation, of three-jet scaled energies and of the $cos\theta_{EK}$ sensitive to the gluon spin, without such identification of jets.

2.1 Quantum Chromodynamics

Quarks have three colors and electric charge. Gluons are the massless vector gauge bosons mediating an interquark interaction and described as an octet representation of SU(3) consisting of the color-anticolor states of the eight gluons. In QCD the gluons exchanged between colored quarks are very analogous to the photons exchanged between charged electrons in Quantum Electrodynamics (QED). The strong force can be described that the quark-quark interactions through gluons, presented by the symmetry group $SU(3)$, are invariant in the space spanned by the three color eigenstates of the quarks. The triplet representation of $SU(3)$ means that a quark can carry one of three possible colors. $SU(3)$ is a non-Abelian group, so QCD is a non-Abelian gauge field theory.

The quark model of hadrons was first postulated by Gell-Mann and Zweig[8]. This model, based on a $SU(3)$ flavor symmetry of half-integer spin and fractionally charged particles, postulated that hadrons were mesons or baryons made of a quark and an antiquark or three quarks. The first direct evidence of quarks came from the SLAC-MIT experiments[9] of deep inelastic electron-nucleon scattering in 1968. They provided the first indication of point-like structure inside the proton. The subsequent discoveries of the J/Ψ and Υ particles introduced two new quark flavors, the c and b. The half-integer spin of the quarks has been proved experimentally[10] in terms of the angular distribution between the jet axis and the beam axis in two-jet hadronic events which is theoretically predicted to be proportional to $(1 + cos^2\theta)$ in case of photon-exchange in the e^+e^- annihilation. The fractionally charged quarks (partons) were verified through comparison between a second structure function ($F_2^{\nu N}$) from neutrino-nucleon scattering at CERN and F_2^{eN} from electron-nucleon scattering at SLAC in the same momentum transfer region. If u and d quarks in the nucleon are assigned 2/3 e and -1/3 e, the two sets of data ($F_2^{\nu N}$ and F_2^{eN}) will be agreed with multiplication of F_2^{eN} by the factor 18/5.

Quarks have a degree of freedom, called color quantum number, which is associated with the strong force interactions between quarks and gluons. The Pauli exclusion principle states that the wave function of baryons is antisymmetric under the interchange of any two constituent quarks. The baryons such as Δ^{++} or Ω^- consists of three up quarks or three strange quarks with their spins aligned. Therefore, the total wave function of their two baryons will be symmetric under the interchange of any two quarks, violating the Pauli exclusion principle. The Pauli exclusion principle of those two baryons will be satisfied by introducing an additional three colors. The number of colors N_c can be determined by experiment. To lowest order in QCD the hadronic to muon cross section in e^+e^- annihilations is:

$$R \equiv \frac{\sigma(e^+e^- \rightarrow hadrons)}{(e^+e^- \rightarrow \mu^+\mu^-)} = N_c \sum_f q_f^2$$

where q_f is the charge of the quark of flavor f and the sum is over all flavors. A

multitude of experiments performed at various center-of-mass energies have shown results that are in excellent agreement with $N_c = 3$.

In QCD, a running coupling constant ($\alpha_s(Q^2)$) can be represented as the strength of the quark interactions. The cross sections to high order in perturbative QCD leads to infinitely large terms. To avoid these, QCD must be renormalized, meaning that the amplitudes should be non-divergent at high energy and to high orders in the coupling constant. Through the procedure of renormalization, the QCD running coupling constant can be expressed to first order:

$$\alpha_s(Q^2) = \frac{12\pi}{(33 - 2n_f)ln(Q^2/\Lambda^2)}$$

or

$$\Lambda^2 = \mu^2 exp\left[\frac{-12\pi}{(33 - 2n_f)\alpha_s(\mu^2)}\right]$$

where n_f is the number of quark flavors (which is five at Z^0 scale) and μ remains as a relic from the renormalization. The color charge will be expanded by the self-coupling of the gluons. As Q^2 increases, the self-coupling of the gluons becomes larger and $\alpha_s(Q^2)$ decreases. At asymtotically large Q^2, quarks behave as essentially free, noninteracting particles (for large Q^2, $\alpha_s \ll 1$), called asymtotic freedom. Therefore, the perturbative QCD calculations will be valid for large enough Q^2. On the contrary, the perturbative QCD is no longer available for low Q^2. The strong coupling constant becomes very large which can be explained the confinement of quarks and gluons inside hadrons (color confinement) at large distance. The color confinement can be proved that any experiment has not seen color and the fractional charge of a free quark. Quark confinement introduces the properties of the string. The quarks can be separated by stretching the string. Since the energy of the string is proportional to its length, energy required to separate the quarks increases in proportional to the distance between quarks. If the string had enough energy to snap it in two, a new quark and antiquark would be created at the breaking point. A meson, bound state of a new quark and antiquark at the broken ends, would be created. Theory and experiment suggest that only colorless states are allowed in the form of physical hadrons, i.e. bound states of quarks and antiquarks (mesons) or triplets of quarks (baryons). Therefore, the state of a free quark could not be existed.

It has been discovered in the electron-nucleon scattering at SLAC[9] that quarks could account for only about half of the nucleon momentum. Thus the remaining momentum can be identified with gluon constituents which are responsible for the interquark binding. The annihilation of e^+e^- decays to a $Q\overline{Q}$ pair, the quarks to hadrons by hadronization process. The most interesting phenomena of quarks in a quasi-free state is jets collimated around the $Q\overline{Q}$ axes which can be explained by the string fragmentation mode, called two-jet events. Occasionally, a quark or a antiquark radiates a gluon, the gluon and quark giving rise to separate hadronic jets[11]. These are called three-jet events. The strong coupling constant α_s can be determined by the

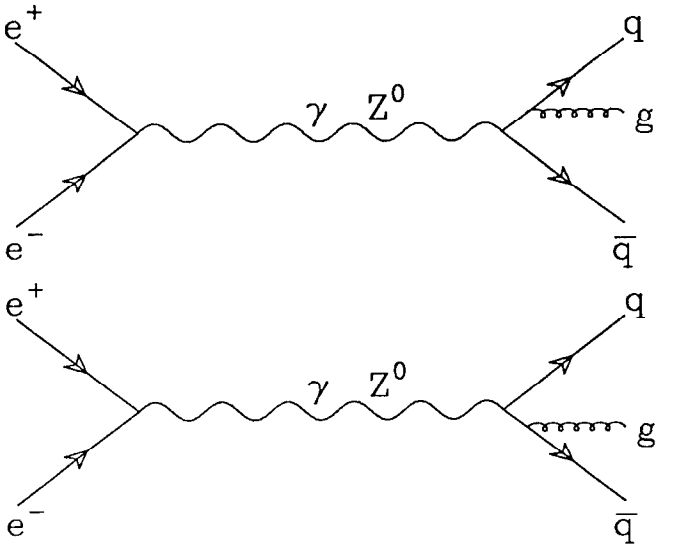

Figure 2.1: Feynman diagram for $e^+e^- \rightarrow q\bar{q}g$ at tree level.

measured rate of three-jet compared with two-jet events. The observation of three-jet events in e^+e^- annihilation can be regarded as direct evidence of gluon. The distributions of three-jet events allows a determination of gluon spin. The data from the TASSO detector[1] strongly favors the vector gluon.

2.2 Three-Jet Event Plane Orientation

2.2.1 The Cross Section of Three-Jet Event

In this section we summarize the theory[7] for $e^+e^- \rightarrow q\bar{q}g$ of first order $\vartheta(\alpha_s)$ for a longitudinally polarized electron beam in the exchange of a virtual photon (γ) and a vector boson (Z^0) as seen in figure 2.1.

The differential cross section for gluon bremsstrahlung , $e^+e^- \rightarrow q\bar{q}g$, from arbitrarily polarized electrons and positrons, summed over quark and gluon polarizations, may then be written as[7]

$$d\sigma = \frac{1}{2}\frac{1}{(2E)^2}\sum_f \sum_{\substack{colours \\ polarizations}} |M|^2 dP \tag{2.1}$$

Here $2E \equiv \sqrt{Q^2}$ is the CMS energy, M is the matrix element and dP is the differential

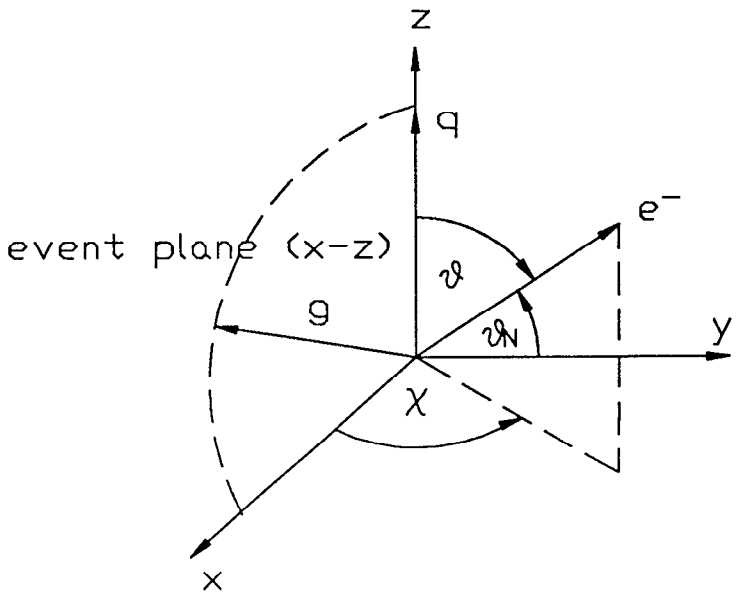

Figure 2.2: Coordinate frame in the CMS. The three-jet event plane ($q\bar{q}g$) is the x-z plane. The gluon has a positive x-component of momentum. θ is the polar angle of the electron relative to the quark direction, and χ is the angle in the x-y plane between the quark-electron plane (production plane) and the three-jet event plane. θ_N is the polar angle of the normal to event plane with respect to the electron beam.

phase-space element, which can be expressed as

$$dP = \frac{1}{(2\pi)^2}\frac{1}{32}Q^2 dx d\bar{x} d(cos\theta) d\chi$$

Here $x = 2E_q/E_{cm}$, $\bar{x} = 2E_{\bar{q}}/E_{cm}$ and $x_g = 2E_g/E_{cm}$ are the scaled energies of quark, antiquark and gluon, satisfying $x + \bar{x} + x_g = 2$. The angles θ, χ and θ_N are defined in figure 2.2. θ is the polar angle of the quark direction with respect to the electron beam, and χ is the angle between the quark-electron plane and the event plane (x,z), defined such that the gluon has a positive x-component of momentum. θ_N is the polar angle of the normal to the event plane with respect to the electron beam. The matrix element M can be written as

$$\begin{aligned} M &= M_\gamma + M_Z \\ &= \frac{-ie^2 g_s T_a}{Q^2}[\bar{v}(e_+)(-Q_f\gamma^\mu)u(e_-)\bar{u}(q)\ \not{\epsilon}^{(\lambda)*}\frac{\not{q}+\not{g}}{(q+g)^2}\gamma_\mu v(\bar{q}) \\ &+ f(Q^2)\bar{v}(e_+)\gamma^\mu(v - a\gamma_5)u(e_-)\bar{u}(q)\ \not{\epsilon}^{(\lambda)*}\frac{\not{q}+\not{g}}{(q+g)^2}\gamma_\mu(v_f - a_f\gamma_5)v(\bar{q})] \\ &+ \textit{crossed terms.} \quad (\bar{q}\ \textit{radiates the gluon}) \end{aligned}$$

where the relative energy dependence of the weak neutral current is given by

$$f(Q^2) = \frac{1}{4sin^2 2\theta_w} \frac{Q^2}{Q^2 - {M_z}^2 + iM_z{\Gamma_z}^{tot}}$$

, g_s is the QCD coupling constant, θ_W is the weak mixing angle and T_a is the color matrix in the fundamental quark representation, normalized such that

$$\sum_{a,b} Tr(T_a T_b) = 4$$

Here v_f and a_f are the vector and axial vector coupling coefficients of quarks, v and a are the vector and axial vector coupling coefficients of the electron and $\not{\epsilon}^{(\lambda)^*}$ is the spin polarization of γ and Z^0. The sum

$$S_f = \sum_{\substack{colours \\ polarizations}} |M_\gamma + M_Z|^2$$

may be decomposed as

$$S_f = \frac{(4\pi)^3 \alpha^2 \alpha_s}{Q^4} (S_{\gamma\gamma} + S_{\gamma Z} + S_{ZZ}) \tag{2.2}$$

where $\alpha_s = g_s^2/4\pi$ and where $S_{\gamma\gamma}$, $S_{\gamma Z}$ and S_{ZZ} refer to the pure electromagnetic, interference and pure weak contributions, respectively. It is convenient to express these in terms of lepton and hadron tensors.

$$\begin{aligned} S_{\gamma\gamma} &= L^{\mu\nu}_{\gamma\gamma} H_{\gamma\gamma\mu\nu} \\ S_{\gamma Z} &= 2Re(f(Q^2) L^{\mu\nu}_{\gamma Z} H_{\gamma Z\mu\nu}) \\ S_{ZZ} &= |f(Q^2)|^2 L^{\mu\nu}_{ZZ} H_{ZZ\mu\nu} \end{aligned} \tag{2.3}$$

Since SLC has a longitudinally polarized electron beam, the lepton composite tensors of equation 2.3 can be written as[7]:

$$\begin{aligned} L^{\mu\nu}_{\gamma\gamma} &= L_1^{\mu\nu} + PL_2^{\mu\nu} \\ L^{\mu\nu}_{\gamma Z} &= -v[L_1^{\mu\nu} + PL_2^{\mu\nu}] + a[L_1^{\mu\nu} + PL_2^{\mu\nu}] \\ L^{\mu\nu}_{ZZ} &= (v^2 + a^2)[L_1^{\mu\nu} + PL_2^{\mu\nu}] - 2av[L_1^{\mu\nu} + PL_2^{\mu\nu}] \end{aligned}$$

where P is the electron longitudinal polarization. The hadron tensors are in general rather complex[7]. However, since we sum over quark and gluon polarizations, these composite hadron tensors of equation 2.3 may be expressed as[7]:

$$
\begin{aligned}
H_{\gamma\gamma\mu\nu} &= Q_f^2 H_{V\mu\nu} \\
H_{\gamma Z\mu\nu} &= Q_f[v_f H_{V\mu\nu} - a_f H_{A\mu\nu}] \\
H_{ZZ\mu\nu} &= (v_f^2 + a_f^2) H_{V\mu\nu} - 2 v_f a_f H_{A\mu\nu}
\end{aligned}
$$

The lepton tensor, L_1 is even under $\mu \leftrightarrow \nu$ ($L_1^{\mu\nu} = L_1^{\nu\mu}$), while L_2 is odd under $\mu \leftrightarrow \nu$ ($L_2^{\mu\nu} = -L_2^{\nu\mu}$). Also, the hadron tensor, $H_{V\mu\nu}$ is even under $q \leftrightarrow \overline{q}$ ($H_{V\mu\nu} = H_{V\nu\mu}$), while $H_{A\mu\nu}$ is odd under $q \leftrightarrow \overline{q}$ ($H_{A\mu\nu} = -H_{A\nu\mu}$)[7]. By these symmetries, the product of lepton and hadron tensor has even properties under $\mu \leftrightarrow \nu$ and $q \leftrightarrow \overline{q}$. Therefore, only two non-zero tensor products will not vanish, $L_1^{\mu\nu} H_{V\mu\nu}$ and $L_2^{\mu\nu} H_{A\mu\nu}$. The polarization sum in equation 2.2 can be written by using the above relations as follows[7]:

$$
S_f = \frac{(4\pi)^3 \alpha^2 \alpha_s}{Q^4} [h_f^1 X_0 + h_f^2 Y_0]
$$

where

$$
\begin{aligned}
h_f^1(Q^2) &= Q_f^2 - 2Q_f Re f(Q^2)(v - aP)v_f + \mid f(Q^2) \mid^2 [(v^2 + a^2) - 2avP](v_f^2 + a_f^2) \\
h_f^2(Q^2) &= -2Q_f Re f(Q^2)(a - vP)a_f + \mid f(Q^2) \mid^2 [-(v^2 + a^2)P + 2av]2v_f a_f \\
X_0 &= \frac{8Q^4}{(q \cdot g)(\bar{q} \cdot g)} [\vec{q}^2 + (\vec{q} \cdot \hat{p}_e)^2 + (\vec{q} \leftrightarrow \bar{\vec{q}})] \\
Y_0 &= \frac{8Q^4}{(q \cdot g)(\bar{q} \cdot g)} [2|\vec{q}|(\vec{q} \cdot \hat{p}_e)^2) - (\vec{q} \leftrightarrow \bar{\vec{q}})]
\end{aligned}
$$

Where $\vec{q}$ is the quark vector and $\bar{\vec{q}}$ is the anti-quark vector.

The differential cross section of equation 2.1 can be written out in terms of the angles θ, χ, x and $\overline{x}$ (θ and χ are described in the figure 2.2)[7].

$$
\begin{aligned}
2\pi \frac{d^4\sigma}{d(cos\theta) d\chi dx d\overline{x}} &= \frac{1}{2\pi} \sum_f \Big[\frac{3}{8}(1 + cos^2\theta) \frac{d^2\sigma_U}{dx d\overline{x}} + \frac{3}{4} sin^2\theta \frac{d^2\sigma_L}{dx d\overline{x}} \\
&+ \frac{3}{4} sin^2\theta cos2\chi \frac{d^2\sigma_T}{dx d\overline{x}} + \frac{3}{2\sqrt{2}} sin2\theta cos\chi \frac{d^2\sigma_I}{dx d\overline{x}} \\
&- \frac{3}{2\sqrt{2}} sin\theta cos\chi \frac{d^2\sigma_A}{dx d\overline{x}} + \frac{3}{4} cos\theta \frac{d^2\sigma_P}{dx d\overline{x}} \Big]
\end{aligned}
\tag{2.4}
$$

Here

$$
\frac{d^2\sigma_i}{dx d\overline{x}} = \left\{ \begin{array}{ll} h_f^1(Q^2) \frac{\tilde{\sigma}}{(1-x)(1-\overline{x})} F_i, & \text{i=U,L,T,I} \\ h_f^2(Q^2) \frac{\tilde{\sigma}}{(1-x)(1-\overline{x})} F_i, & \text{i=A,P} \end{array} \right\}
$$

where

$$\tilde{\sigma} = \frac{\alpha_s(Q^2)}{\pi}\frac{4\pi}{3}\frac{\alpha^2}{Q^2}$$

The factors $F_i(x, \overline{x})$ can be expressed in terms of the fractional energies of quark and antiquark with respect to the beam energy.

The various parts of the cross section correspond to the following combination of (γ, Z) helicities[12]:

U = unpolarized transverse
L = longitudinally polarized
I,A = longitudinal/transverse interference
T = +/− interference
P = difference between right/left polarization

The cross sections for σ_U, σ_L, σ_I and σ_T are associated with the parity even part (parity-even current combinations in the lepton and quark-gluon sector) and those for σ_A and σ_P with the parity-odd part (parity-odd V-A current products in the lepton sector as well as in the quark-gluon sector). The parity-even part has the vector-vector (VV) and axial vector-axial vector (AA) terms. If we neglected all quark masses, assuming $m_q^2/s^2 \ll 1$, the VV and AA terms give identical distributions in the vector gluon[12]. The parity-odd part has a vector-axial vector interference (VA) term. But in contrast to the vector gluon case, the VV and AA terms are now different as a consequence of the γ_5-noninvariant scalar coupling, where quark and antiquark have the same helicity as the scalar gluon case[12]. While $d\sigma_L$ is equal to $2d\sigma_T$ in the vector gluon case, $d\sigma_L$ is not equal to $2d\sigma_T$ in the AA term of the scalar gluon[12].

2.2.2 Three-Jet Event Plane Orientation for Identified Jet

If we did not identify explicitly in each event the jet originality (which jet is the quark, the antiquark or the gluon), the cross sections of the parity odd part would disappear due to the antisymmetry under $(q \leftrightarrow \bar{q})$[12]. In order to measure distributions of the event plane orientation whose shapes depend on the degree of longitudinal polarization of the electron beam, it is necessary to know the cross sections of the parity odd part through the jet originality identification. The SLD vertex detector is useful in studying heavy quark tagging which provide the possibility to separate quark/antiquark from gluon jets in three jet events[13]. The techniques of tagging quark and antiquark jets are distinction of the sign of the lepton emitted in their semi-leptonic decays or the jet charge techniques[13].

2.2.3 Three-Jet Event Plane Orientation without Identifying Jet Originality

Paying attention to a calorimeter type experiment measuring just jet energies without identifying jet origin, the VA interference terms drop out because they are

parity and charge conjugation odd[12]. Defining $T \equiv max(x, \overline{x}, x_g)$[12], equation 2.4 without the VA interference term may be expressed as[7]:

$$\begin{aligned} 2\pi \frac{d^3\sigma}{d(cos\theta)d\chi dT} &= \frac{1}{2\pi}\sum_f \Big[\frac{3}{8}(1+cos^2\theta)\frac{d\sigma_U}{dT} + \frac{3}{4}sin^2\theta\frac{d\sigma_L}{dT} \\ &+ \frac{3}{4}sin^2\theta cos2\chi\frac{d\sigma_T}{dT} + \frac{3}{2\sqrt{2}}sin2\theta cos\chi\frac{d\sigma_I}{dT}\Big] \end{aligned} \tag{2.5}$$

Here, following references[14][15], the differential cross sections for vector gluons of QCD is:

$$\begin{aligned} \sigma_U(T) &\equiv \frac{1}{2\pi}\sum_f \frac{d\sigma_U}{dT} = \frac{1}{2\pi}\sum_f 2h_f^1(Q^2)\tilde{\sigma}\Big[\frac{2(3T^2-3T+2)}{T(1-T)}ln\frac{2T-1}{1-T} \\ &- (3T-2)(2-T)\Big(\frac{3}{1-T}+\frac{2}{T^2}\Big)\Big] \\ \sigma_L(T) &\equiv \frac{1}{2\pi}\sum_f \frac{d\sigma_L}{dT} = \frac{1}{2\pi}\sum_f 2h_f^1(Q^2)\tilde{\sigma}\Big[\frac{2}{T^2}(3T-2)(2-T)\Big] \\ \sigma_T(T) &= \frac{1}{2}\sigma_L(T) \\ \sigma_I(T) &\equiv \frac{1}{2\pi}\sum_f \frac{d\sigma_I}{dT} = -\frac{1}{2\pi}\sum_f 2h_f^1(Q^2)\tilde{\sigma}\Big[\frac{\sqrt{2}}{T}(T^2-2T+2)\Big(\frac{1}{\sqrt{1-T}}-\frac{2}{T}\sqrt{2T-1}\Big)\Big] \end{aligned} \tag{2.6}$$

The differential cross sections for scalar gluons for only VV terms[14][15] is:

$$\begin{aligned} \sigma_U(T) &\equiv \frac{1}{2\pi}\sum_f \frac{d\sigma_U}{dT} = \frac{1}{2\pi}\sum_f 2h_f^1(Q^2)\tilde{\sigma}\frac{3}{8}\Big[\frac{(3T-2)(4-3T)}{(1-T)} + 2ln\frac{2T-1}{1-T} - \frac{2(3T-2)}{T}\Big] \\ \sigma_L(T) &\equiv \frac{1}{2\pi}\sum_f \frac{d\sigma_L}{dT} = \frac{1}{2\pi}\sum_f 2h_f^1(Q^2)\tilde{\sigma}\Big[\frac{3(3T-2)}{4T}\Big] \\ \sigma_T(T) &= \frac{1}{2}\sigma_L(T) \\ \sigma_I(T) &\equiv \frac{1}{2\pi}\sum_f \frac{d\sigma_I}{dT} = -\frac{1}{2\pi}\sum_f 2h_f^1(Q^2)\tilde{\sigma}\frac{3}{4\sqrt{2}}\Big[\sqrt{1-T} - \frac{2(1-T)}{T}\sqrt{2T-1}\Big] \end{aligned} \tag{2.7}$$

Equation 2.5 may be expressed simply as

$$\begin{aligned} \frac{16\pi}{3}\frac{d^3\sigma}{dcos\theta d\chi dT} &= (1+cos^2\theta)\sigma_U(T) + 2\sigma_L(T)sin^2\theta \\ &+ 2\sigma_T(T)sin^2\theta cos2\chi - 2\sqrt{2}\sigma_I(T)sin2\theta cos\chi \end{aligned} \tag{2.8}$$

After integration of equation 2.8 over χ or $cos\theta$ one obtains, respectively[6],

$$\frac{1}{\sigma}\frac{d^2\sigma}{dcos\theta\, dT} = \frac{1+\alpha(T)cos^2\theta}{2(1+\frac{1}{3}\alpha(T))}$$

$$\frac{1}{\sigma}\frac{d^2\sigma}{d\chi\, dT} = \frac{1+\beta(T)cos2\chi}{2\pi}$$

where parameters α and β (depending on T of the event) can be expressed in terms of the various cross sections as

$$\alpha(T) = \frac{1-2\sigma_L(T)/\sigma_U(T)}{1+2\sigma_L(T)/\sigma_U(T)} \tag{2.9}$$

$$\beta(T) = \frac{\sigma_T(T)/\sigma_U(T)}{1+\sigma_L(T)/\sigma_U(T)} \tag{2.10}$$

Therefore, $\alpha(T)$ and $\beta(T)$ parameters can be obtained with the differential cross sections of the vector (2.6) and scalar (2.7) gluon[14] theory (see figure 5.23).

The distribution of the polar angle (θ_N) of the normal to the three-jet event plane is[6][16]:

$$\frac{1}{\sigma}\frac{d^2\sigma}{dcos\theta_N\, dT} = \frac{1+\alpha_N(T)cos^2\theta_N}{2(1+\frac{1}{3}\alpha_N(T))}$$

with

$$\alpha_N(T) = -\frac{1}{3}\frac{\sigma_U(T)+\sigma_L(T)-3(\sigma_L(T)-2\sigma_T(T))}{\sigma_U(T)+\sigma_L(T)-\frac{1}{3}(\sigma_L(T)-2\sigma_T(T))} \tag{2.11}$$

The parameter $\alpha_N(T)$ is expected to be $-1/3$ independently of the T value chosen and this tests the QCD $O(\alpha_s)$ prediction $\sigma_L(T) = 2\sigma_T(T)$[15]. But, in the scalar gluon model $\alpha_N(T)$ depends on T because $\sigma_L(T) \neq 2\sigma_T(T)$ for the AA terms[16] (see figure 5.23).

2.3 Distributions of Three-Jet Scaled Energies and Ellis-Karliner Angle

The theory in this section is described more detail in reference[17]. Therefore, this theory will be summarized briefly from reference[17].

2.3.1 Vector Gluon Model

Integrating of equation 2.4 over χ and $cos\theta$, the differential cross section of the vector gluon can be reduced into a simple form[7][17]:

$$\frac{1}{\sigma}\frac{d^2\sigma^V}{dx\,d\overline{x}} \propto \frac{x^2+\overline{x}^2}{(1-x)(1-\overline{x})} \tag{2.12}$$

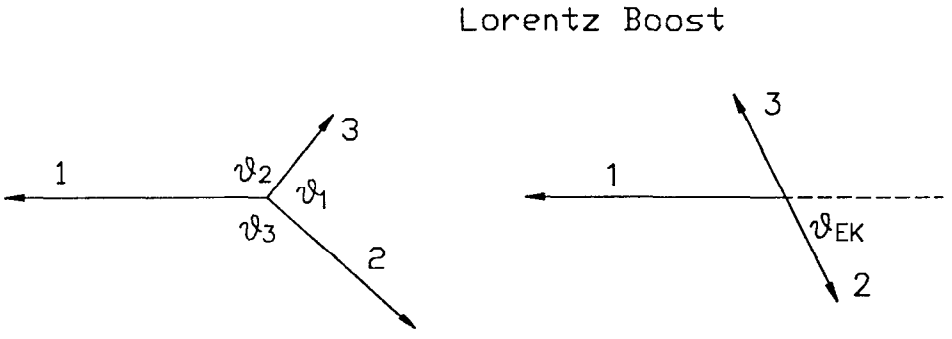

Figure 2.3: The three-jet event and the Ellis-Karliner angle.

where σ is the total cross section for $e^+e^- \rightarrow q\bar{q}g$.

In a three-jet event, the jets can be expressed according to their energies (jet 1 is the most energetic and jet 3 is the least energetic). The scaled energies of the three jets are:

$$x_i = \frac{2E_i}{E_{cm}} \qquad (i = 1, 2, 3)$$

where E_{cm} is the total energy of the event. $x_1 + x_2 + x_3 = 2.$, $x_1 > x_2 > x_3$. Making a Lorentz boost of the three-jet event into the rest frame of the jet 2 and jet 3 combined system, the Ellis-Karliner angle (θ_{EK}) is defined to be the angle between jets 1 and 2 in this frame, as in figure 2.3. For massless partons:

$$cos\theta_{EK} = \frac{x_2 - x_3}{x_1} \tag{2.13}$$

Equation 2.13 is derived in Appendix B of [17].

Since any one of the three jets could be the gluon, one has to sum all the three cases where the gluon is jet 1, 2 or 3 in order to get the differential cross section in terms of x_1 and x_2. The cross section of equation 2.12 can be expressed as the scaled energies from quark, anti-quark and gluon. The cross section of the scaled energies for vector gluons(V), derived in Appendix B of [17], is given as:

$$\frac{1}{\sigma}\frac{d^2\sigma^V}{dx_1 dx_2} \propto \frac{x_1^3 + x_2^3 + (2 - x_1 - x_2)^2}{(1 - x_1)(1 - x_2)(x_1 + x_2 - 1)} \tag{2.14}$$

2.3.2 Scalar Gluon Model

The scalar gluon model is a same theory as QCD except that the colored gluons are assumed to have spin 0. The cross section of scalar gluons(S):

$$\frac{1}{\sigma}\frac{d^2\sigma^S}{dxd\overline{x}} \propto \left[\frac{(2-x-\overline{x})^2}{(1-x)(1-\overline{x})} - \frac{R}{5}(3-x-\overline{x})\right] \tag{2.15}$$

$$R = \frac{10C_a^2}{C_v^2 + C_a^2} \tag{2.16}$$

where C_a^2 and C_v^2 are the axial and vector couplings for u,d,s,c,b quarks. The cross section of equation 2.15 can be expressed in terms of the scaled energies like the vector gluon model. The cross section of the scaled energies is given as:

$$\frac{1}{\sigma}\frac{d^2\sigma^S}{dx_1dx_2} \propto \left[\frac{x_1^2(1-x_1)+x_2^2(1-x_2)+(2-x_1-x_2)^2(x_1+x_2-1)}{(1-x_1)(1-x_2)(x_1+x_2-1)} - R\right] \tag{2.17}$$

2.4 The Hadronization and Monte Carlo Models

The Monte Carlo simulation of complete hadronic events constitutes one of the main tools for improving our understanding of QCD due to the limited usefulness of purely analytic techniques for experimental studies. The different Monte Carlo (MC) programs have been installed with different hadronization schemes and higher order corrections. Therefore, the theoretical systematic errors arise from the choice of the different MC programs (see section 5.8). The explanations of this section are summarized and taken from these references[17][18].

The schematic structure of a multihadronic event in e^+e^- annihilation can be characterized by four phases. In a first phase, an e^+e^- pair annihilates into a virtual γ/Z^0 state, which decays into a primary quark-antiquark pair $q\overline{q}$.

In the second phase, the initial $q\overline{q}$ pair may radiate gluons g, which in turn may radiate more gluons or quark-antiquark pairs. While the primary $q\overline{q}$ production is given by electroweak perturbation theory, strong perturbation theory must be used to describe this second stage. Here the spin of the gluon is a dominating factor in determining the production rate of the secondary quarks and gluons and in determining the energy distributions between them. The first/second order matrix element calculations from perturbative QCD give a fairly reasonable description of this process. The parton shower model is another approach to describe the process.

The theory of QCD requires that colored quarks and gluons can not exist in free form. A third phase is needed, in which partons fragment into a number of colorless partons, called the hadronization process. Since the strong coupling constant α_s is no longer small at the energy scales as low as 1 GeV, the fragmentation process can not be predicted by perturbative QCD, but must instead be explained by phenomenological

models. The string fragmentation, the cluster fragmentation and the independent fragmentation are three popular fragmentation models.

The fourth stage, where unstable hadrons decay into more stable ones and are tracked through the detector, is a rather empirical process. The main input here comes from experimentally determined branching ratios and detector simulation.

2.4.1 Parton Showers

Parton showers (PS)[19] are a different approach to parton generation. Partons are generated in an iterative fashion by the leading logarithm approximation (LLA). In the LLA, only the leading terms in the perturbative expansion are kept, limiting the parton splittings to $1 \rightarrow 2$ partons. This method is an attempt to approximate the real picture by generating more and softer partons than in the matrix element(ME) approach. The implementation of this approximation is via a set of Altarelli-Parisi[20] parton splitting functions that incorporate the allowed splittings to leading order: $g \rightarrow gg$, $g \rightarrow q\bar{q}$ and $q \rightarrow qg$. With the definition of the evolution parameter $t = ln(Q^2/\Lambda^2)$, where Q is the invariant mass of the parton and Λ is the QCD scale parameter for the parton shower process, the probability that a parton will branch $a \rightarrow bc$ is given by the Altarelli-Parisi evolution equation[20]. Starting at the maximum allowed mass for parton a, the evolution parameter t will be successively degraded until a branching occurs. The resultant partons b and c are allowed to branch in their turn, and so on. This whole iteration process terminates when the parton mass is evolved below the cut off value Q_0 ($t_{min} = ln(Q_0^2/\Lambda^2)$.

2.4.2 The Hadronization Process

A) The String Fragmentation Model

The string fragmentation model[21][22] is based on the concept of linear confinement of partons. Due to the gluon self-coupling, the color flux lines are rather confined to a thin tubelike region and uniform along its length. As the partons move apart, the color potential energy inside the tube increases like a stretched elastic string. The string can break into new quark pairs when the color potential energy is large enough. This fragmentation process continues, and more quarks pairs are produced, until the energy in the string is not enough to produce a quark pair. These new produced quarks and antiquarks pair up to form hadrons within a narrow cone about the direction of the parent quarks - jets. The probability that a color string will break is given by the Lund systematic fragmentation function:

$$f(z) = \frac{1}{z}(1-z)^a exp(-\frac{bm_T^2}{z})$$

where $m_T = \sqrt{p_T^2 + m^2}$ is called the transverse mass of the hadron, p_T is the momentum of the hadron transverse to the parent quark direction, and variables a and b are

arbitrary constants to be determined from experiment. The parameter z is defined as the energy and momentum parallel to the parent quark direction carried by the primary hadron divided by of the energy and momentum of the parent quark.

B) The Cluster Fragmentation Model

The cluster fragmentation model[23] characterizes the clusters by their total mass and color charge, with no internal structures. Each gluon is forced to split into a $q\overline{q}$ pair at the end of the parton shower. Every final cluster is assumed to decay isotropically into the observable hadrons.

C) The Independent Fragmentation Model

This model[23][24] is another simplification of the string fragmentation model. Gluons split into a pair of parallel q and $\overline{q}$, and the resultant quarks and antiquarks fragment on their own. This straight forward approach inevitably leads to the non-conservation of flavour, momentum and energy during the fragmentation process.

2.4.3 Monte Carlo Programs

A) The JETSET program

The JETSET program[25] is a popular Monte Carlo simulation package in e^+e^- annihilation physics. Partons can be generated with the first order or second order matrix element (ME) calculations or with the parton shower calculation. The string fragmentation model is the default for the simulation of the hadronization process in JETSET 6.3, while the independent fragmentation model is also available in JETSET 6.3. The JETSET 6.3 is a fully implemented generator used officially in the SLD environment. The JETSET 7.3 and JETSET 7.4 also optionally include the scalar gluon model and the abelian vector gluon model.

B) The HERWIG program

The HERWIG program[26] is an alternative MC program used widely. It has the parton shower and the Webber cluster fragmentation model for the hadronization process as a default. In the Webber Cluster model[27], two hadrons are produced from each final cluster, with the relative probability for different decay channels given by the phase space and spin counting factors.

2.5 Jet-Finding Schemes

A jet-finding algorithm must specify clearly jet configuration starting from particles detected in the final state. There are several jet-finding algorithms : YCLUS (JADE)[28], LUCLUS algorithm[29], and other algorithms suggested at Durham[30] and at CERN[31]. J. Lauber's thesis[18] has a more detailed explanation of jet-finding

algorithms. The YCLUS and LUCLUS are two of the most popular jet cluster algorithm. Here the YCLUS[28] algorithm used in this analysis will explained.

2.5.1 YCLUS Algorithm

The YCLUS, called JADE, algorithm is an iterative process: assuming all particles are massless, a scaled invariant mass y_{ij} of two particles can be expressed as:

$$y_{ij} = \frac{2E_iE_j(1 - cos\theta_{ij})}{E_{vis}^2}$$

Where E_i and E_j are the particle energies and θ_{ij} is the angle between them. E_{vis} is the total visible energy in the event. In the first step, the two particles with the smallest invariant mass y_{ij}, are combined into one cluster (particle) by adding up their four-momenta. One then repeats the above procedure to the remaining particles, until all the scaled invariant masses left have $y_{ij} > y_{cut}$, where y_{cut} is a user defined cut off value. The clusters (or particles) at the end of this process are called jets, which depend on the cut-off value y_{cut}.

CHAPTER III

SLD AND THE SLAC LINEAR COLLIDER

The data used in this analysis were obtained with the SLAC Large Detector (SLD) operating at the SLAC Linear Collider (SLC). The SLC is located at the Stanford Linear Accelerator Center (SLAC), an e^+e^- collider, and was constructed for producing Z^0 particles at center-of-mass energy around 90 GeV for studying Z^0 physics.

The 1992 SLC run began with an unpolarized electron beam. In April of 1992, a polarized electron source was installed and commissioned. From May through August, SLC produced approximately 10,000 Z^0 events with an average electron beam polarization of 22%. SLD logged approximately 50,000 Z^0 events to tape with an electron beam polarization of 63% in March through August of 1993.

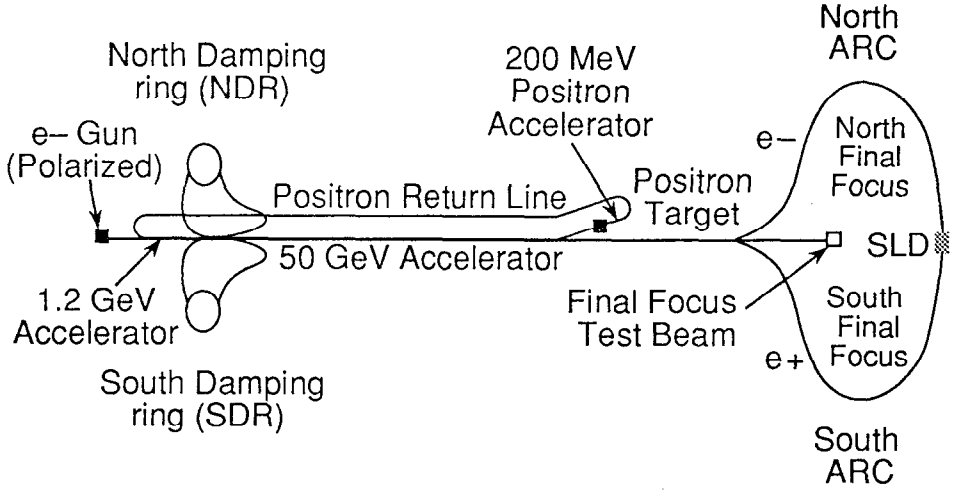

Figure 3.1: The SLAC Linear Collider (SLC).

3.1 The SLC

The SLC is the linear collider made for the first time[32]. Figure 3.1 displays a schematic layout of the SLC. Electron bunches from the source are injected into the north damping ring. Every alternate electron bunches extracted from this damping are directed into a fixed target at the 33 GeV point (two thirds point of the linear accelerator). The positrons are produced from the electro-magnetic shower and are returned to the beginning of linac sector. After the electron and positron bunches are accelerated to 1.2 GeV, they are moved to the north and the south damping rings. They are divided by a dipole magnet and sent to two arcs, loosing about 1 GeV energy due to the synchrotron radiation in the arcs. Before the beams collide, a small transverse beam size of about 2μm $\times$ 1μm is made through a set of superconducting focus quadrupole magnets (SCFF) in order to increase the luminosity.

Advantages of the linear collider compared to a circular storage ring are: the low energy loss due to synchrotron radiation, the ability to deliver longitudinally polarized beams, small beam spot size for increasing the luminosity and a smaller vertex detector with higher resolving power by a smaller beampipe. Disadvantages are: use of one crossing and a low repetition rate.

The luminosity can be expressed:

$$L = \frac{N^+ N^- f}{4\pi\sigma_x\sigma_y}$$

where N^+ and N^- are numbers of positrons and electrons in each bunch about 3×10^{10}, f = 120 Hz is the collision rate, and σ_x and σ_y are the beam spot size in x and y ($\approx 2\mu$m).

3.2 Polarization at SLC

The electron beam of the SLC is the first ever longitudinal polarization in e^+e^- annihilation. When a GaAs absorbs a circularly polarized laser beam, longitudinally polarized electrons are produced[33]. The energy of the photons must be slightly greater than the band gap energy in order to make photoemission. Angular momentum conservation allows the $P_{\frac{3}{2}}$ valence band electrons to transfer to the $S_{\frac{1}{2}}$ conduction band by absorbing the circularly polarized photons in a 3:1 ratio. Therefore, if the 100% circularly polarized laser light is applied to a GaAs, the maximum possible polarization of a GaAs is theoretically 50%. The excitation of conduction band electrons make the real polarization smaller than the theoretical polarization.

Figure 3.2 displays the electron polarization depending on different types of cathodes and laser wavelength. In 1992, SLC produced an electron beam with 28% polarization by using a bulk GaAs cathode and a laser wavelength of 715 nm. The strained GaAs cathodes theoretically allows for 100 % polarization by removing the degeneracy of the $P_{\frac{3}{2}}$ valence state and shows the polarizations more than 50%[34].

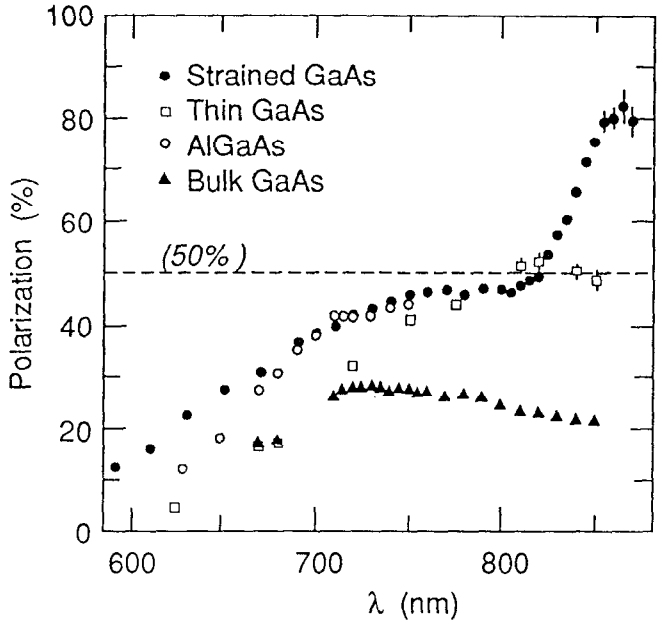

Figure 3.2: Electron polarization as a function of source laser wavelength (λ). SLC utilized a bulk GaAs cathode in 1992 and a strained GaAs cathode in 1993.

In 1993, an average electron beam polarization with 63% was obtained by using 865 nm of the laser wavelength.

Two kinds of polarimeters are used to measure the polarization. A Møller polarimeter at the end of the linac is used for diagnostic purposes. It makes use of the polarized asymmetry of the cross section in electron-electron elastic scattering in a thin iron foil which can be moved into the beam line. A compton polarimeter is used to continually monitor the polarization of the electron beam after it has passed through the IP and before the beam is extracted. The electron beam collides with polarized photon beam that is produced by a frequency-doubled Nd:YAG laser. A diagram of the polarimeter is shown in figure 3.10.

The Compton scattering cross section of the electron-photon collisions has a large asymmetry[33], which depends on the photon beam polarization, electron beam polarization and the energy of the scattered electrons. Accurate measurements of the photon beam polarization and the energy of scattered electrons provide a good determination of the electron beam polarization.

3.3 Overview of SLD

The SLD (SLAC Large Detector), shown in figure 3.3, consists of many individual detectors, which use state of the art technology, designed to study physics at the Z^0

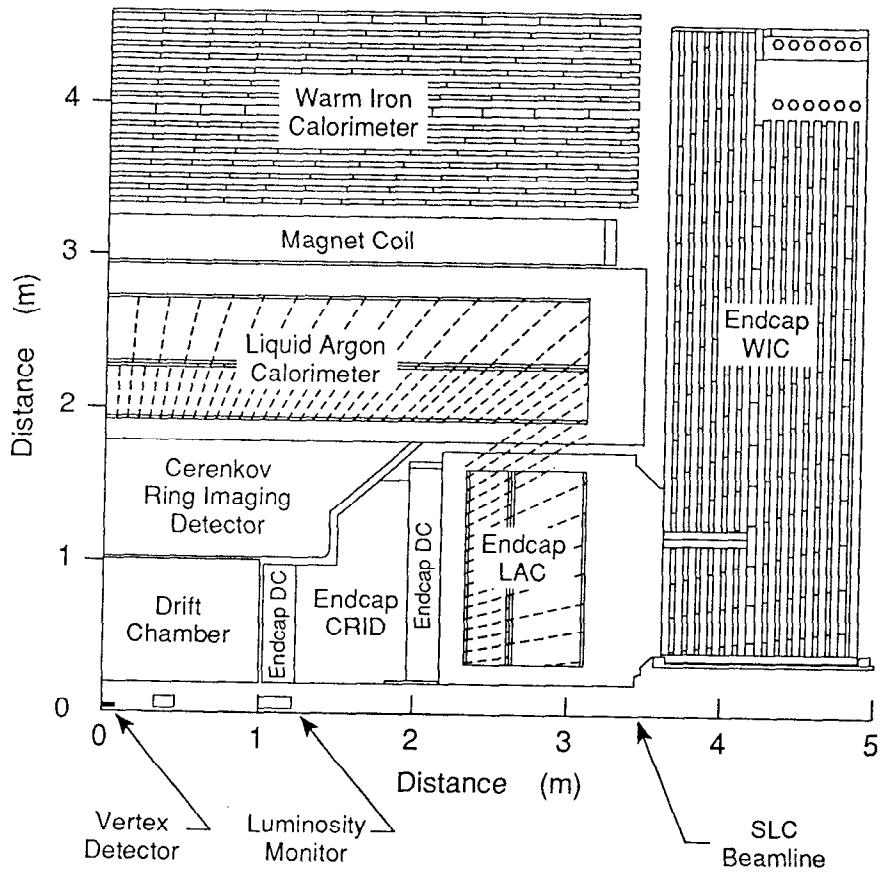

Figure 3.3: Quadrant view of the SLD.

mass energy scale[35]. All detector components are contained in a 9 m diameter octagonal steel structure. Particle tracking is done with a silicon vertex detector (VXD) and a precision central drift chamber (CDC) and a set of endcap drift chambers (EDC) for low angle tracks. Particle identification is provided by a set of Cherenkov Ring Imaging Detectors (CRID). Calorimetry is provided by three parts: a Liquid Argon Calorimeter (LAC), measuring the electromagnetic part of the energy and 85% of the hadronic energy, a Warm Iron Calorimeter (WIC), that measures the tail ends of the hadronic showers and is also capable to track the escaping muons, and a Luminosity Monitor (LUM) which measures energies deposited in the extreme forward and backward directions. All the components, except for the WIC are placed inside a magnet coil producing a 0.6 Telsa magnetic field.

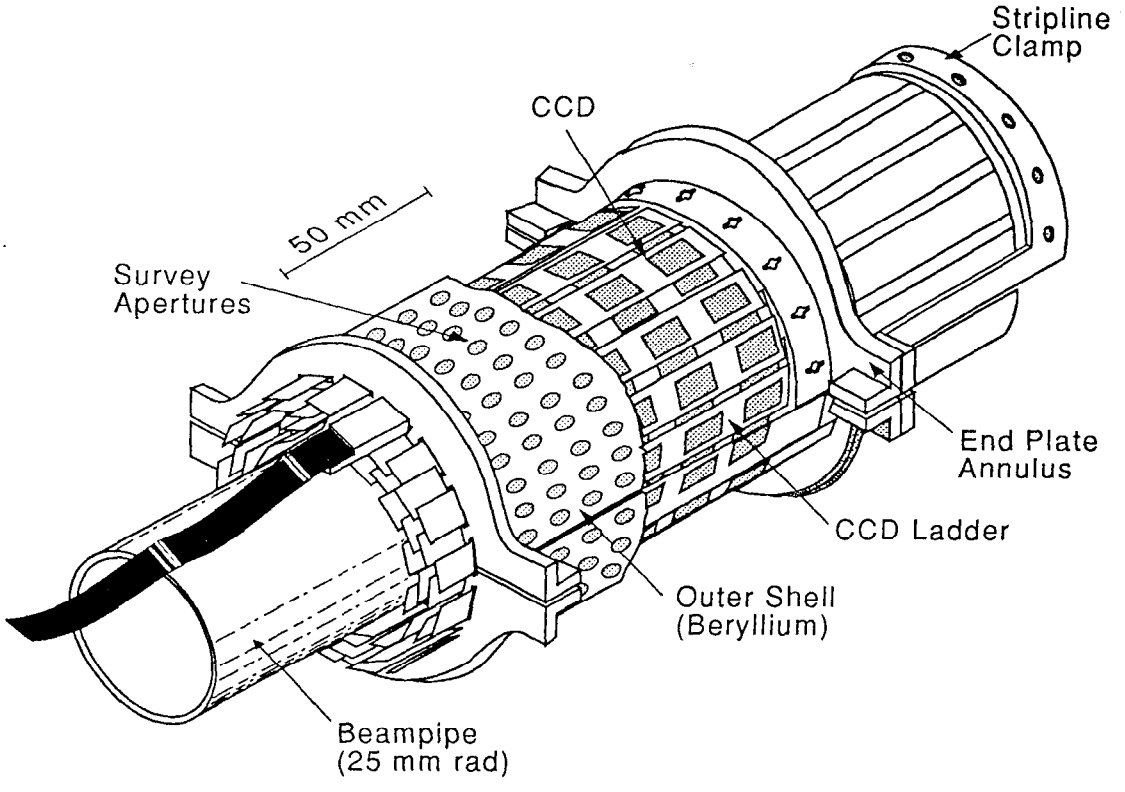

Figure 3.4: The SLD Vertex Detector.

3.3.1 Vertex detector

The Vertex Detector (shown in figure 3.4) is based on silicon charged coupled devices (CCD)[36]. It comprises 480 CCD chips, each CCD contains approximately 400× 600 pixels, adding up to a total of 120 million pixels. Each pixel functions as an independent particle detection element, providing space point measurements of charged particle tracks with a typical precision of 5 μm in each coordinate.

When track points are linked with tracks reconstructed by the Central Drift Chamber, secondary vertices from heavy quark and tau lepton decays can be resolved with high precision.

3.3.2 Drift Chambers

The drift chambers are gas-wire tracking systems. The Central Drift Chamber (CDC) contains a cylindrical arrangement of wires which run approximately parallel to the beam line. Ionization from charged particles passing through the chamber drifts to the wires in the presence of large electrostatic fields. The wires are instrumented

on both ends, so the z component of the tracks may be found via charge division.

The Endcap Drift Chambers have wires running perpendicular to the beamline for track reconstruction at smaller angles. The chambers are divided into an inner and outer chamber. Backgrounds from the SLC as well as material in front of the EDCs have thus far hampered their ability to find charged tracks.

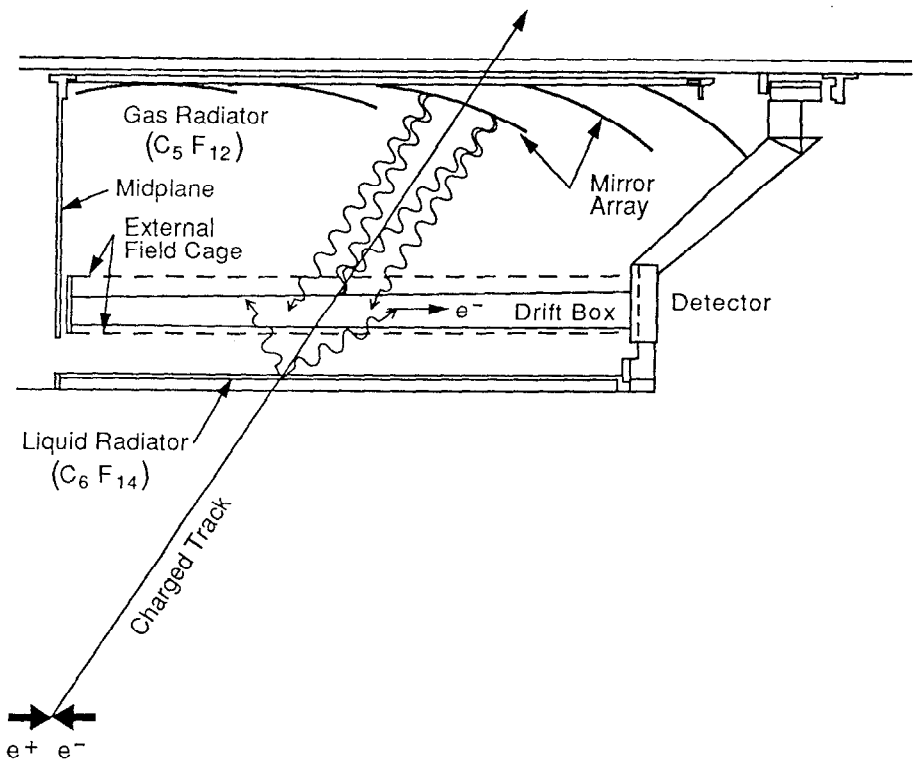

Figure 3.5: The SLD Cherenkov Ring Imaging Detector (CRID).

3.3.3 CRID

The Cherenkov Ring Imaging Detector (CRID) is used for particle identification and flavor tagging. When a charged particle passed through a medium, exceeding the speed of light in that medium, the atoms get polarized and emit photons (Cherenkov radiation). The opening angle of the light cone with respect to the incident track is inversely proportional to the velocity. The emitted light is focused onto a photon detector and by measuring the radius of the light circle one can determine the velocity of the particle. Together with a momentum measurement of the particle the mass and hence type of the particle can be determined[37].

The CRID is shown schematically in figure 3.5. The barrel CRID sits between the CDC and the LAC. In the case of the endcap, the CRID is sandwiched between layers of the Endcap Drift Chamber.

3.3.4 The Liquid Argon Calorimeter

The Liquid Argon Calorimeter (LAC) is composed of a cylindrical barrel and two endcap calorimeters, forming three distinct mechanical and cryogenic systems. The barrel and endcap calorimeter system cover 98% of the full solid angle for both electromagnetic and hadronic showers. The LAC is designed to contain about 85% of the energy of the jets in a hadronic Z^0 decay. The LAC design is based on getting equalization of electromagnetic and hadronic response (e/h = 1) for sampling calorimeter of an absorber/radiator[38, 39]. Electromagnetic energy response is suppressed in calorimeters built from high Z absorber, compensating the invisible hadronic energy expended in nuclear breakup. Therefore, the e/h $\approx$ 1 can be achieved by using a high Z absorber such as lead or uranium for liquid argon devices.

The barrel LAC extends from 177 cm to 291 cm in radius and 6.2 m long in the axial (z) direction. It is composed of 288 modules of EM and HAD mounted within a large cylindrical cryostat and sharing a common liquid argon volume. It covers the angular region $35^0 \leq \theta \leq 145^0$, where θ is the polar angle from the beam line. The barrel LAC has 192 EM towers in the azimuthal angle (ϕ), each with an opening angle $\delta\phi$ = 33 mr. The barrel has 34 EM towers in polar angle (θ) for the north and south sides. Each EM tower has the opening angle from $\delta\theta$ = 36 mr at the center of the barrel to $\delta\theta$ = 21 mr at the end of barrel for providing a constant projection area for electomagnetic showers. HAD towers are twice as large as EM towers in both transverse dimensions. The full azimuth of the cylinder is spanned by 48 modules of width $\approx$ 30 cm. The axial direction is spanned by 3 modules of length $\approx$ 2 m attached to and separated by annular "washers" which are integral parts of the cryostat structure. In the radial direction, two separate type of modules, electromagnetic modules (EM) covering the radial region of 193 - 222 cm, and hadronic modules (HAD: 222 - 271 cm), are mounted concentrically about the beam line (figure 3.6).

The two endcap sections of the LAC, extending from 0.33 to 1.60 m in radius and from 2.32 to 3.10 m in the axial direction at both ends, are composed of 16 wedge-shaped modules, again mounted within a common cryostat and sharing a common liquid argon volume (Figure 3.7). It comes from the angular range $8^0 \leq \theta \leq 35^0$ and $145^0 \leq \theta \leq 172^0$. The most worst energy degradation in the overlap region ($31^0 \leq \theta \leq 35^0$) with barrel comes from dewar and support. Endcap modules incorporate both EM and HAD sections in one mechanical unit. They are functionally identical to barrel modules but different in module design and construction. The azimuthal segmentation of the EM sections are 192, 96 and 48 towers depending on the radius for maintaining a contant projection area.

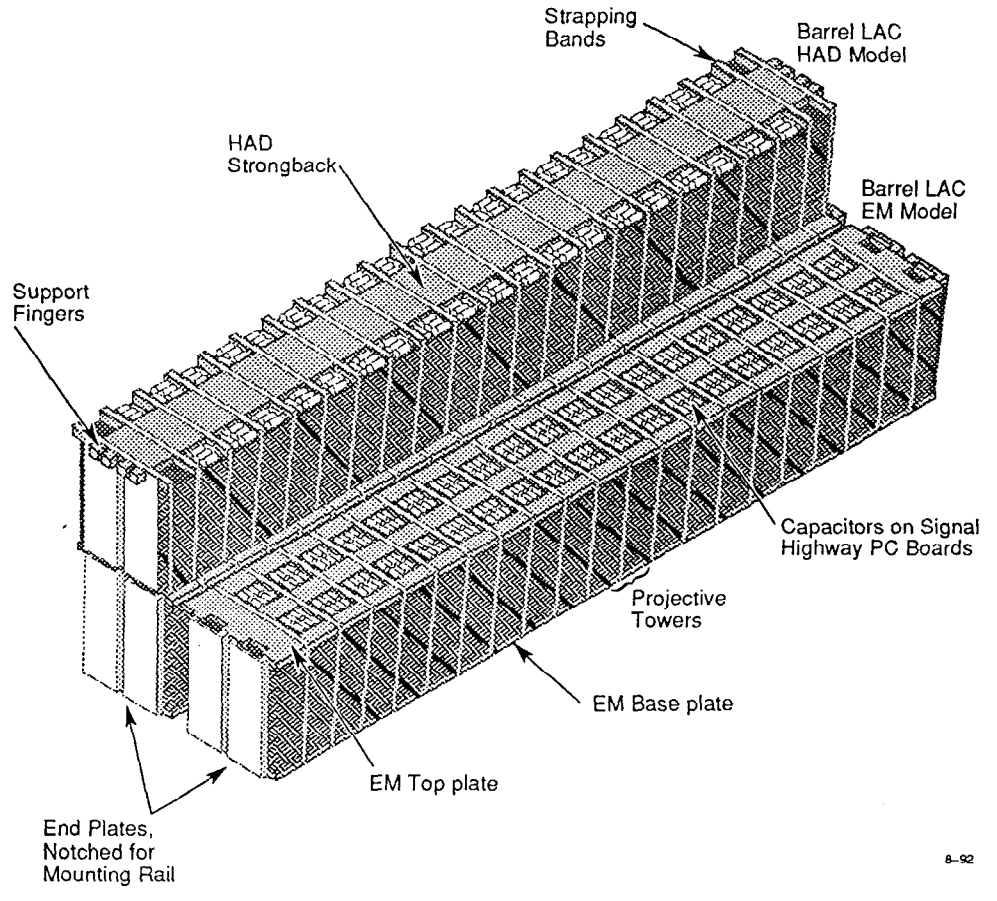

Figure 3.6: A LAC barrel module.

LAC modules consist of alternate planes of large lead sheets (plates) and segmented lead tiles (figure 3.8), with liquid argon filling gaps between the planes. The lead plates are grounded, while the tiles are held at negative high voltage and serve as the charge collecting electrodes. The EM calorimeter modules consist of lead plates and tiles, each of 0.2 cm thick, $\approx$ 200 cm long and 25 -29 cm wide, separated from each other by 0.275 cm with liquid argon in between. The lead plates and tiles in the HAD modules are 0.6 cm thick, $\approx$200 cm long and 29-35 cm wide, and are separated by 0.275 cm gaps filled with liquid argon.

The EM calorimeter is divided radially into two separate readout sections to provide information on longitudinal shower development for electron/pion discrimination. The front section (EM1) contains 6 radiation lengths of material, while the back section (EM2) contains 15 radiation lengths. The total of 21 radiation lengths in the EM calorimeter is sufficient to contain 50 GeV electrons, with leakage of 1-2%. The HAD calorimeter is also divided into two separate read out sections (HAD1 and HAD2), each has one interaction length in thickness. The total LAC thickness of

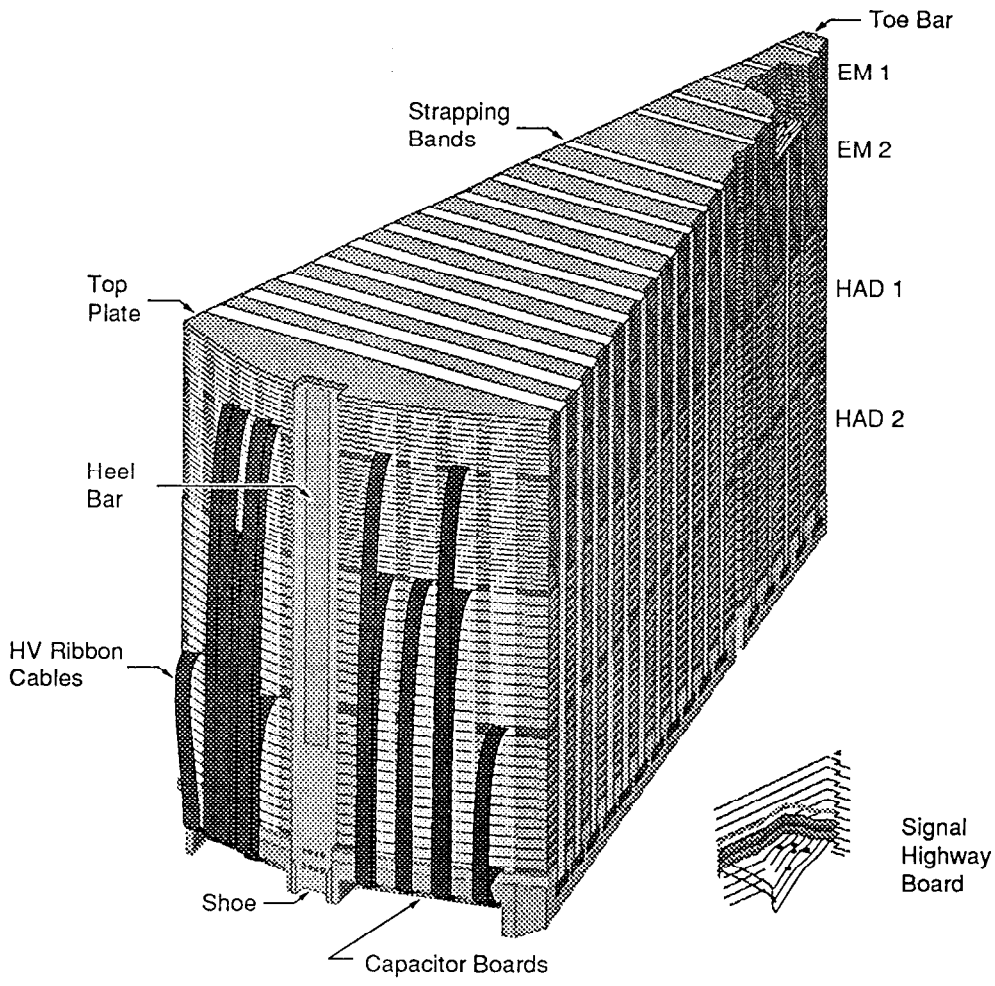

Figure 3.7: A LAC endcap module.

2.8 interaction lengths is enough to contain 80-90 % of the hadronic shower energy. Energy leaking out of the LAC is measured in the WIC calorimeter. The energy resolution of electromagnetic showers is expected to be 10-20 %, while the energy resolution of hadrons is expected to be $\approx 60\%/\sqrt{E}$[38].

3.3.5 The Luminosity Monitor

The luminosity monitor system[40][41] is divided into two separate modules displayed in Figure 3.9: the luminosity monitor small angle tagger (LMSAT) and the medium angle silicon calorimeter (MASC). This system is essentially a very low angle and high precision electromagnetic calorimeter. The LMSAT/MASC system is a silicon sampling calorimeter with a tungsten radiator and a 1.54% sampling fraction. The LMSAT was built at the University of Oregon. A precise measurement of the luminosity is made through tagging forward e^+e^- final states.

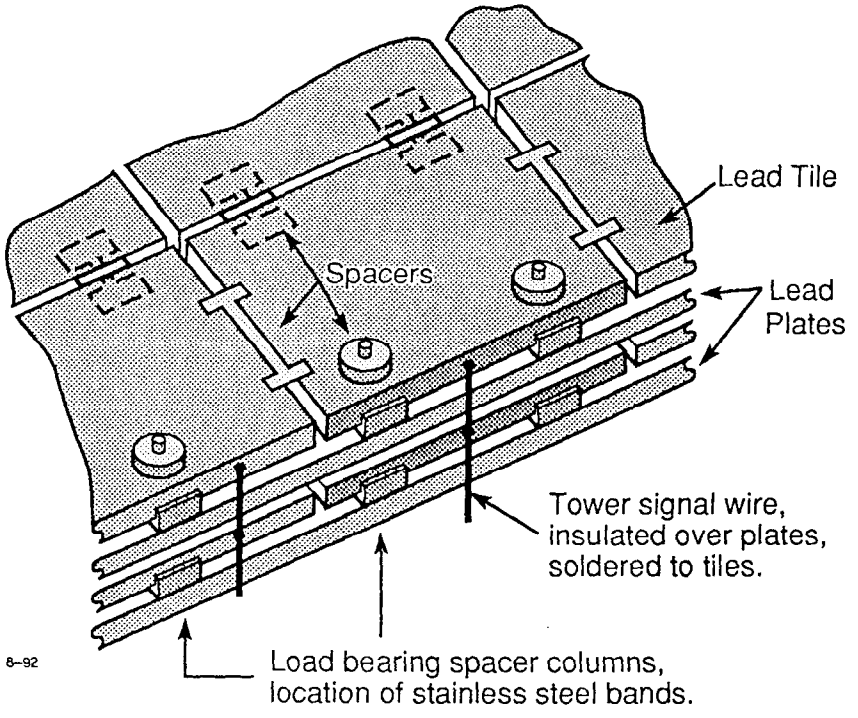

Figure 3.8: One cell from the barrel LAC.

The LMSAT provide an angular coverage of 23 to 68 miliradians from the SLD beampipe at a distance of 100 cm from the interaction point. The total depth of the calorimeter is 21 X_0, containing $> 99.5\%$ of a 45 GeV electromagnetic shower. The LMSAT consists of 23 radiator plates, each approximately one radiation length deep, instrumented with silicon detectors between the plate gaps. The MASC covers the area of 68 to 190 milliradians and sat 31 cm away from the IP. The radiator plates are made of a 90% tungsten, 10% Cu-Ni heavy met alloy. Since the differential cross section of the small angle Bhabha process is large and rapidly changes at small angles, the LMSAT is required to have excellent angular resolution. Each layer is transversely segmented in a projective tower geometry. The polar segmentation is 9 milliradians and the segmentation in ϕ is 11.25 degrees.

Readout electronics for both the LMSAT and MASC are contained in one "tophat" which mounts behind the luminosity monitor. The LMSAT and MASC consist of a total of 640 and 384 electronic channels respectively. They have two readout electronics sections. The first six layers are connected in parallel and called to be EM1.

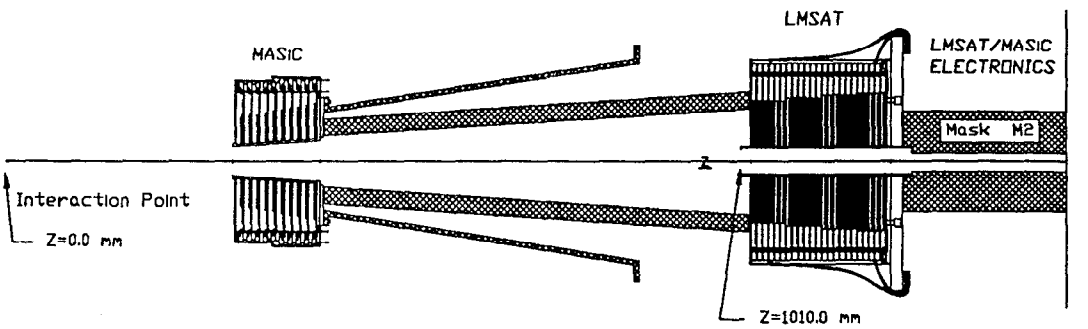

Figure 3.9: Side view of LMSAT and MASC.

The second seventeen layers are connected in paralled and called to be EM2.

3.3.6 Warm Iron Calorimeter(WIC)

The Warm Iron Calorimeter (WIC) is located outside the SLD solenoidal magnet, which also functions as the flux return of the magnetic field[42]. The total thickness of the WIC is 4.2 nuclear interaction lengths (λ), comprised of 14 steel plates 5 cm thick. In addition, there are two iron endcaps which support the remainder of the endcap components.

The WIC provides a complete hadronic shower measurement, muon identification and muon tracking. The limited streamer tubes are read out with strip electrodes for muon tracking and identification, and pad electrodes for hadron calorimetry.

3.3.7 Trigger and Data Acquisition

Four independent triggers were used for taking 1993 data with polarized electron beams. Energy and track triggers were used for triggering Z^0 events, a bhabha trigger for small angle Bhabha events, and a random trigger for background studies. There is a non-independent trigger called the hadron trigger. This trigger used information of both the LAC and CDC, and it required the total LAC energy to be above 8 GeV with high tower threshold and a least a single track in the CDC.

The CDMs (Calorimeter Data Modules) form tower energy sums for use in the trigger decision. For triggered events, the CDMs compact the event data using layer-dependent threshold cuts, and attaches a tower identification tag to each hit above tower threshold. The AEBs (Aleph Event Builders) coordinates the operation of the CDMs[43], ensuring that they deliver information belonging to the same event. The AEB also reorganizes the tower identification tags and converts the data collected from the CDMs to the proper offline format for logging.

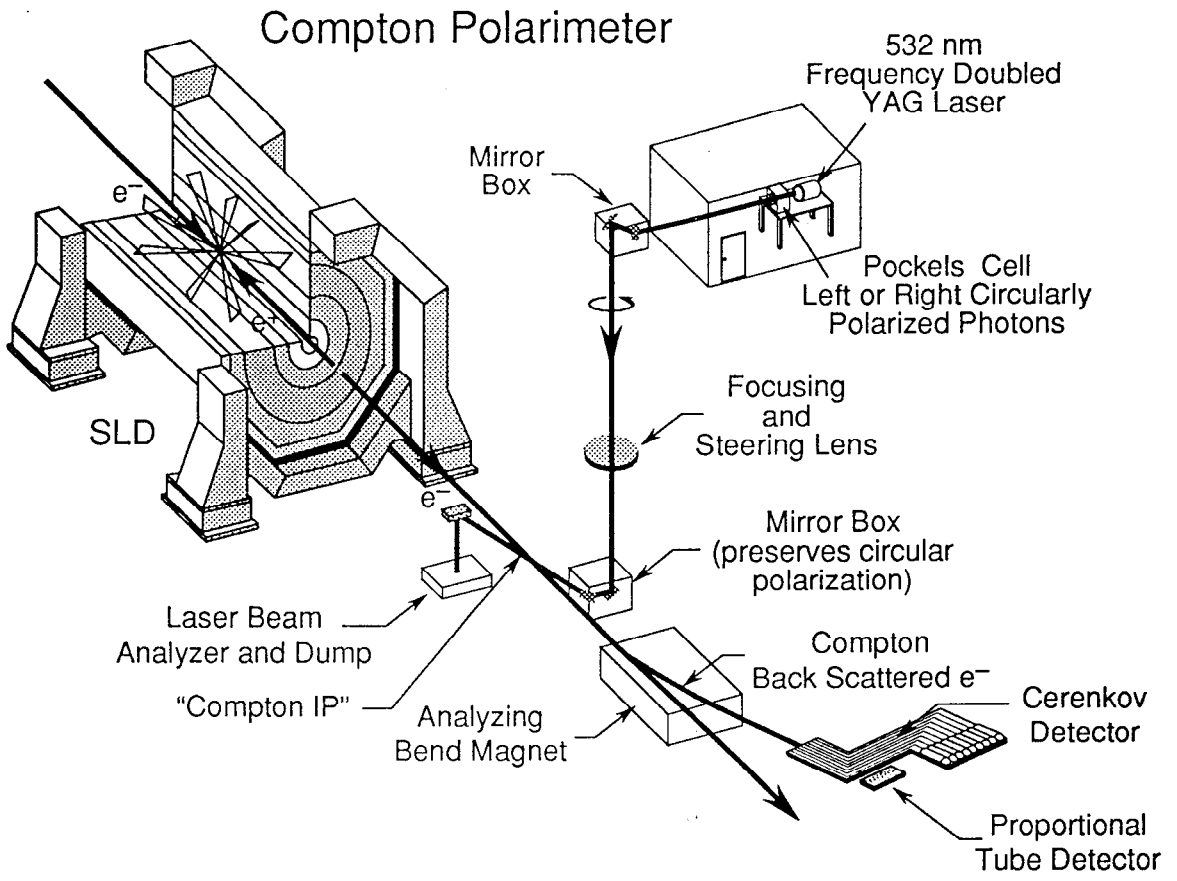

Figure 3.10: The Compton Polarimeter. Polarized photons are scattered off the extracted electrons. The electrons are momentum analyzed to determine the beam polarization.

CHAPTER IV

HADRONIC Z^0 EVENT SELECTION AND ENERGY RESPONSE CORRECTION IN THE SLD LAC

This chapter will describe the data processing and selection algorithm used to identify hadronic events reconstructed to three-jet events. The Monte Carlo simulation of the SLD detector will be described in the context of calculating the correction factors to be applied to the data due to endcap LAC energy response inefficiency. The event selection, data processing and detector simulation described is based on these references[44][45]. Much of the discussion in 4.1 and 4.2 sections is taken or summarized from the reference[45]. Some parts of 4.4 and 4.3.2 are taken from the reference[45].

4.1 Data Processing

4.1.1 Trigger

A trigger is contained within the on-line data acquisition system to identify electron-positron interactions in the SLD during a beam crossing. This trigger starts by considering only events which satisfy the ENERGY trigger[46]. The ENERGY trigger performs several sets of energy sums and tower counts based on two thresholds, defined as the "low" and "high" thresholds. The high threshold requires the energy in a tower to be above the energy deposited by a minimum ionizing particle, while the low threshold is placed slightly above the typical electronics noise.

The conversion from ADC to energy for the LAC is 524 MeV/128 ADC counts in the EM sections and 1384 MeV/128 ADC counts in the HAD sections.[1]

The following sums are made in the trigger:

- ELO = the sum of the energy in all towers above the low threshold

[1]The energy scale used here is the minimum ionizing energy scale, which means no e/μ or π/μ correction factor has been applied.

- EHI = the sum of the energy in all towers above the high threshold
- NLO = the numbers of towers above the low threshold
- NEMHI = the numbers of towers in the EM section above the high threshold.

The high thresholds for the EM and HAD layers were 60 and 120 ADC counts, respectively, for eliminating the SLC muon background. Due to the unique SLC muon background there are lots of SLC muon hits on the west and east side of the barrel LAC and this is called the "ring of fire". For reducing the ring of fire, the towers at $\Theta_{bin} = 48$ were excluded in the tower energy sum, which corresponds to the angular value $|cos\theta| = 0.98$. The low threshold is 8 ADC counts in the EM sections and 12 ADC counts in the HAD.

The trigger requirement is such that the sum of energy in towers above the high threshold be EHI $\geq$ 8 GeV for the 1992 run. This trigger was made more stringent for the 1993 run with EHI $\geq$ 12 GeV. It is also very robust against the muon background from upstream in the SLC. The trigger is vetoed if more than 1000 towers contribute to the low threshold sum (NLO $<$ 1000). This veto protects against particularly bad pulses.

4.2 PASS 1 Filter

Events which satisfy the trigger are written to tape. Before reconstruction, these events are subjected to the PASS 1 filter, which greatly enriches with events with interactions. The PASS 1 requirements are as follows:

- NEMHI $\geq$ 10 towers
- EHI $>$ 15 GeV
- ELO $<$ 140 GeV
- ELO $< \frac{2}{3}$ EHI + 70 GeV

PASS 1 is effectively a tightening of the trigger. Figure 4.1 [2] shows the quantity EHI plotted against ELO. The number of towers contributing to the EHI sum is always less than or equal to the number of towers contributing to the ELO sum, making the region EHI $>$ ELO forbidden. Events in the region centered at roughly 60 GeV on the ELO axis and 40 GeV on the EHI axis are primarily hadronic decays of the Z^0, while events with ELO $>$ 60 GeV and EHI $\simeq$ ELO are the wide angle Bhabha events, where most of the energy is deposited in relatively few towers [44].

[2]There were 18,393 PASS 1 events in 1992 and 63,553 PASS 1 events in 1993. In many plots, every 15th event has been selected to make the plots legible and to demonstrate the trends. Figure 4.1 shows a sample of 4,236 PASS 1 events from the 1993 run. The trends seen in the full sample are identical to those displayed in the figure. mip refers to the minimum ionizing energy scale.

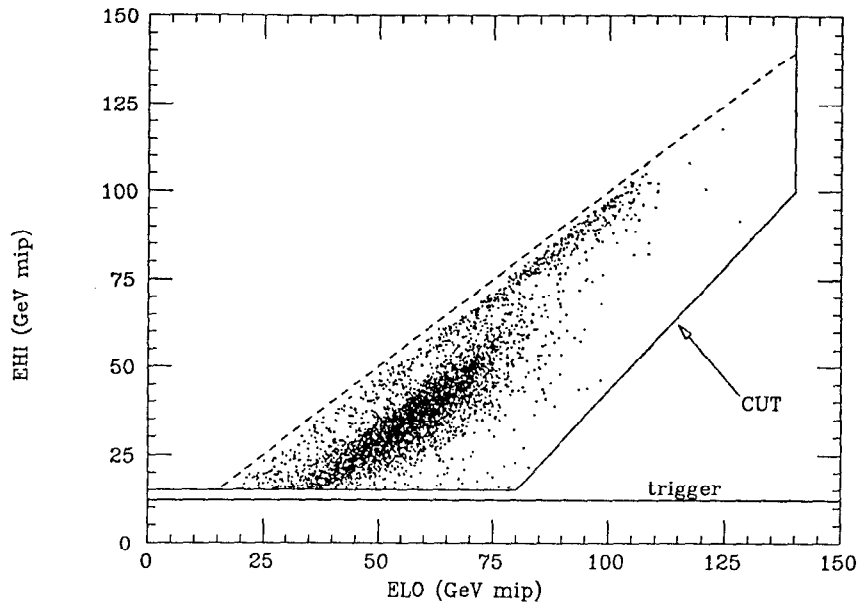

Figure 4.1: PASS 1 energy sums (EHI vs. ELO).

4.2.1 Reconstruction

Events which satisfy the PASS 1 filter are passed through the calorimeter reconstruction. The reconstruction forms "clusters" of localized energy based on the UCLUS algorithm[47]. The WIC PADs, Luminosity Monitor and the Medium Angle Silicon Calorimeter are not included in the reconstruction. Also, LAC towers below 7 ADC counts in the EM section and 9 ADC counts in the HAD section are excluded from clusters. The effect of this on the energy response is virtually nil, while drastically cutting the number of clusters in each event. These single-hit clusters arise from beam background and electronics noise.

The reconstruction attempts to separate clusters if it appears the cluster was formed by more than one incident particle. This primarily affects the response in the jet environment of the hadronic events, as the algorithm tries to break-off hadronic and electromagnetic showers which partially overlap.

Cluster position is calculated as an energy weighted mean summed over all towers in the cluster. Each cluster is then defined by E (cluster energy), ϕ (azimuthal angle) and $cos\theta$ (polar angle) with respect to the beam axis.

Clusters are subjected to a pattern recognition routine which looks for strings of calorimeter hits which run approximately parallel to the beam line and deposit minimum ionizing energy into the liquid argon[48]. These clusters are flagged as muons produced by the tails of the beam hitting the SLC upstream collimation[49]. The SLC muon background is the dominant form of background for the LAC. There

is enough material between the beam line and the LAC to stop most of the low energy radiation coming from the final focusing of the beams. The only exception to this is the ring of LAC towers which surround the beamline.

4.3 Detector Simulation

4.3.1 Generator Level Simulation

The hadronic events were generated with the parameters of HERWIG5.7[26] listed in table 4.1. The parameters such as Λ_{QCD}, m_g and M_{max} are the main parameters for the control of the momentum distribution of hadrons. Λ_{QCD} is the QCD scale parameter related with branching of partons. m_g is the effective gluon mass belongs to the parton shower evolution. M_{max} is the maximum allowed mass of a cluster made from two quarks. Since the YCLUS algorithm with $y_c = 0.02$[28] (see section 2.5.1) was used in the reconstruction of three-jet events, T_{max} (maximum thrust in the production of three partons) was changed from 0.9 to 0.98.

Parameter	MC name	Default value	Value used
Λ_{QCD}	QCDLAM	0.18 GeV	0.18 GeV
m_g	RMASS(13)	0.75 GeV	0.75 GeV
M_{max}	CLMAX	3.35 GeV	3.35 GeV
T_{max}	THMAX	0.9	0.98

Table 4.1: Main default parameters of HERWIG5.7 version.

4.3.2 Geant Simulation

Figure 4.2 shows the LAC response for events which have satisfied PASS1 requirements and hadronic Z^0 selection conditions (see section 4.4). A degraded response may be clearly seen in the overlap region ($0.65 < |cos\theta_T| < 0.85$) and the endcap region ($|cos\theta_T| > 0.85$). The reason for this degraded response is the electronics, cables, plumbing and material in front of the LAC serving other systems.

To understand the poor response seen in the LAC at $|cos\theta_T| > 0.7$, a study of some of the materials such as electronics and cables known to be inside the detector, but not in the simulation, was undertaken by K.T. Pitts[45]. He installed the approximate amount of material in radiation lengths a particle must traverse before reaching the first active layer of argon as a function of angle like figure 4.3[45]. The

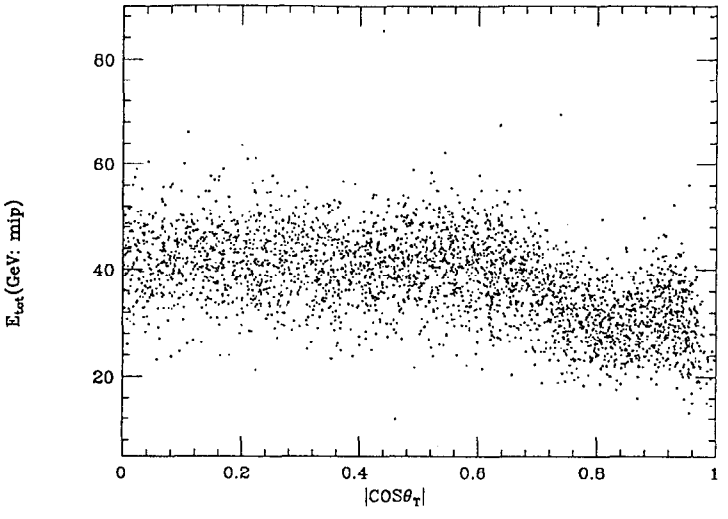

Figure 4.2: Calorimeter energy response as a function of thrust angle for data. The events in this plot are required to satisfy PASS1 and hadronic Z^0 selection condition. They are selected for every fifteenth event in order to see structure. mip refers to the minimum ionizing energy scale.

dashed line is the original SLD Monte Carlo, the solid line is the Monte Carlo after adding approximations to the materials in regions where they are known to exist.

The detector simulation is done with GEANT[50] and material at the front of LAC installed by K.T. Pitts. Electromagnetic and hadronic showers are simulated via the GFLASH algorithm[51]. After the events are passed through the GEANT simulation, they are superimposed ("overlayed") on a set of luminosity-weighted random triggers to accurately simulate the backgrounds produced by the SLC. It is useful to check how many hadronic events were lost after the PASS1 filter in order to calculate the efficiency. Figure 4.4 shows EHI versus ELO before PASS1 filter for Monte Carlo simulation of hadronic events. Approximately 2% hadronic events are not passed after PASS1 filter. Most failed events comes from the endcap region around the beam pipe as seen in figure 4.5. Here $cos\theta_T$ is the angle of the thrust axis of the generated event relative to the beam axis.

47,411 Monte Carlo events are passed through trigger, PASS1 Filter and calorimeter reconstruction using the same method as the actual data. Figure 4.6 shows the calorimeter energy response as a function of thrust angle for the Monte Carlo. The data and the Monte Carlo after the material has been added agree quite well.

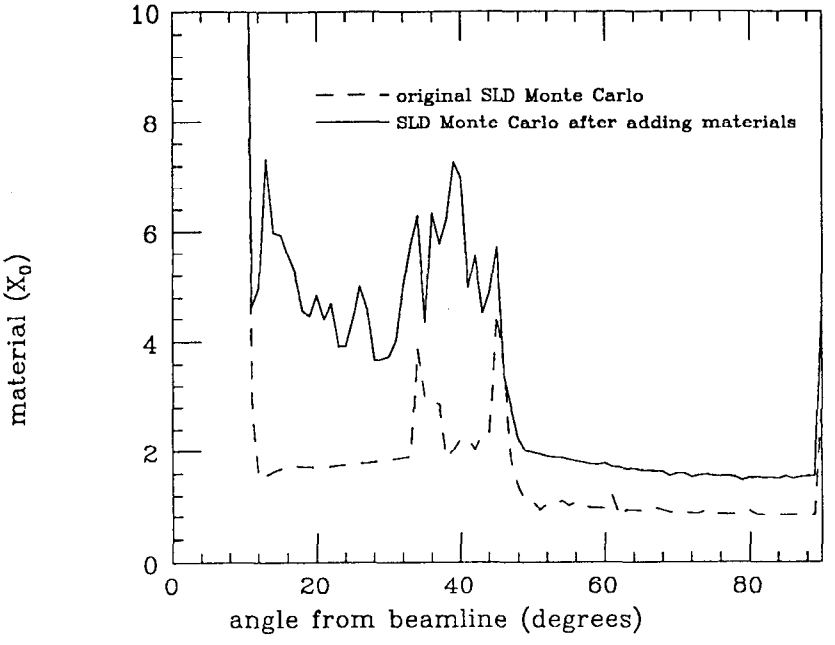

Figure 4.3: Estimation of the amount of material in front of the Liquid Argon Calorimeter as a function of angle. The solid curve shows the estimated amount of material a particle must traverse before it reaches the first argon gap. The dashed curve was the simulation before improvement. This figure was taken from reference[45].

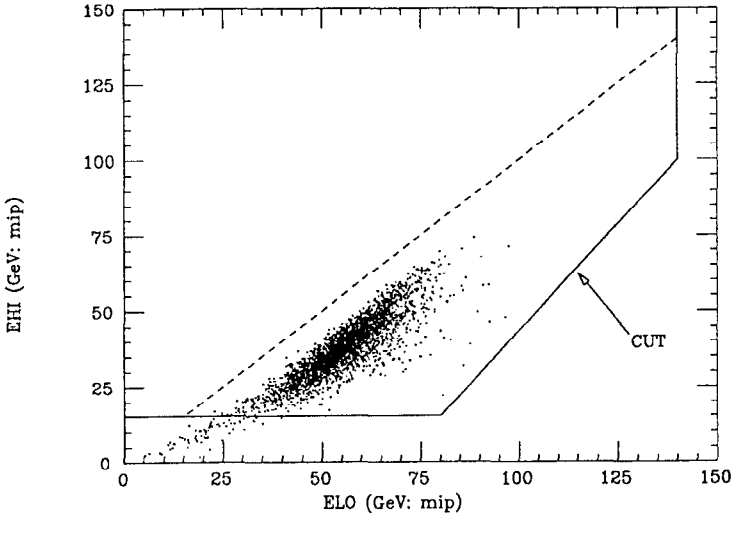

Figure 4.4: Energy sums for Monte Carlo before PASS1 filter (EHI vs. ELO).

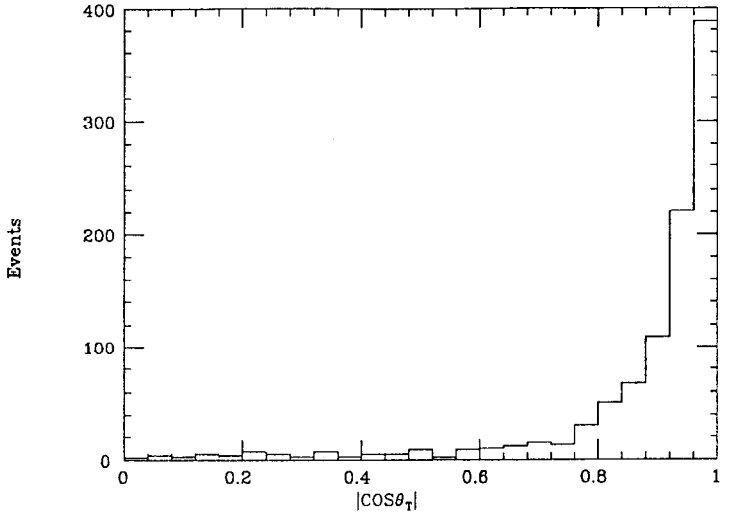

Figure 4.5: The failed events versus $|cos\theta_T|$ after PASS1 filter in Monte Carlo simulation: Most failed events comes from the endcap region around the beam pipe. $cos\theta_T$ is the angle of the thrust axis of the generated event relative to the beam axis.

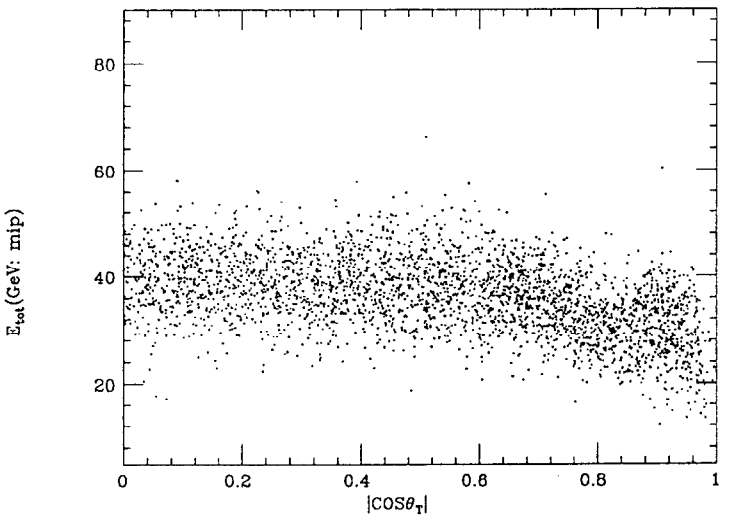

Figure 4.6: Calorimeter energy response as a function of thrust angle for Monte Carlo. The events in this plot are required to satisfy PASS1 and hadronic Z^0 selection condition. They are selected for every fifteenth event in order to see structure. mip refers to the minimum ionizing energy scale.

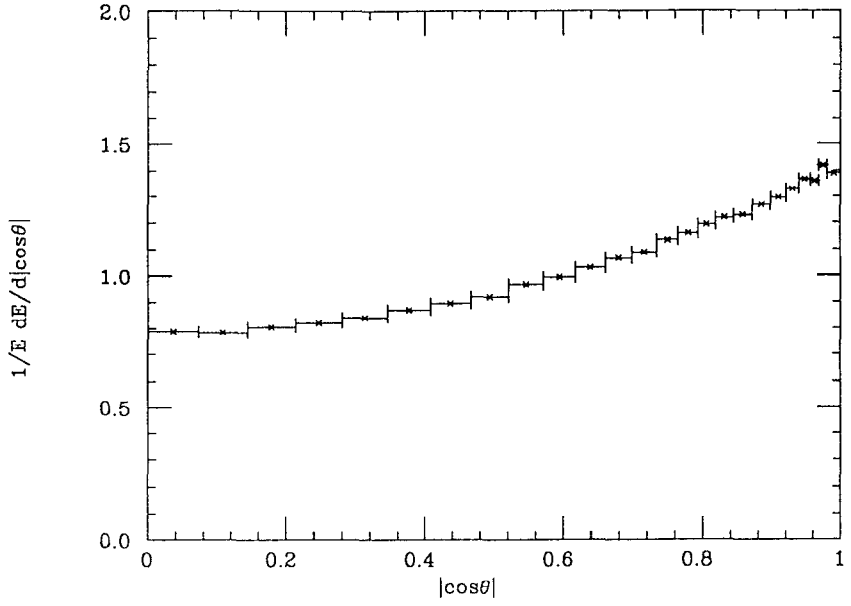

Figure 4.7: The normalized energy of hadrons from GEANT as a function of $|cos\theta|$.

4.3.3 Correction of LAC Energy Response

The LAC energy response as a function of $|cos\theta|$ may be compensated by comparing energies of hadrons at the generator level to energies of clusters in the GEANT simulation. θ is the scattering angle with respect to the electron direction. The energies of clusters in the GEANT simulation are reconstructed without using beam background or the PASS1 filter in order to just see the energy response of hadrons through the detector simulation.

The transverse segmentation of the LAC is provided by the segmented lead tiles. Tiles from successive layers are laid out in a projective pattern, and stacks of these tiles are ganged electrically into towers. The tile size increases with polar angle (θ), so as to maintain a constant projective area for electromagnetic showers. The opening angle of an EM tower thus decreases from $\delta\theta = 36$ mr at the center of the barrel to $\delta\theta = 21$ mr at the end of the barrel. HAD towers are twice as large as EM towers in both transverse dimensions. The polar angle segmentation of the endcap follows the same philosophy of barrel segmentation, with the range $8^0 < \theta < 35^0$ divided into 17 segments. The transverse segmentation in the HAD sections is again twice as coarse as in the EM sections[52].

The energies of hadrons as a function of $|cos\theta|$ are accumulated for $\approx$ 50,000 events. The bin sizes are chosen to match LAC tower boundaries. Figure 4.7 shows the energy distribution after normalization.

The energies of clusters in the GEANT simulation were also accumulated. Fig-

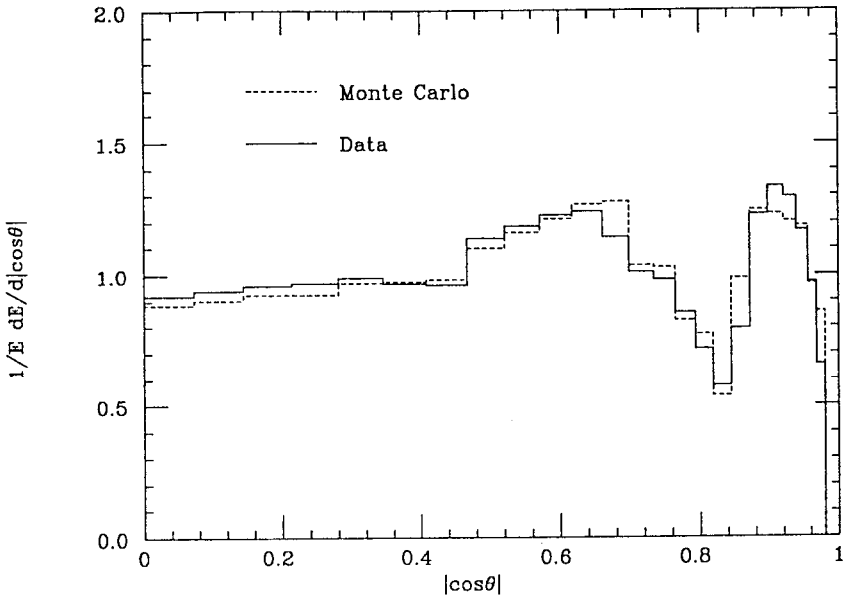

Figure 4.8: The normalized energy of clusters in the GEANT simulation and Data as a function of $|cos\theta|$.

ure 4.8 shows the normalized energy of clusters in the GEANT simulation as a function of $|cos\theta|$. To determine the relative LAC energy response, each bin of figure 4.8 is divided by each bin of figure 4.7. The relative LAC energy response as a function of $|cos\theta|$ can be seen in figure 4.9. Here the value of each bin calculated above is normalized to the value of the bin with the maximum ratio ($0.618 < |cos\theta| \leq 0.660$). The correction factor of LAC energy response can be obtained as the reciprocal value of the relative LAC energy response as seen in the figure 4.10 and listed in table 4.2 as a function of $|cos\theta|$.

The LAC towers greater than $|cos\theta| = 0.98$ were excluded in the tower energy sum due to the SLC muon background (see section 4.1.1). The energy response around $|cos\theta| = 0.63$ has the maximum response (minimum correction factor) due to maximum longitudinal length of LAC tower (see figure 3.3).

Figure 4.9 shows the behavior seen previously by K.T. Pitts [45]. The degraded response seen for $0.408 < |cos\theta| \leq 0.466$ is due to the LAC washer, where the central and two end sections of the barrel LAC come together. The region between 0.76 and 0.88 in $|cos\theta|$ demonstrates a highly degraded response, due to the electronics, cables and plumbing necessary to operate the inner systems. The electronics and cables for the barrel CRID, the endcap CRID and endcap Drift Chambers all reside in this region. Further into the endcap ($0.88 < |cos\theta| < 0.94$) the response recovers somewhat, but does not come near the response of the barrel. At smallest angles ($|cos\theta| > 0.95$) the cables, electronics and cryogenics of the Vertex Detector, as well

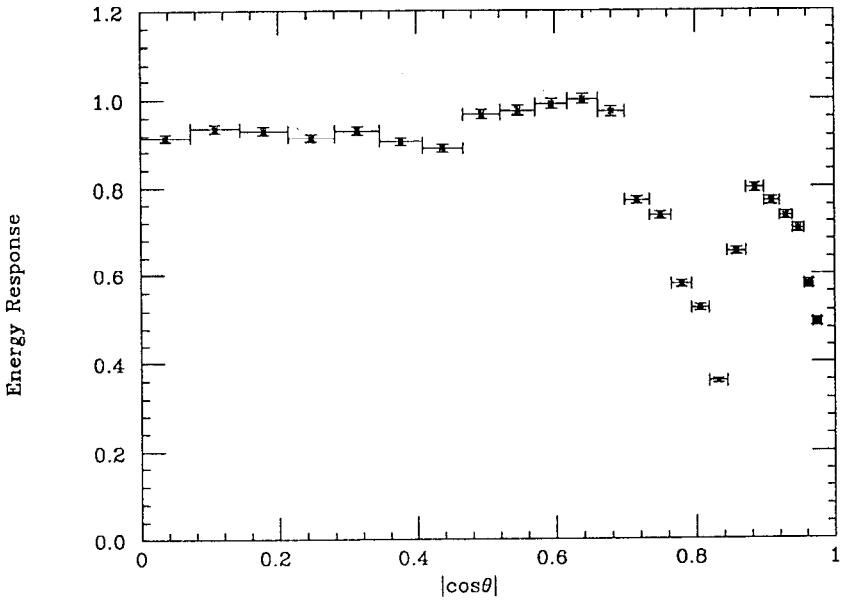

Figure 4.9: Relative LAC energy response as a function of $|cos\theta|$.

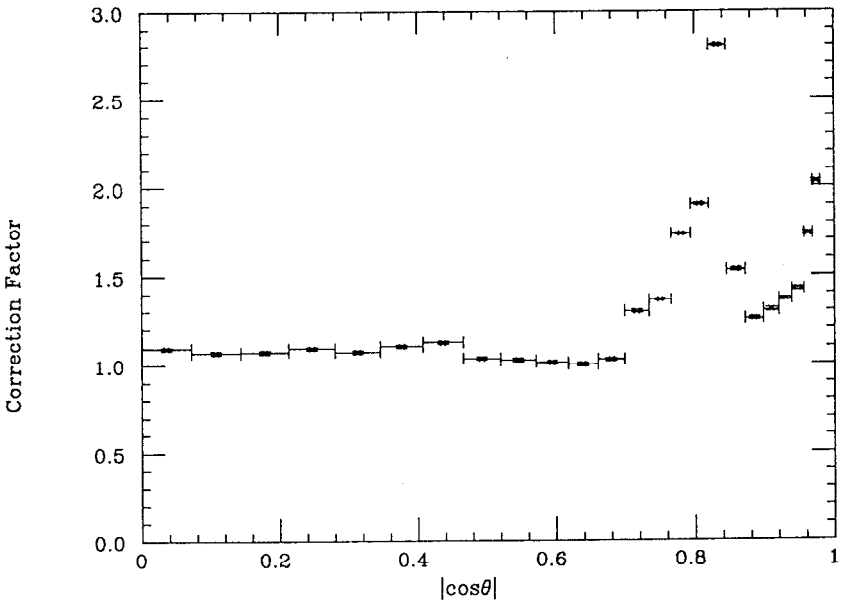

Figure 4.10: The correction factor of LAC energy response as a function of $|cos\theta|$.

Bin Number	Bin Interval	Correction Factor
1	$0.0 < \|cos\theta\| \leq 0.072$	1.094
2	$0.072 < \|cos\theta\| \leq 0.143$	1.068
3	$0.143 < \|cos\theta\| \leq 0.213$	1.073
4	$0.213 < \|cos\theta\| \leq 0.280$	1.094
5	$0.280 < \|cos\theta\| \leq 0.346$	1.073
6	$0.346 < \|cos\theta\| \leq 0.408$	1.105
7	$0.408 < \|cos\theta\| \leq 0.466$	1.126
8	$0.466 < \|cos\theta\| \leq 0.520$	1.034
9	$0.52 < \|cos\theta\| \leq 0.571$	1.025
10	$0.571 < \|cos\theta\| \leq 0.618$	1.010
11	$0.618 < \|cos\theta\| \leq 0.660$	1.000
12	$0.660 < \|cos\theta\| \leq 0.699$	1.028
13	$0.699 < \|cos\theta\| \leq 0.734$	1.295
14	$0.734 < \|cos\theta\| \leq 0.766$	1.362
15	$0.766 < \|cos\theta\| \leq 0.794$	1.734
16	$0.794 < \|cos\theta\| \leq 0.819$	1.904
17	$0.819 < \|cos\theta\| \leq 0.845$	2.80
18	$0.845 < \|cos\theta\| \leq 0.872$	1.532
19	$0.872 < \|cos\theta\| \leq 0.898$	1.252
20	$0.898 < \|cos\theta\| \leq 0.920$	1.299
21	$0.920 < \|cos\theta\| \leq 0.939$	1.365
22	$0.939 < \|cos\theta\| \leq 0.956$	1.421
23	$0.956 < \|cos\theta\| \leq 0.968$	1.735
24	$0.968 < \|cos\theta\| \leq 0.980$	2.028

Table 4.2: Correction factors for LAC energy response.

as the cables and connectors serving the MASC serves to degrade the response even more.

The application of the energy response correction factor of figure 4.10 and table 4.2 results in a much more uniform LAC energy response as seen by comparing figure 4.2 and figure 4.19 in section 4.5.

4.4 Hadronic Z^0 Event Selection

After the reconstruction stage, clusters are required to have the following properties:

- $E_{EM} > 0.0$ MeV
- $E_{clus} > 100.$ MeV
- not flagged as an SLC μ.

Clusters failing any of these criteria are not included in the following analysis. The cluster energies, E_{clus}, are multiplied by the LAC energy response correction factors (table 4.2) after the cluster selection. The imbalance (I) and total reconstructed energy (E_{tot}) are calculated:

$$E_{tot} = \sum_{i=1}^{N_{cl}} |\vec{k}| \tag{4.1}$$

$$I = \frac{|\sum_{i=1}^{N_{cl}} \vec{k}|}{E_{tot}} \tag{4.2}$$

where $\vec{k}$ may be thought of as a three-vector for a massless particle derived from the cluster quantities and N_{cl} is the number of clusters. E_{tot} is the total energy of the reconstructed event, while the imbalance (I) is a measure of how symmetric the energy is deposited. Events with uniform energy deposition will have low imbalance, while events with all of the energy deposited in one location will have an imbalance near unity. Also calculated at this time is the thrust

$$Thrust = max\left(\frac{\sum_{i=1}^{N_{cl}} |\vec{k}_i \cdot \hat{n}|}{\sum_{i=1}^{N_{cl}} |\vec{k}_i|}\right) \tag{4.3}$$

where $\hat{n}$ is a unit vector chosen to maximize the numerator and defines the thrust axis. In the limit of no radiation, the thrust axis is parallel to the axis defined by the final state fermions.

In the following discussion we use the following definitions:

- E_{tot}^{uncor} = the total reconstructed energy without energy response correction
- E_{tot}^{cor} = the total reconstructed energy with energy response correction

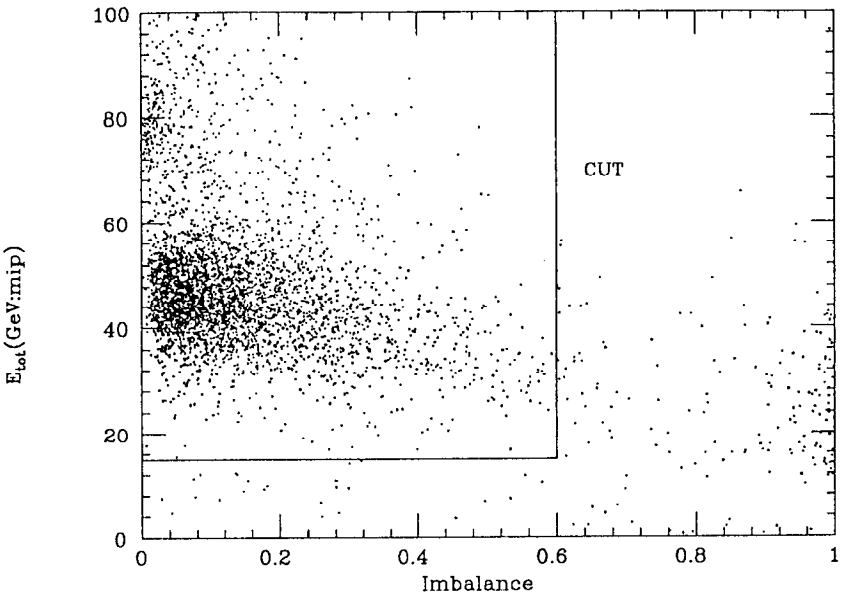

Figure 4.11: Total reconstructed energy versus imbalance with energy response correction for data events selected for every fifteenth event.

- I_{uncor} = the Imbalance without energy response correction
- I_{cor} = the Imbalance with energy response correction
- $Thrust_{uncor}$ = the thrust without energy response correction
- $Thrust_{cor}$ = the thrust with energy response correction
- $\theta_{Thrust_{uncor}}$ = the angle between the thrust without energy response correction and electron beam
- $\theta_{Thrust_{cor}}$ = the angle between the thrust with energy response correction and electron beam

Events are then required to have:

- $E_{tot}^{cor} > 15$ GeV
- $I_{cor} < 0.6$

Figure 4.11 shows the total reconstructed energy versus the imbalance with energy response correction for data events before either of these cuts has been applied. By comparing data events with MC hadron events as seen in figure 4.12, the several facts are known. Events with very high imbalance are beam-related background. The

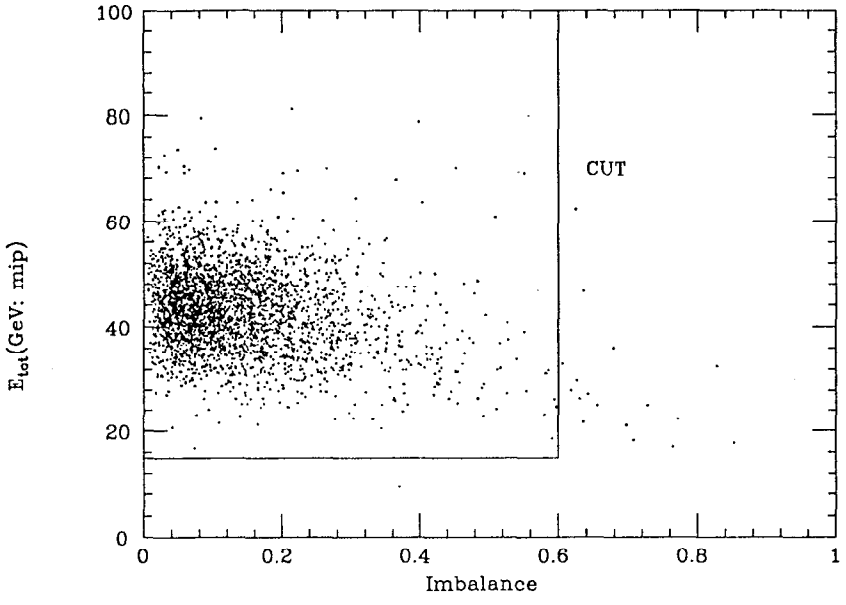

Figure 4.12: Total reconstructed energy versus imbalance with energy response correction for MC hadron events selected for every fifteenth event.

large grouping of events with low imbalance ($I_{cor} < 0.3$) and E_{tot}^{cor} near 45 GeV are hadronic Z^0 decays. The Bhabha events are seen at higher E_{tot}^{cor} with an imbalance near zero. A total of 3,321 events (5.23%) did not pass after imbalance and energy cuts from a total of 63,553 events.

The distributions of the number of clusters for events which pass imbalance and energy are seen in figures 4.13 and 4.14. Figure 4.13 shows the distribution of the number of clusters in the region ($|cos\theta_{Thrust_{cor}}| > 0.8$) and figure 4.14 shows the distribution of the number of clusters in the region ($|cos\theta_{Thrust_{cor}}| \leq 0.8$).

At low multiplicity are the wide angle Bhabhas, tau pairs and beam background. One can see that the number of clusters (N_{cl}) increases when the thrust axis points towards the endcaps. This results from significant amount of material between the IR and the calorimeter in the endcap which causes early shower development of wide angle Bhabha and tau pairs. Therefore, it is natural to define two cuts for the number of clusters according to the regions.

The cuts for the numbers of clusters (N_{cl}) to eliminate wide angle bhabhas, tau pairs and beam background are the following:

- $N_{cl} > 8$, $|cos\theta_{Thrust_{cor}}| \leq 0.8$
- $N_{cl} > 11$, $|cos\theta_{Thrust_{cor}}| > 0.8$

The 51,000 events, hadronic events of 1993 data, are survived after the cuts for the numbers of clusters from 60,232 events passed from the energy and imbalance cuts.

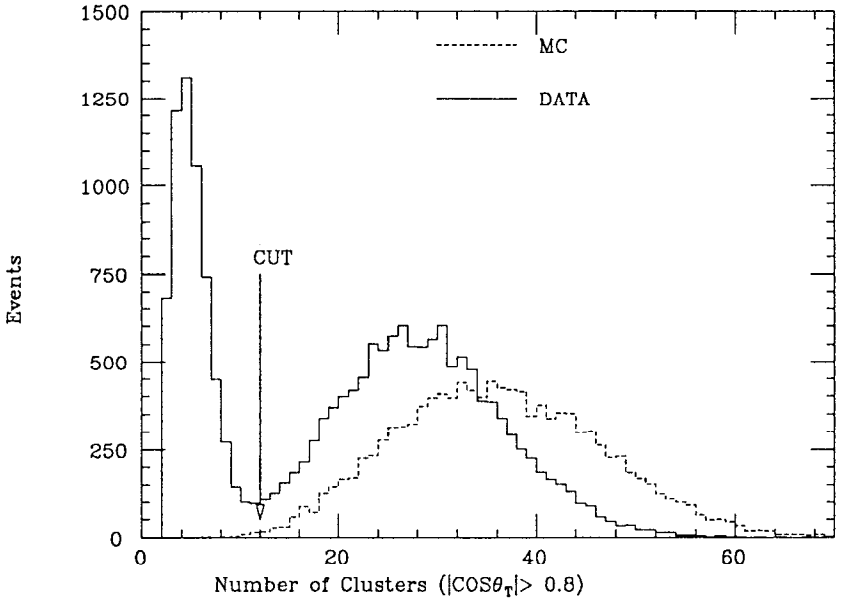

Figure 4.13: The distribution of cluster multiplicity in the region ($|cos\theta_{Thrust_{cor}}| > 0.8$): The dashed line histogram is the distribution of cluster multiplicity in Monte Carlo hadron events in the same region.

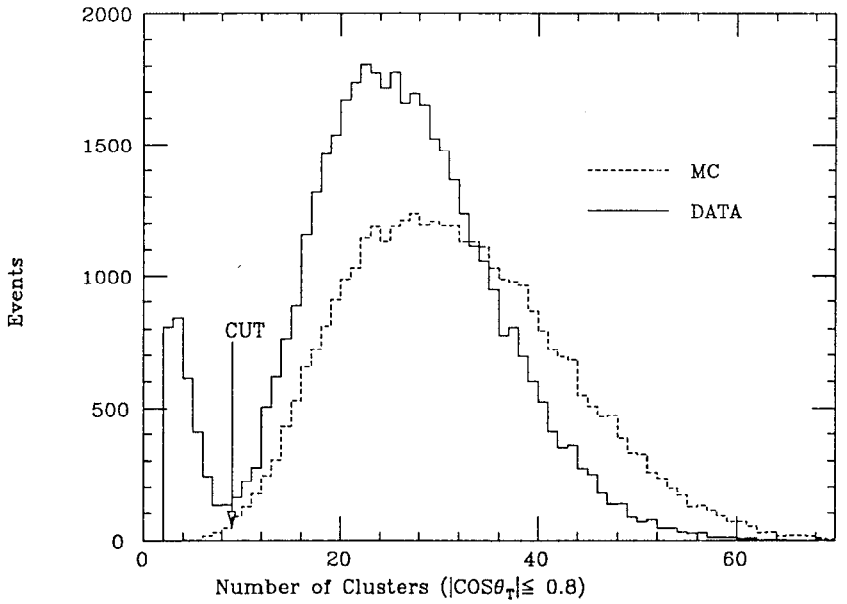

Figure 4.14: The distribution of cluster multiplicity in the region ($|cos\theta_{Thrust_{cor}}| \leq 0.8$): The dashed line histogram is the distribution of cluster multiplicity in Monte Carlo hadron events in the same region.

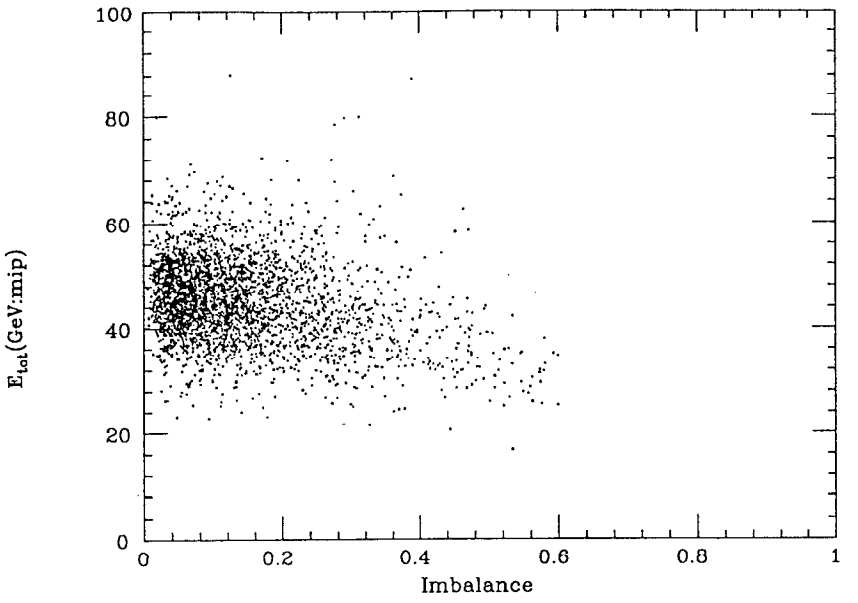

Figure 4.15: Total reconstructed energy versus imbalance with energy response correction after hadronic Z^0 selection for data events selected for every fifteenth event.

That is, $\approx$ 80% from 63,553 events survive. The 1993 data has lower background for hadronic events than the 1992 data which has 10,002 events from 18,383 events after the same hadronic Z^0 event selection as 1993. In the 1992 data, the background are $>$ 0.1%, 0.1%, and 0.2% for wide angle Bhabhas, beam background, and taus, respectively [44]. The background of 1993 data would be much smaller.

Figures 4.15 shows total reconstructed energy versus imbalance with energy response correction after hadronic Z^0 selection for data events selected for every fifteenth event. Figure 4.16 shows the same plot as figure 4.15 for MC hadron events. The condition of hadronic Z^0 event selection looks reasonable in comparing figure 4.15 with figure 4.16.

As seen in figures 4.13 and 4.14, the multiplicity of MC is approximately 5-6 more clusters than the data due to limitation of the transverse parameterization of fast EM and HAD shower in the SLD GEANT code[53]. As a minor effect, the material location at the front of LAC can be considered[53]. Figure 4.17 shows the normalized events versus total reconstructed energy without energy response correction after hadronic Z^0 selection for MC hadron events and data. Figure 4.18 shows the normalized events versus $|cos\theta_{Thrust_{uncor}}|$ without energy response correction after hadronic Z^0 selection for MC hadron events (dashed line histogram) and data (solid line histogram). The MC and data looks agree well, but, the slight difference in figures 4.17 and 4.18 may be considered due to factors mentioned above and the precise modeling for the boundary gap of the LAC. In order to get good agreement between

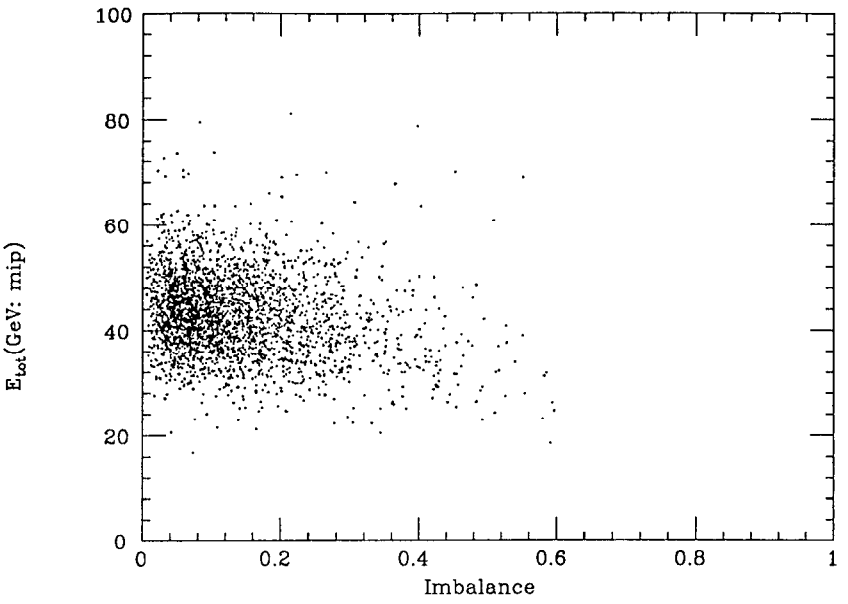

Figure 4.16: Total reconstructed energy versus imbalance with energy response correction after hadronic Z^0 selection for MC hadron events selected for every fifteenth event.

data and MC, there needs to be a precise transverse parameterization and modeling of the materials.

4.5 Improved results after LAC energy response correction

The LAC energy response as function of $|cos\theta_{Thrust_{cor}}|$ is reasonably uniform as a function of $|cos\theta_{Thrust_{cor}}|$ after energy response correction, as seen in figure 4.19 and compared to figure 4.2. Also, the LAC energy response for MC after correction has the same flat shape as seen in figure 4.20 changed from figure 4.6.

The events around $|cos\theta_{Thrust_{uncor}}| = 0.8$ are compensated with energy response correction as the shape of $1 + |cos\theta_{Thrust_{cor}}|^2$ which is the expected distribution of thrust angle (see figure 4.21). The average of total reconstructed energy is changed from 37.73 to 44.89 GeV and the deviation of that changed from 7.828 to 7.409 GeV through correction as seen in figure 4.22. This represents a change of energy resolution from a $21\%/\sqrt{E}$ to a $17\%/\sqrt{E}$. The tail at low energy, which comes from the endcap LAC, has almost disappeared. The energy response correction gives good improvement for the thrust axis direction and the total reconstructed energy as demonstrated by figures 4.21 and 4.22.

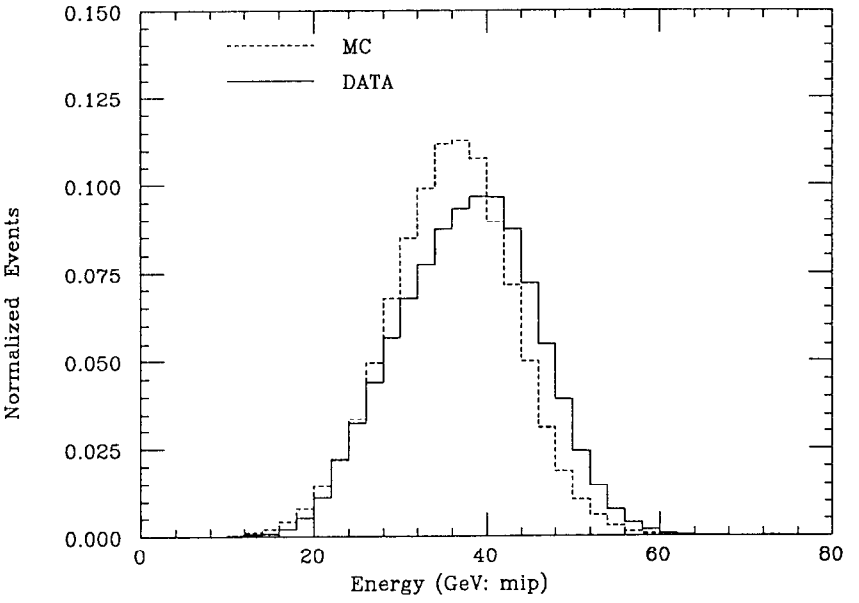

Figure 4.17: The normalized events versus total reconstructed energy without energy response correction after hadronic Z^0 selection for MC hadron events (dashed line histogram) and data (solid line histogram).

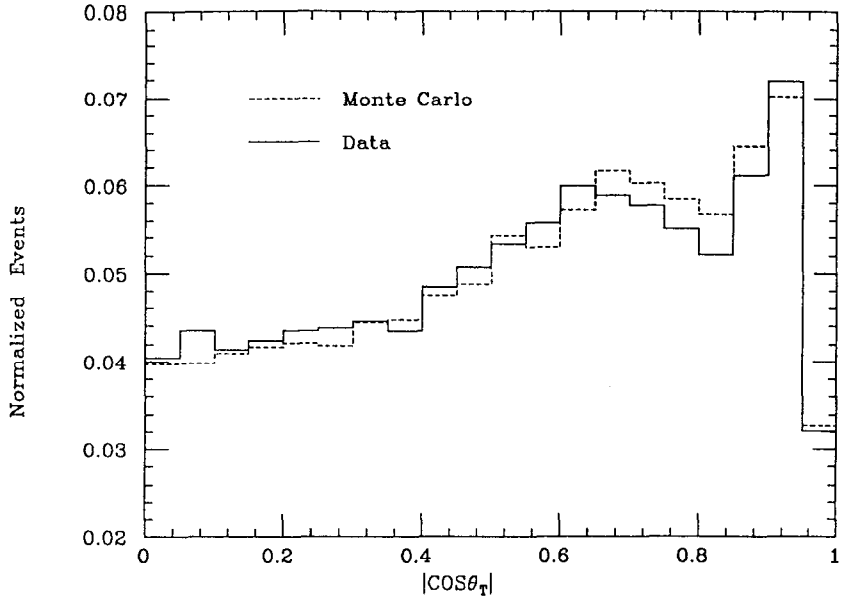

Figure 4.18: The normalized events versus $|cos\theta_{Thrust_{uncor}}|$ without energy response correction after hadronic Z^0 selection for MC hadron events (dashed line histogram) and data (solid line histogram).

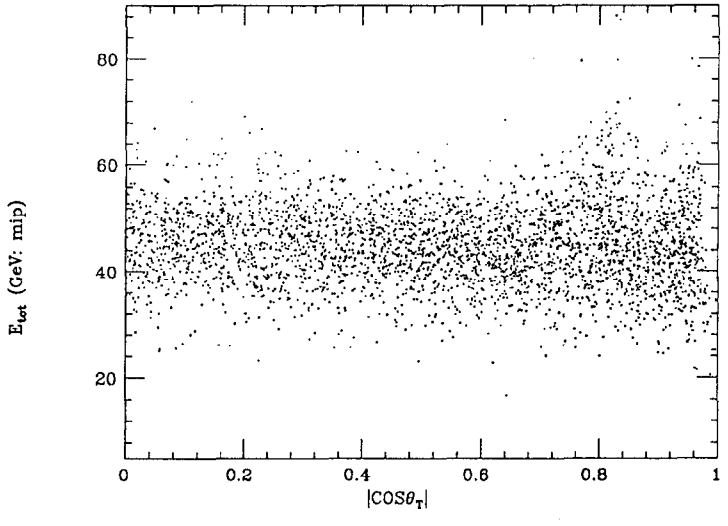

Figure 4.19: LAC energy response as a function of thrust angle for data with energy response correction. The events in this plot are required to satisfy PASS1 and hadronic Z^0 selection condition. They are selected for every fifteenth event in order to see structure.

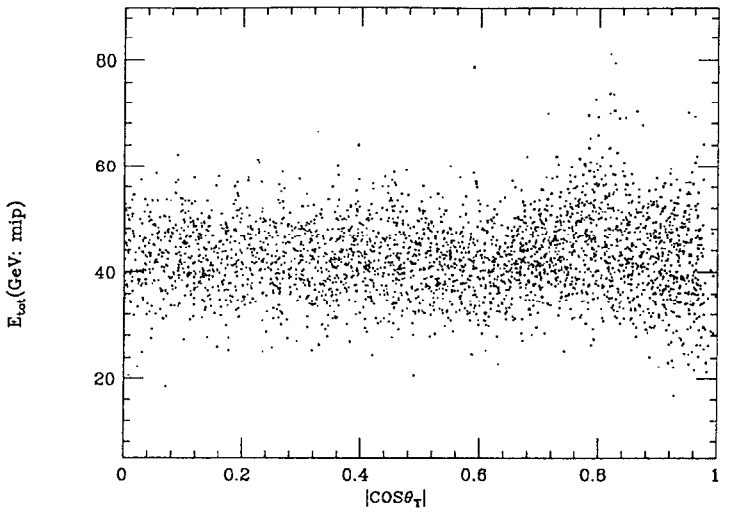

Figure 4.20: LAC energy response as a function of thrust angle for Monte Carlo with energy response correction. The events in this plot are required to satisfy PASS1 and hadronic Z^0 selection condition. They are selected for every fifteenth event in order to see structure.

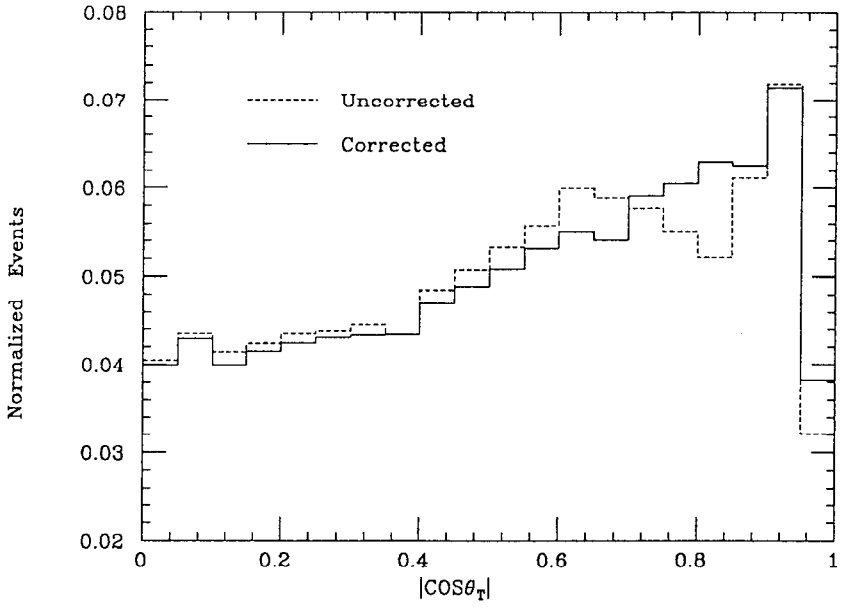

Figure 4.21: The normalized events versus $|cos\theta_{Thrust}|$ after hadronic Z^0 selection without energy response correction (dashed line histogram) and with energy response correction (solid line histogram) for data.

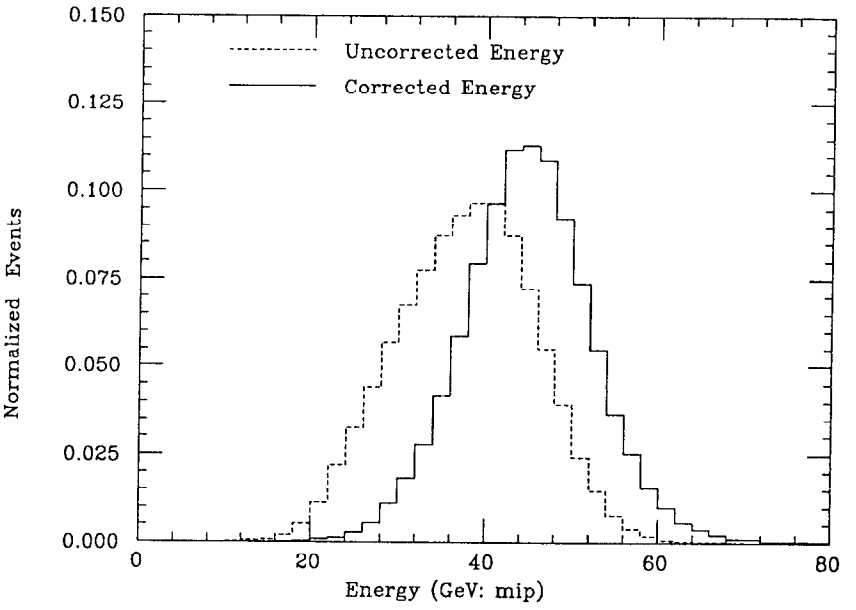

Figure 4.22: The normalized events versus total reconstructed energy after hadronic Z^0 selection without energy response correction (dashed line histogram) and with energy response correction (solid line histogram) for data.

CHAPTER V

ANALYSIS AND RESULTS OF THREE-JET EVENTS IN SLD

This chapter will describe the procedure for reconstructing three-jet events, the rescaling three-jet energies by momentum conservation and corrections for hadronization and detector effects. The energies, directions and variables of three-jet events will be compared between hadron level and SLD detector level. The raw data are found to be in good agreement with the Monte Carlo simulations passing the same set of event selection cuts. The distributions of variables for three-jet events are done with a bin-to-bin correction to explain the effects of hadronization, detector acceptance and resolution based on the reference[17]. The some explanations of this section are taken from the reference[17]. The corrected data was fit using equations presented in Chapter II for event plane orientation. Parameters (α, α_N, β) associated with these equations are obtained. The corrected data is compared to the expected parton level distributions of variables for three-jet events simulated from the vector QCD model and a scalar gluon model, respectively. Systematic errors, calculated for all the bins in these distributions, are obtained by comparing the results from different sets of event selection cuts and from different Monte Carlo programs installed with different hadronization models with those from the standard cut. Good agreement is found between data and the vector QCD model for the distributions of x_1, x_2, x_3 and $cos\theta_{EK}$.

5.1 Reconstruction of Three-Jet Events

The 1993 hadronic event sample is 51,000 events. For comparison we generated 46,421 events with full detector level simulation using the HERWIG5.7 MC as generator. These events all pass the same data hadronic selection cut (see the section 4.4).

The hadronic events are analyzed to select three-jet events with the YCLUS algorithm and $y_c = 0.02$[28] which have the largest three-jet fraction[18]. The three-jet sample is 22,114 events (43.36%) in the 1993 data and 22,725 events (48.95%) in the MC. The rate of three-jet events in the MC is higher than the data. This results from the higher cluster multiplicity of the MC (see figures 4.13 and 4.14 in

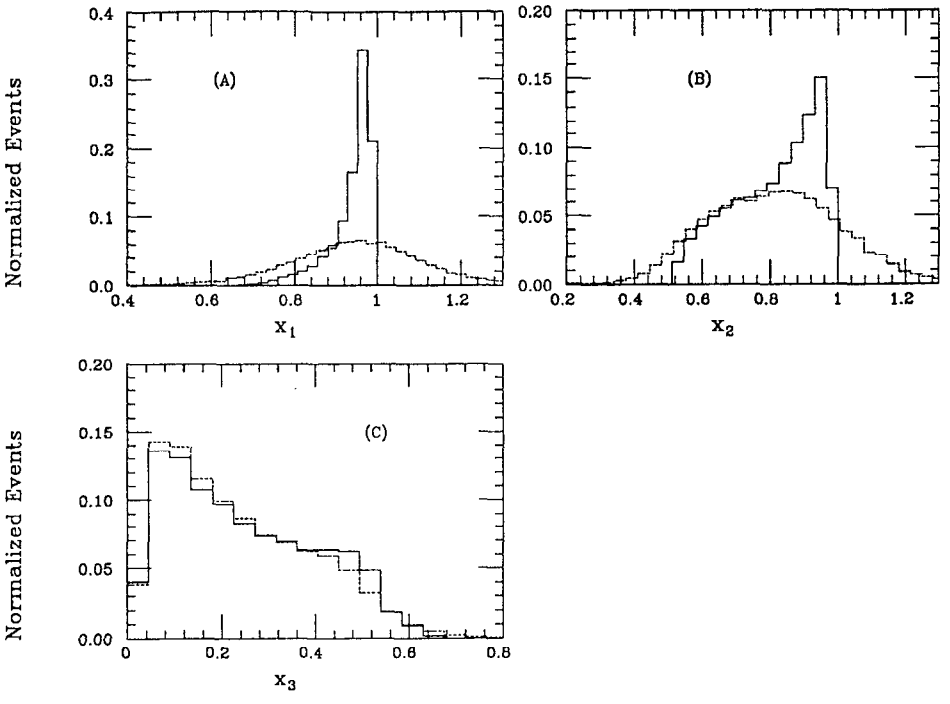

Figure 5.1: Normalized number of events vs. the scaled energies ((A) x_1, (B) x_2 and (C) x_3): Dashed line histogram (Before correction of momentum conservation) and Solid line histogram (After correction of momentum conservation.)

the chapter IV). That is, at lower y_c, the MC three-jet events occur more often than the data because of a higher multiplicity of low cluster energies in the MC.

5.2 Three Jets Rescaled by Momentum Conservation

The three jets must conserve momentum and energy. However, the three jets measured in the detector will not conserve energy and momentum due to undetected particles and detector imperfection. We apply corrections to jet energies to balance momentum and energy.

Let momentum vectors of three jets before correction be $\vec{P}_1$, $\vec{P}_2$ and $\vec{P}_3$. Suppose that the momentum vectors of three jets after correction are $\vec{P}_1'$, $\vec{P}_2'$ and $\vec{P}_3'$. In order to have the condition that the sum of the momentum vectors of three jets after correction is zero which is $\vec{P}_1' + \vec{P}_2' + \vec{P}_3' = 0$, we apply the following correction:

$$P_i'^j = P_i^j - R^j |P_i^j| \tag{5.1}$$

$$R^j = \frac{\sum_{i=1}^{3} P_i^j}{\sum_{i=1}^{3} |P_i^j|} \tag{5.2}$$

where $i = 1, 2, 3$ (order number of jets) and $j = x, y, z$ (coordinates of jets)

The scaled energies of the three jets are

$$x_i = \frac{2E_i}{E} \qquad (i = 1, 2, 3)$$

where E is the total energy of the three jets with $x_1 + x_2 + x_3 = 2$, and $x_1 > x_2 > x_3$. Figure 5.1 shows the normalized number of events versus the scaled energies of three-jet events. The dashed line histogram is before correction of momentum conservation and the solid line histogram is after correction of that.

5.3 Comparisons of Three Jets for Hadron Particles, Corrected and Uncorrected LAC Clusters

The directions and energies of hadronic particles at the generator level simulation will be converted into those of clusters by the SLD detector level simulation due to electromagnetic and hadron showers through the GEANT simulation and calorimeter reconstruction. Each clusters are corrected by using the correction factor in order to compensate a degraded response region due to the electronics, cables, plumbing and materials in front of the LAC. The three jets are reconstructed with the corrected, the uncorrected LAC clusters and hadron particles by using the YCLUS algorithm and $y_c = 0.02$. While the three jets of the corrected clusters are rescaled to three jets by momentum conservation (the rescaled three jets of the corrected LAC clusters), the three jets of the uncorrected clusters are not rescaled (the no rescaled three jets of the uncorrected LAC clusters).

How does the rescaled three jets of the corrected LAC clusters improve better than the no rescaled three jet of the uncorrected LAC clusters with comparisons to the three jets of hadron particles for the variables of three jets ? We compared quantitatively the variables of the rescaled three jets of the corrected LAC clusters with the variables of the no rescaled three jets of the uncorrected LAC clusters based on the variables of three jets of hadron particles. Here the variables of three jets are $cos\theta$, χ, $cos\theta_N$, x_1, x_2, x_3 and angles of three jets. The angles of three jets have the polar and azimuthal angles, $cos\theta_i$ and ϕ_i with i = 1,2,3 (magnitude order number of jets).

The hadron particles were generated at the HERWIG5.7 generator and the LAC clusters made through the GEANT simulation, not including the beam backgrounds produced by the SLC, and calorimeter reconstruction. The variables of three jets are calculated at three different cases: one is the variables of three jets of hadron particles level (the variables of hadron particles), the others are the variables of the rescaled three jets with the corrected LAC clusters (the variables of corrected clusters) and those of the no rescaled three jets with the uncorrected LAC clusters (the variables of uncorrected clusters). Also, the thrust ($Thrust$) and thrust axis angle ($cos\theta_{Thrust}$), another variables of three jets, are calculated at three different cases: hadron particles, the corrected LAC clusters and the uncorrected LAC clusters.

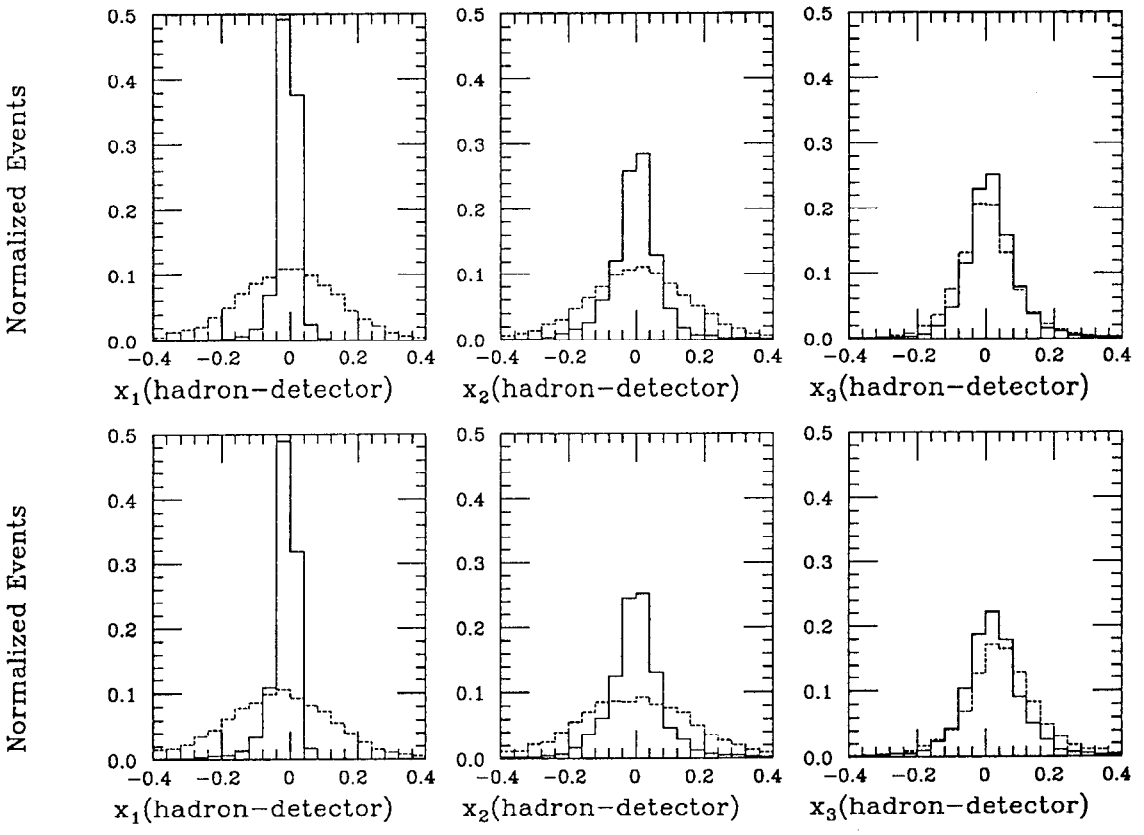

Figure 5.2: Normalized number of events vs. the scaled three jets (x_1, x_2 and x_3) in the difference between hadrons at the generator level and clusters at the detector level: upper part (barrel region) and lower part (endcap region): the solid line histograms are associated with the rescaled three jets of the corrected LAC clusters and the dashed line histograms are associated with the no rescaled three jets of the uncorrected LAC clusters.

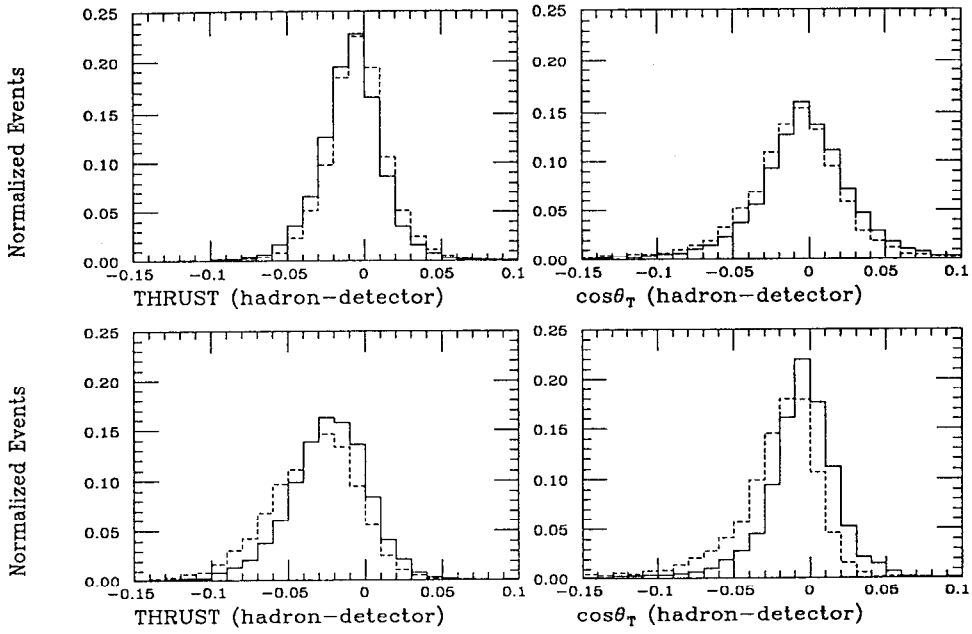

Figure 5.3: Normalized number of events vs. thrust and thrust axis angle in the difference between hadrons at the generator level and clusters at the detector level: upper part (barrel region) and lower part (endcap region): the solid line histograms are associated with the corrected LAC clusters and the dashed line histograms are associated with the uncorrected LAC clusters.

The $cos\theta_{Thrust}$ and $Thrust$ are calculated with hadron particles. The three-jet events have the four interesting categories: barrel ($cos\theta_{Thrust} \leq 0.65$) and endcap ($cos\theta_{Thrust} \geq 0.65$) regions, high ($Thrust \geq 0.9$) and low ($Thrust \leq 0.9$) thrust regions. There are two calculated values for all variables of three jets mentioned above : one is the corrected values subtracted the variables of corrected clusters from the variables of hadron particles and the other is the uncorrected values subtracted the variables of uncorrected clusters from the variables of hadron particles. The distributions of the corrected and uncorrected values are accumulated and histogrammed for all three-jet events. All the histogram plots are normalized so that integration of any distribution over the plotted range equals unity. The solid line and dashed line histograms of all figures (5.2, 5.3, 5.4, 5.5 and 5.6) are the normalized number of events for the corrected values and for the uncorrected values.

The upper and lower part of figure 5.2 display the barrel and endcap region for variables of x_1, x_2 and x_3. We can see there is a big improvement after corrections in the both regions. The upper and lower part of figure 5.3 show the barrel and endcap region for the variables of $Thrust$ and $cos\theta_{Thrust}$. There is the improvement for thrust and thrust axis angle in the endcap region as we expected. The upper and lower part of figure 5.4 display the barrel and endcap region for the variables of $cos\theta_3$ and ϕ_3. Figure 5.5 shows $cos\theta_1$, ϕ_1, $cos\theta_2$ and ϕ_2. We can see that the directions after correction are slightly worse than those before correction. The upper and lower

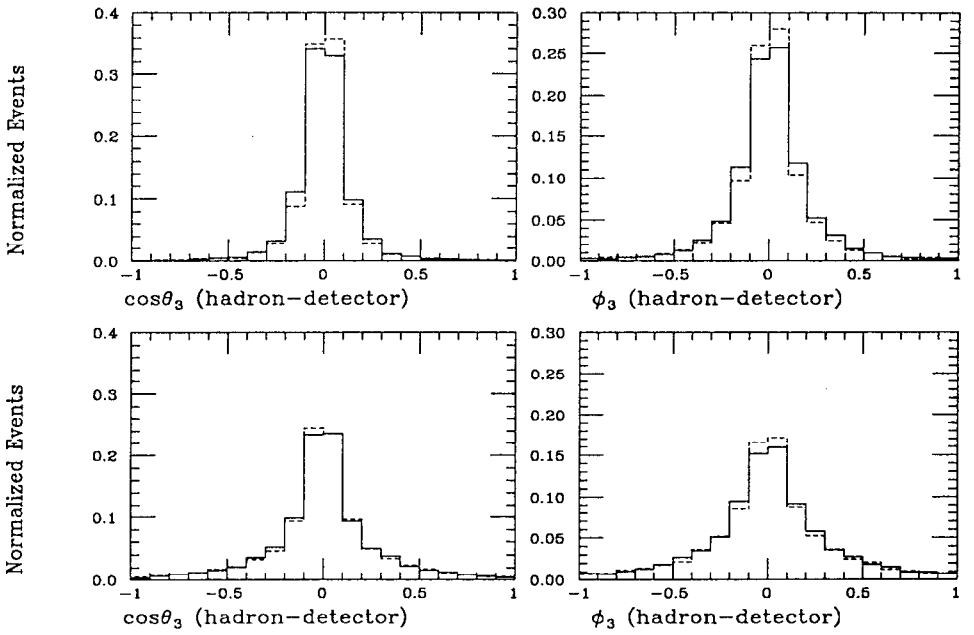

Figure 5.4: Normalized number of events vs. $cos\theta_3$ and ϕ_3 in the difference between hadrons at the generator level and clusters at the detector level: upper part (barrel region) and lower part (endcap region): the solid line histograms are associated with the rescaled three jets of the corrected LAC clusters and the dashed line histograms are associated with the no rescaled three jets of the uncorrected LAC clusters. Unit of angles (radian).

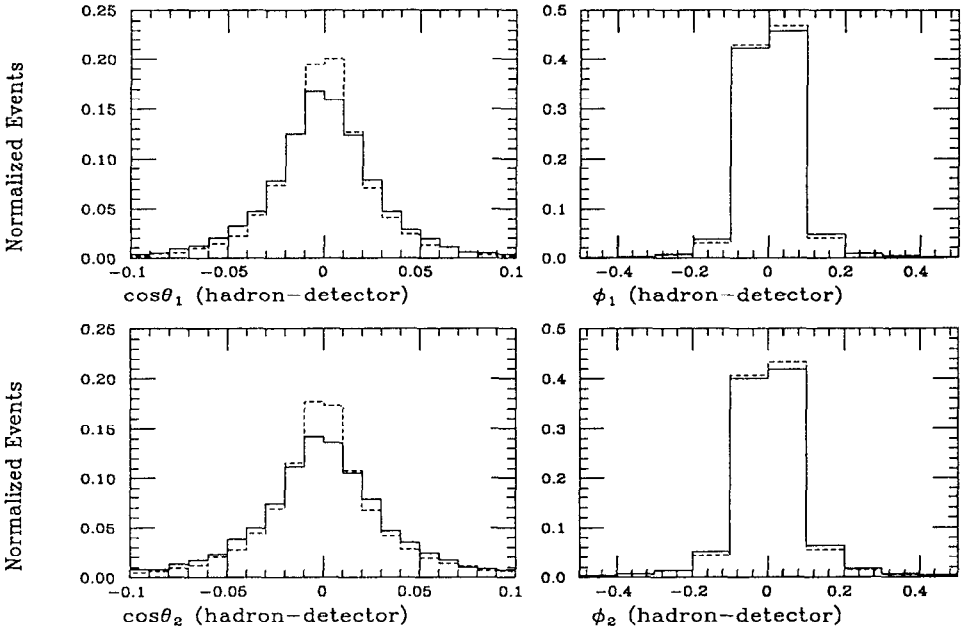

Figure 5.5: Normalized number of events vs. $cos\theta_1$, ϕ_1, $cos\theta_2$ and ϕ_2 in the difference between hadrons at the generator level and clusters at the detector level: upper part ($cos\theta_1$ and ϕ_1) and lower part ($cos\theta_2$, ϕ_2): the solid line histograms are associated with the rescaled three jets of the corrected LAC clusters and the dashed line histograms are associated with no rescaled three jets of the uncorrected LAC clusters. Unit of angles (radian).

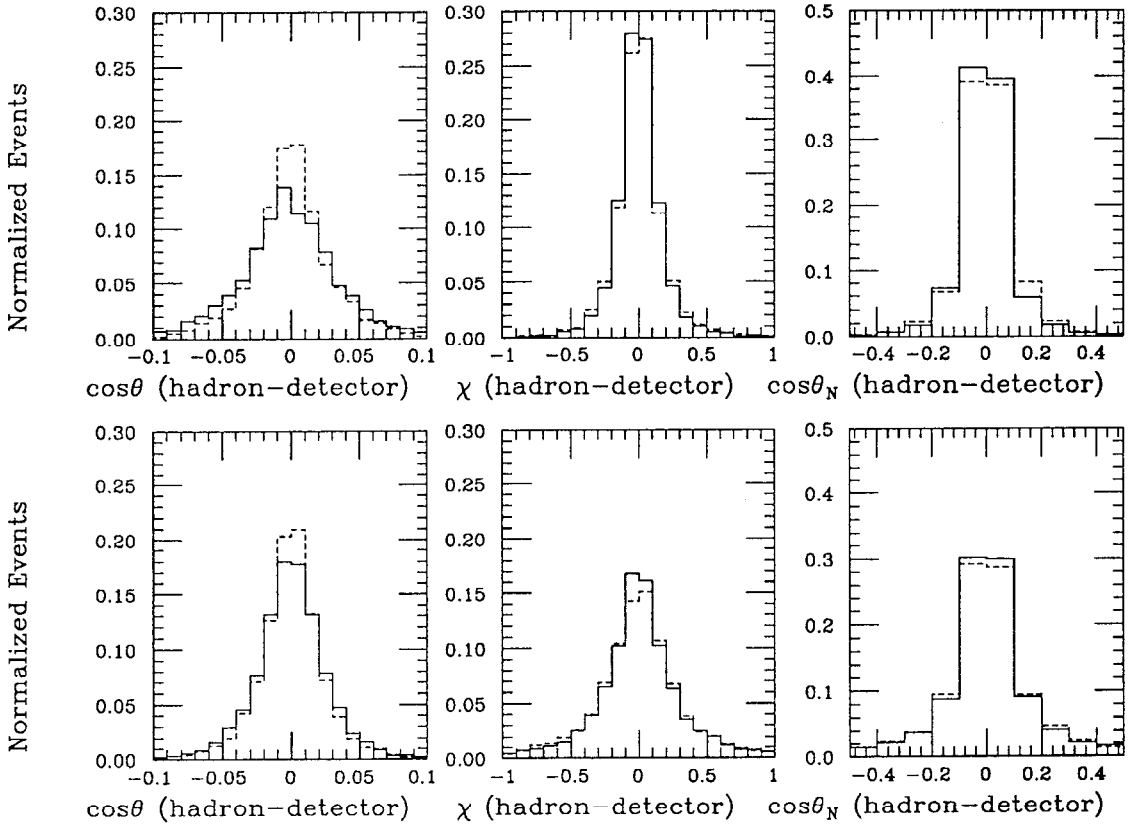

Figure 5.6: Normalized number of events vs. ($cos\theta$, χ and $cos\theta_N$) in the difference between hadrons at the generator level and clusters at the detector level: upper part ($Thrust \leq 0.9$) and lower part ($Thrust \geq 0.9$): the solid line histograms are associated with the rescaled three jets of the corrected LAC clusters and the dashed line histograms are associated with the no rescaled three jets of the uncorrected LAC clusters. Unit of χ angle (radian).

part of figure 5.6 display the low and high thrust region for the variables of $cos\theta$, χ and $cos\theta_N$. The $cos\theta$ is more stable in the high thrust region than in the low thrust region due to the better directionality in the high thrust than in the low thrust. The χ and $cos\theta_N$ are more stable in the low thrust region than in the high thrust region. The reason comes that the event plane in the low thrust is defined better than that in the high thrust.

5.4 Distributions of Three-Jet Events in Raw Data and Detector Level MC

There are 22,114 three-jet events in the 1993 data and 22,725 three-jet events in the MC. They are studied as function of the three-jet event variables x_1, x_2, x_3, $cos\theta_{EK}$, $cos\theta$, $cos\theta_N$ and χ defined in the section 2.2.3. The χ distribution has been folded in the different angular intervals in the following way: χ=χ for the $0 \rightarrow \pi/2$ interval, χ=π-χ for the $\pi/2 \rightarrow \pi$ interval, χ=χ-π for the $\pi \rightarrow 3\pi/2$ interval and χ=2π-χ for the $3\pi/2 \rightarrow 2\pi$ interval. All the histogram plots are normalized so that integration of any distribution over the plotted range equals unity.

The figure 5.7 shows the raw data distributions of x_1, x_2, x_3, and $cos\theta_{EK}$ compared with full detector level MC simulation. The raw data means the uncorrected data before the parton level correction. The difference between raw data and MC shows up largely in the upper ends of the x_1, x_2 and $cos\theta_{EK}$ distributions and in the lower ends of the x_3 distribution as seen in figure 5.7. As mentioned in the section 5.1, at lower y_c, in the MC are more likely to be tagged as three-jet events than those in data because of the higher multiplicity of lower cluster energies in the MC.

Figures 5.8, 5.9 and 5.10 show the raw data distributions of $cos\theta$, $cos\theta_N$ and χ for selected values of x_1 compared with full detector level HERWIG5.7 MC simulation. The angular ($cos\theta$, $cos\theta_N$ and χ) distributions has the discrepancy between raw data and MC as seen in the figures 5.8, 5.9 and 5.10. However, the discrepancy is within the range of statistical error as listed in the table 5.1 except several bins. The table 5.1 shows the events and approximate statistical errors at each bin of raw data and MC in the angular distributions.

5.5 Monte Carlo Simulations

The generator and detector level simulation of HERWIG5.7 was explained in sections 4.3.1 and 4.3.2 in detail. JETSET6.3, the official version (MC300K.IDA), was used in the generator level simulation with the optimized values of the main parameters for the control of the momentum distribution of hadrons listed in table 5.2. JETSET7.4 was generated with the first and second order matrix element (ME) and parton shower (PS) in order to check the theoretical uncertainty.

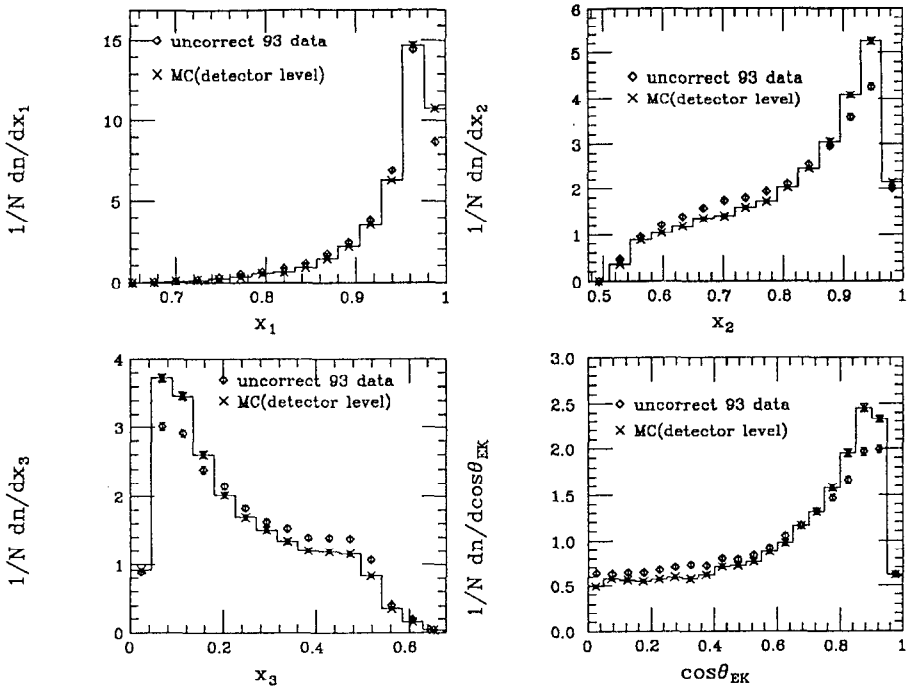

Figure 5.7: The raw data distributions of x_1, x_2, x_3, and $cos\theta_{EK}$ compared with full detector level MC simulation. Diamond points: raw data; solid histo: HERWIG5.7 MC simulation at detector level.

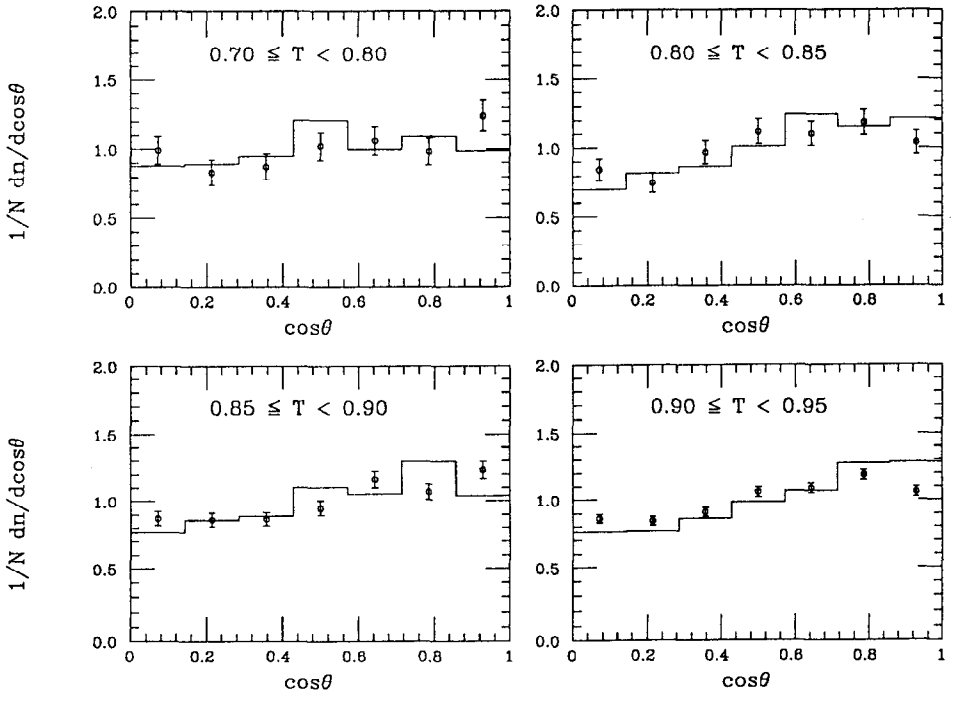

Figure 5.8: The raw data distributions of $cos\theta$ for selected values of $T = x_1$ compared with full detector level MC simulation. Points: raw data; solid histo: HERWIG5.7 MC simulation at detector level.

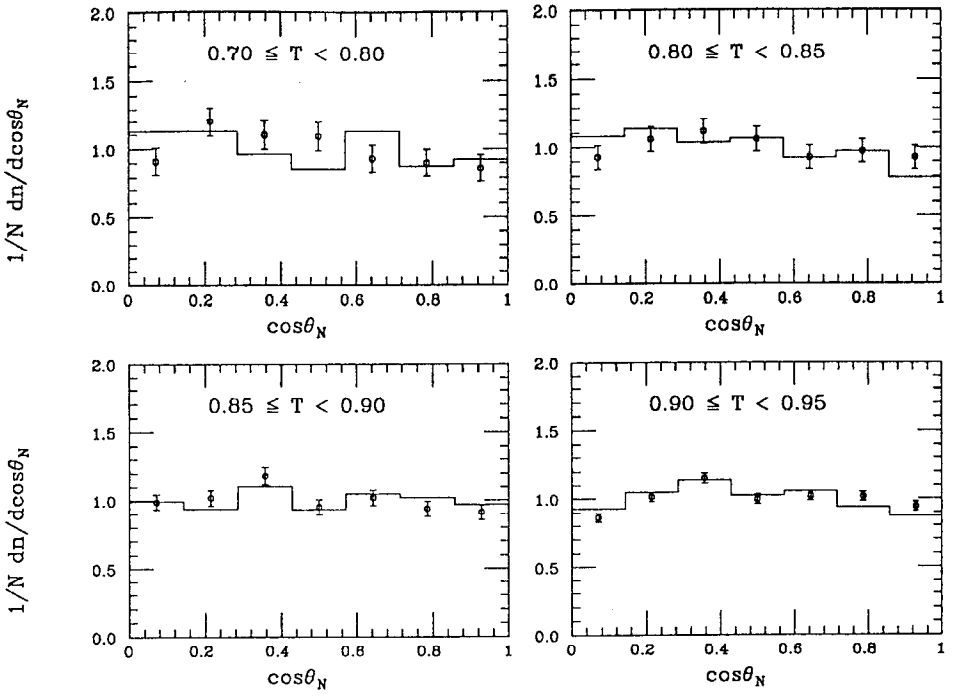

Figure 5.9: The raw data distributions of $cos\theta_N$ for selected values of $T = x_1$ compared with full detector level MC simulation. Points: raw data; solid histo: HERWIG5.7 MC simulation at detector level.

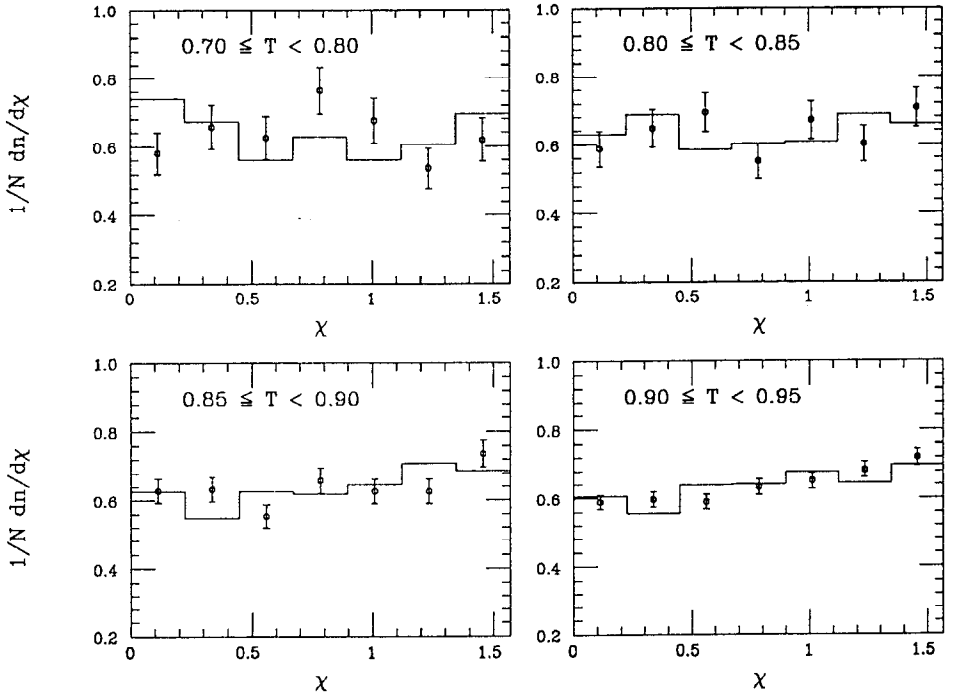

Figure 5.10: The raw data distributions of χ for selected values of $T = x_1$ compared with full detector level MC simulation. Points: raw data; solid histo: HERWIG5.7 MC simulation at detector level.

T	Data Events	MC Events	Data Statistical Error	MC Statistical Error
0.7-0.8	706	597	10.1%	10.8%
0.8-0.85	971	778	8.5%	9.5%
0.85-0.9	2,137	1,917	5.7%	6.2%
0.9-0.95	5,596	5,244	3.5%	3.7%

Table 5.1: The events and statistical errors only of raw data and MC for selected values of $T = x_1$ in the distribution of $cos\theta$, $cos\theta_N$ and χ.

	JETSET6.3		JETSET7.4	
Parameter	Name	Optimized value	Name	Optimized value
Λ_{QCD}	Pare(21)	0.26 GeV	Pare(81)	0.3 GeV
Q_0	Pare(22)	1.0 GeV	Pare(82)	1.0 GeV
σ_q	Par(12)	0.39 GeV	Parj(21)	0.39 GeV
a	Par(31)	0.18	Parj(41)	0.18
b	Par(32)	0.34 GeV^{-2}	Parj(42)	0.34 GeV^{-2}

Table 5.2: Main parameters of JETSET6.3 and JETSET7.4 which control the momentum distribution of hadrons.

The parameter Λ_{QCD} and Q_0 are the QCD scale parameter and the invariant mass cutoff to the parton shower process. The parameters σ_q, a and b are related with the fragmentation process and the symmetric Lund fragmentation function.

The generator level simulation of JETSET6.3 was done with the parton shower simulation. Here approximately 250K events of HERWIG5.7 and 200K events of JETSET6.3 are generated in the generator level. Also, all cases of JETSET7.4, the first and second order matrix element (ME) and parton shower (PS), are generated in the generator level with approximately 200K events.

5.6 Corrections for Hadronization and Detector Effects

The data was corrected for hadronization and detector effects according to the vector QCD simulations. The corrected data was compared with the parton level simulations from vector and scalar gluon models, assuming that the hadronization and detector effects are independent of the models. The partons and hadrons are reconstructed to three jets with YCLUS algorithm and $y_c = 0.02$[28]. Variables of three-jet events are made with histogram distributions as mentioned in the section 5.4.

The correction factors are got through the bin by bin correction at the hadronization and detector effects separately. For the parton-to-hadron level corrections, each bin of the parton level histogram is divided by each bin of the hadron level histogram.

$$C_{ph} = \frac{V_{parton}(i)}{V_{hadron}(i)}$$

Where i is the bin number, $V_{parton}(i)$ is the value in the ith bin of the parton level histogram and $V_{hadron}(i)$ is the value in the ith bin of the hadron level histogram. The correction of parton-to-hadron was calculated with the first, second order matrix element, the parton shower of JETSET7.4, the parton shower of JETSET6.3 and the parton shower of HERWIG5.7.

Figure 5.11 shows the parton-to-hadron correction factors for x_1, x_2, x_3 and $cos\theta_{EK}$. The big difference in the lowest bin of x_1 mainly comes from the statistical error as seen in the upper-left of figure 5.11. In a two-parton hadronic event, the YCLUS algorithm tend to combine some soft particles, which are perpendicular to the original parton direction, to form a third jet. Since this third jet is very soft in energy, we can see largely the difference in the upper ends of the x_1, x_2 and $cos\theta_{EK}$ distributions and in the lower ends of the x_3 distribution [17]. The corrections are within 20% from unity in the distributions of x_1, x_2, x_3 and $cos\theta_{EK}$.

Figures 5.12, 5.13 and 5.14 show the parton-to-hadron correction factors for $cos\theta$, $cos\theta_N$ and χ. The parton level agrees well with the hadron level within the range of 10% correction in the distributions of $cos\theta$, $cos\theta_N$ and χ for selected values of $T = x_1$.

The similar procedure applies to the hadron-to-detector level corrections.

$$C_{hd} = \frac{V_{hadron}(i)}{V_{detector(i)}}$$

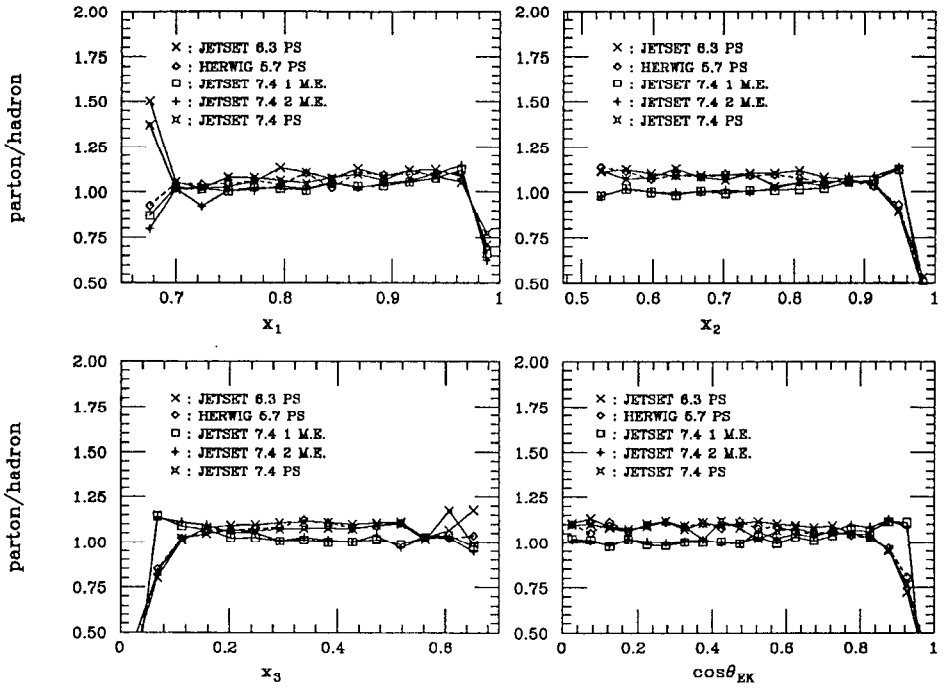

Figure 5.11: The parton-to-hadron correction factors for x_1, x_2, x_3 and $cos\theta_{EK}$.

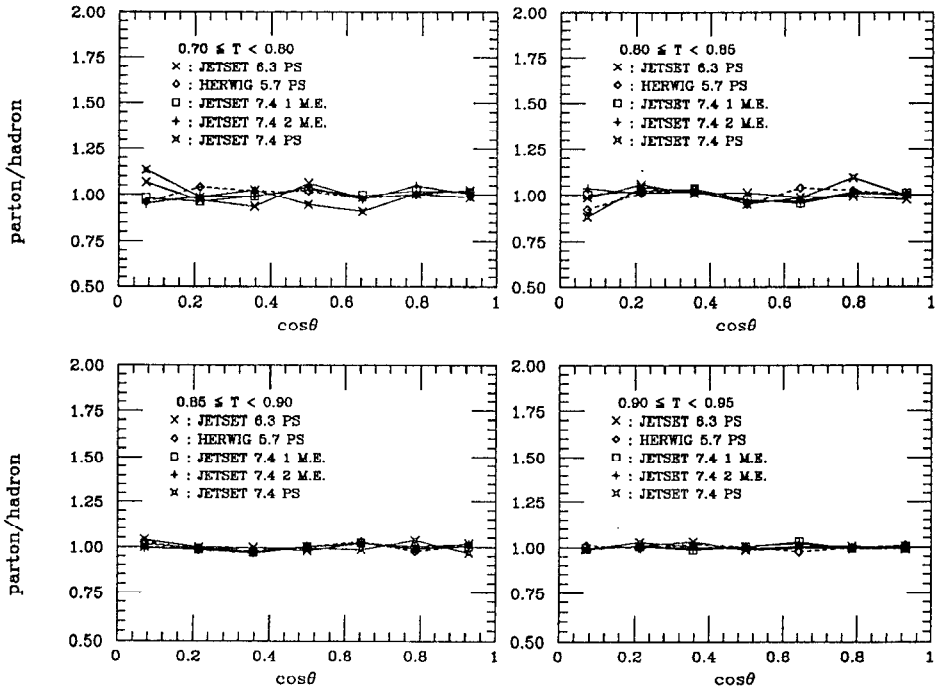

Figure 5.12: The parton-to-hadron correction factors of $cos\theta$ for selected values of $T = x_1$.

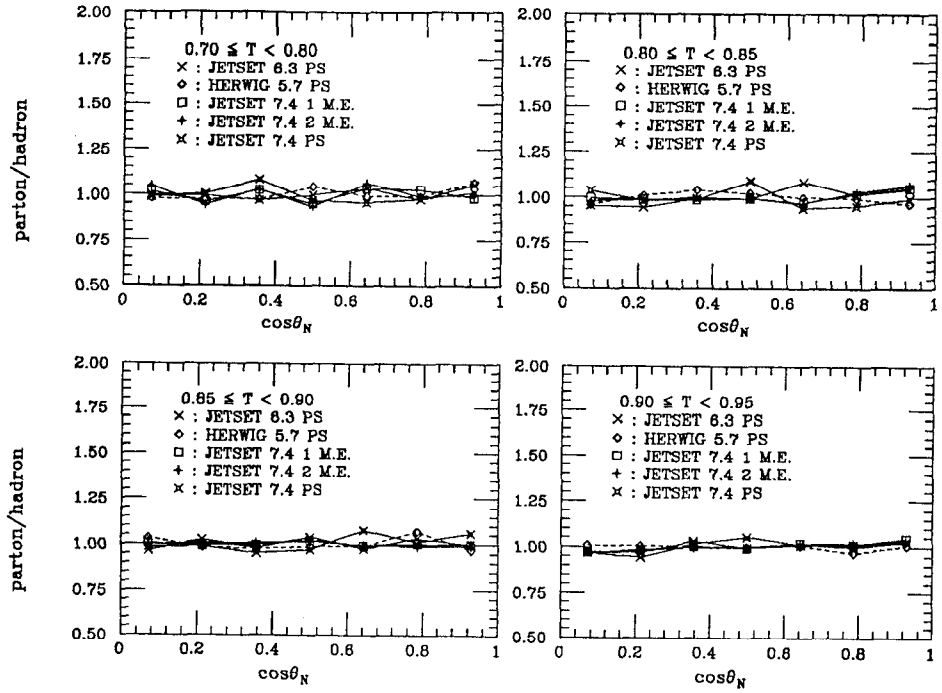

Figure 5.13: The parton-to-hadron correction factors of $cos\theta_N$ for selected values of $T = x_1$.

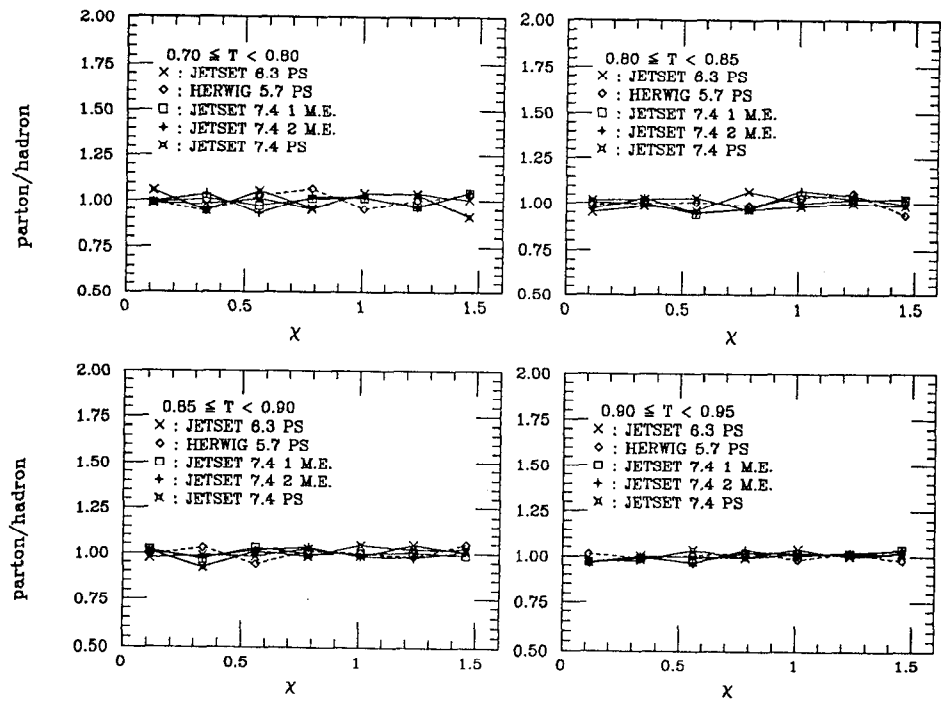

Figure 5.14: The parton-to-hadron correction factors of χ for selected values of $T = x_1$.

Where i is the bin number, $V_{hadron}(i)$ is the value in the ith bin of the hadron level histogram and $V_{detector}(i)$ is the value in the ith bin of the detector level histogram which passes the same data selection cuts as does the SLD data.

The correction of hadron-to-detector level was calculated with the parton shower simulation of HERWIG5.7. The detector level MC distribution of HERWIG5.7 pass the same data selection cuts and processes. Figure 5.15 shows the hadron-to-detector correction factors for x_1, x_2, x_3 and $cos\theta_{EK}$. We can see the difference in the upper ends of the x_1, x_2, $cos\theta_{EK}$ and in the lower ends of the x_3 distributions because of more three-jet events due to higher multiplicity of lower cluster energies at a lower y_c.

Figures 5.16, 5.17 and 5.18 show the hadron-to-detector correction factors for $cos\theta$, $cos\theta_N$ and χ for selected values of $T = x_1$. The table 5.3 describes statistical errors only at the correction of parton-to-hadron and hadron-to-detector in the distributions of $cos\theta$, $cos\theta_N$ and χ for selected values of $T = x_1$. The statistical errors are calculated at each bins of the histogram. There is a large statistical errors due to small events of low T.

The tables 5.4 and 5.5 describes statistical errors at the correction of parton-to-hadron and hadron-to-detector in the distributions of x_1, x_2, x_3 and $cos\theta_{EK}$. We can see the large statistical errors in the lower ends of x_1, x_2 distributions and in the upper end of x_3 distribution due to small events.

These two correction factors are multiplied together with the number of entries $D(i)$ in the experimentally measured distributions, to give the corrected value $V_{corr}(i)$ at the parton level:

$$V_{corr}(i) = C_{ph}(i) * C_{hd}(i) * D(i) \tag{5.3}$$

	$(p/h)_{sta}(\%)$			$(h/d)_{sta}(\%)$		
T	$cos\theta$	$cos\theta_N$	χ	$cos\theta$	$cos\theta_N$	χ
0.7-0.8	10	10	10.5	14.7	17.5	16.5
0.8-0.85	9	8.5	8.5	12.5	13	14.5
0.85-0.9	6.4	6.3	5.8	9.2	8.8	9.2
0.9-0.95	3.8	3.5	3.5	5	5.5	5.5

Table 5.3: Statistical errors only of corrections for hadronization and detector effects for $cos\theta$, $cos\theta_N$ and χ variables for selected values of $T = x_1$: $(p/h)_{sta}$ is the statistical error only in the correction of parton to hadron level: $(h/d)_{sta}$ is the statistical error only for the correction of hadron-to-detector levels.

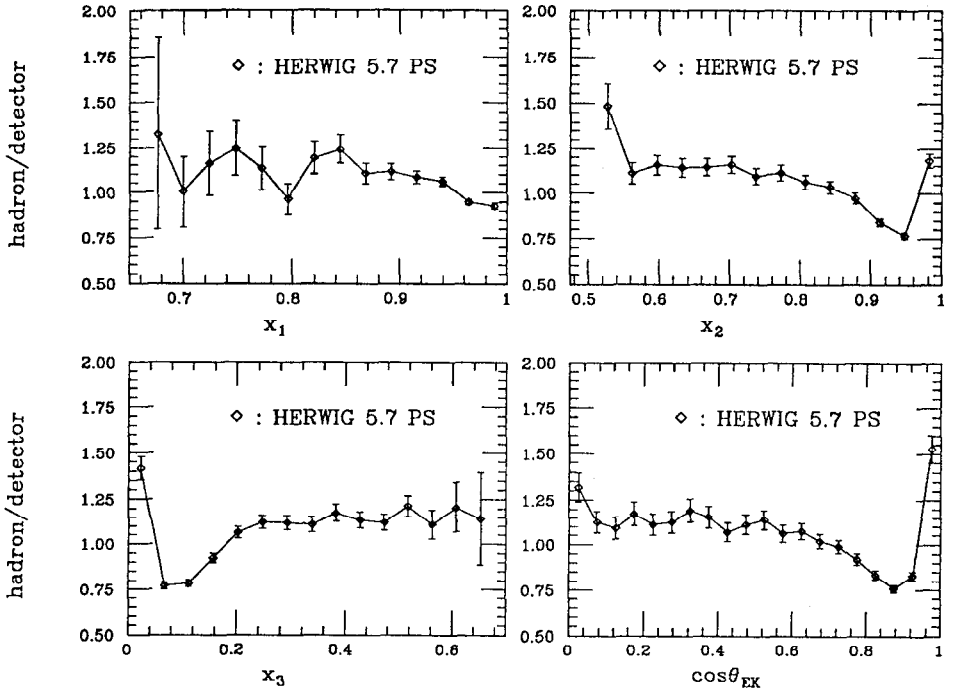

Figure 5.15: The hadron-to-detector correction factors for x_1, x_2, x_3 and $cos\theta_{EK}$.

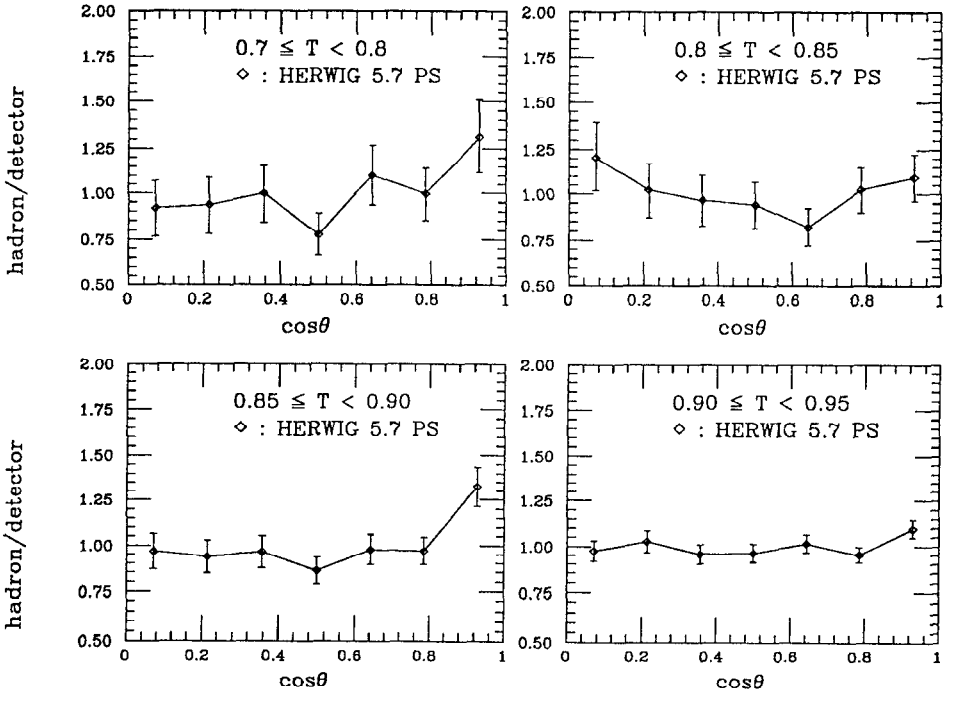

Figure 5.16: The hadron-to-detector correction factors of $cos\theta$ for selected values of $T = x_1$.

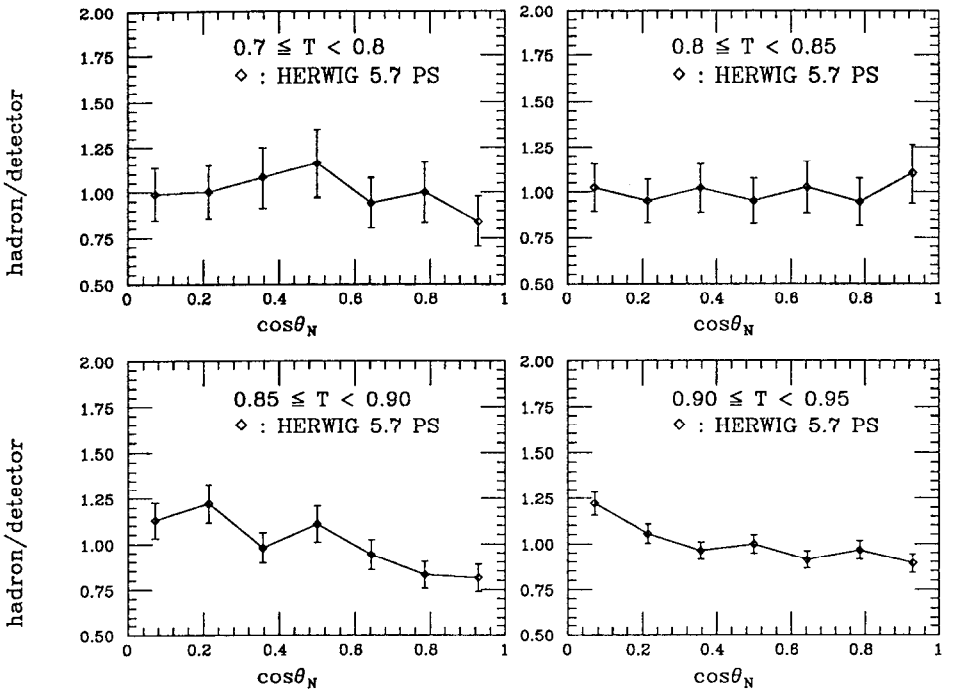

Figure 5.17: The hadron-to-detector correction factors of $cos\theta_N$ for selected values of $T = x_1$.

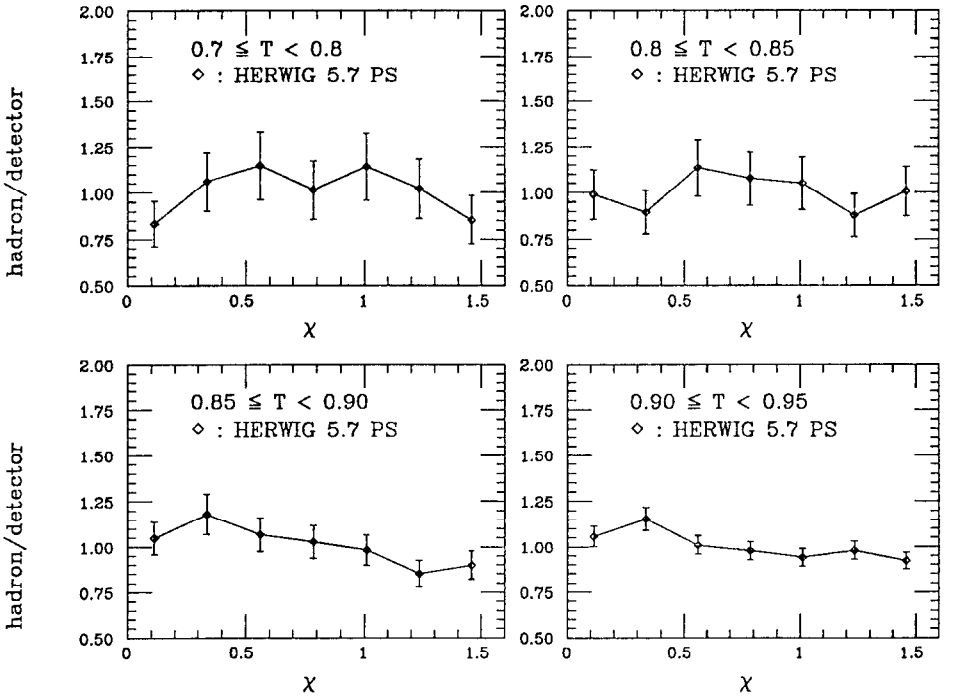

Figure 5.18: The hadron-to-detector correction factors of χ for selected values of $T = x_1$.

x_1	$(p/h)_{sta}(\%)$	$(h/d)_{sta}(\%)$	x_2	$(p/h)_{sta}(\%)$	$(h/d)_{sta}(\%)$
0.676	29	41.1	0.527	4.7	7.9
0.700	13.7	20.4	0.563	3.4	5.5
0.724	10.4	15.8	0.598	3.1	4.8
0.748	8.1	12.0	0.632	2.8	4.6
0.772	6.7	10.6	0.668	2.7	4.4
0.796	5.7	8.7	0.702	2.6	4.2
0.820	4.8	7.8	0.738	2.5	4.0
0.844	4.1	6.3	0.772	2.5	3.8
0.868	3.4	5.1	0.808	2.3	3.6
0.892	2.7	4.1	0.842	2.2	3.2
0.916	2.1	3.3	0.877	2.1	2.9
0.940	1.6	2.4	0.913	2.0	2.6
0.964	1.1	1.6	0.947	1.9	2.3
0.988	1.4	1.9	0.983	2.6	3.4

Table 5.4: Statistical errors only of corrections for hadronization and detector effects for x_1 and x_2 variables: $(p/h)_{sta}$ is statistical error only for the correction of parton-to-hadron level: $(h/d)_{sta}$ is the statistical error only for the correction of hadron-to-detector level. The first and the fourth columns are the middle points of the histogram bins.

x_3	$(p/h)_{sta}(\%)$	$(h/d)_{sta}(\%)$	$cos\theta_{EK}$	$(p/h)_{sta}(\%)$	$(h/d)_{sta}(\%)$
0.023	3.4	4.5	0.025	3.6	5.8
0.067	2.0	2.4	0.075	3.5	5.6
0.113	2.0	2.5	0.125	3.5	5.6
0.158	2.0	2.8	0.175	3.5	5.6
0.202	2.1	3.1	0.225	3.5	5.6
0.248	2.2	3.4	0.275	3.4	5.5
0.293	2.3	3.6	0.325	3.4	5.5
0.337	2.4	3.9	0.375	3.3	5.3
0.382	2.5	4.0	0.425	3.2	5.1
0.428	2.6	4.1	0.475	3.2	5.0
0.473	2.6	4.1	0.525	3.0	4.7
0.517	3.0	4.8	0.575	2.9	4.6
0.563	4.8	7.5	0.625	2.8	4.2
0.608	7.2	11.	0.675	2.7	4.0
0.652	15.7	22.7	0.725	2.6	3.7
			0.775	2.5	3.4
			0.825	2.4	3.1
			0.875	2.3	2.8
			0.925	2.3	2.9
			0.975	3.9	5.2

Table 5.5: Statistical errors only of corrections for hadronization and detector effects for x_3 and $cos\theta_{EK}$ variables: $(p/h)_{sta}$ is statistical error only for the correction of parton to hadron level: $(h/d)_{sta}$ is the statistical error only for the correction of hadron to detector level. The first and the fourth columns are the middle points of the histogram bins.

5.7 The Corrected Data

By applying equation 5.3 to the raw data as described in section 5.6, we get the corrected data at the parton level as seen in figures 5.19, 5.20, 5.21 and 5.22. Here the parton shower simulation of JETSET6.3 is used in calculating the parton-to-hadron correction factor $C_{ph}(i)$, and the parton shower simulation of HERWIG5.7 is used for the hadron-to-detector level correction factor $C_{hd}(i)$. The errors on these plots are statistical errors only. Also shown in figure 5.19 is the parton shower simulation of JETSET6.3 for vector QCD model and scalar gluon model of the first order M.E. of JETSET7.3 obtained from reference[17] as comparison.

The corrected data of angular distributions ($cos\theta$, $cos\theta_N$ and β) are fitted using the equations in section 2.2.3. The α, α_N and β parameters associated with ($cos\theta$, $cos\theta_N$ and β) are obtained. Figures 5.20, 5.21 and 5.22 show the fitting curves, values of fitting parameters, statistical errors of fitting parameters and χ^2 with the corrected data. Figure 5.23 shows values of parameters (α, α_N and β) depending on T with statistical errors. T of figure 5.23 is assigned with the midpoint of each range.

The theoretical gluon curves of figure 5.23 ($\alpha(T)$, $\beta(T)$, $\alpha_N(T)$) are calculated with equations (2.9, 2.10 and 2.11) and the differential equations (2.6) for vector gluon theory and those (2.7) for scalar gluon theory in the section 2.2.3[14]. Where the vector-vector (VV) terms are equal to the axialvector-axialvector (AA) terms in the vector gluon theory, but, VV $\neq$ AA in the scalar gluon theory (see the section 2.2.3). The scalar gluon curves of figure 5.23 ($\alpha(T)$, $\beta(T)$) are made with only VV terms[14] of scalar gluon theory. But, the scalar gluon curve of $\alpha_N(T)$ was obtained from the paper[16] with VV and AA terms.

5.8 Systematic and Statistical Errors

The systematic errors of a measurement consist of experimental and theoretical systematic errors. The experimental systematic errors come from the detector acceptance, efficiency and resolution, the detector simulation and reconstruction programs, and from event selection cuts applied to the data. The theoretical systematic errors come from the choice of hadronization schemes, the higher order corrections. The systematic errors are calculated for all the bins in the histogram plots.

The systematic errors from various sources are calculated through the following variations applied to data and MC. The standard cut condition mentioned in the section 4.4 is described.

(I) Experimental Systematic Errors

- **Event Selection**

  s) Standard Cuts on the total corrected energy, imbalance, numbers of clusters (N_{cl}) depending on the regions:

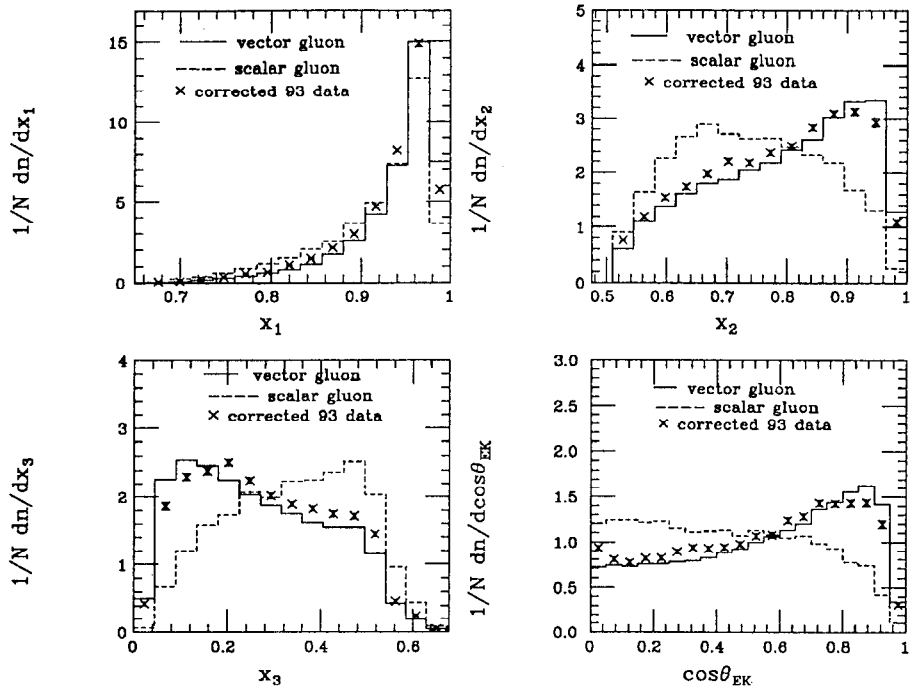

Figure 5.19: The corrected 93 data of x_1, x_2, x_3 and $cos\theta_{EK}$ distributions with **statistical error only** compared with parton level simulations for vector QCD model and scalar gluon model.

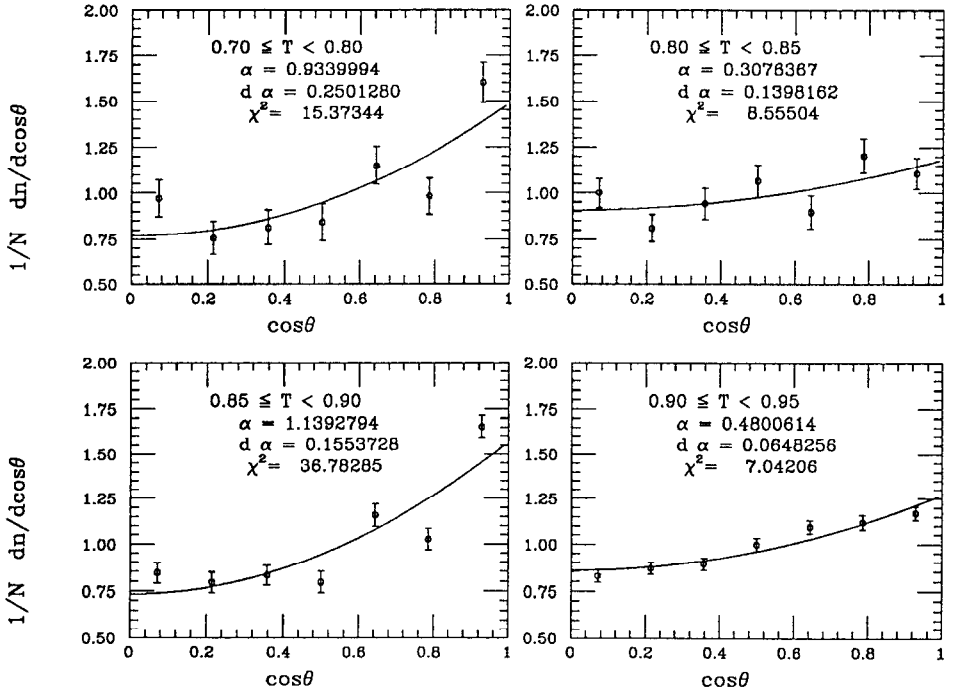

Figure 5.20: The corrected 93 data of $cos\theta$ distribution : α (the fitting parameter): $d\alpha$ (the **statistical error only** of the fitting parameter) with χ^2.

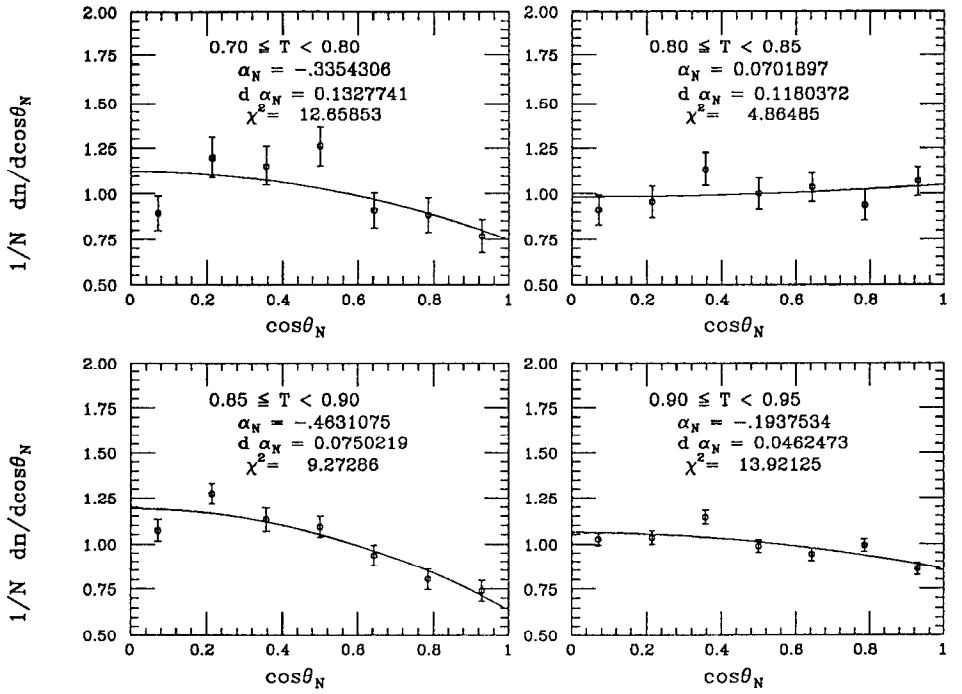

Figure 5.21: The corrected 93 data of $cos\theta_N$ distribution : α_N (the fitting parameter): $d\alpha_N$ (the **statistical error only** of the fitting parameter) with χ^2.

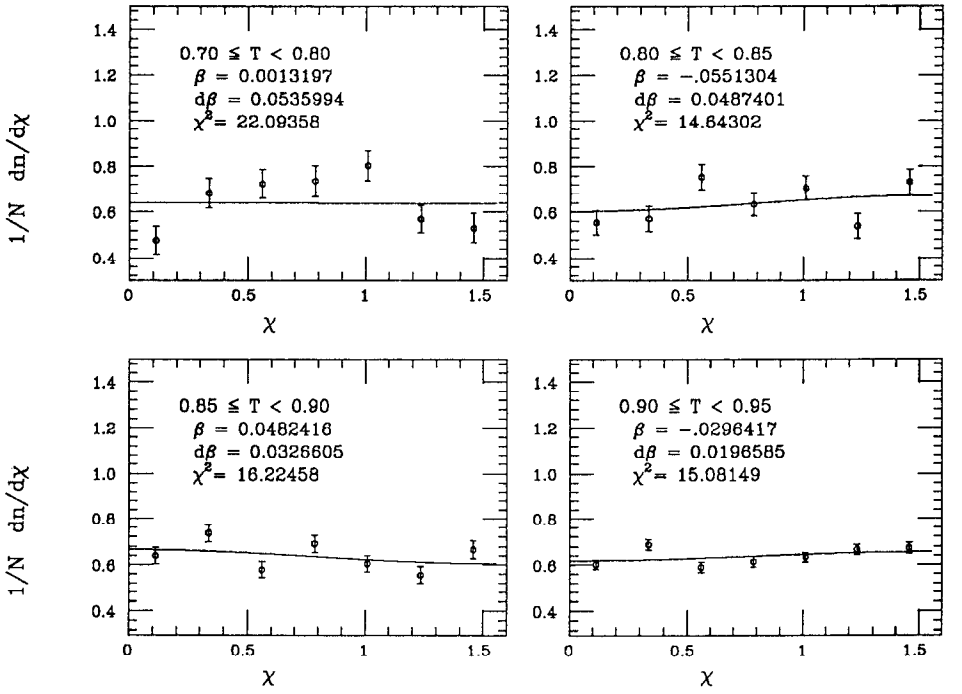

Figure 5.22: The corrected 93 data of χ distribution: β (the fitting parameter): $d\beta$ (the **statistical error only** of the fitting parameter) with χ^2.

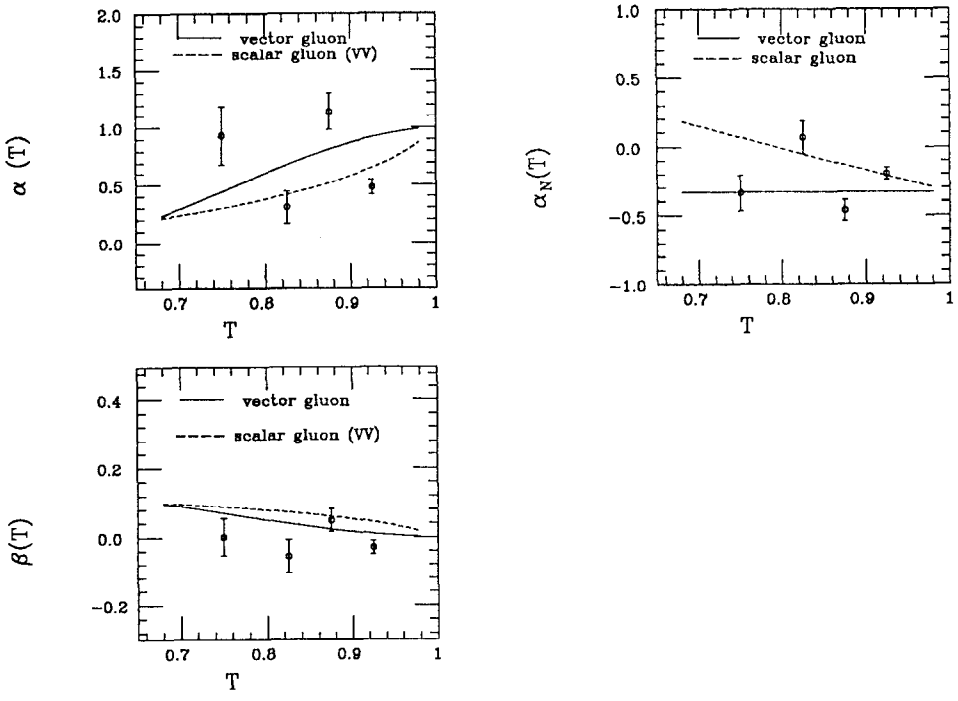

Figure 5.23: O: The data points of the parameters (α, α_N and β) for selected values of $T = x_1$ with **statistical error only**: solid line (vector gluon theory): dashed line (scalar gluon theory: only VV terms.)

- $E_{tot}^{cor} > 15$ GeV
- $I_{cor} < 0.6$
- $N_{cl} > 8$, $|cos\theta_{Thrust_{cor}}| \leq 0.8$
- $N_{cl} > 11$, $|cos\theta_{Thrust_{cor}}| > 0.8$

a) Tighten the cuts on the total corrected energy, imbalance, numbers of clusters (N_{cl}) depending on the regions:

- $E_{tot}^{cor} > 25$ GeV
- $I_{cor} < 0.3$
- $N_{cl} > 10$, $|cos\theta_{Thrust_{cor}}| \leq 0.8$
- $N_{cl} > 13$, $|cos\theta_{Thrust_{cor}}| > 0.8$

b) Loosen the cuts on the total corrected energy, imbalance, numbers of clusters (N_{cl}) depending on the regions:

- $E_{tot}^{cor} > 10$ GeV
- $I_{cor} < 0.8$

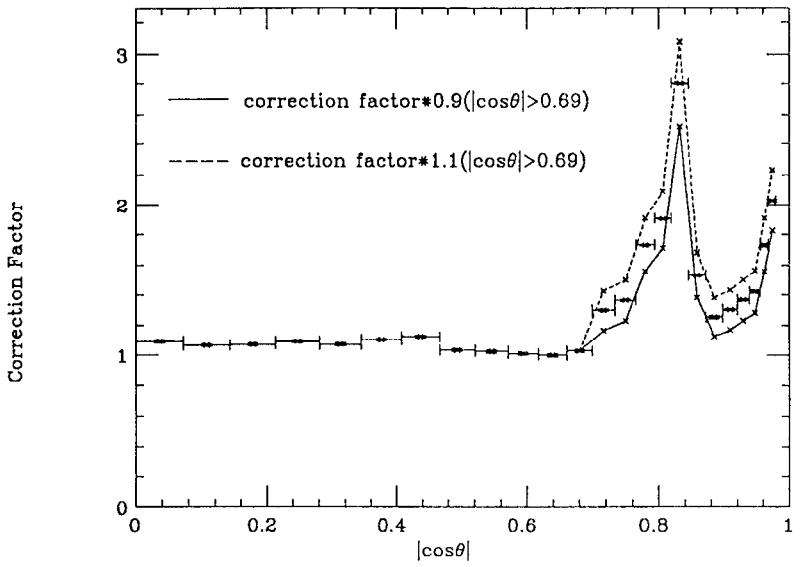

Figure 5.24: The correction factors of LAC energy response: solid line: 0.9×correction factor for $cos\theta > 0.69$ and dashed Line: 1.1×Correction Factor for $cos\theta > 0.69$.

- $N_{cl} > 6$, $|cos\theta_{Thrust_{cor}}| \leq 0.8$
- $N_{cl} > 9$, $|cos\theta_{Thrust_{cor}}| > 0.8$

c) Tighten the cut for detector acceptance:

- $|cos\theta_{Thrust_{cor}}| < 0.9$

- **Change of Correction Factor of LAC Energy Response**

To estimate the errors due to the correction of LAC energy response for ENDCAP region,

d) applied 0.9 value to correction factor of LAC energy response for $|cos\theta| > 0.69$ like figure 5.24.

e) applied 1.1 value to correction factor of LAC energy response for $|cos\theta| > 0.69$ like figure 5.24

Variations **a)-e)** are applied to both the Monte Carlo (HERWIG5.7) and the raw data. The hadron-to-detector level correction factors C_{hd} are calculated for each case and the raw data passing cuts **a)-e)** are corrected accordingly. In the above five cases, the parton-to-hadron correction factors C_{ph} are obtained from the parton shower simulation of JETSET6.3 as shown in figures 5.11, 5.12, 5.13 and 5.14.

(II) The theoretical systematic errors

f) Use the first order matrix element simulation of JETSET7.4 to calculate the parton-to-hadron correction factor C_{ph}.

g) Use the second order matrix element simulation of JETSET7.4. to calculate C_{ph}.

h) Use the parton shower simulation of JETSET7.4 to calculate C_{ph}.

In calculating all theoretical systematic errors, use the detector level simulation of HERWIG5.7 with parton shower and the raw data, passing the standard selection cut to calculate the hadron-to-detector correction factors C_{hd}.

The systematic error from each source is calculated with the difference between corrected data from each variation and that from the standard set. All fitting parameters (α, α_N and β) depending on T are calculated in corrected data from each variation and that from the standard set. Also, the difference between the fitting parameters from each variation and those from standard set gives the systematic errors from each source. The systematic errors from various sources are plotted in figure 5.25 for distributions of x_1,x_2,x_3 and $cos\theta_{EK}$ and figure 5.26 for parameters of α, α_N and β.

The experimental systematic errors can be classified as event selection (σ_{sel}) and change of correction factor of LAC energy response (σ_{cor}). The theoretical systematic error can be written as σ_{the}. The biggest value of errors from variations **a-c** gives an upper limit to the systematic error (σ_{sel}). Similarly, σ_{cor} and σ_{the} are the biggest values of errors from variations **d-e** and from variations **f-h**. The systematic error (σ_{syst}) is calculated through adding up errors of σ_{sel}, σ_{cor} and σ_{the} in quadrature.

The each systematic errors are calculated at each bin of x_1, x_2, x_3 and $cos\theta_{EK}$ distributions and at each parameters (α, α_N and β) depending on T. They are all listed in tables 5.6, 5.7 and 5.8. Additionally, tables 5.9, 5.10 and 5.11 show values of parameters (α, α_N and β), statistical errors of parameters, χ^2 per degree of freedom (χ^2/ndf) and differences between parameters with standard cut (s) and parameters with different cuts (a-h) depending on T.

5.9 Results and Conclusions

The total error (σ_{tot}) is calculated adding up the systematic error (σ_{syst}) and the statistical error (σ_{sta}) in quadrature. The corrected data with the total errors are shown in figures 5.27 and 5.28. The corrected data (figure 5.19) with total errors of LAC (Calorimeter module) is compared with the corrected data with statistical errors of CDC (Central Drift Chamber) module made by the reference[17] as seen in figure 5.29.

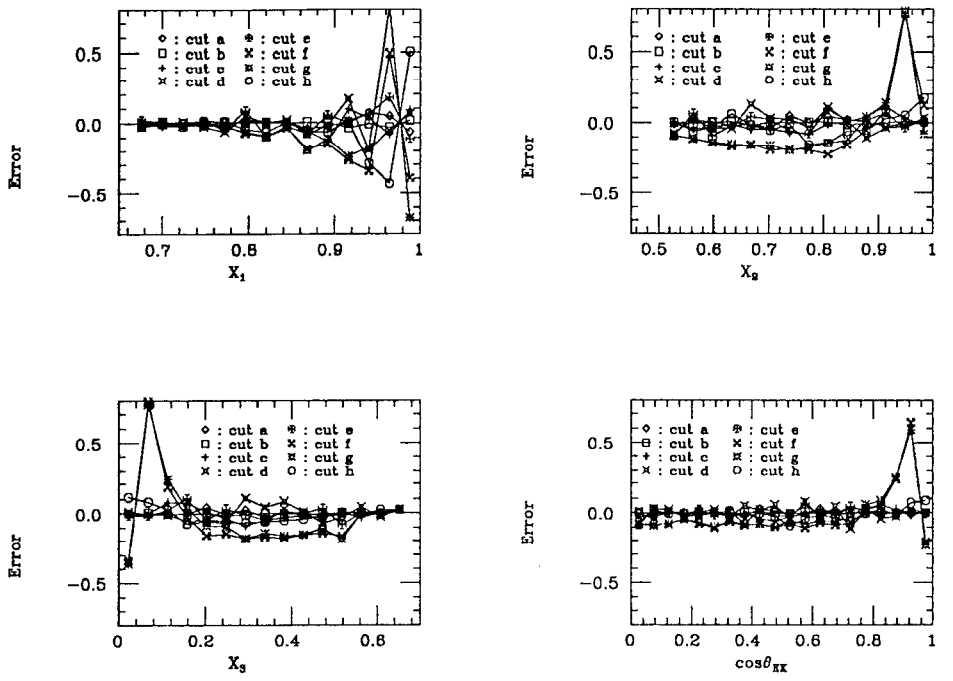

Figure 5.25: The systematic errors from various sources for x_1, x_2, x_3 and $cos\theta_{EK}$.

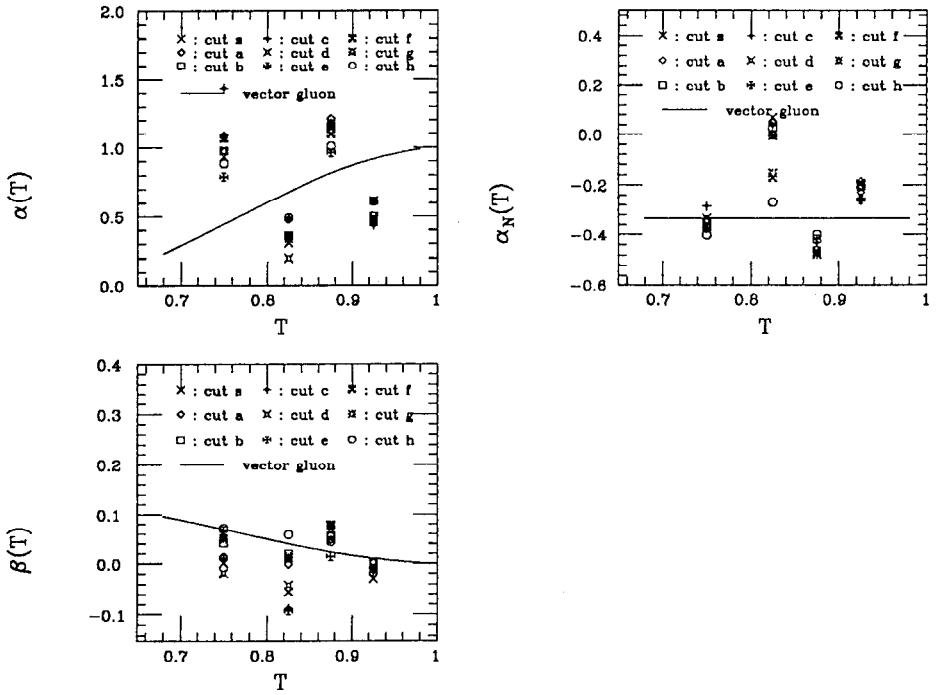

Figure 5.26: The systematic errors from various sources for α, α_N and β: solid line (vector QCD model).

x_1	data	σ_{sta}	σ_{sel}	σ_{cor}	σ_{the}	σ_{syst}
0.676	0.049	0.007	0.009	0.019	0.023	0.031
0.700	0.078	0.012	0.015	0.013	0.003	0.021
0.724	0.188	0.017	0.017	0.024	0.017	0.034
0.748	0.355	0.023	0.017	0.024	0.018	0.034
0.772	0.570	0.030	0.014	0.058	0.024	0.064
0.796	0.661	0.034	0.026	0.087	0.067	0.113
0.820	1.090	0.039	0.007	0.091	0.094	0.131
0.844	1.472	0.046	0.011	0.022	0.150*	0.152*
0.868	2.128	0.057	0.053	0.075	0.197	0.218
0.892	2.954	0.068	0.127	0.052	0.144	0.199
0.916	4.702	0.086	0.093	0.167	0.266	0.328
0.940	8.238	0.114	0.070	0.192	0.346	0.401
0.964	14.865	0.165	0.076	0.176	0.823	0.845
0.988	5.742	0.128	0.083	0.109	0.680	0.694

x_2	data	σ_{sta}	σ_{sel}	σ_{cor}	σ_{the}	σ_{syst}
0.527	0.756	0.024	0.006	0.091	0.090	0.128
0.563	1.191	0.035	0.039	0.064	0.114	0.136
0.598	1.543	0.040	0.030	0.090	0.142	0.171
0.632	1.742	0.043	0.021	0.038	0.170	0.175
0.668	1.975	0.045	0.046	0.125	0.160	0.208
0.702	2.201	0.047	0.044	0.030	0.196	0.203
0.738	2.173	0.048	0.066	0.055	0.198	0.215
0.772	2.375	0.050	0.078	0.075	0.195	0.223
0.808	2.498	0.052	0.043	0.103	0.226	0.252
0.842	2.835	0.057	0.019	0.015	0.156	0.158
0.877	3.087	0.062	0.041	0.107	0.052	0.126
0.913	3.128	0.068	0.111	0.068	0.135	0.188
0.947	2.930	0.074	0.026	0.037	0.790	0.791
0.983	1.091	0.051	0.010	0.033	0.172	0.176

Table 5.6: The corrected data with experimental systematic (σ_{sel} and σ_{cor}), theoretical systematic (σ_{the}), total systematic (σ_{syst}) and statistical errors (σ_{sta}) for x_1 and x_2. The first column is the middle point of the histogram bin. (*: correction based on deviations of adjacent bins; this error was increased from fluctuation shown in figure 5.25.)

x_3	data	σ_{sta}	σ_{sel}	σ_{cor}	σ_{the}	σ_{syst}
0.023	0.429	0.030	0.007	0.014	0.363	0.363
0.067	1.859	0.055	0.010	0.014	0.794	0.794
0.113	2.298	0.054	0.076	0.026	0.235	0.248
0.158	2.384	0.049	0.072	0.102	0.074	0.145
0.202	2.508	0.047	0.042	0.045	0.159	0.171
0.248	2.246	0.043	0.036	0.054	0.147	0.161
0.293	2.014	0.040	0.088	0.103	0.183	0.228
0.337	1.888	0.039	0.046	0.047	0.171	0.183
0.382	1.821	0.037	0.029	0.081	0.181	0.200
0.428	1.744	0.037	0.014	0.013	0.154	0.156
0.473	1.715	0.037	0.031	0.070	0.144	0.163
0.517	1.450	0.033	0.009	0.082	0.188	0.205
0.563	0.465	0.020	0.028	0.045	0.006	0.053
0.608	0.248	0.014	0.008	0.025	0.024	0.036
0.652	0.051	0.006	0.010	0.003	0.010	0.015
$cos\theta_{EK}$	data	σ_{sta}	σ_{sel}	σ_{cor}	σ_{the}	σ_{syst}
0.025	0.931	0.024	0.025	0.087	0.080	0.121
0.075	0.804	0.024	0.030	0.027	0.089	0.098
0.125	0.770	0.024	0.012	0.023	0.079	0.083
0.175	0.816	0.024	0.027	0.019	0.044	0.055
0.225	0.819	0.025	0.016	0.021	0.076	0.080
0.275	0.889	0.025	0.003	0.023	0.106	0.109
0.325	0.934	0.026	0.024	0.024	0.063	0.072
0.375	0.924	0.026	0.017	0.050	0.087	0.102
0.425	0.941	0.027	0.040	0.019	0.081	0.092
0.475	0.975	0.027	0.056	0.056	0.100	0.127
0.525	1.067	0.028	0.027	0.032	0.093	0.102
0.575	1.078	0.029	0.007	0.077	0.107	0.132
0.625	1.238	0.031	0.031	0.037	0.071	0.086
0.675	1.281	0.032	0.005	0.045	0.086	0.098
0.725	1.428	0.035	0.027	0.112	0.072	0.136
0.775	1.424	0.036	0.032	0.025	0.058	0.071
0.825	1.427	0.039	0.057	0.040	0.081	0.107
0.875	1.433	0.042	0.022	0.024	0.245	0.247
0.925	1.198	0.042	0.013	0.026	0.641	0.642
0.975	0.312	0.024	0.005	0.005	0.237	0.237

Table 5.7: The corrected data with experimental systematic (σ_{sel} and σ_{cor}), theoretical systematic (σ_{the}), total systematic (σ_{syst}) and statistical errors (σ_{sta}) for x_3 and $cos\theta_{EK}$. The first column is the middle point of the histogram bin.

T	α	σ_{sta}	σ_{sel}	σ_{cor}	σ_{the}	σ_{syst}
$0.7 \leq$ T < 0.8	0.934	0.250	0.501	0.145	0.133	0.538
$0.8 \leq$ T < 0.85	0.308	0.140	0.181	0.108	0.182	0.278
$0.85 \leq$ T < 0.9	1.139	0.155	0.074	0.177	0.132	0.232
$0.9 \leq$ T < 0.95	0.480	0.065	0.049	0.136	0.016	0.145
T	α_N	σ_{sta}	σ_{sel}	σ_{cor}	σ_{the}	σ_{syst}
$0.7 \leq$ T < 0.8	-.335	0.133	0.051	0.037	0.066	0.092
$0.8 \leq$ T < 0.85	0.070	0.118	0.040	0.075	0.337	0.348
$0.85 \leq$ T < 0.9	-.463	0.075	0.030	0.045	0.065	0.085
$0.9 \leq$ T < 0.95	-.194	0.046	0.069	0.063	0.012	0.094
T	β	σ_{sta}	σ_{sel}	σ_{cor}	σ_{the}	σ_{syst}
$0.7 \leq$ T < 0.8	0.001	0.054	0.041	0.066	0.070	0.105
$0.8 \leq$ T < 0.85	-.055	0.049	0.073	0.038	0.114	0.140
$0.85 \leq$ T < 0.9	0.048	0.033	0.028	0.034	0.030	0.054
$0.9 \leq$ T < 0.95	-.030	0.020	0.033	0.025	0.032	0.052

Table 5.8: Experimental systematic (σ_{sel} and σ_{cor}), theoretical systematic (σ_{the}), total systematic (σ_{syst}) and statistical errors (σ_{sta}) for α, α_N and β for selected values of $T = x_1$.

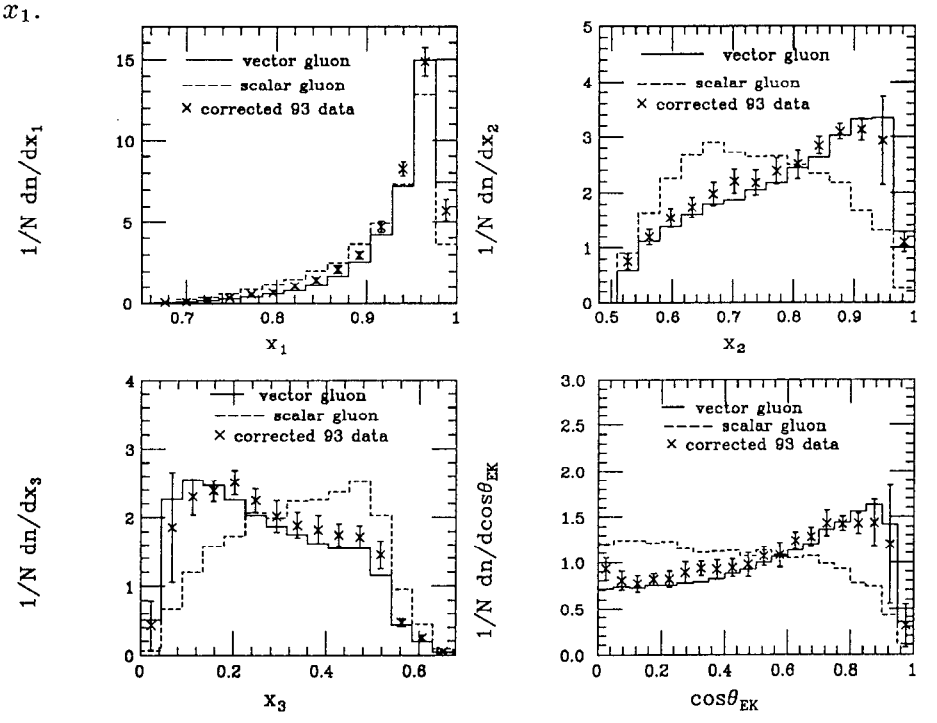

Figure 5.27: The corrected 93 data of x_1, x_2, x_3 and $cos\theta_{EK}$ distributions with **total errors** compared with parton level simulations for vector QCD model and scalar gluon model.

	cut condition	α	$d\alpha_{sta}$	χ^2/ndf	dα
$0.7 \leq T < 0.8$	s	0.934	0.250	2.196	0.000
	a	1.086	0.282	3.339	0.152
	b	0.977	0.252	2.769	0.043
	c	1.435	0.296	3.801	0.501
	d	0.974	0.255	3.354	0.040
	e	0.789	0.231	3.204	-.145
	f	1.065	0.268	2.037	0.131
	g	1.067	0.268	1.560	0.133
	h	0.886	0.242	3.220	-.048
	cut condition	α	$d\alpha_{sta}$	χ^2/ndf	dα
$0.8 \leq T < 0.85$	s	0.308	0.140	1.222	0.000
	a	0.476	0.163	0.767	0.168
	b	0.360	0.143	1.339	0.052
	c	0.489	0.141	0.863	0.181
	d	0.200	0.127	1.280	-.108
	e	0.348	0.144	0.786	0.041
	f	0.355	0.144	1.602	0.048
	g	0.337	0.142	1.869	0.029
	h	0.490	0.158	1.465	0.182
	cut condition	α	$d\alpha_{sta}$	χ^2/ndf	dα
$0.85 \leq T < 0.9$	s	1.139	0.155	5.255	0.000
	a	1.213	0.167	5.729	0.074
	b	1.136	0.154	4.886	-.003
	c	1.181	0.144	3.428	0.042
	d	1.143	0.155	3.550	0.004
	e	0.963	0.144	2.943	-.177
	f	1.097	0.152	4.904	-.042
	g	1.170	0.158	4.744	0.031
	h	1.007	0.145	3.566	-.132
	cut condition	α	$d\alpha_{sta}$	χ^2/ndf	dα
$0.9 \leq T < 0.95$	s	0.480	0.065	1.006	0.000
	a	0.474	0.067	0.784	-.006
	b	0.499	0.065	0.922	0.019
	c	0.431	0.056	0.989	-.049
	d	0.616	0.070	0.864	0.136
	e	0.611	0.070	0.834	0.131
	f	0.484	0.065	2.338	0.004
	g	0.475	0.065	2.105	-.005
	h	0.465	0.064	1.675	-.016

Table 5.9: Parameter α, statistical error (dα), χ^2 per degree of freedom (χ^2/ndf) and difference between α with standard cut (s) and α's with different cuts (a-h) (dα) for selected values of $T = x_1$.

	cut condition	α_N	$d\alpha_{Nsta}$	χ^2/ndf	dα_N
$0.7 \leq T < 0.8$	s	-.335	0.133	1.808	0.000
	a	-.339	0.139	0.842	-.004
	b	-.356	0.131	1.767	-.021
	c	-.284	0.145	1.220	0.051
	d	-.333	0.133	1.179	0.003
	e	-.373	0.134	1.407	-.037
	f	-.368	0.132	2.698	-.032
	g	-.378	0.132	2.172	-.043
	h	-.402	0.132	3.597	-.066
	cut condition	α_N	$d\alpha_{Nsta}$	χ^2/ndf	dα_N
$0.8 \leq T < 0.85$	s	0.070	0.118	0.695	0.000
	a	0.049	0.122	0.931	-.021
	b	0.031	0.113	0.525	-.040
	c	0.036	0.123	1.682	-.034
	d	-.005	0.111	0.719	-.075
	e	-.004	0.111	1.770	-.074
	f	-.171	0.114	0.291	-.241
	g	-.153	0.114	0.385	-.223
	h	-.267	0.115	0.600	-.337
	cut condition	α_N	$d\alpha_{Nsta}$	χ^2/ndf	dα_N
$0.85 \leq T < 0.9$	s	-.463	0.075	1.325	0.000
	a	-.458	0.079	2.371	0.005
	b	-.465	0.074	1.175	-.001
	c	-.433	0.079	2.422	0.030
	d	-.468	0.076	2.588	-.004
	e	-.419	0.075	8.446	0.045
	f	-.464	0.075	0.350	-.001
	g	-.477	0.075	0.453	-.014
	h	-.398	0.075	0.596	0.065
	cut condition	α_N	$d\alpha_{Nsta}$	χ^2/ndf	dα_N
$0.90 \leq T < 0.95$	s	-.194	0.046	1.989	0.000
	a	-.187	0.048	2.481	0.007
	b	-.200	0.046	1.974	-.007
	c	-.262	0.049	2.410	-.069
	d	-.242	0.046	2.299	-.048
	e	-.257	0.046	1.462	-.063
	f	-.198	0.046	0.292	-.004
	g	-.201	0.046	0.254	-.008
	h	-.206	0.046	0.489	-.012

Table 5.10: Parameter α_N, statistical error (dα_N), χ^2 per degree of freedom (χ^2/ndf) and difference between α_N with standard cut (s) and α_N's with different cuts (a-h) (dα_N) for selected values of $T = x_1$.

	cut condition	β	$d\beta_{sta}$	χ^2/ndf	dβ
$0.7 \leq T < 0.8$	s	0.001	0.054	3.156	0.000
	a	0.014	0.057	2.166	0.013
	b	0.042	0.055	2.430	0.041
	c	0.009	0.059	1.746	0.007
	d	-.019	0.055	1.356	-.020
	e	0.068	0.057	1.690	0.066
	f	0.049	0.056	2.958	0.048
	g	0.051	0.056	3.090	0.050
	h	0.072	0.056	2.757	0.070
	cut condition	β	$d\beta_{sta}$	χ^2/ndf	dβ
$0.8 \leq T < 0.85$	s	-.055	0.049	2.092	0.000
	a	-.001	0.049	0.907	0.054
	b	0.018	0.047	1.227	0.073
	c	-.087	0.053	2.543	-.032
	d	-.042	0.047	2.245	0.013
	e	-.093	0.050	3.029	-.038
	f	0.014	0.048	1.656	0.069
	g	0.012	0.047	1.764	0.067
	h	0.059	0.049	2.093	0.114
	cut condition	β	$d\beta_{sta}$	χ^2/ndf	dβ
$0.85 \leq T < 0.9$	s	0.048	0.033	2.318	0.000
	a	0.048	0.034	2.407	0.000
	b	0.056	0.033	2.833	0.008
	c	0.077	0.036	2.220	0.028
	d	0.065	0.033	1.527	0.016
	e	0.014	0.032	0.581	-.034
	f	0.079	0.033	2.060	0.030
	g	0.078	0.033	2.841	0.030
	h	0.044	0.033	2.283	-.004
	cut condition	β	$d\beta_{sta}$	χ^2/ndf	dβ
$0.9 \leq T < 0.95$	s	-.030	0.020	2.154	0.000
	a	0.001	0.020	2.587	0.031
	b	0.003	0.019	2.029	0.033
	c	-.016	0.021	2.010	0.014
	d	-.005	0.019	1.741	0.025
	e	-.009	0.019	1.265	0.020
	f	-.010	0.019	2.844	0.019
	g	-.010	0.019	3.631	0.020
	h	0.002	0.019	1.313	0.032

Table 5.11: Parameter β, statistical error (dβ), χ^2 per degree of freedom (χ^2/ndf) and difference between β with standard cut (s) and β's with different cuts (a-h) (dβ) for selected values of $T = x_1$.

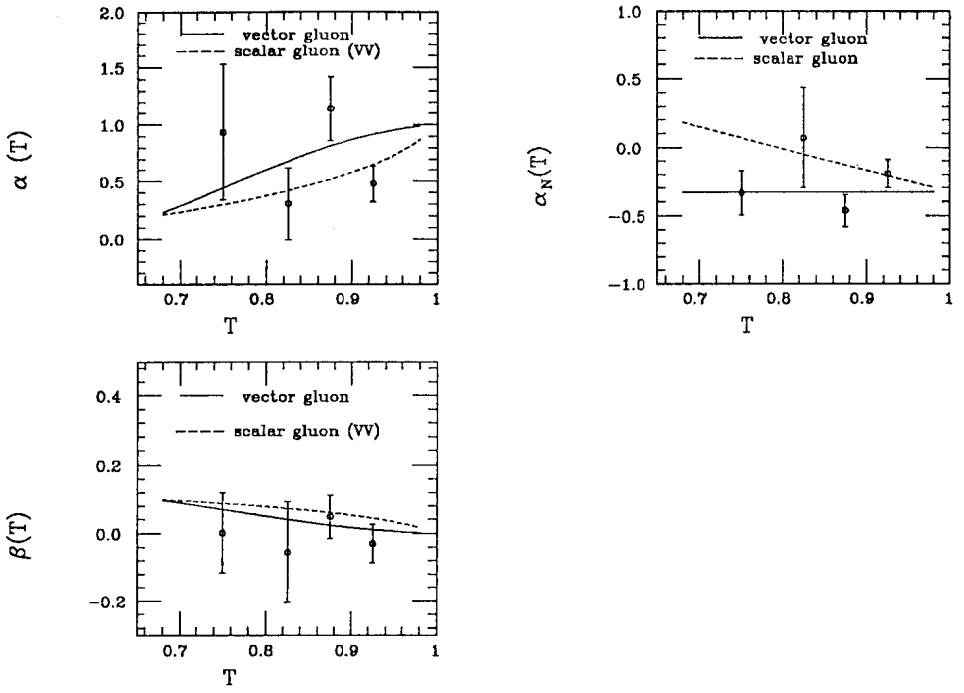

Figure 5.28: Parameters (α, α_N and β) with **total errors** for selected values of $T = x_1$: solid line (vector gluon): dashed line (scalar gluon).

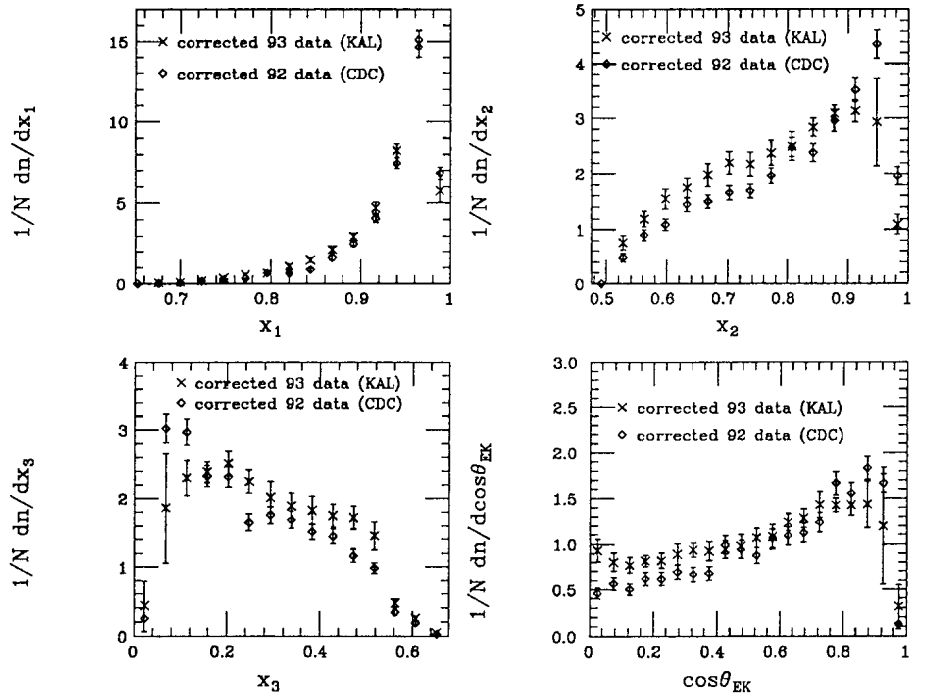

Figure 5.29: Comparison between the corrected data of LAC and the corrected Data of CDC: × (corrected data of LAC with **total errors**): ◇ (corrected data of CDC with **statistical errors only**).

	x_1	x_2	x_3	$\cos\theta_{EK}$
Vector Gluon	38.75*	11.99	14.28	16.46
Scalar Gluon	189.60*	212.81	230.43	240.81
NDF	13	13	14	19

Table 5.12: χ^2 between data and vector/scalar gluon predictions: (*: correction based on deviations of adjacent bins: see table 5.6 and figure 5.25.)

As one can see, the data favours the vector gluon model in the distributions of x_1, x_2, x_3 and $cos\theta_{EK}$. The scalar gluon model can not describe the data at all. The χ^2's between data and vector QCD simulation and between data and scalar gluon simulation are calculated as a quantitative comparison, which are listed in table 5.12.

The $cos\theta_N$ was suggested as the variable of T violation[54]. T violation has been searched according to right or left helicities with an electron beam polarization 63% accumulated in the SLD LAC in March through August of 1993. We used the rescaled three jets of the corrected LAC clusters (see the section 5.3) before parton level correction. However, the signature of T violation has not been found as seen in figure 5.30.

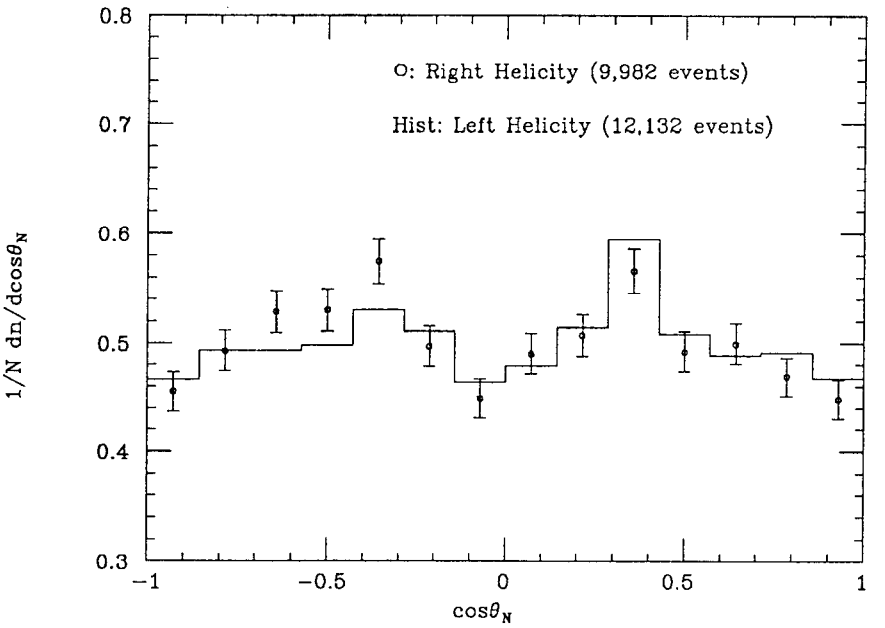

Figure 5.30: $Cos\theta_N$ depending on right or left helicities of an electron beam polarization 63% during 93 run with **statistical errors only**: hist (left helicity) and O (right helicity)

CHAPTER VI

$H^0 \rightarrow \gamma\gamma$ IN THE INTERMEDIATE HIGGS MASS AT HIGH ENERGY HADRON COLLIDERS

The theory of electroweak interaction based on Minimal Standard Model (MSM) explains vast amount of experimental data[55]. Underlying framework of a Higgs field, yet to be experimentally confirmed, can be explained as follows. Because a Higgs field has a non-zero vacuum expectation value, intermediate vector bosons ($W^{\pm}$, Z^0) and fermions can have massses through interaction with a Higgs field. The states with one or more Higgs fields carry non-zero SU(2) and U(1) quantum numbers, so the SU(2) and U(1) symmetries are effectively broken. That symmetry is valid for the Lagrangian, but not for the ground state of the system, it is said to be a spontaneously broken symmetry.

In the simplest one doublet Standard Model (SM) case, the original doublet contains four Higgs fields such as the longitudinal polarization state of $W^{\pm}$, Z^0 and H^0 (neutral Higgs boson). Above a mass of about 160 GeV the Higgs decay is dominated by intermediate vector bosons ($W^{\pm}$, Z^0). Below 160 GeV (the Intermediate Higgs mass) other channels are important.

It has also been pointed out by many authors[56] that, depending on the number of Higgs' and their masses, the $H^0 \rightarrow \gamma\gamma$ channel may be the only way to directly measure the Higgs. That is, because top quark mass is over Z^0 mass in CDF, we do not need to think about top quarks decay mode in the intermediate mass region. Therefore, branching ratio ($H^0 \rightarrow \gamma\gamma$) increases relatively. Since the preferred decay to a pair of heavy quarks (b and c quarks) are buried under the much larger QCD two jets background, the possible hope for finding an intermediate mass Higgs at High Energy Hadron Collider is through a rare decay with a relatively clean and distinctive signature such as $H^0 \rightarrow \gamma\gamma$. But, there are many backgrounds here too (see the reference[57]).

6.1 Production of $H^0 \rightarrow \gamma\gamma$

The H^0 production process of proton-proton collision can be divided as $q\overline{q}$ fusion, gg fusion and W^+W^- and ZZ fusion[58]. The H^0 production due to gg fusion have the largest value because the value of gluon structure function at small $x = m_{H^0}/\sqrt{s}$ is larger than that of valence or sea quark structure functions. H^0 will decay to various modes such as $f\overline{f}$, $\gamma\gamma$, W^*W^*, Z^*Z^* and $Z\gamma$[59]. Here f is fermions. The cross section of $H^0 \rightarrow \gamma\gamma$ can be calculated with H^0 production of gg fusion multiplied by the branching ratio of $H^0 \rightarrow \gamma\gamma$. The cross section of $H^0 \rightarrow \gamma\gamma$ is approximately from 50 fb to 140 fb[57]. Suppose luminosity in High Energy Hadron Collider per year be 10 fb^{-1}, number of events per year of $H^0 \rightarrow \gamma\gamma$ are expected to be found in 500 to 1400 events.

6.2 Background Production of $H^0 \rightarrow \gamma\gamma$

The background production consists of the direct photon production (irreducible background) and QCD production. The decay modes of the direct photon production are $gg \rightarrow \gamma\gamma$ and $q\overline{q} \rightarrow \gamma\gamma$[60]. The decay modes of the QCD are $q\overline{q} \rightarrow \gamma g$, $qg \rightarrow q\gamma$ and $pp \rightarrow 2jets$[61].

The irreducible background can be suppressed with rapidity, energy and angular cuts as follows[57].

- $|cos\theta^*| < 0.8$ (θ^* is the photon angle in the $\gamma\gamma$ rest frame: while H^0 signal is isotropic, the background ($gg \rightarrow \gamma\gamma$) is forward.)
- $E_T^\gamma > 20$ GeV (E_T^γ is transverse energy of photon: the range of intermediate H^0 mass)
- $|\eta_\gamma| < 2.5$ (Geometrical cut of detector design)
- $|\eta_{\gamma\gamma}| < 3$ (Reduce the background($gg \rightarrow \gamma\gamma$))

The Isolation Cut is used to reduce the QCD background[62]. A particle (photon, electron or muon) is isolated if $\sum_R E_T - E_T^P < E_c + 0.1E_T^P$, where E_T^P is the transverse energy of the particle, E_T is the transverse energy of clusters found in the calorimeter, and E_c is the energy cut. The sum is taken inside a cone around the particle with radius $R = \sqrt{(\delta\eta)^2 + (\delta\phi)^2}$. We can take the tight Isolation Cut with larger R and smaller E_c if calorimeter had a good energy resolution.

6.3 How to Take the Tight Isolation Cut

The electronic noise of a liquid argon calorimeter increases due to a shorter integration time (16 ns period) of the SSC. If we reduced the electronic noise through

off-line analysis as seen in the chapter VIII, it would be possible to get better energy resolution. The QCD background would be suppressed with the tight Isolation Cut.

6.4 How to Reduce High Energetic π^0 Background

The background photon pairs from π^0 decay were reduced greatly through the Isolation Cut. However, since the photon pairs from the high energetic π^0 behave like a single photon due to the small opening angle of photon pairs, it would not be isolated by an Isolation Cut. The preradiator at front of EM calorimeter can distinguish between the photon signal from H^0 and the photon background from high energetic π^0. The test beam result of prototype silicon preradiator was explained in detail (see chapter VII).

CHAPTER VII

ANALYSIS OF A PROTOTYPE SILICON PRERADIATOR FOR HIGH ENERGY HADRON COLLIDERS

7.1 Introduction

We describe the design and first results from the test of a prototype of a preradiator detector. Such a detector could be used to enhance the identification of photons and electrons at the Superconducting Super Collider (SSC) or Large Hadron Collider (LHC) of high energy hadron colliders. Specifically, it may be used by the GEM detector to distinguish between single photons from Higgs decay and background photon pairs from π^0 decay.

Our prototype consists of tungsten radiator followed by silicon strip detectors. The tungsten thickness was changeable, varying from 0 to 3 radiation lengths. Two silicon detectors, oriented in X and Y, each consisting of 48 strips, each of length 48mm. The pitch is 1mm. This granularity is required for separating single and multi-photons at the SSC. The readout is achieved by low-noise, low-power custom preamplifier chips mounted directly on the detectors via custom circuit boards.

This preradiator was tested in a beam at Brookhaven National Laboratory (BNL) in July 1992. A lead glass array placed behind the silicon was used to determine energy resolution effects. The results from the test on spatial distributions and energy resolution, including correction for the energy deposited in the preradiator are presented, along with comparisons to EGS simulations.

It would be very difficult to tag the $H^0 \rightarrow \gamma\gamma$ signal from the high energetic $\pi^0 \rightarrow \gamma\gamma$ background. A more quantitative understanding of preradiator requirements for the $H^0 \rightarrow \gamma\gamma$ has been explained in the introduction of the paper[63]. The narrow width of electromagnetic showers after a few radiation lengths for high-Z radiator allow nearby showers to be distinguished at the $\approx$ 3 mm level, as required by the $H^0 \rightarrow \gamma\gamma$ kinematics[63]. Even if energies for the $H^0 \rightarrow \gamma\gamma$ signal were 50-100 GeV, electron energies took from BNL beam test are 5 GeV which has to be scaled up. The important question for the physics performance of SSC preradiator is how well

the 5 GeV showers can be modelled by the EGS monte carlo, and hence allow for an extrapolation to higher energy to be made with some confidence.

The contents related with theory and hardware system are explained in detail in the paper[63]. The paper[63] describes a quantitative understanding of preradiator requirements for the $H^0 \rightarrow \gamma\gamma$ signal, a quantitative estimate of preradiator effectiveness, the γ detection, and π^0 rejection efficiencies in the introduction section of it. In the preradiator prototype section of paper[63], describes components, setup of hardware system, and the test beam configuration in detail. In this report, there will be presented in detail the analysis processes of preradiator beam test results including pedestal correction, cut conditions for selecting good electron events and shower spatial distribution.

The data taking was limited to a two day period. Data was taken at 2, 4, and 5 GeV, mostly with electron triggers, although some pion data for calibration was also taken. In addition to separate pedestal runs, pedestal events were also taken out of time with the beam spill. Data was taken with 0, 1, and 3 radiation lengths of tungsten in front of the silicon. A run was also made with 4 cm (≈ 1.5 ") of aluminum between the preradiator and the lead glass in order to simulate the effect of a dewar wall. Table 7.1 describes run number, events, radiator, energy, and comments for the runs used in this analysis.

Run number	Events	Radiator	Energy	Comments
100	72,976	3 X_0 W	2.0 GeV	O.K
104	11,976	3 X_0 W	4.0 GeV	O.K
106	11,422	3 X_0 W	5.0 GeV	O.K
108	9,350	0 X_0 W	5.0 GeV	O.K
116	7,944	1 X_0 W	5.0 GeV	2 modules of Y strips are dead
118	5,564	3 X_0 W+1.5" AL	5.0 GeV	2 modules of Y strips are dead
120	5,350	3 X_0 W+1.5" AL	5.0 GeV	1 module of Y strips is dead
122	1,550	1 X_0 W	5.0 GeV	1 module of Y strip
W: tungsten				
AL: aluminum				
": inch				

Table 7.1: Run data information of preradiator beam test.

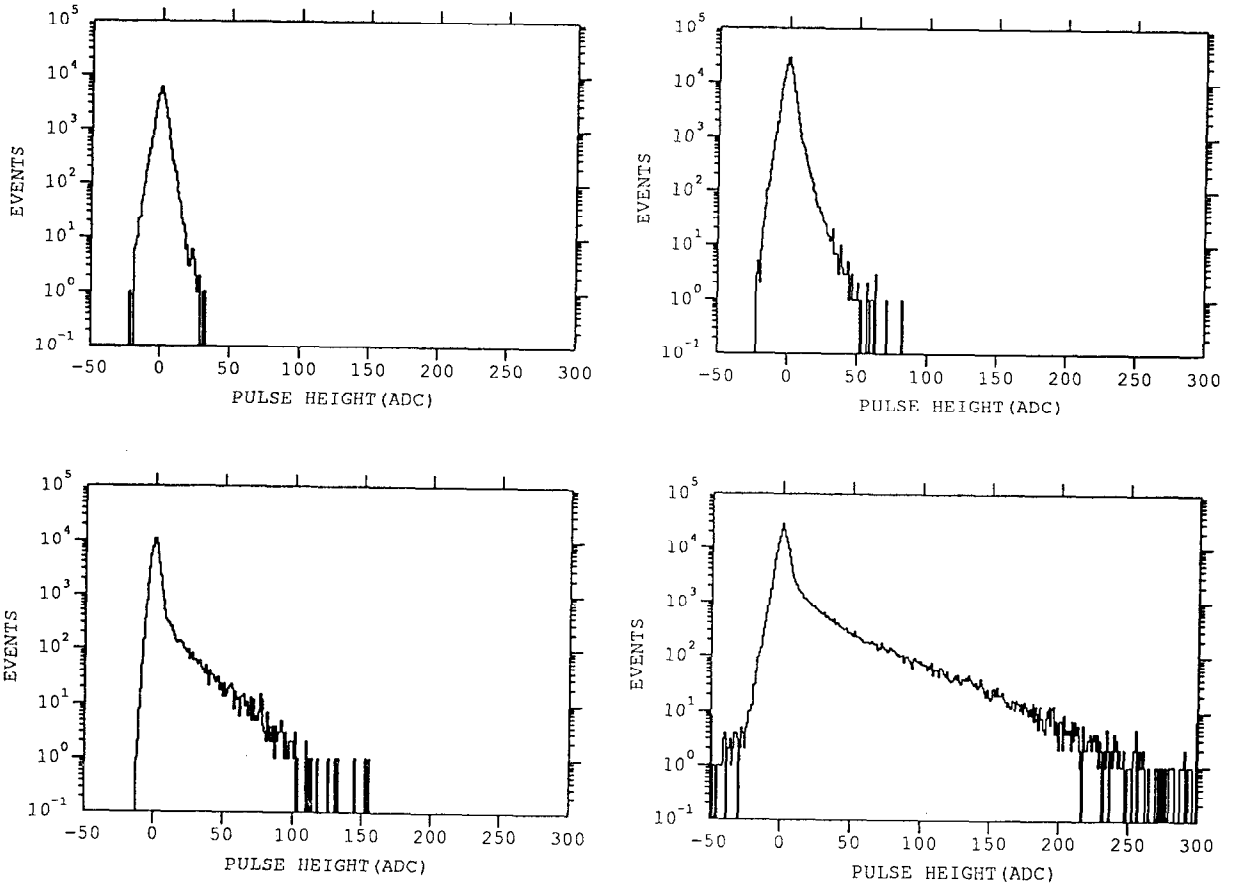

Figure 7.1: Pulse height distributions for all 96 strips under different conditions: (a) upper-left (pedestals only); (b) upper-right (5 GeV electrons with no radiator); (c) lower-left (1 X_0 of tungsten); (d) lower-right (3 X_0 of tungsten).

7.2 Analysis of Preradiator Beam Test Results

The test beam results are organized below into two sections which reflect the two important questions for the physics performance of an SSC preradiator:

- Can an electromagnetic shower be readily distinguished from nearly showers ?
- What effect does the preradiator have on the energy resolution of the electromagnetic calorimeter ?

First, we present some basic distributions. Figure 7.1 gives the pulse height distributions for the silicon strips under different conditions. The upper-left of figure 7.1 is for a pedestal run. This shows that the RMS noise is roughly 3.8 ADC counts with a pedestal correction (will be explained in the next section 7.2.1). This pedestal can be compared to a single MIP, which is about 10 ADC counts on average. The MIPs can, in fact, be seen in the shoulder of upper-right of figure 7.1, which is for a run with no preradiator in front of the silicon strips. Plots lower-left and lower-right are for runs with 1 X_0 and 3 X_0 of tungsten, respectively. One can clearly see the measurement of localized energy distributions from electromagnetic showers.

All data mentioned in section 7.1 were analyzed. For example, data with 5 GeV electrons and 3 X_0 of tungsten (example data) will be explained because data analysis process with other runs were exactly same as those of example data.

7.2.1 Pedestal Correction of Silicon Strip Detector

Because of the shortness of time for data taking, we had little opportunity to correct the coherent pickup in the hardware. Pedestal data of silicon strip detector have a coherent noise in relation with each channel, and so, we must remove the coherent noise. At first, choose reference channels which have the least possibility in taking data. Therefore, reference channels would be located at the edges of silicon strip detector. Since the beam is centered in the detector, the channels 9 and 48 are the edge channels of X strip, while 57 and 96 are the edge channels of Y strip in figure 7.12. We choose 9, 48, 57 and 96 as reference channels.

We can see plots of arbitrary correlative channels vs. reference channels before pedestal correction in figures 7.3, 7.4, 7.5 and 7.6. Some channels have strong correlation with reference channels, but, 57 reference channel has anti-correlation with other channels as you see in figure 7.5. Figures 7.3, 7.4, 7.5 and 7.6 were made with 500 pedestal events.

The $p(ref)$, pulse height of pedestal at reference channel , can be calculated as the following method at each event. At first, we can calculate $p(ref)$ with four reference channels (9,48,57,96),

$$\begin{aligned} p(ref) &= [(p(9) - < p(9) >) + (p(48) - < p(48) >) \\ &- (p(57) - < p(57) >) + (p(96) - < p(96) >)]/4 \end{aligned}$$

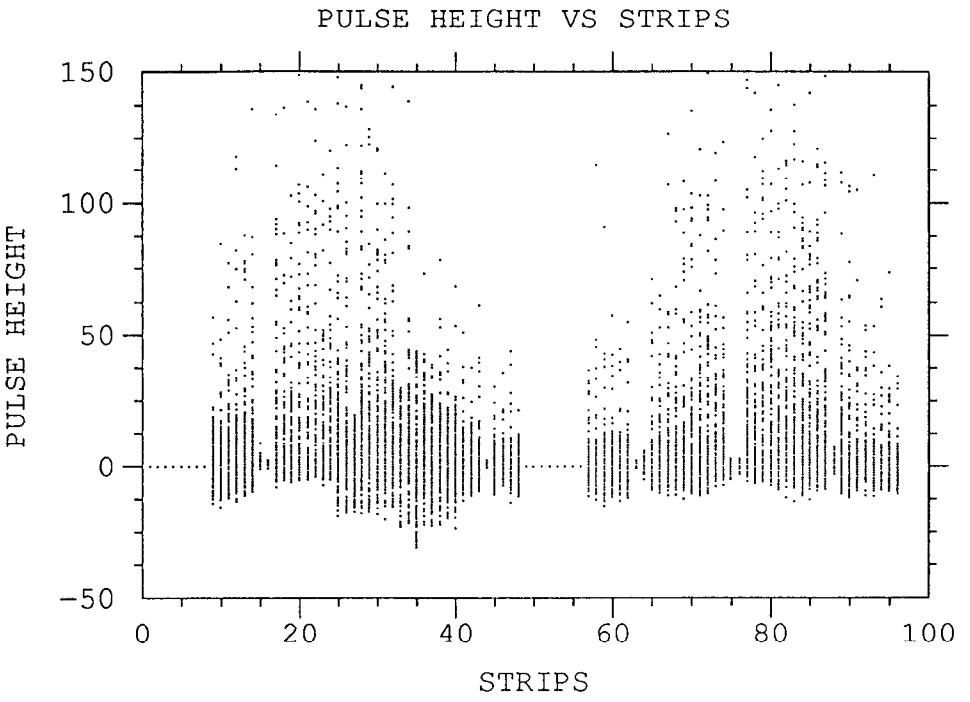

Figure 7.2: Uncorrected pulse height versus strips: unit of pulse height is ADC counts; the pulse height is obtained from uncorrected data.

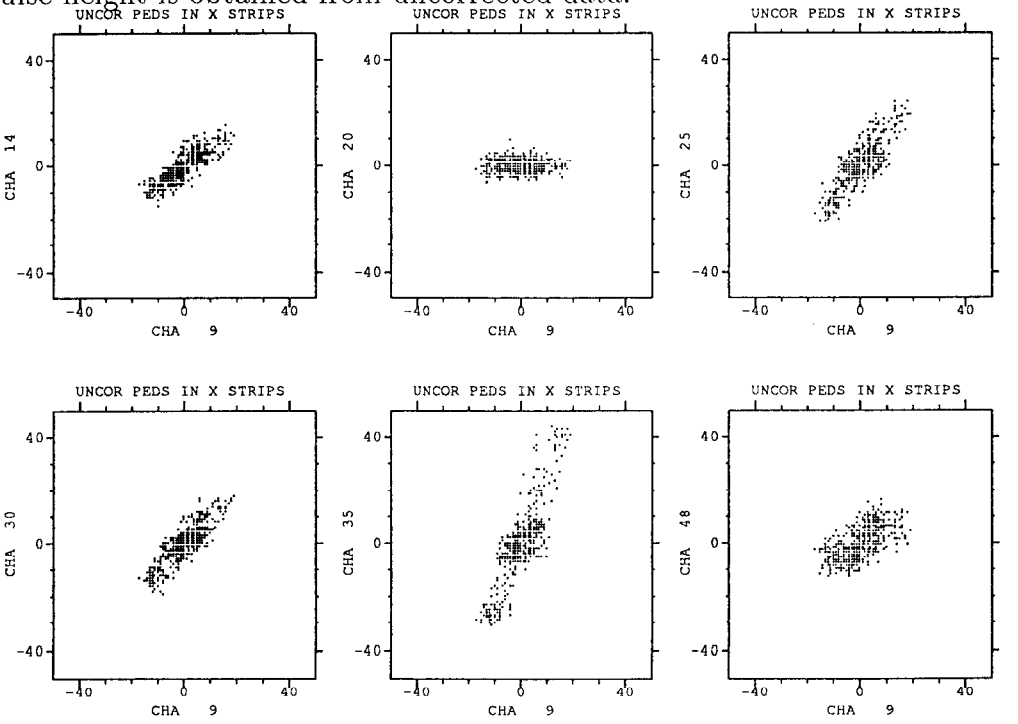

Figure 7.3: Correlative relations for arbitrary channels (14, 20,25,30,35,48) vs. reference channel (9) for the uncorrected pedestals.

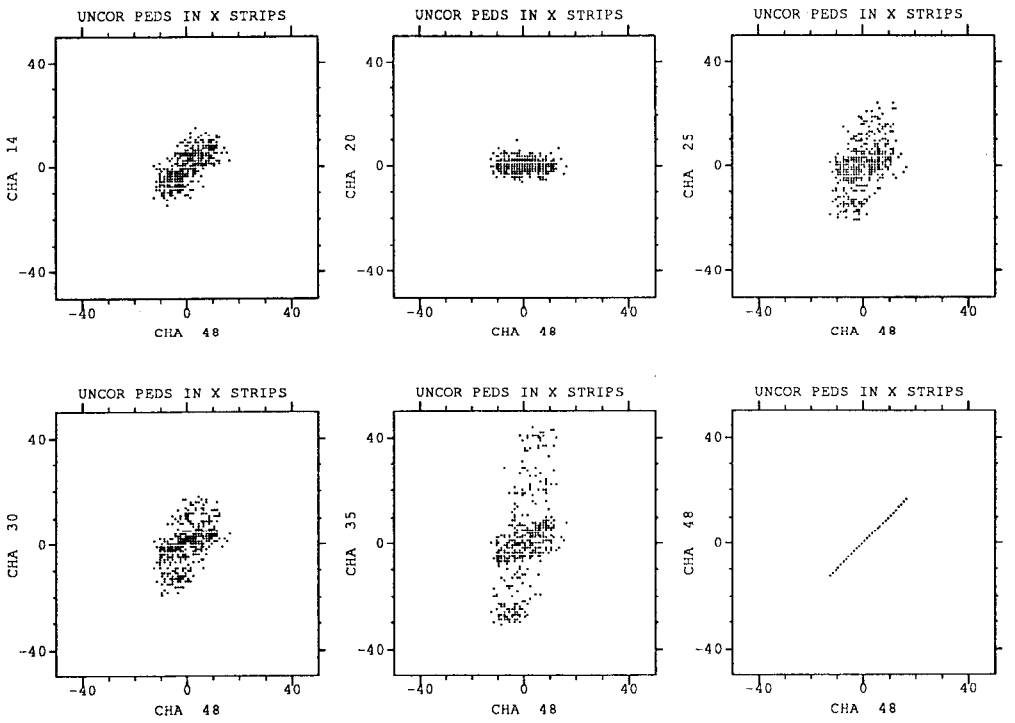

Figure 7.4: Correlative relations for arbitrary channels (14, 20,25,30,35,48) vs. reference channel (48) for the uncorrected pedestals.

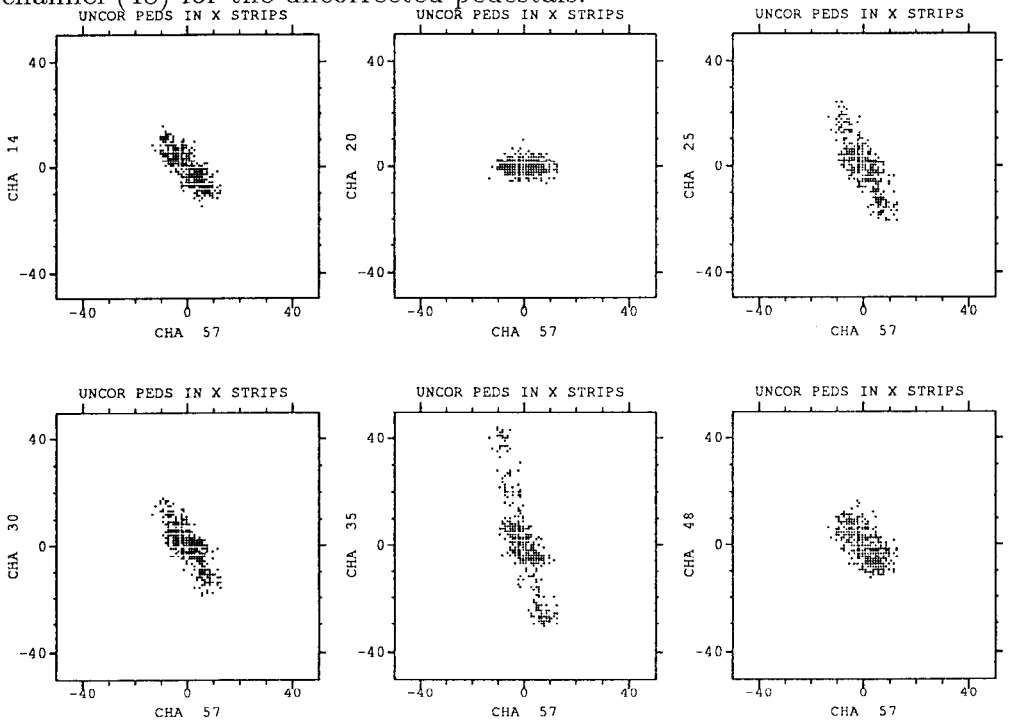

Figure 7.5: Correlative relations for arbitrary channels (14, 20,25,30,35,48) vs. reference channel (57) for the uncorrected pedestals.

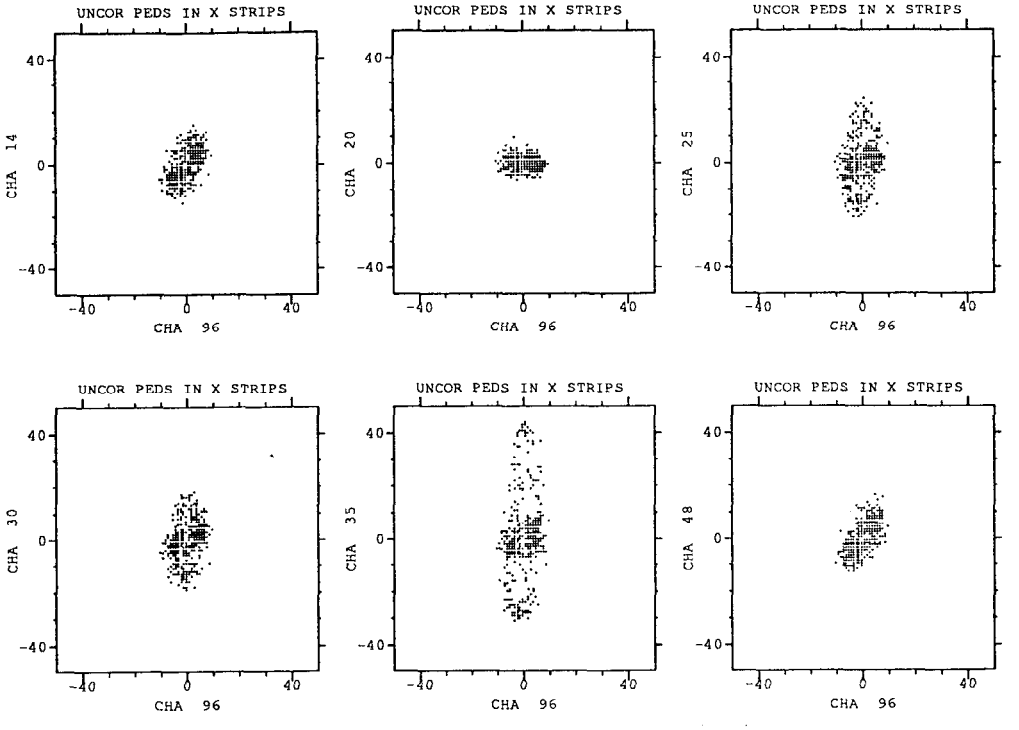

Figure 7.6: Correlative relations for arbitrary channels (14, 20,25,30,35,48) vs. reference channel (96) for the uncorrected pedestals.

The 57 channel was subtracted because that channel had anti-correlation.

where k: each channel number

$p(k)$: pulse height of pedestal at each channel

$< p(k) >$: average pulse height of pedestal at each channel for all pedestal events

If pulse heights of any reference channels were more than 15 from $p(ref)$, we removed them. That is, if $|p(ref) - (p(r) - < p(r) >)|$ were greater than 15, we removed them. Where r=9, 48, 96. Because 57 had anti-correlation, we use $|p(ref) + (p(r) - < p(r) >)|$.

For example, if passed reference channels are 9, 48, and 57, $p(ref)$ is

$$p(ref) = ((p(9) - < p(9) >) + (p(48) - < p(48) >) - (p(57) - < p(57) >))/3$$

The $d(ref)$, pulse height of data at reference channel, was also calculated with same algorithm.

We assigned reference channel as 97. When we compare figures 7.7 and 7.8, we can see that there is stronger correlation in using four reference channels than in using one reference channel, and so, we can get the better corrected pedestal in using four reference channels. Figures 7.7 and 7.8 describe plots of arbitrary correlative channels vs. reference channel (97) before and after pedestal correction with 500 pedestal events.

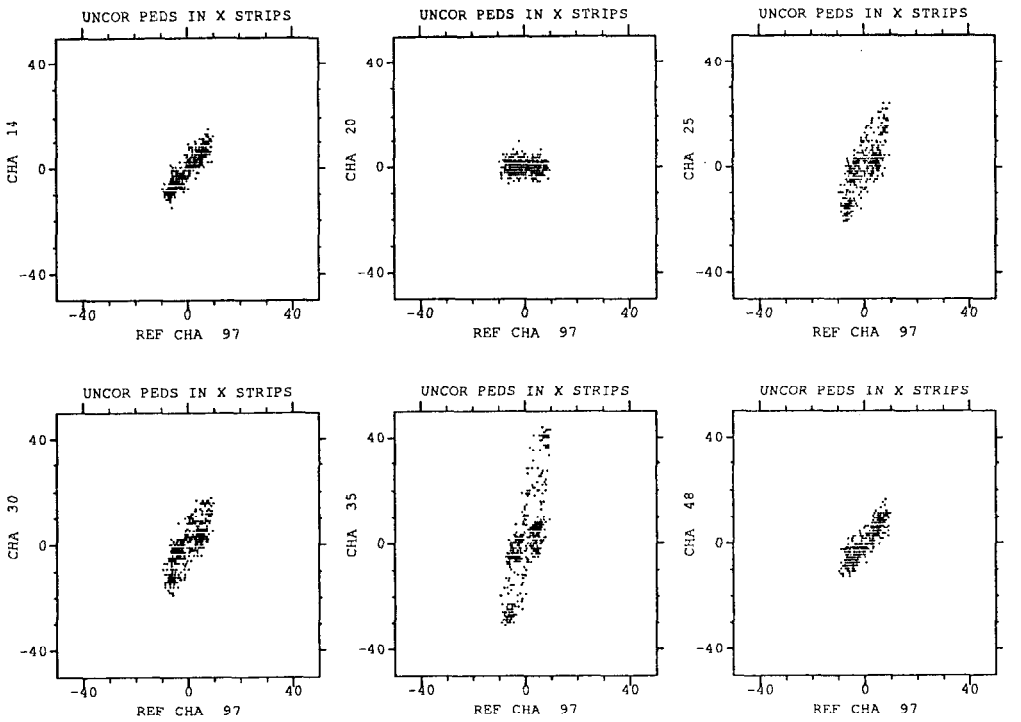

Figure 7.7: Correlative relations for arbitrary channels (14, 20,25,30,35,48) vs. reference channel (97) for the uncorrected pedestals.

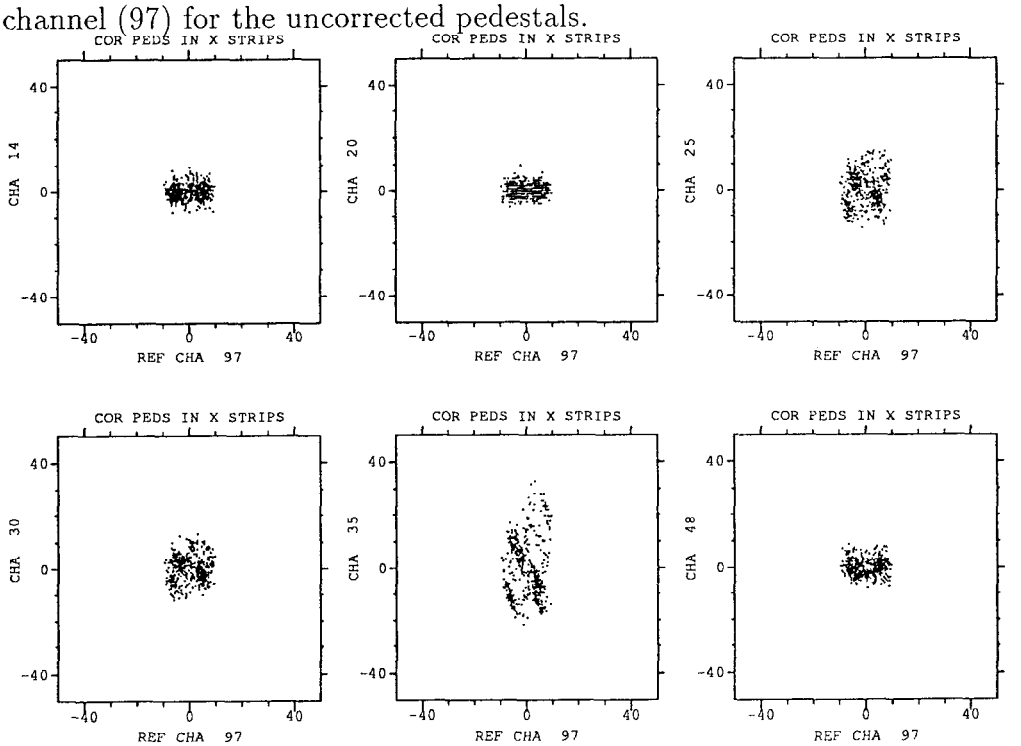

Figure 7.8: Correlative relations for arbitrary channels (14, 20,25,30,35,48) vs. reference channel (97) for the corrected pedestals.

There are four equations: uncorrected pedestal, corrected pedestal, uncorrected data and corrected data at each channel for each event. The pedestals and data of all events were calculated as the following four equations for each event. All pedestal and data have 500 and 9,100 events.

- Uncorrected pedestal equation:

$$p'(k) = p(k) - < p(k) >$$

- Corrected pedestal equation:

$$p''(k) = p(k) - < p(k) > - cref(k) * p(ref)$$

- Uncorrected data equation:

$$d'(k) = d(k) - < p(k) >$$

- Corrected data equation:

$$d''(k) = d(k) - < p(k) > - cref(k) * d(ref)$$

where k: each channel number

$p(k)$: pulse height of pedestal at each channel

$< p(k) >$: average pulse height of pedestal at each channel for all pedestal events

$d(k)$: pulse height of data at each channel

$p(ref)$: pulse height of pedestal at reference channel

$d(ref)$: pulse height of data at reference channel

$cref(k)$: linear correlation coefficient between uncorrected pedestal of each channel and pedestal of reference channel ($p(ref)$), calculated with method of least squares for all pedestal events (the slope of linear line calculated with least square in figure 7.7)

In order to check whether pedestal correction works well or not, it is useful to make histograms that show the sum of all events and all channels versus pulse heights. The upper-left and lower-left of figure 7.9 show the sum of all events and all channels versus pulse heights for 9,100 data events at uncorrected and corrected data. The upper-right and lower-right of figure 7.9 show the sum of all events and all channels vs. pulse heights for 500 pedestal events at uncorrected and corrected pedestals. As you see in upper-right and lower-right of figure 7.9, standard deviation of pedestals was changed from 5.77 ADC counts to 3.825 ADC counts before and after pedestal correction. Figures 7.2 and 7.10 show plots of pulse heights vs. channels for 200 data events at uncorrected and corrected data. We had a good progress for pedestal correction.

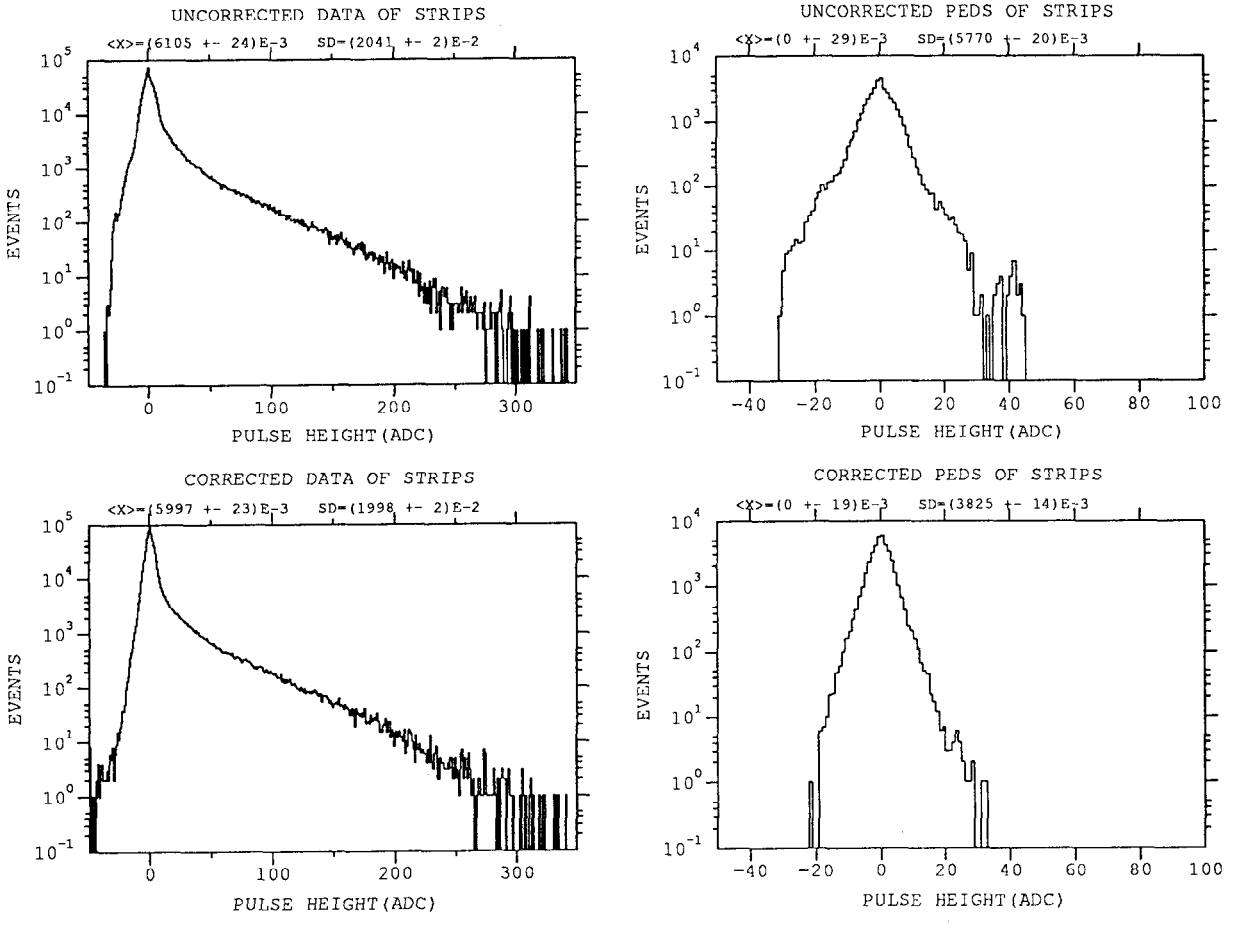

Figure 7.9: The sum of all events and all channels versus pulse heights: (a) Uncorrected data (Upper-Left), (b) Uncorrected pedestal (Upper-Right), (c) Corrected data (Lower-Left), (d) Corrected pedestal (Lower-Right).

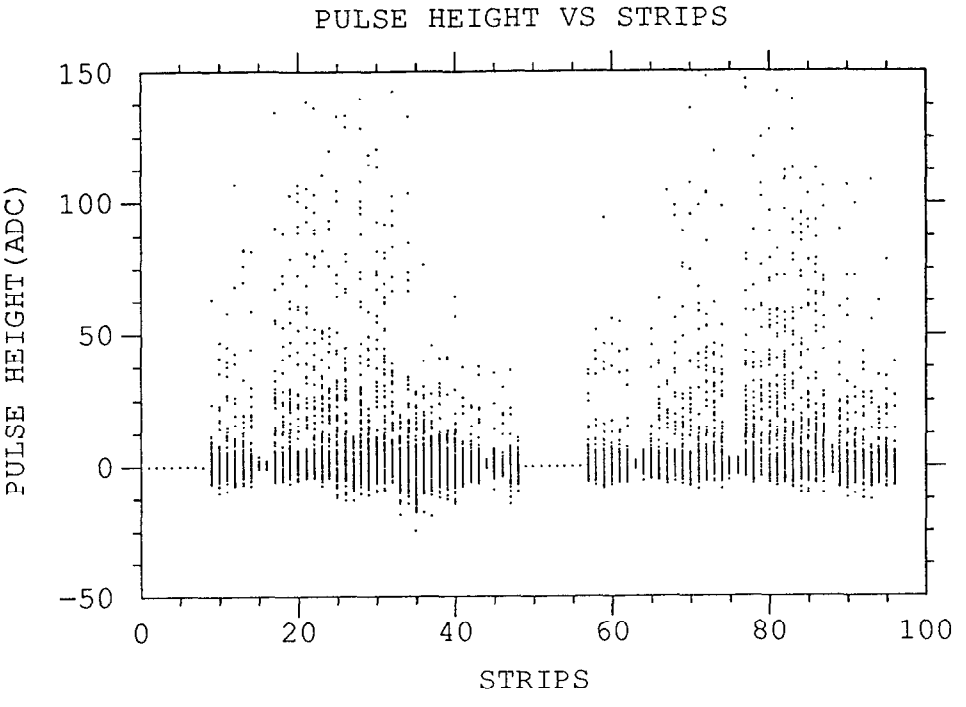

Figure 7.10: Corrected pulse height versus strips: unit of pulse height is ADC counts; The pulse height is obtained from corrected data equation.

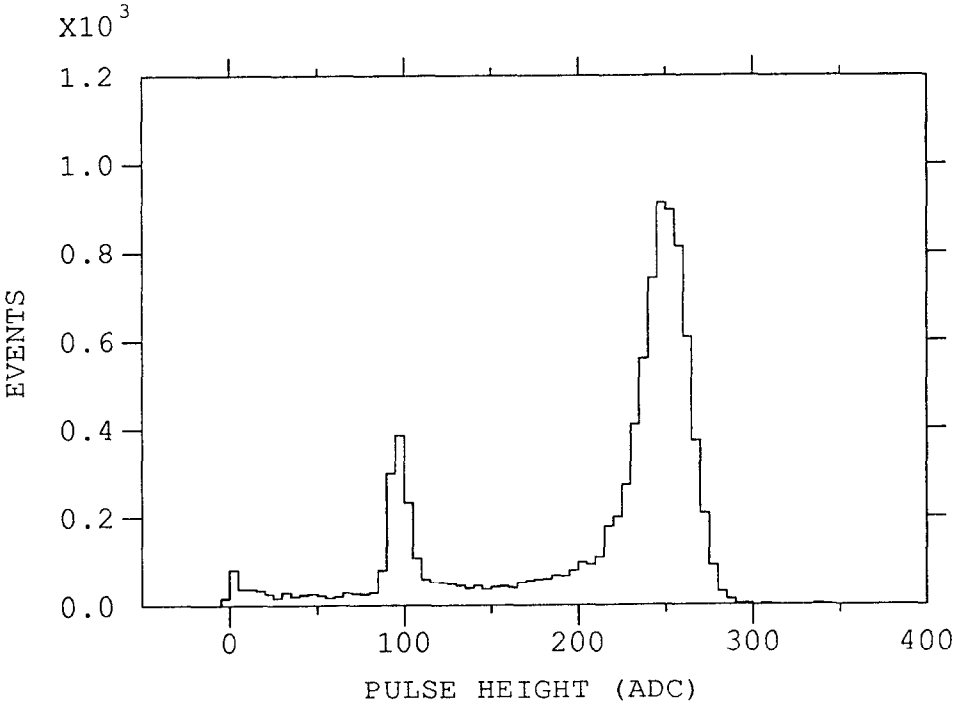

Figure 7.11: Distribution of deposited energy taken at center block of lead glass for 9,100 particles which passed through the silicon strip detector.

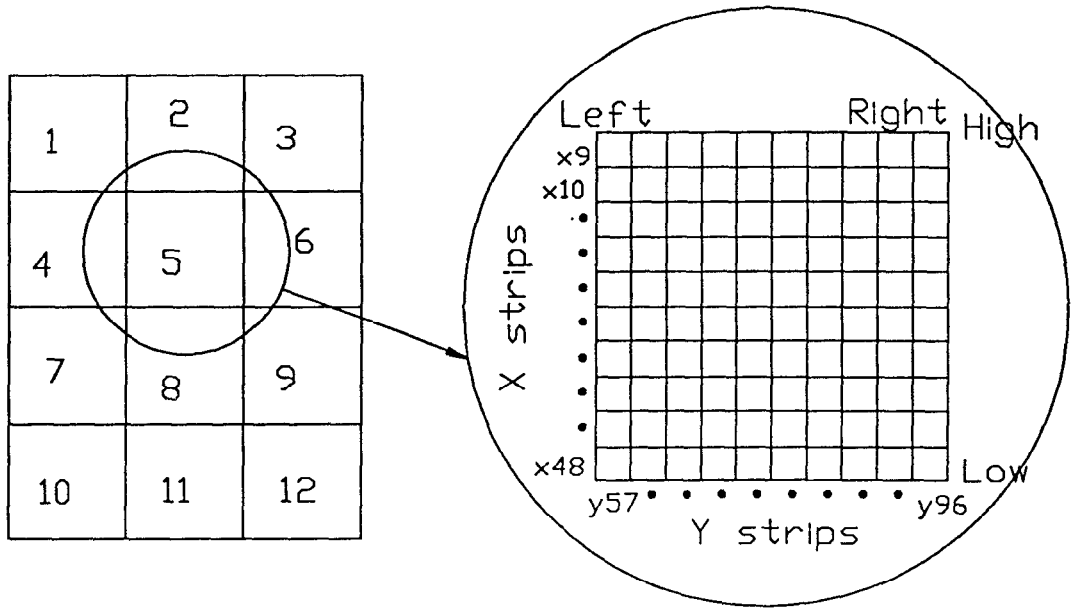

Figure 7.12: Left: a 3 × 4 block array of lead; right: the silicon strip detector.

7.2.2 Cut Conditions for Selecting Good Electron Events

Silicon strip detector is 48 mm × 48 mm, segmented into 48 strips of 1 mm pitch and 0.9 mm width. The X strips are numbered 1-48, and the Y strips are 49-96. The 1-8 X strips and 49-56 Y strips were not connected into LRS FERA ADCs, and so, those channels were not used.

A 3 × 4 block array of lead glass, previously used in BNL experiment E865, was stacked behind the silicon strip detectors as seen in figure 7.12. Each of the lead glass blocks had dimensions 6.4 cm × 6.4 cm × 50 cm. The silicon strip detector was approximately located at the center point of lead glass 5 (center block of lead glass).

The Y strips were located along the horizontal axis of center block of lead glass and the X strips along the vertical axis of that as seen in figure 7.12. Therefore, the 9 and 48 channels were located at the edges of high and low side at the vertical axis of center block of lead glass, while the 57 and 96 channels were located at the edges of left and right side at the horizontal axis of that.

(A) Cut condition for center block of lead glass

Figure 7.11 gives distribution of deposited energy taken at center block of lead glass for 9,100 particles passed through silicon strip detector. We can see that the possible electron candidates will be above 200 ADC counts and muon particles around 100 ADC counts at center block of lead glass from figure 7.11. We made a cut condition that electron candidates should be above 200 ADC counts at center block

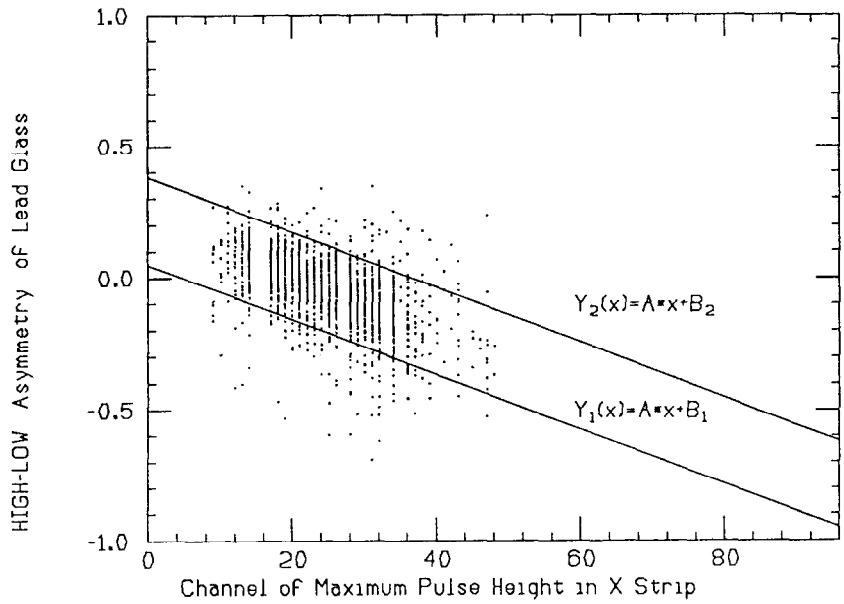

Figure 7.13: The normalized high and low asymmetry of lead glass versus channel of maximum pulse height in X silicon strip detector.

of lead glass.

(B) Cut condition for correlation between silicon strip and central lead glass depending on electron positions

There is some correlation between silicon strip detector and central lead glass detector depending on the electron positions. If electrons hit the upper side of center block of lead glass (central lead glass), the channel of maximum pulse height would be 9 of X strip and pulse height at upper side of central lead glass would be increased. Also, if electrons hit the left side of center block of lead glass, the channel of maximum pulse height would be 57 of Y strip and pulse height at left side of central lead glass would be increased.

We assigned lead glass located at upper side of central lead glass as 2, lead glass located at down side of central lead glass as 8, lead glass located at left side of central block of lead glass as 4, and lead glass located at right side of central block of lead glass as 6. We took the channel of maximum pulse height in silicon detector at each event.

We denoted the pulse height of upper side of central lead glass as PBU(2), the pulse height of down side of that as PBD(8), the pulse height of left side of that as PBL(4), the pulse height of right side of that as PBR(6), and the center block of lead glass as PBC(5).

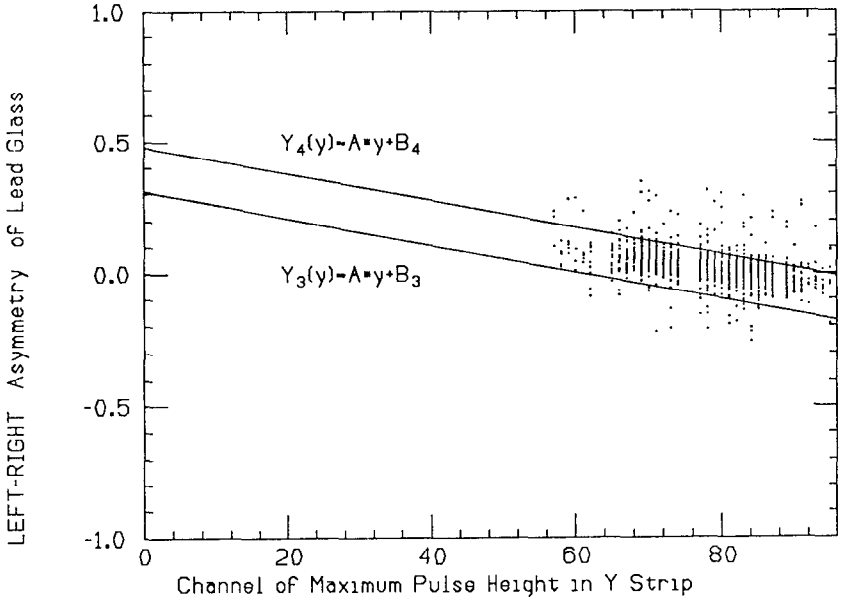

Figure 7.14: The normalized left and right asymmetry of lead glass versus channel of maximum pulse height in Y silicon strip detector.

The normalized high and low asymmetry of lead glass can be expressed as

$$H - L \quad ASYM = (PBH(2) - PBL(8))/(PBH(2) + PBC(5) + PBL(8))$$

The normalized left and right asymmetry of lead glass can be expressed as

$$L - R \quad ASYM = (PBH(4) - PBL(6))/(PBH(4) + PBC(5) + PBL(6))$$

Figure 7.13 shows high and low asymmetry versus channel of maximum pulse height in X silicon strip detector. Figure 7.14 gives left and right asymmetry versus channel of maximum pulse height in Y silicon strip detector. We made linear lines on the plots of high-low asymmetry and left-right asymmetry in order to select good candidates of electrons.

The equations of linear lines on the plot of high-low asymmetry are as follows.

- Lower line equation of high-low asymmetry :

$$Y_1(x) = Ax + B_1$$

- Upper line equation of high-low asymmetry :

$$Y_2(x) = Ax + B_2$$

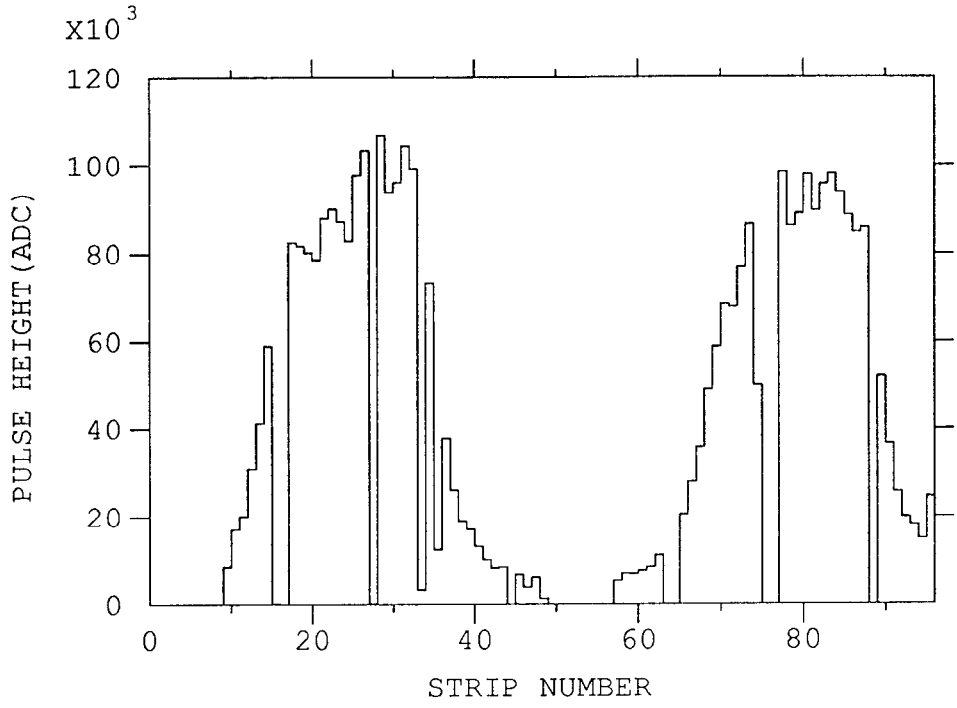

Figure 7.15: The sum for all events of pulse height greater than 15 ADC as a function of strip number.

The equations of linear lines on the plot of left-right asymmetry are as follows.

- Lower line equation of left-right asymmetry :

$$Y_3(y) = By + B_3$$

- Upper line equation of left-right asymmetry :

$$Y_4(y) = By + B_4$$

Where x : channel number of maximum pulse height in X silicon strip detector.
y : channel number of maximum pulse height in Y silicon strip detector.

We can calculate slopes (A, B) and intersections (B_1, B_2, B_3, B_4) from the drawn linear lines of figures 7.13 and 7.14. We made that A is -0.01042, B is -0.00510, B_1 is 0.05, B_2 is 0.38, B_3 is 0.31, and B_4 is 0.48 with cut conditions.

(C) Cut condition for region of electron positions hitting at silicon strip detector

Since the electron has approximately cluster of 5 strips, it has some problem in analyzing the electron spots hitting at the edge of silicon strip detector. Those spots do not have full information of cluster, and so, it had better throw away them.

Figure 7.15 gives a histogram that shows the sum of all events pulse heights greater than 15 ADC as a function of channel number. Also, figure 7.15 shows which

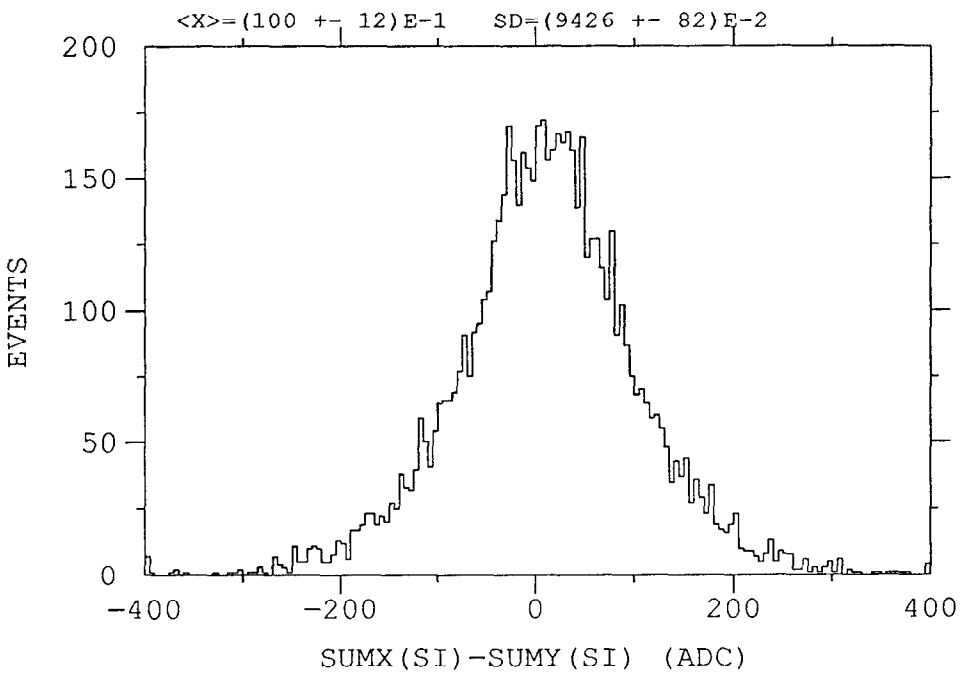

Figure 7.16: The distribution of difference between X and Y cluster values.

channels are dead channels and the status of electron spots hitting at silicon strip detector. We made a cut condition that the region of X strip is from 17 to 32 and that of Y strip from 70 to 87 from figure 7.15.

(D) Cut condition for relation between clusters of X strip and those of Y strip

The cluster is made of sum of pulse heights of 5 strips which are four nearest channels around channel of maximum pulse height and channel of maximum pulse height itself.

When electron pass through X and Y strips, cluster value of X strip is approximately equal to that of Y strip in order to be good electron candidates because X and Y strips are located close together.

Figure 7.16 shows the distribution of difference between X and Y cluster value. We made a cut condition that the difference between X and Y cluster value is 100 as an absolute value.

(E) Table for cut conditions

Table 7.2 gives cut conditions explained above. We can see 2,862 electron events survived after cut conditions from Table 7.2.

7.2.3 Comparison between BNL Data and MC Simulation

(A) Shower Spatial Distribution

Run number			106
Cut values for selecting electrons			
Cut value for PBG(5)			200 ADC
Min and Max channel of X strip		17	32
Min and Max channel of Y strip		70	87
Cut value for $\|Sisumx - Sisumy\|$			100 ADC
Slope and Intersection of H - L	-0.01042	0.05	0.38
Slope and Intersection of L - R	-0.0051	0.31	0.48
The passing events			
Total events			9100
Events after PBG(5) $\geq$ 200 ADC			6606
Events after region of maximum X channel			5141
Events after region of maximum Y channel			4213
Events after cut of $\|sisumx - sisumy\|$			3185
Events after H - L in X strip			3018
Events after H - L in Y strip			2862
PBG(5): Central lead glass			
$sisumx$: Sum of pulse heights of 5 strips which are four nearest channels around channel of maximum pulse height and channel of maximum pulse height itself in X strip			
$sisumy$: Same definition as $sisumx$ in Y strip			

Table 7.2: Cut conditions for selecting good electrons.

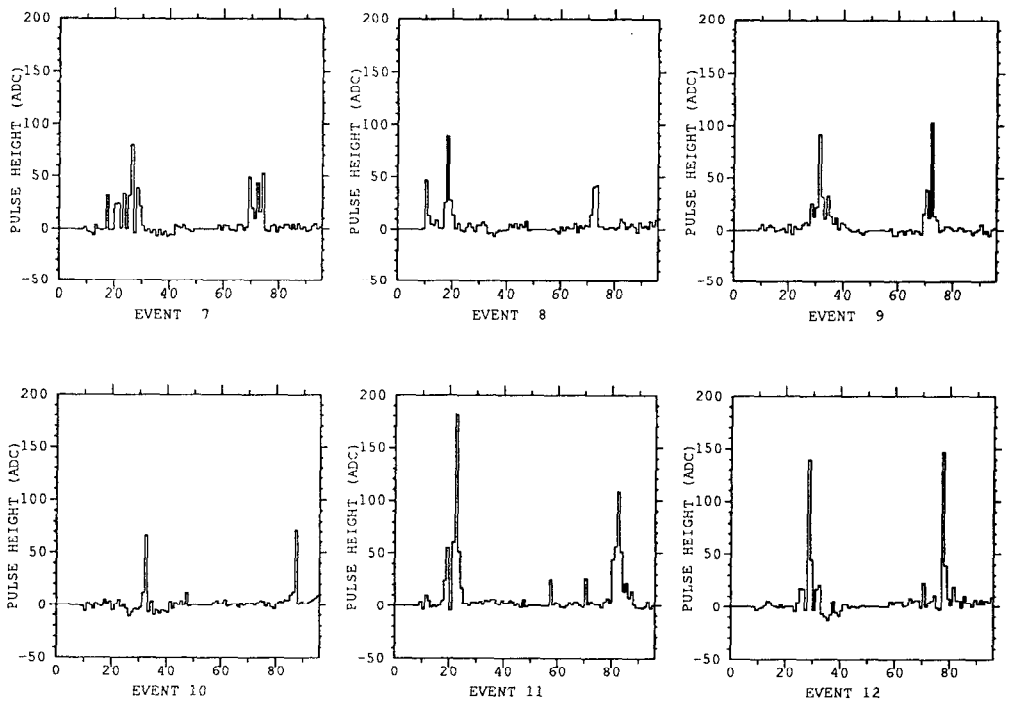

Figure 7.17: Event displays of data for the first 6 events of a run with 5 GeV electrons and 3 X_0 of tungsten. These displays give pulse height (measured charge in ADC counts) versus strip number.

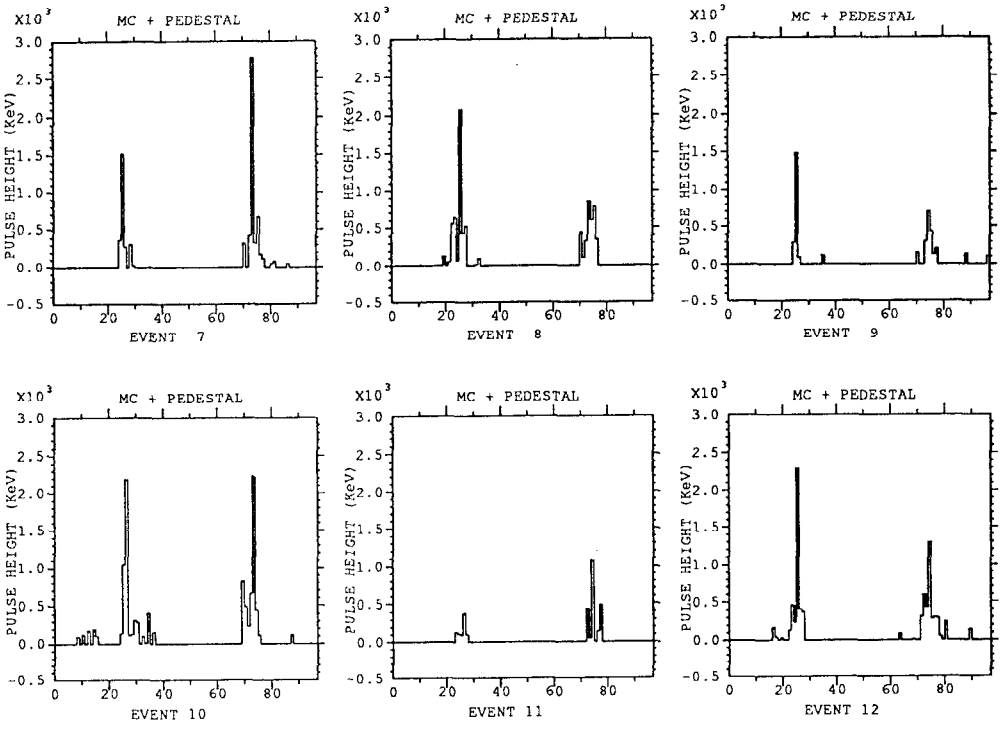

Figure 7.18: Event displays of MC simulated with 5 GeV electrons and 3 X_0 of tungsten: These displays give pulse height (measured charge in ADC counts) versus strip number. The energy conversion is 13.5KeV/ADC.

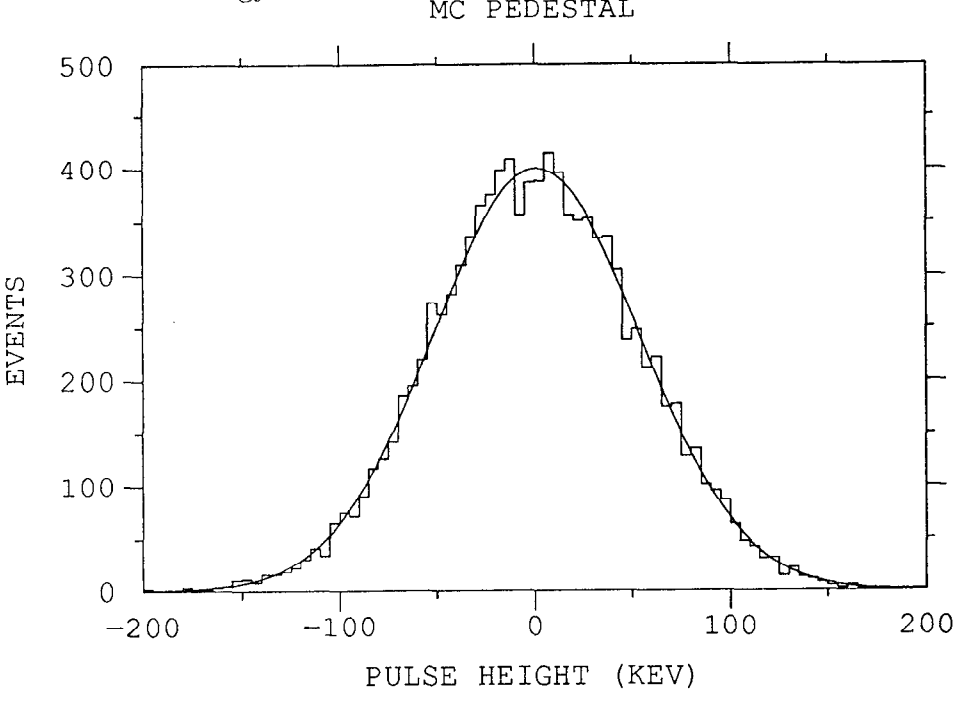

Figure 7.19: Pulse height distribution of MC pedestal simulated with corrected pedestal data.

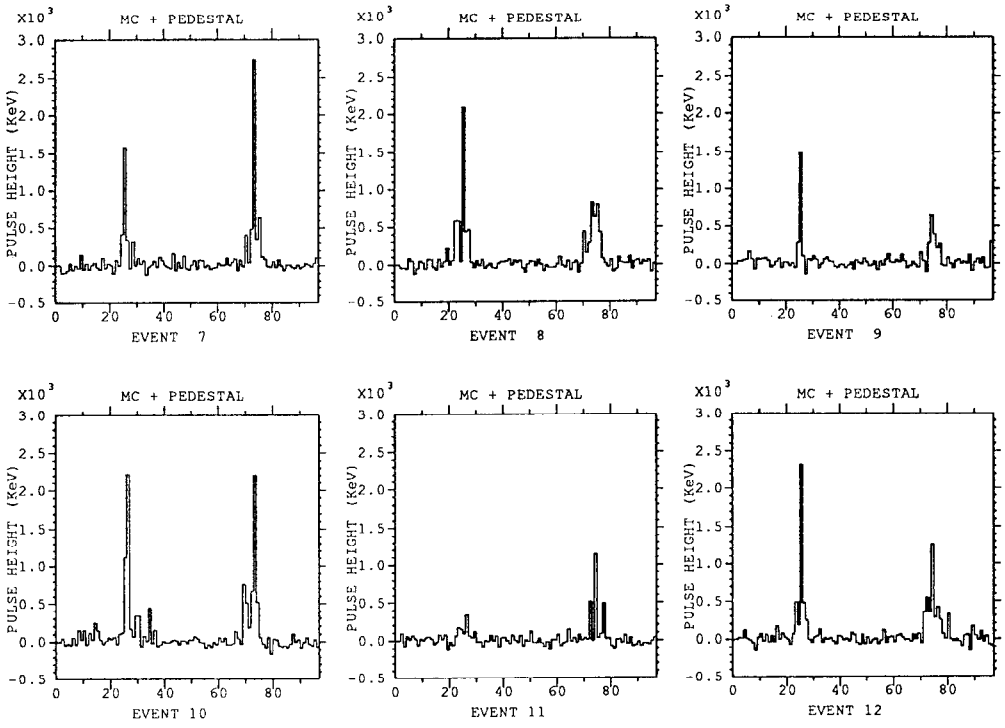

Figure 7.20: Event displays of MC with added noise effect.

One sees that while the 5 GeV electron showers are not as substantial as those expected for energies relevant for an SSC preradiator (the relevant photon energy showers will be 50-100 GeV), they still appear to be reasonably well-defined in transverse profile. In lieu of a high energy electron beam, the important question is how well the 5 GeV showers can be modelled by the EGS monte carlo, and hence allow for an extrapolation to higher energy to be made with some confidence.

Figure 7.17 gives event displays of data for 6 events of a run with 5 GeV electrons and 3 X_0 of tungsten. These displays give pulse height (measured charge in ADC counts) versus strip number. Figure 7.18 gives event displays of MC simulated with the condition of 5 GeV electrons and 3 X_0 of tungsten. These displays give pulse height (measured charge in KeV counts) versus strip number.

In order to add noise effect to MC values, we simulate gaussian MC noise with sigma (3.825 ADC counts) of corrected pedestal data of lower-right of figure 7.9. One ADC count corresponds to about 13.5 KeV of deposited energy. That calculation will be explained later. Therefore, the gaussian noise was multiplied by 13.5 KeV/ADC. Figure 7.19 shows pulse height distribution of MC pedestal. MC pedestals (figure 7.19 were added into MC signals (figure 7.18). Figure 7.20 gives event displays of MC added noise effect with condition of 5 GeV electrons and 3 X_0 of tungsten.

The average shower profile can be calculated from the event displays by placing the strip with maximum pulse height at the center of the distribution. We take the channel of maximum pulse height as 0, the left side channel of that as the negative, and the right side channel of that as the positive seen in figure 7.21. The BNL data

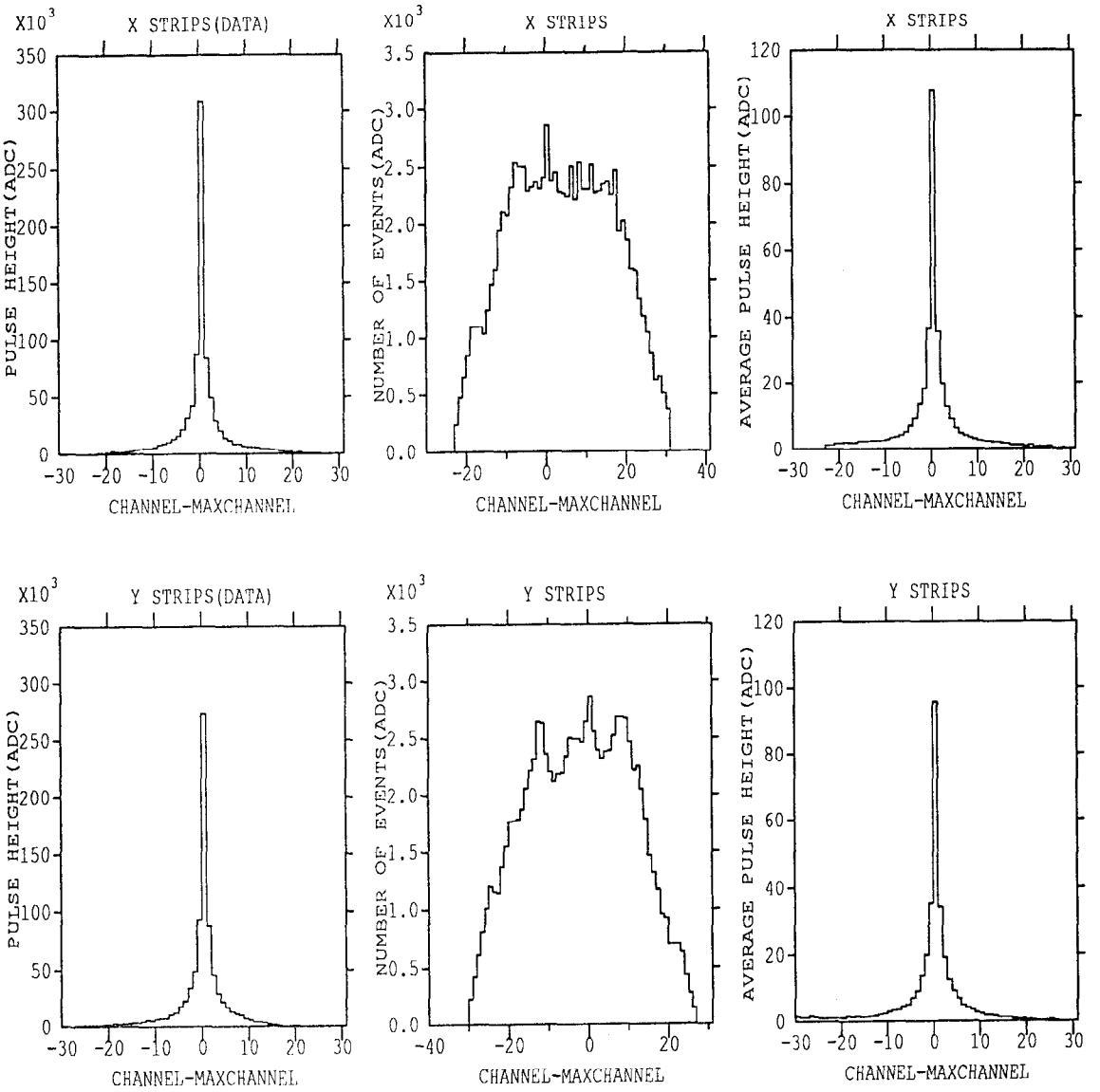

Figure 7.21: Data (2862 electron events). Upper row describes X strips: left (sum of pulse heights of all events), middle (sum of all events), and right (average value) as a function of channels): bottom row describe Y strips: left, middle, and right same as X strips.

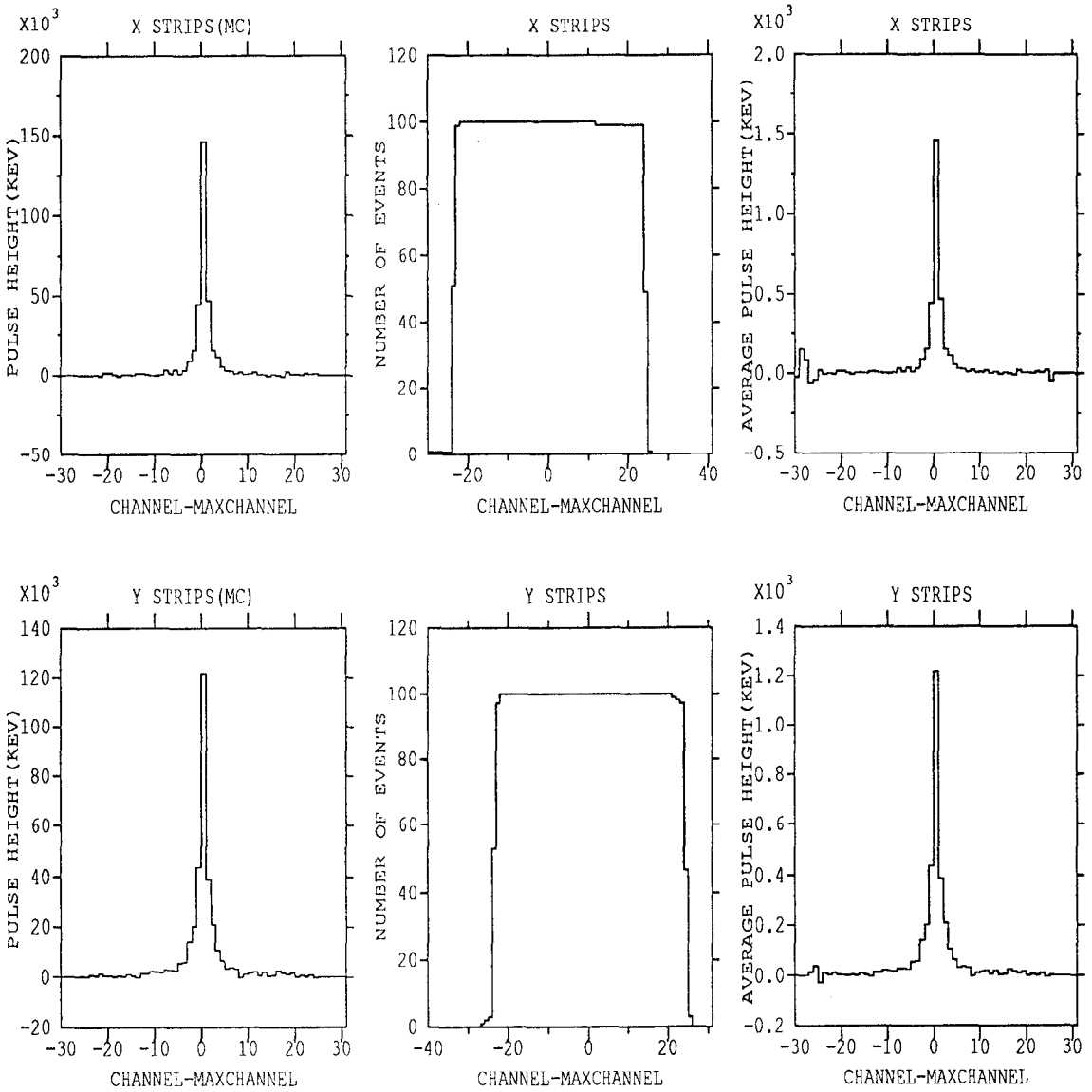

Figure 7.22: MC (100 simulation events). Upper row describes X strips: left (sum of pulse heights of all events), middle (sum of all events), and right (average value) as a function of channels): bottom row describe Y strips: left, middle, and right same as X strips.

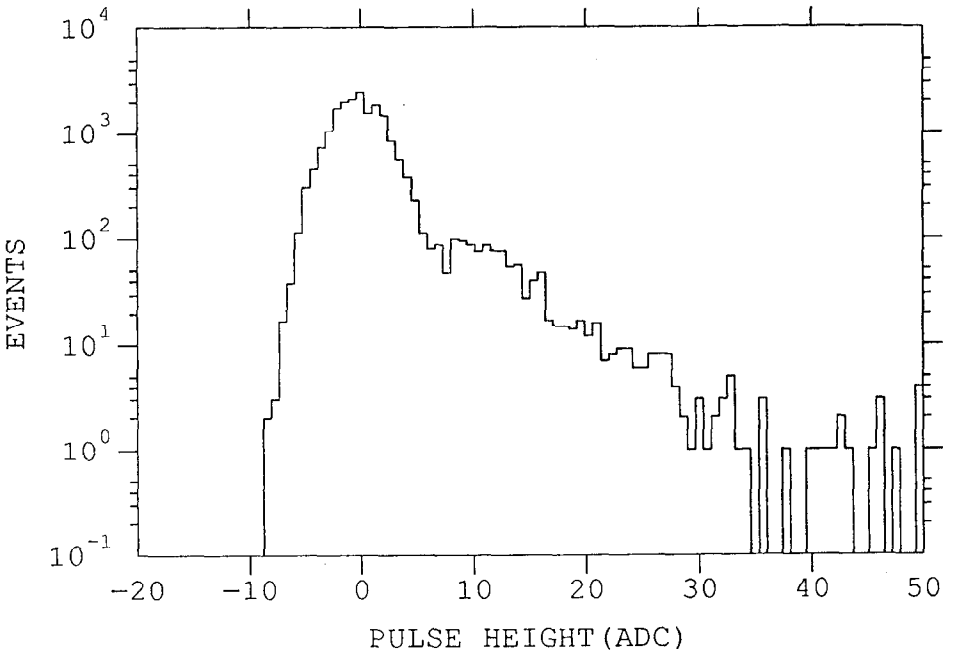

Figure 7.23: Pulse height distribution of 8 strips(17-24) of X strips for all events: the average of MIPs is about 8.5 ADC counts.

represent 2862 good electron events, while the MC data do 100 simulation events. We removed informations of dead channels in calculating the average shower profile of data.

The upper-left and lower-left section of figure 7.21 show the sum of pulse heights of all electron events at X and Y strips. The upper-middle and lower-middle section of figure 7.21 show the sum of all electron events at X and Y strips which depend on the channels because of removing dead channels and change of electron position at each event. The upper-right and lower-right section of figure 7.21 show the average shower profiles of X strips (the first section divided by the second section) and Y strips (the fourth section divided by the fifth section).

Table 7.3 gives informations of the average shower profiles of X and Y strips at BNL data. Figure 7.22 shows the average shower profiles of MC simulation like figure 7.21, also, table 7.4 gives informations of MC simulation. We can get the average value of maximum pulse height of X strips (107.66 ADC counts) of BNL data from table 7.3, and the average value of maximum pulse height of X strips (1455.11 KeV) of MC simulation from table 7.4. Therefore, One ADC count corresponds to about 13.5 KeV of deposited energy. The other conversion between ADC count and KeV can be calculated as the other way: The MIP energy of silicon with thickness of 300 μm is 116 KeV. The average of MIPs, seen in the shoulder of figure 7.23, is about 8.5 ADC counts which is cluster value of 8 strips(17-24) of X strips (116 KeV/8.5 ADC counts $\simeq$ 13.5 KeV/ADC).

The average shower profile of X and Y strips for BNL data				
X strip			Y strip	
Channel	Average pulse height (ADC)	normalized value with maximum of X strip	Average pulse height (ADC)	normalized value with maximum of Y strip
-11	2.47	0.02297	2.31	0.02426
-10	2.83	0.02624	3.01	0.03154
-9	3.41	0.03166	3.45	0.03614
-8	3.60	0.03344	3.54	0.03716
-7	4.19	0.03889	4.67	0.049
-6	5.12	0.04756	5.26	0.05514
-5	6.89	0.06403	7.18	0.0753
-4	9.14	0.08487	9.24	0.09689
-3	13.42	0.12461	13.69	0.14358
-2	18.11	0.16817	19.79	0.20754
-1	36.52	0.33923	35.27	0.36984
0	107.66	1.00000	95.36	1.00
1	35.59	0.33060	34.22	0.35888
2	19.90	0.18485	19.14	0.20071
3	12.71	0.11807	12.66	0.13274
4	9.10	0.08456	9.38	0.09834
5	6.23	0.05787	7.09	0.07431
6	4.74	0.04402	5.14	0.05389
7	3.93	0.03647	4.25	0.04453
8	3.37	0.03126	3.63	0.03807
9	2.89	0.02682	2.72	0.02855
10	2.54	0.02361	2.42	0.02539
11	2.33	0.02167	1.83	0.01920

Table 7.3: Average shower profile of X and Y strips for BNL data.

The average shower profile of X and Y strips at MC simulation				
	X strip		Y strip	
Channel	Average pulse height (KeV)	normalized value with maximum of X strip	Average pulse height (KeV)	normalized value with maximum of Y strip
-11	2.06	0.00141	22.06	0.01814
-10	0.62	0.00042	19.15	0.01575
-9	6.08	0.00418	17.31	0.01424
-8	29.81	0.02048	27.83	0.02289
-7	12.79	0.00879	27.65	0.02274
-6	34.01	0.02337	24.34	0.02002
-5	9.28	0.00638	53.82	0.04427
-4	31.22	0.02145	58.96	0.0485
-3	84.27	0.05791	143.38	0.11793
-2	149.97	0.10307	202.87	0.16686
-1	450.64	0.3097	438.54	0.3607
0	1455.11	1.00000	1215.80	1.00
1	473.14	0.32516	390.27	0.321
2	149.78	0.10293	208.83	0.17177
3	106.11	0.07293	107.55	0.08846
4	48.76	0.03351	63.63	0.05234
5	28.54	0.01961	31.56	0.02596
6	23.75	0.01632	36.51	0.03003
7	8.67	0.00596	31.48	0.02589
8	16.83	0.01156	-1.61	-0.00133
9	5.65	0.00388	10.42	0.00857
10	9.29	0.00638	15.61	0.01284
11	19.82	0.01362	19.11	0.01572

Table 7.4: Average shower profile of X and Y strips for MC simulation.

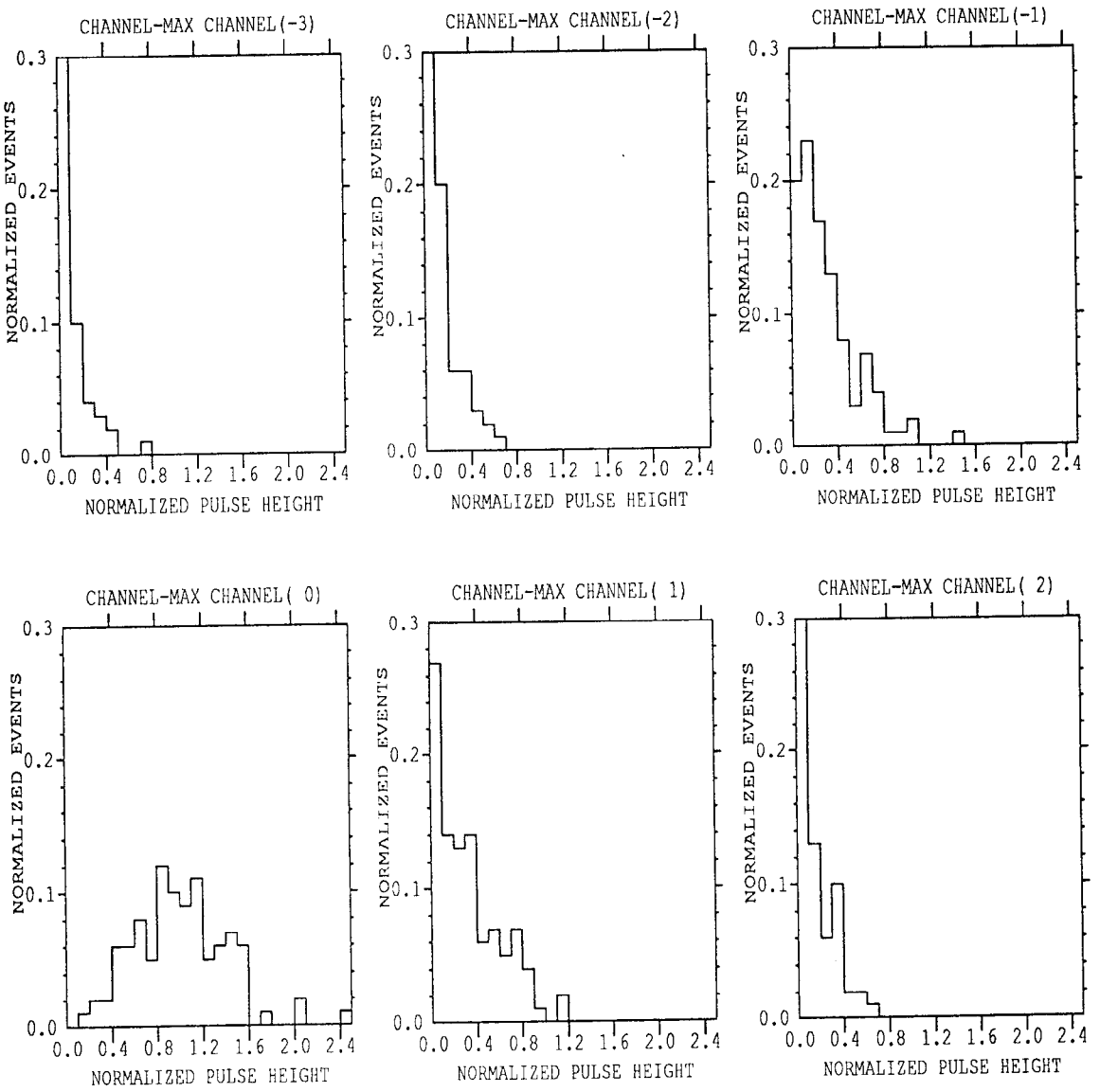

Figure 7.24: The normalized pulse height distributions of each channel (-3 to 2) around the channel of maximum pulse height at MC simulation (100 events).

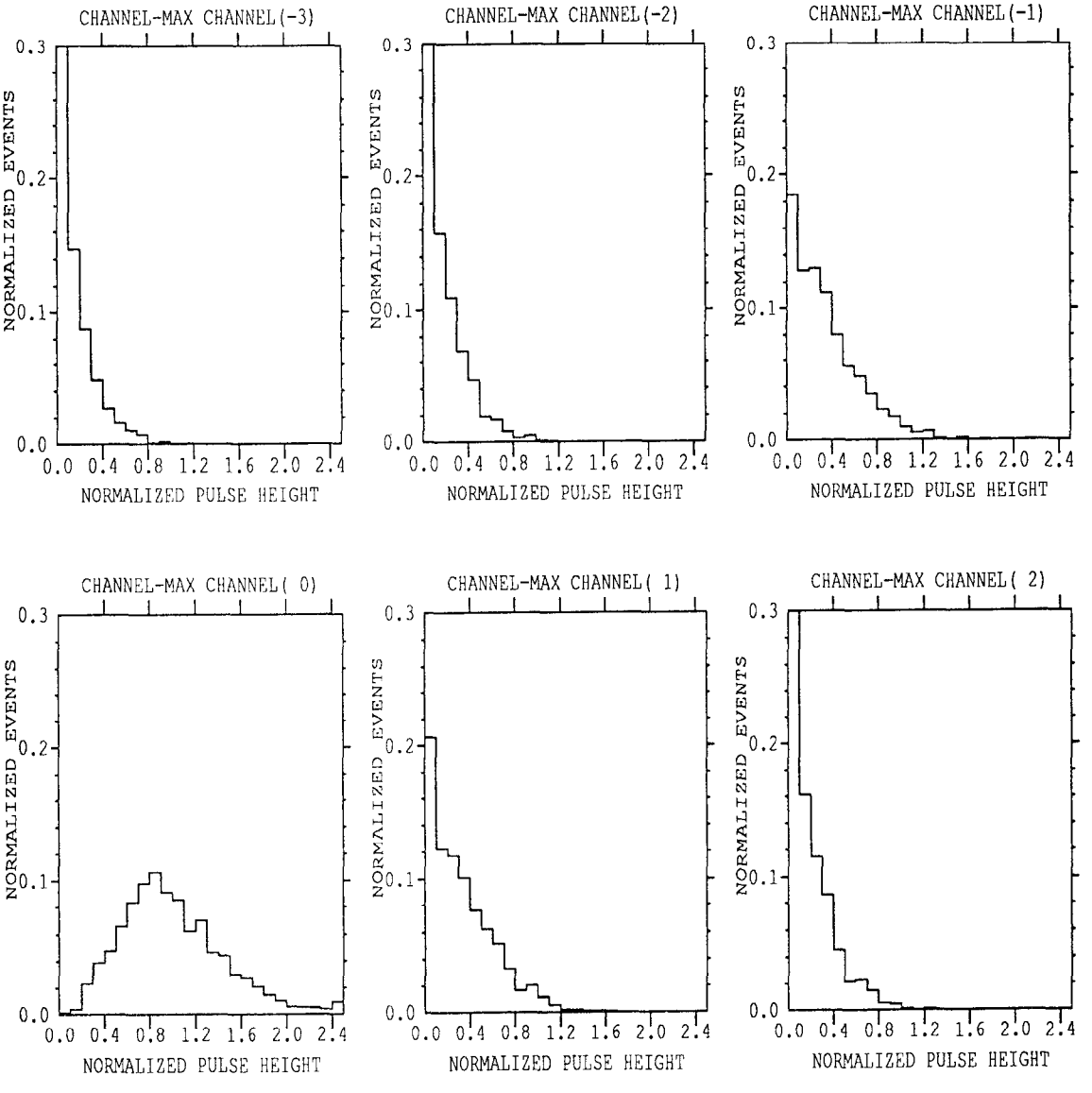

Figure 7.25: The normalized pulse height distributions of each channel (-3 to 2) around the channel of maximum pulse height at data (2862 events).

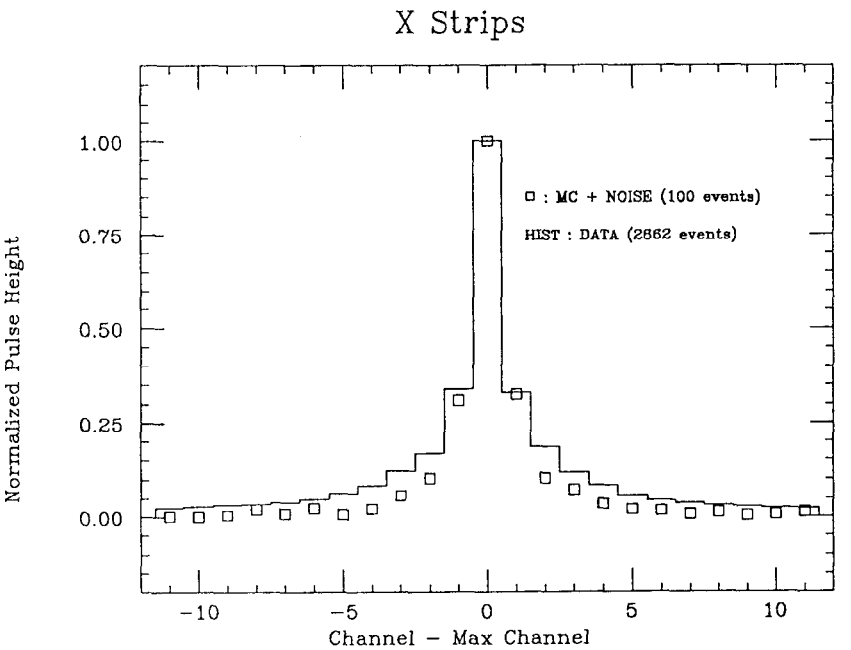

Figure 7.26: Transverse shower profile for X strips averaged 2862 events for 5 GeV electrons with 3 X_0 of tungsten radiator (squares). The histogram is the corresponding EGS simulation for 100 events.

The normalized pulse height distribution in X strip of BNL data		
Channel	Normalized pulse height	σ of normalized pulse height
-3	0.12463	0.17383
-2	0.16819	0.19520
-1	0.33931	0.29171
0	1.000	0.45437
1	0.33068	0.29081
2	0.18487	0.20978

Table 7.5: The normalized pulse height distribution in X strip of BNL data.

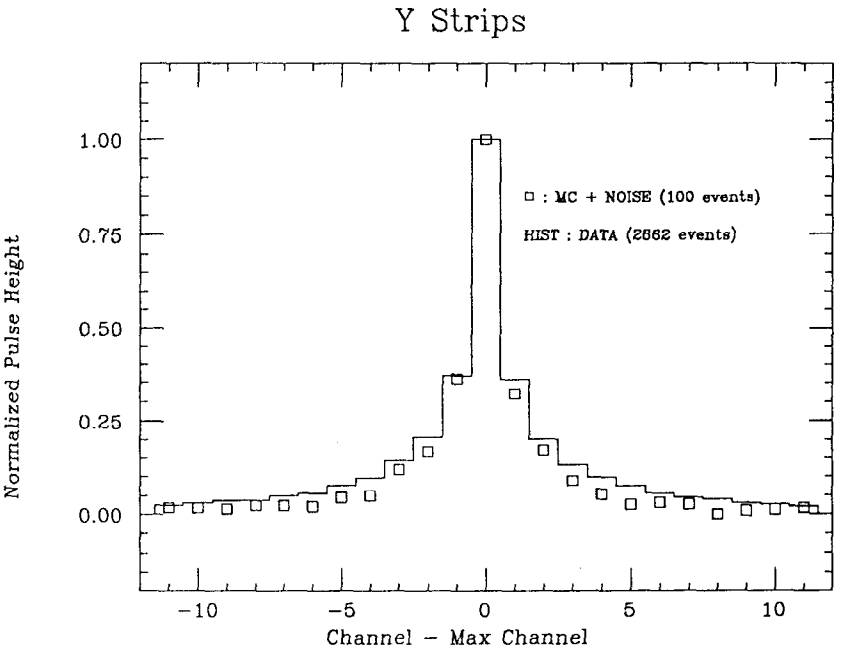

Figure 7.27: Transverse shower profile for Y strips averaged 2862 events for 5 GeV electrons with 3 X_0 of tungsten radiator (squares). The histogram is the corresponding EGS simulation for 100 events.

The normalized pulse height distribution in X strip of MC simulation		
Channel	Normalized pulse height	σ of normalized pulse height
-3	0.05792	0.12594
-2	0.10307	0.14803
-1	0.3097	0.27306
0	1.000	0.40474
1	0.32516	0.27870
2	0.10293	0.15046

Table 7.6: The normalized pulse height distribution in X strip of MC simulation.

It is useful to see the normalized pulse height distribution of each channels in order to check statistics of the normalized pulse height distribution of each channels. The pulse heights of each channels were normalized for average maximum pulse heights of BNL data and MC simulation, and events of normalized pulse heights were normalized with total events which are 2862 events for BNL data and 100 events for MC simulation.

Figure 7.24 shows the normalized pulse height distributions of each channels (-3 to 2) around the channel of maximum pulse height at MC simulation. Also, figures 7.25 shows the normalized pulse height distributions of each channels (-3 to 2) around the channel of maximum pulse height at BNL data. Tables 7.5 and 7.6 give informations of the normalized pulse height distributions of BNL data and MC simulation. The standard deviations of normalized maximum pulse height are 0.45 and 0.404 for BNL data and MC simulation.

The average pulse heights of each channels of BNL data and MC simulation were separately normalized for average maximum pulse heights of BNL data and MC simulation in order to avoid trouble in difference of deposited energy unit between BNL data and MC simulation. Figure 7.26 shows average shower profile normalized for average maximum pulse height of X strip for BNL data and MC simulation. Figure 7.27 shows average shower profile normalized for average maximum pulse height of Y strip for BNL data and MC simulation.

One can see a reasonably good agreement, but with some differences in the shoulders of the distribution. Deviations from EGS in thin-sampling detectors, specifically silicon, have been noted[64] previously. In accordance with these studies, we have taken care in the EGS description of the geometry, cutoffs (10 KeV for electrons and photons in silicon and nearby materials), and step sizes (ESTEPE option with 0.3% step in silicon and 1% elsewhere). The origin of the small deviations in transverse profile is not yet understood. We note that comparisons to EGS with this transverse granularity (1 mm) after a few radiation lengths of high-Z radiator are not commonplace.

(B) Quantitative Comparison between BNL data and MC simulation

The differences in the shoulders of the average shower profile are supposed to come from EGS4 simulation program which does not have multiple scattering of low energy of soft photons and electrons which come from back scattering of the lead glass. We checked strips for cross talk, but, did not find any cross talk. Also, gain calibration of strips is not changed a lot channel by channel.

It is interesting to check some points quantitatively in order to understand the differences between BNL data and MC simulation. As a first point, how many channels exceed a certain threshold as a function of that threshold ? The certain thresholds were normalized for average maximum pulse heights of BNL data and MC simulation. The all channels exceed a certain threshold were divided by total events which are 2862 events for BNL data and 100 events for MC simulation in order to check channels per event exceed a certain normalized threshold. Therefore, we can get plots

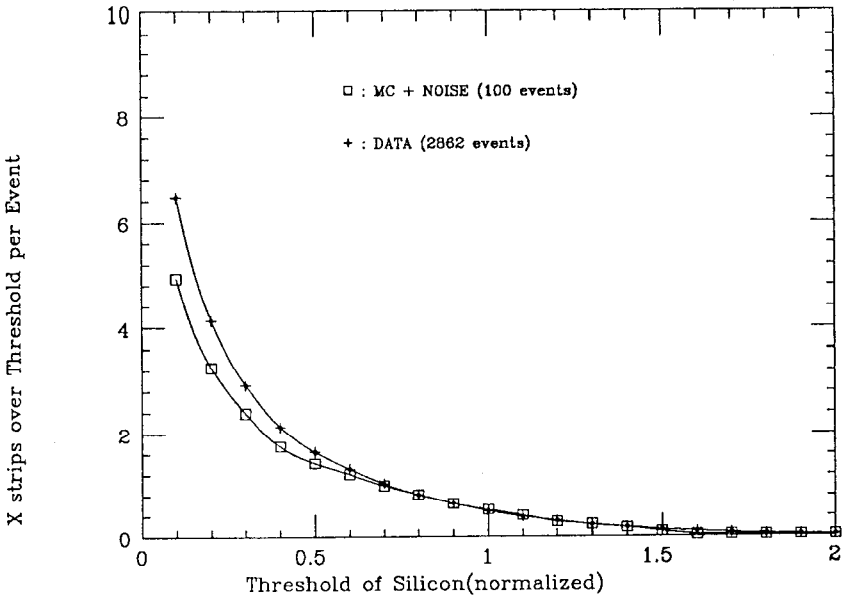

Figure 7.28: Distribution of number of strips over threshold as a function of that threshold for data and EGS simulation in X strips.

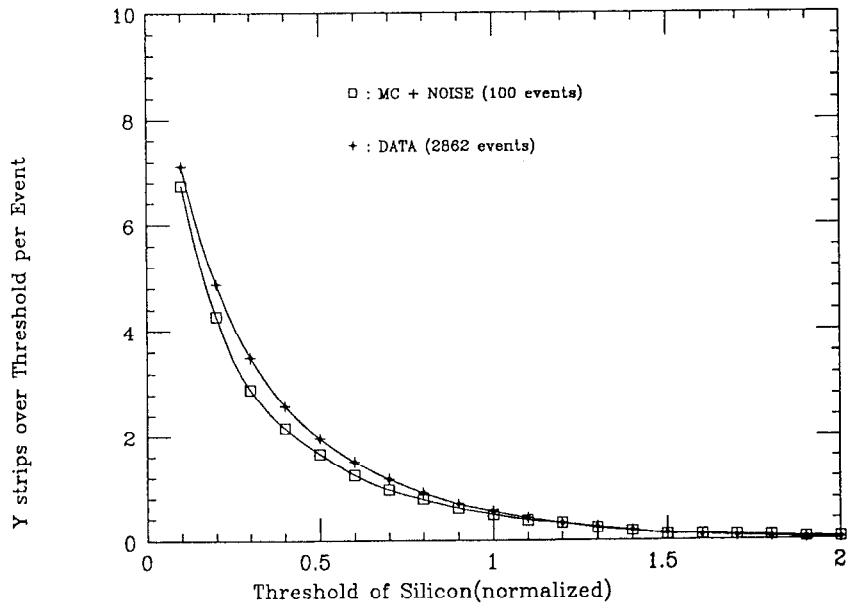

Figure 7.29: Distribution of number of strips over threshold as a function of that threshold for data and EGS simulation in Y strips.

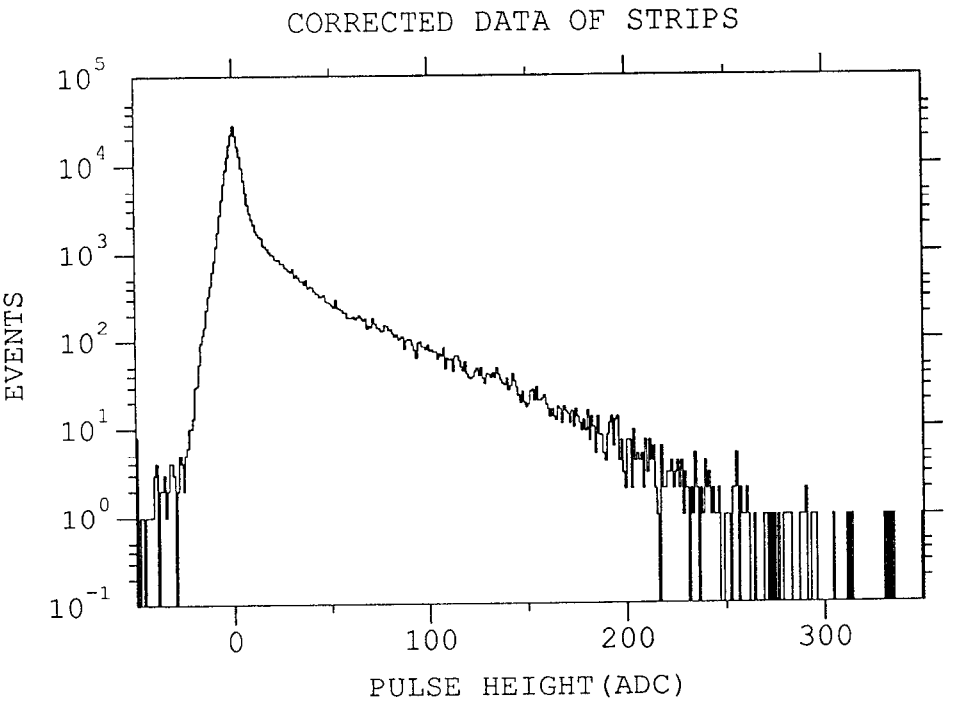

Figure 7.30: Summation of all events versus pulse height (ADC counts) for BNL data for the good 2862 events.

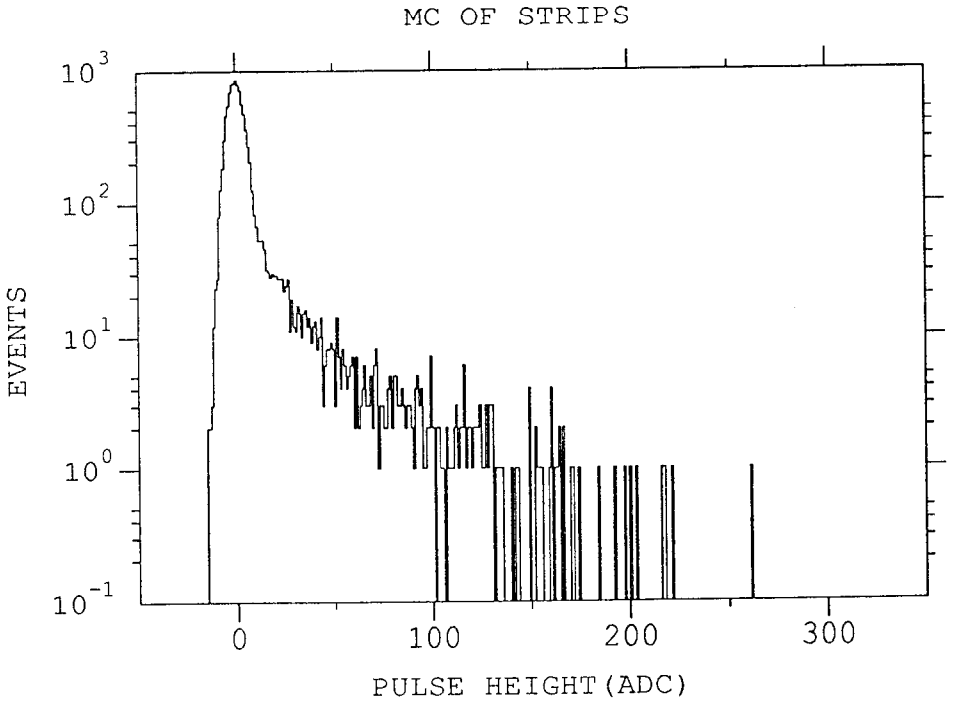

Figure 7.31: Summation of all events versus pulse height (ADC counts) for MC for the 100 simulation events.

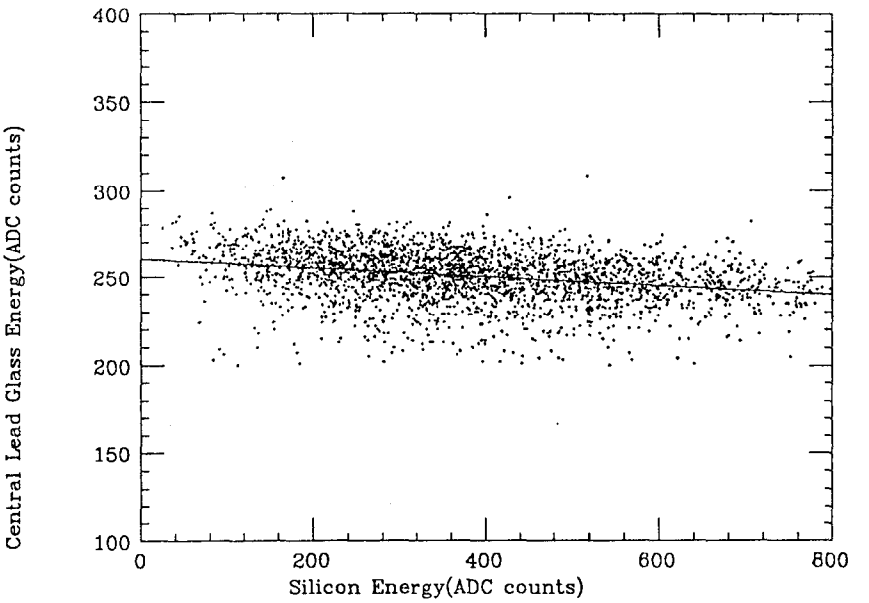

Figure 7.32: Scatter plot of total measured silicon energy versus measured lead glass energy. The line indicates the fitted correlation between these quantities.

of how many channels per event exceed a certain normalized threshold as a function of that normalized threshold of X and Y strips such as figures 7.28 and 7.29.

As a second point, we compare summation of all events versus pulse height for BNL data with good 2862 events and MC 100 simulation events. As you see figures 7.30 and 7.31, there is reasonably a good agreement between slope of BNL data and that of MC data in the range from 20 to 200 ADC.

7.2.4 Energy Resolution and Correction

While a preradiator may be very useful where a highly granular electromagnetic presampler is important, especially for identifying multi-particle showers as discussed above, one must decide if this benefit is outweighed by the effect of the preradiator on the overall energy resolution of the electromagnetic calorimeter. We use the present data to demonstrate that the energy deposited in the preradiator can be used to correct the calorimeter resolution in a straightforward way.

In the BNL test, the electromagnetic calorimeter consisted of a lead glass array, as described in the reference[63]. By taking data with no material before the lead glass, we obtained its energy resolution. Unfortunately, we did not have an opportunity to do a good block-to-block calibration of the array. Hence the energy resolution of the entire array is not better than that of the central lead glass block. Therefore, we use only the central block in this discussion.

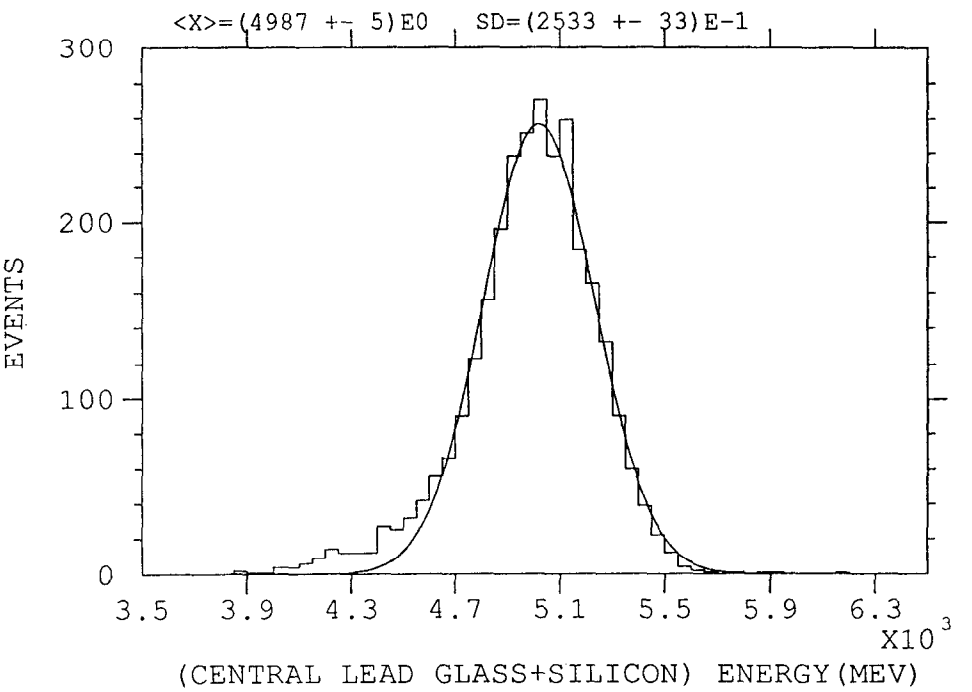

Figure 7.33: The corrected energy resolution of 3 X_0 of tungsten for the minimization method for data.

Figure 7.32 shows the measured correlation between the silicon response and the response of the central lead glass block. Since we do not have absolute gain calibration relationship between central block lead glass and silicon preradiator, it is useful to use the minimization method in order to get the correlation between two materials in making the energy correction.

The equation of minimization is as follows.

$$\chi^2 = \sum_{j=1}^{all\ events} (E_0 - \sum_{i=1}^{2} g_i P_{ij})^2$$

where g_i : gains of central lead glass block and preradiator

P_{ij}: pulse height at each component(i) and event(j)

E_0 : total energy of central lead glass and preradiator (5 GeV)

After two gain factors were applied to the central lead glass and silicon preradiator, we can get figure 7.33 as corrected energy resolution of 3 X_0 of tungsten through minimization method. We just used central lead glass block in order to get the uncorrected energy resolution of 3 X_0 of tungsten like figure 7.34. Also, we get the energy resolution of central lead glass with no preradiator and MC simulation with same conditions like figures 7.35 and 7.36.

All energy distributions were fit by gaussian distributions, and the resulting resolutions are summarized in the Table 7.7. The EGS result with no radiator is not

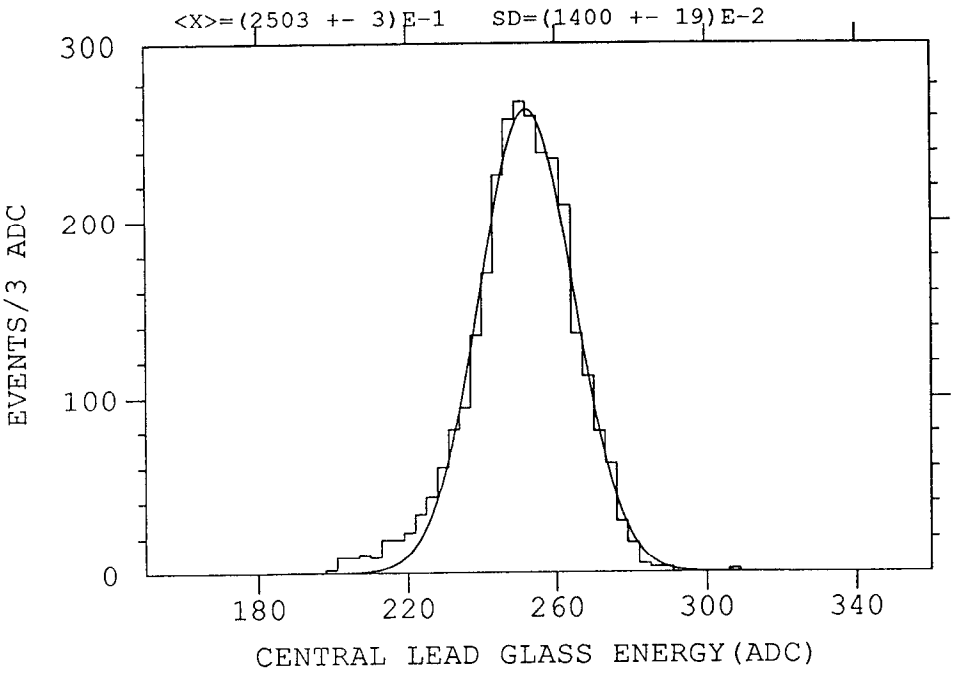

Figure 7.34: The uncorrected energy resolution of central lead glass for 3 X_0 tungsten data.

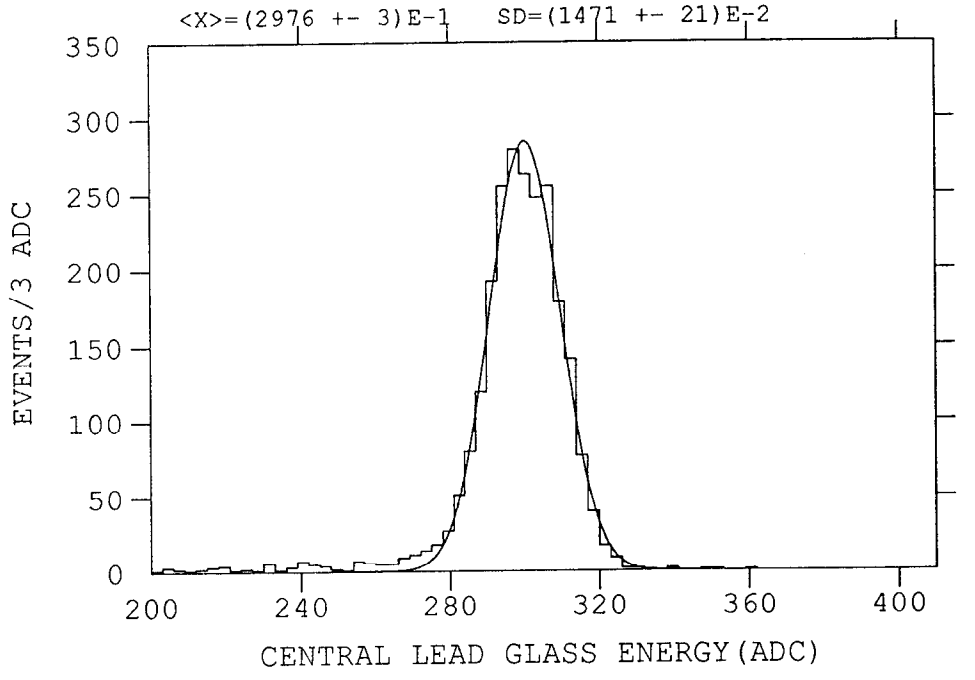

Figure 7.35: The energy resolution of central lead glass with no preradiator data.

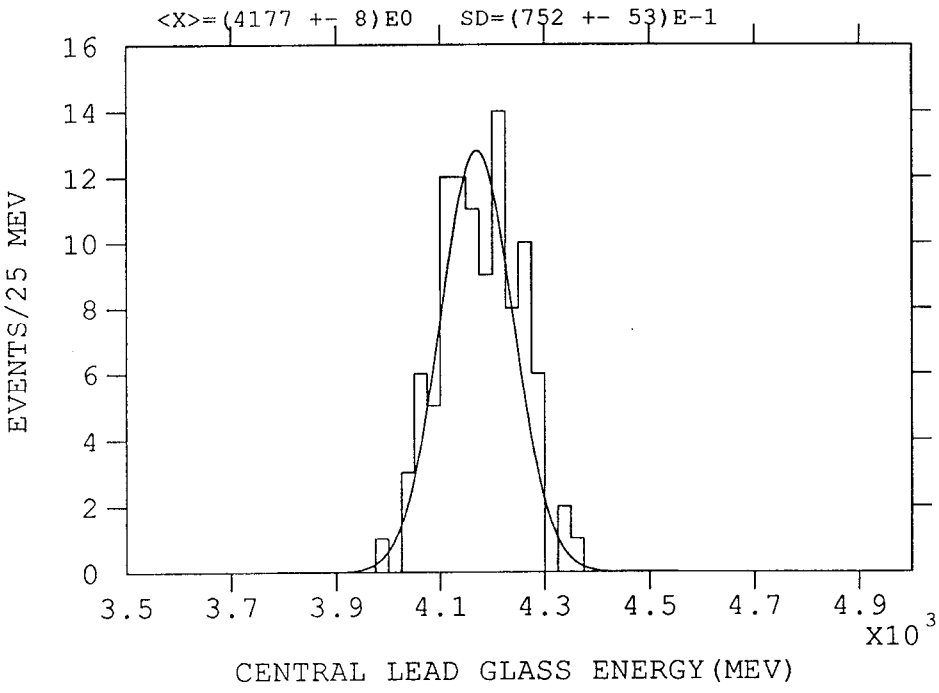

Figure 7.36: The energy resolution of central lead glass with no preradiator MC simulation.

No preradiator	3.15±0.07 %	-
3 X_0 W - no correction	4.98±0.10 %	4.9 %
3 X_0 W - corrected	4.24±0.09 %	4.1 %

Table 7.7: One-block lead glass resolution for 5 GeV electrons for data and EGS simulation.

shown, since in this case photon statistics, which is not included in the simulation, makes a substantial contribution (about 1.8 %) to the resolution. However, if the estimate for the photon statistics is included, the simulation and data agree. This contribution is negligible in the cases with radiator present. One can see that a substantial correction can be made to the energy resolution using the preradiator information and that this correction seems to be well-modelled by an EGS simulation.

CHAPTER VIII

ANALYSIS OF LIQUID ARGON HADRON CALORIMETER PROTOTYPE FOR HIGH ENERGY HADRON COLLIDERS

8.1 Introduction

In 1991, Gamma Electron Muon (GEM) liquid argon hadron calorimeter was tested at the Brookhaven National Laboratory (BNL) [65]. This calorimeter test was conducted as the part of the GEM *R&D* program. GEM detector was designed for the Superconducting Super Collider (SSC) or Large Hadron Collider (LHC) of high energy hadron colliders. The data from this test was obtained from the GEM calorimeter group and re-analyzed at the university of oregon. Typically, the slow drift of charges in liquid argon calorimeters require relatively long integration times to fully collect charges and to minimize noise. The 16 ns period of the SSC demands a shorter integration time, increasing the electronic noise of a liquid argon calorimeter above an optimally low value. Through off-line analysis we have investigated decreasing the electronic noise, which can be important in an isolation cut (See chapter VIII) to reduce QCD background and to get better energy resolution.

8.2 The Calorimeter Construction and Beam Test

The GEM prototype liquid argon calorimeter was 1 meter by 1 meter wide and 7.5 integration lengths deep[65]. The calorimeter was divided into three identical modules, each 2.5 interaction lengths deep. Each module is divided into two stacks with 40 transverse readout channels (one vertical and one horizontal). The calorimeter unit cell consisted of a 12 mm lead sheet, a 2 mm argon gap, a readout board, and another 2 mm argon gap as in figure 8.1. A readout board has 40 readout strips. The readout strips were oriented alternatively in X and Y directions, with X and Y interleaved (see figure 8.2). Longitudinally, the 16 unit cells of each stack were ganged together to form one readout channel.

Since the 12 mm lead sampling is rather coarse (eq. SLD hadron calorimeter is

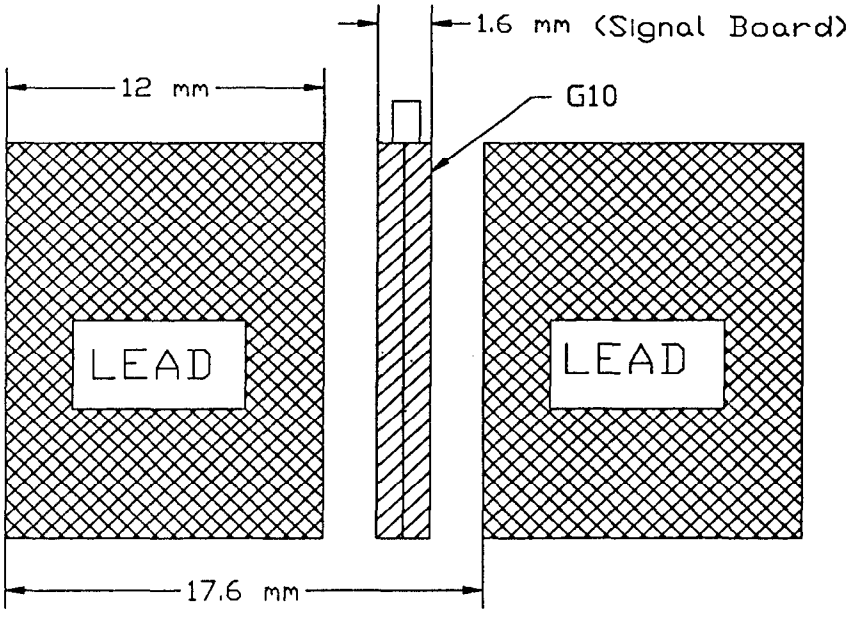

Figure 8.1: Side view of layers in the calorimeter module.

6mm lead and $60\%/\sqrt{E}$[52]), the resolution presented is poor (see the section 8.7), but, allows demonstration of performance which can be scaled for finer sampling (eq. GEM hadron calorimeter was designed as $60\%/\sqrt{E}$ [67]).

The stacks are numbered from the first to the sixth stack along the beam direction. The odd number stacks (1,3,5) have 40 Y readout channels. The even number stacks (2,4,6) have 40 X readout channels. The readout channels are numbered 1 through 240. Channels 1 through 40 are the first Y stack, channels 41-80 are the second X stack, channels 81-120 are the third Y stack, channels 121-160 are the fourth X stack, channels 161-200 are the fifth Y stack, and channels 201-240 are the sixth X stack.

The liquid argon calorimeter was placed in the A3 line at the Brookhaven National Laboratory. An X-Y hodoscope of 1 mm diameter scintillating fibers defined the beam position near the calorimeter. The maximum beam intensity was 2,000,000 particles in a spill of approximately one second.

8.3 BNL Data and Monte Carlo (MC) Simulation

The data used in this analysis were the 10 and 20 GeV π^- energies with 100 ns shaping time[1]. These are runs 922 (for 10 GeV) and 926 (for 20 GeV). We made files of 10 GeV pedestal data with 584 events and beam data with 1,516 events, and of

[1]These data were obtained from Hong Ma at BNL.

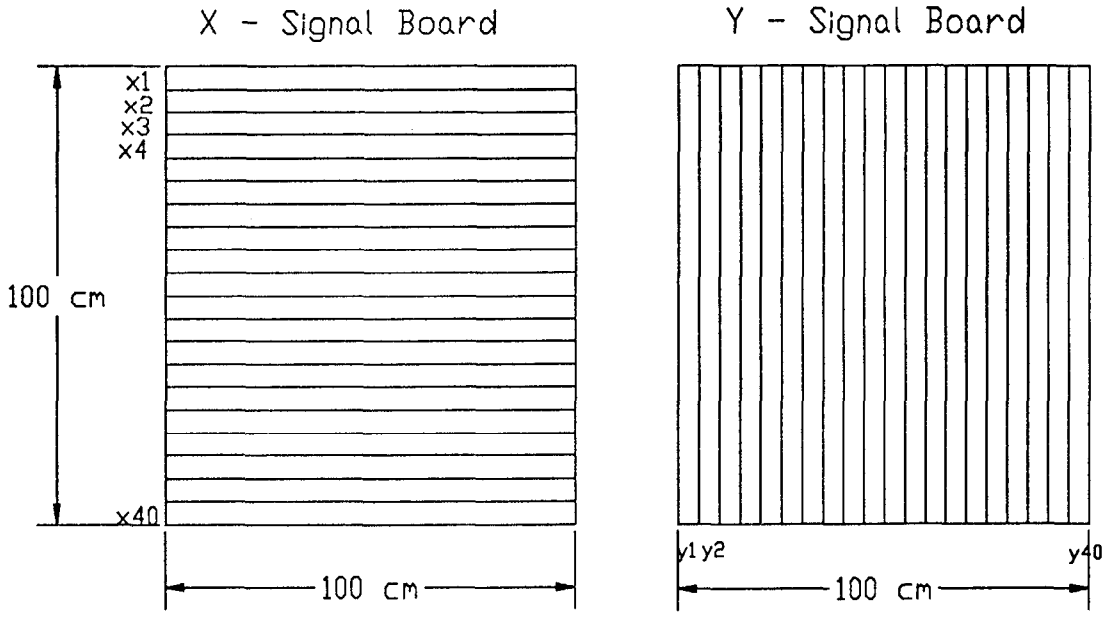

Figure 8.2: Signal boards for the calorimeter.

20 GeV pedestal beam data with 1,634 events and signal data with 1,430 events. All data were analyzed with the first 1,000 events except for 10 GeV pedestal data with 584 events. Also, we generated Monte Carlo (MC) data with 1,000 events with the CALOR89[66] program applying the same conditions as the BNL data.

8.3.1 Pedestal Distribution of BNL Data and MC Simulation

The pedestal (electronic noise) distributions of BNL data were analyzed at the 10 and 20 GeV π^- energies. The MC noise distributions were done through simulation by using a random number generator with averages and standard deviations of pedestal data. The following example used the 10 GeV case. The same method was also used for 20 GeV.

Figure 8.3 shows the average and standard deviation in the pedestal distribution of each strip of BNL data, 0.223 and 27.38 for 430 events. Figure 8.4 shows a MC simulation of the pedestals based on the average and standard deviation of figure 8.3. Figure 8.5 displays the pedestal distribution of BNL data in summation of all 240 strips with an average of 46 ADC counts and a deviation of 428 ADC counts for 584 events. Figure 8.6 shows a MC distribution of pedestals summation of all 240 strips with an average of 37 ADC counts and a standard deviation of 432 ADC counts for 1,000 events. There is good agreement between the pedestal distribution of BNL data and the MC noise distribution.

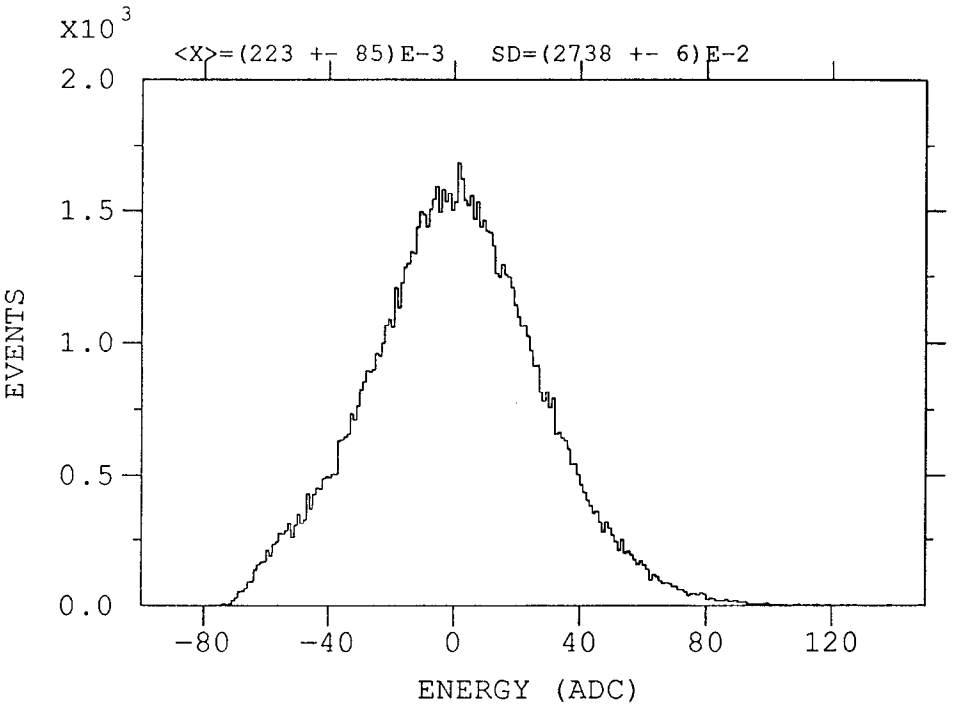

Figure 8.3: Pedestal distribution of 10 GeV π^- with 430 events.

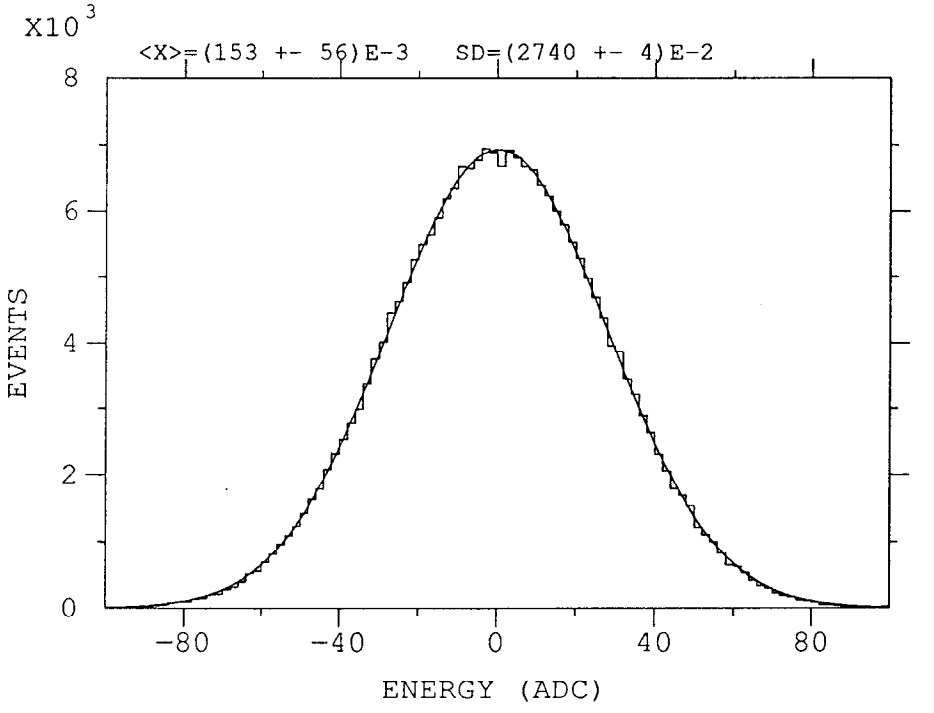

Figure 8.4: MC simulation with condition of pedestal distribution of 10 GeV π^-.

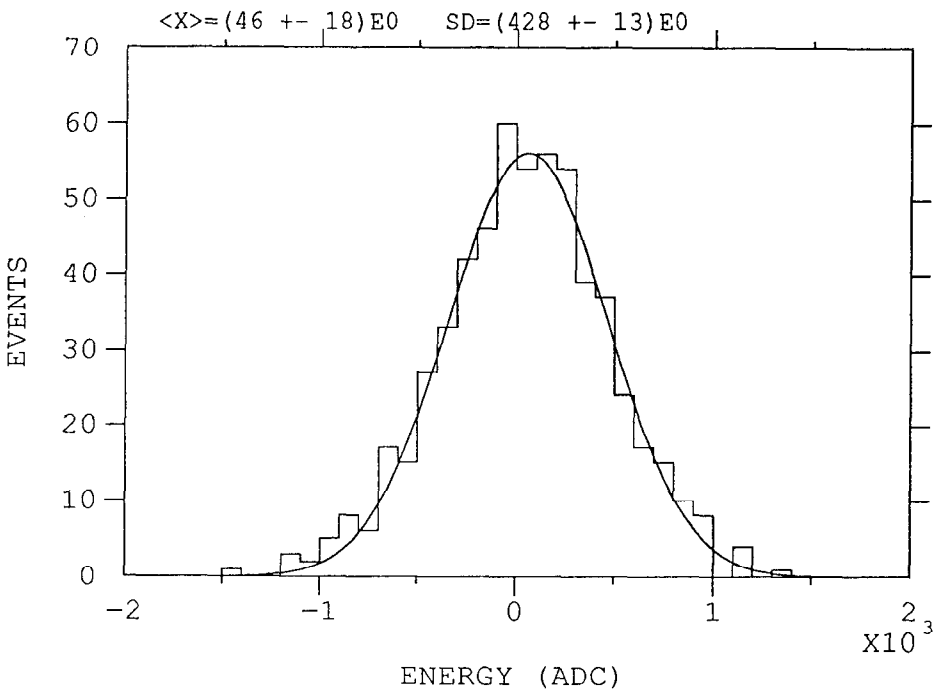

Figure 8.5: Pedestal distribution of BNL data in summation of all 240 strips with an average of 46 ADC counts and a standard deviation of 428 ADC counts with 584 events.

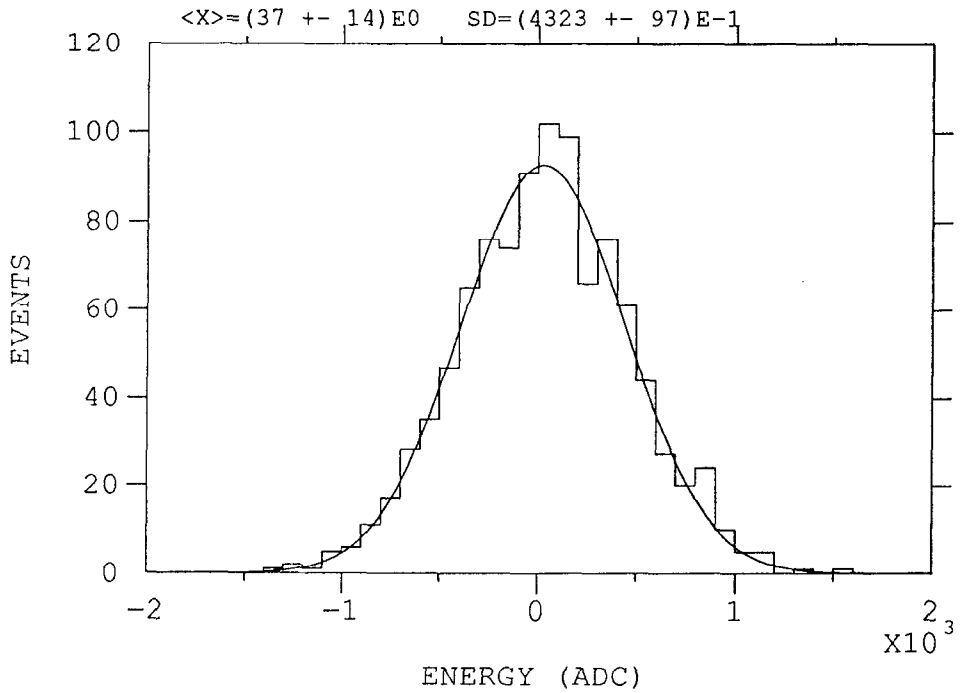

Figure 8.6: MC distribution in summation of all 240 strips with an average 37 ADC counts and a standard deviation of 432 ADC counts with 1,000 events.

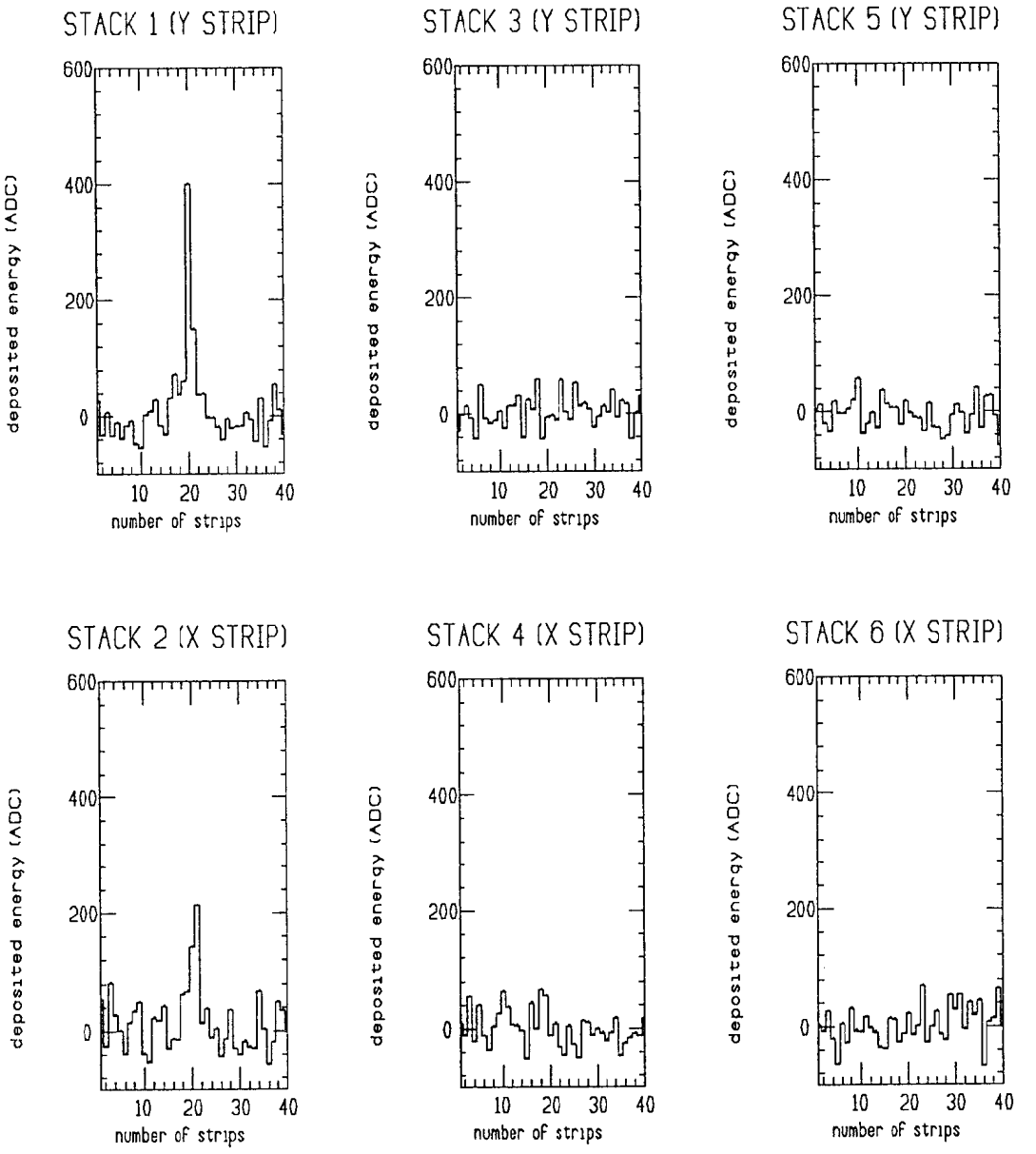

Figure 8.7: The deposited (signal + pedestal) energies versus strips in each stack for an arbitrary event (BNL data for 10 GeV π^-).

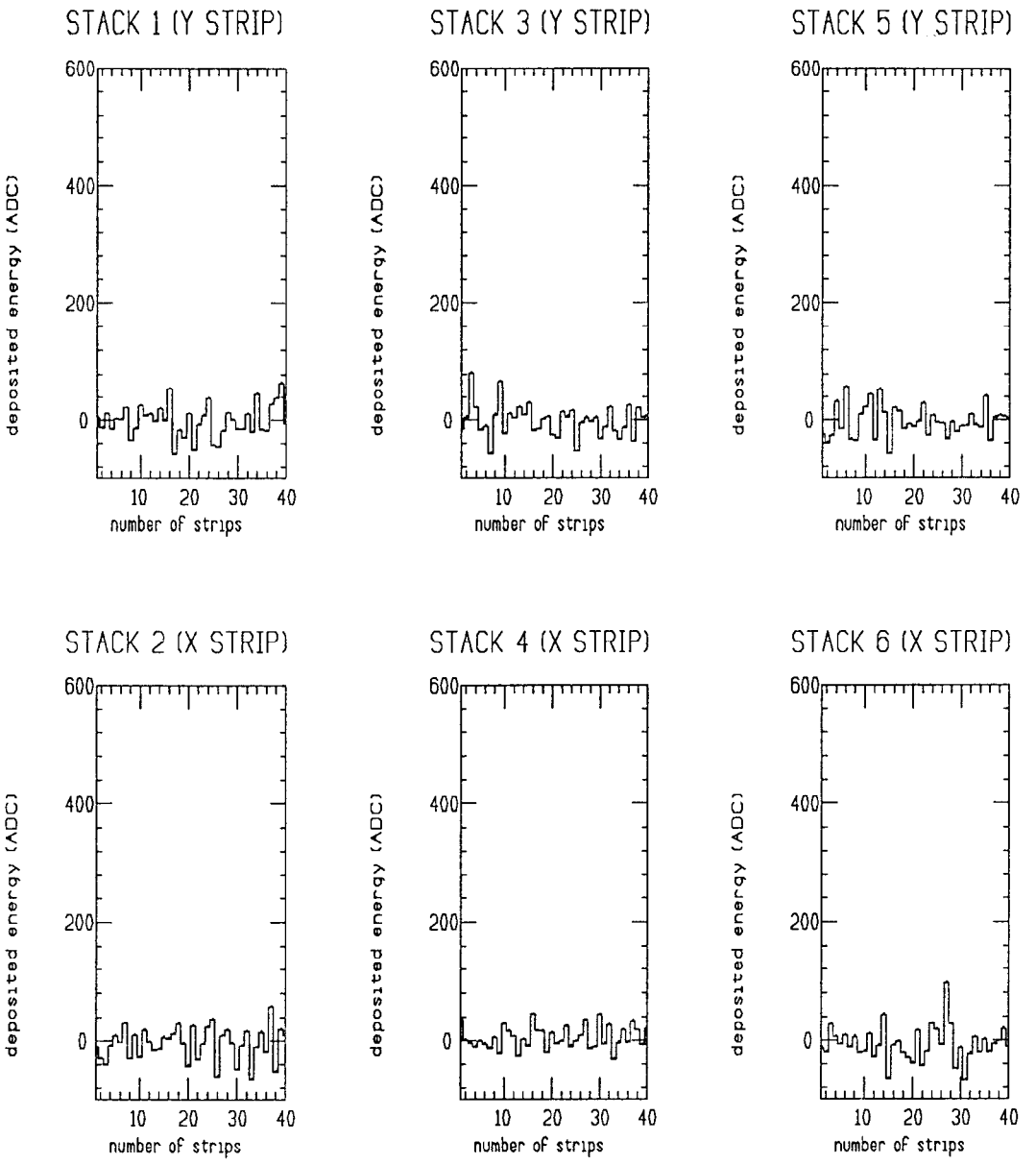

Figure 8.8: The pedestal energies versus strips in each stack for an arbitrary event (BNL data for 10 GeV π^-).

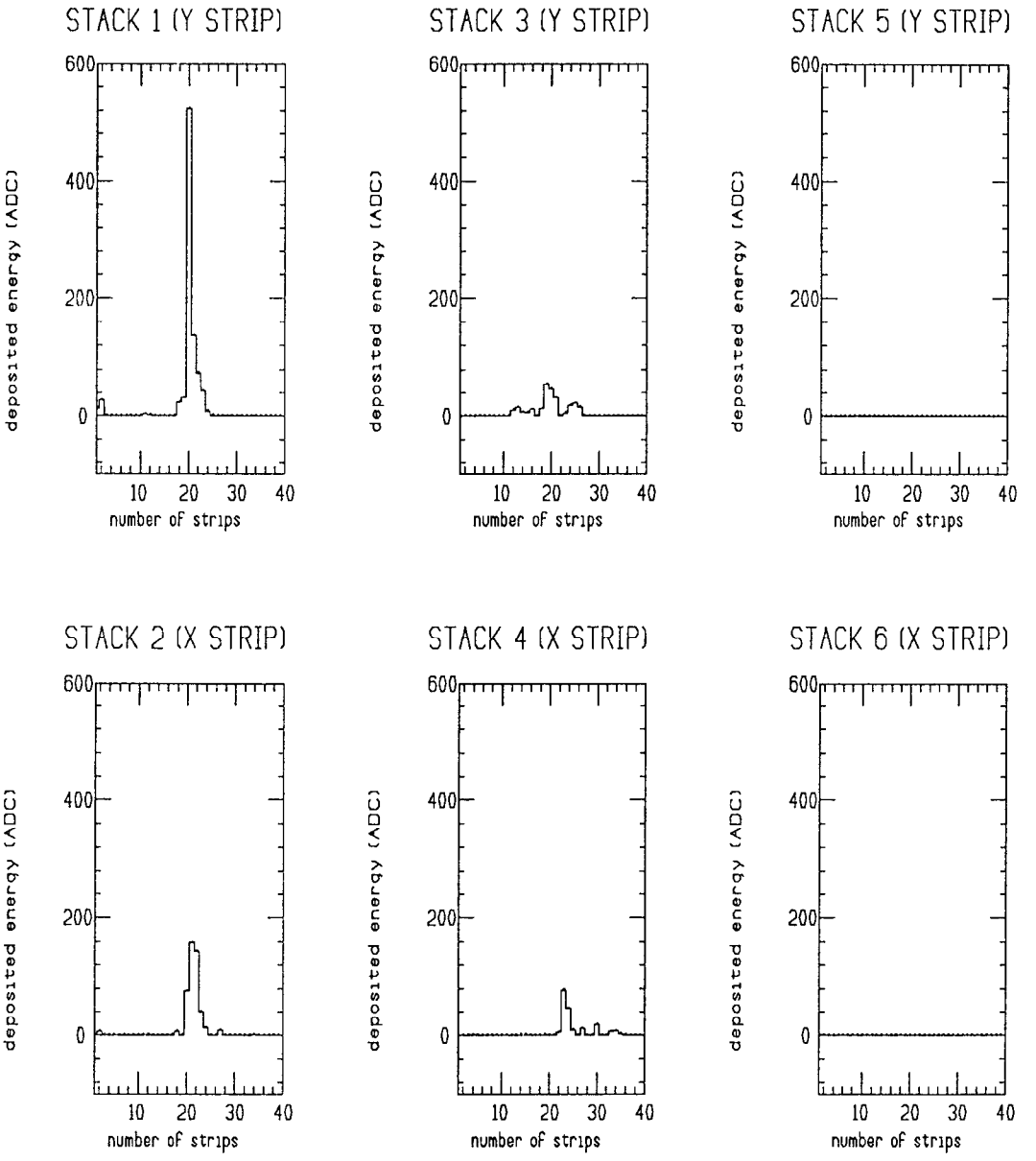

Figure 8.9: The simulated (signal) energies versus strips in each stack for an arbitrary event (MC simulation for 10 GeV π^-).

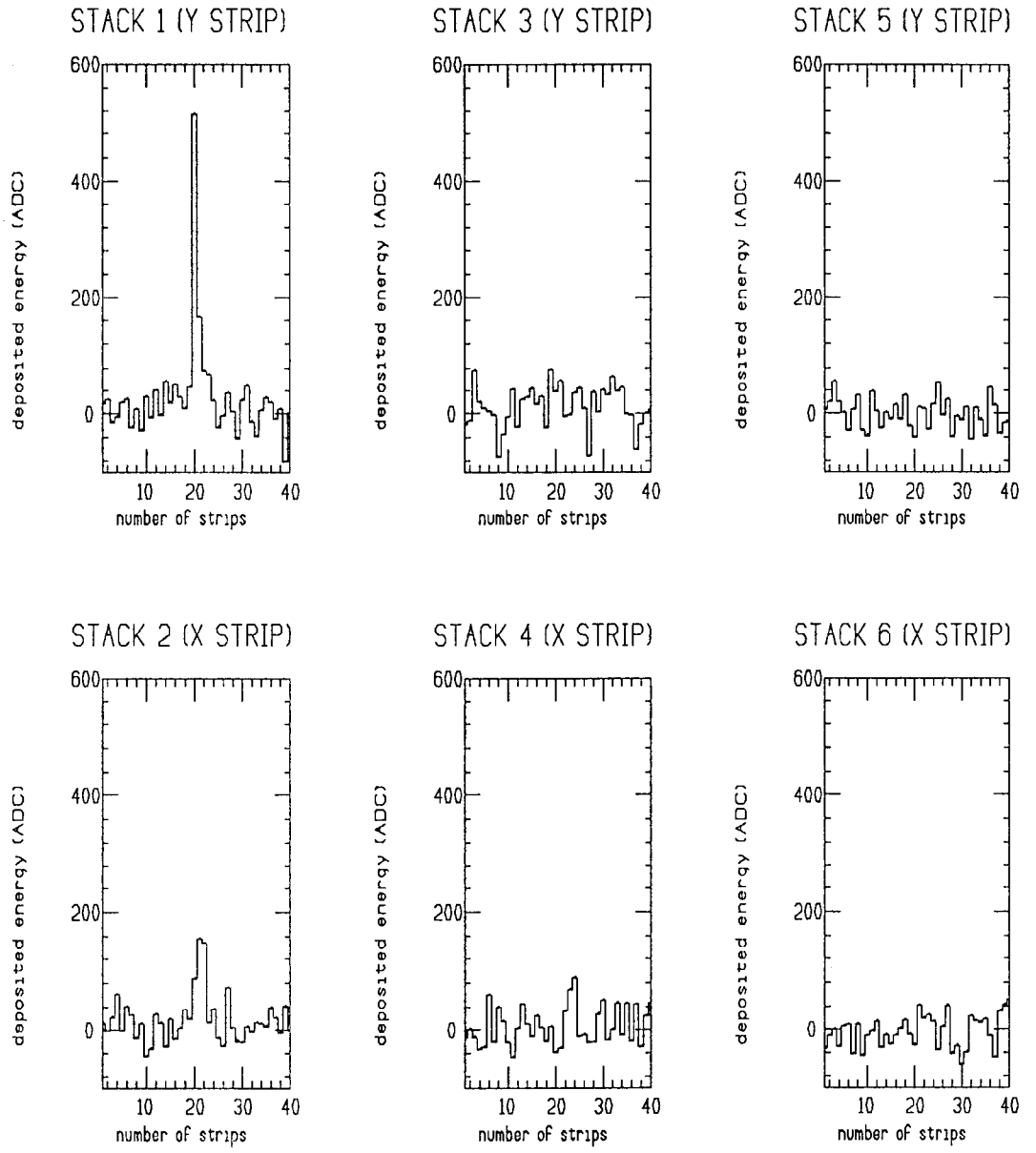

Figure 8.10: The simulated (signal + pedestal) energies versus strips in each stack for an arbitrary event (MC simulation for 10 GeV π^-).

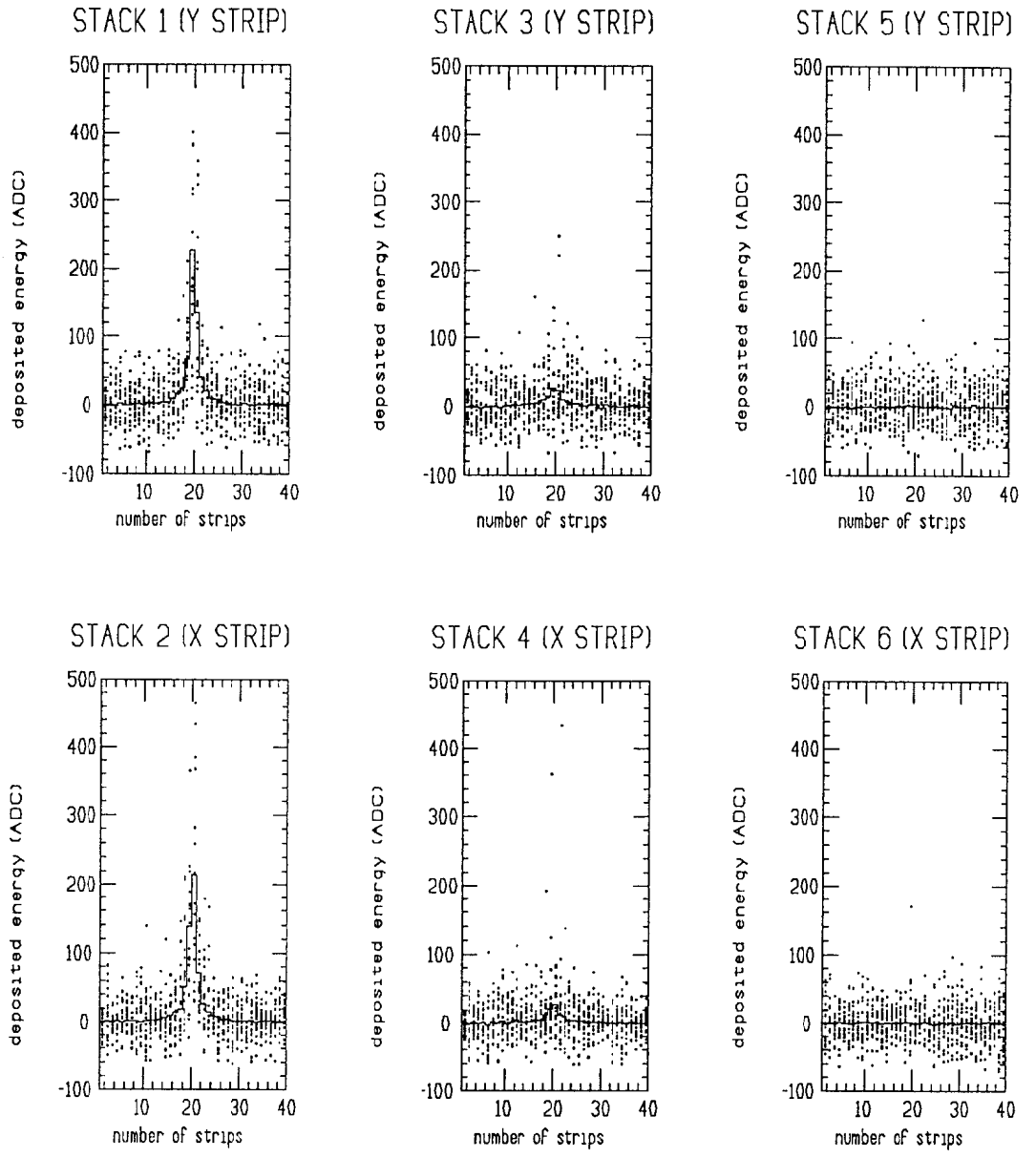

Figure 8.11: The deposited (signal + pedestal) energies versus strips in each stack for arbitrary events (BNL data for 10 GeV π^-: The dot points represent data values for each event. The solid line histograms show average values of calculated data values for 100 events).

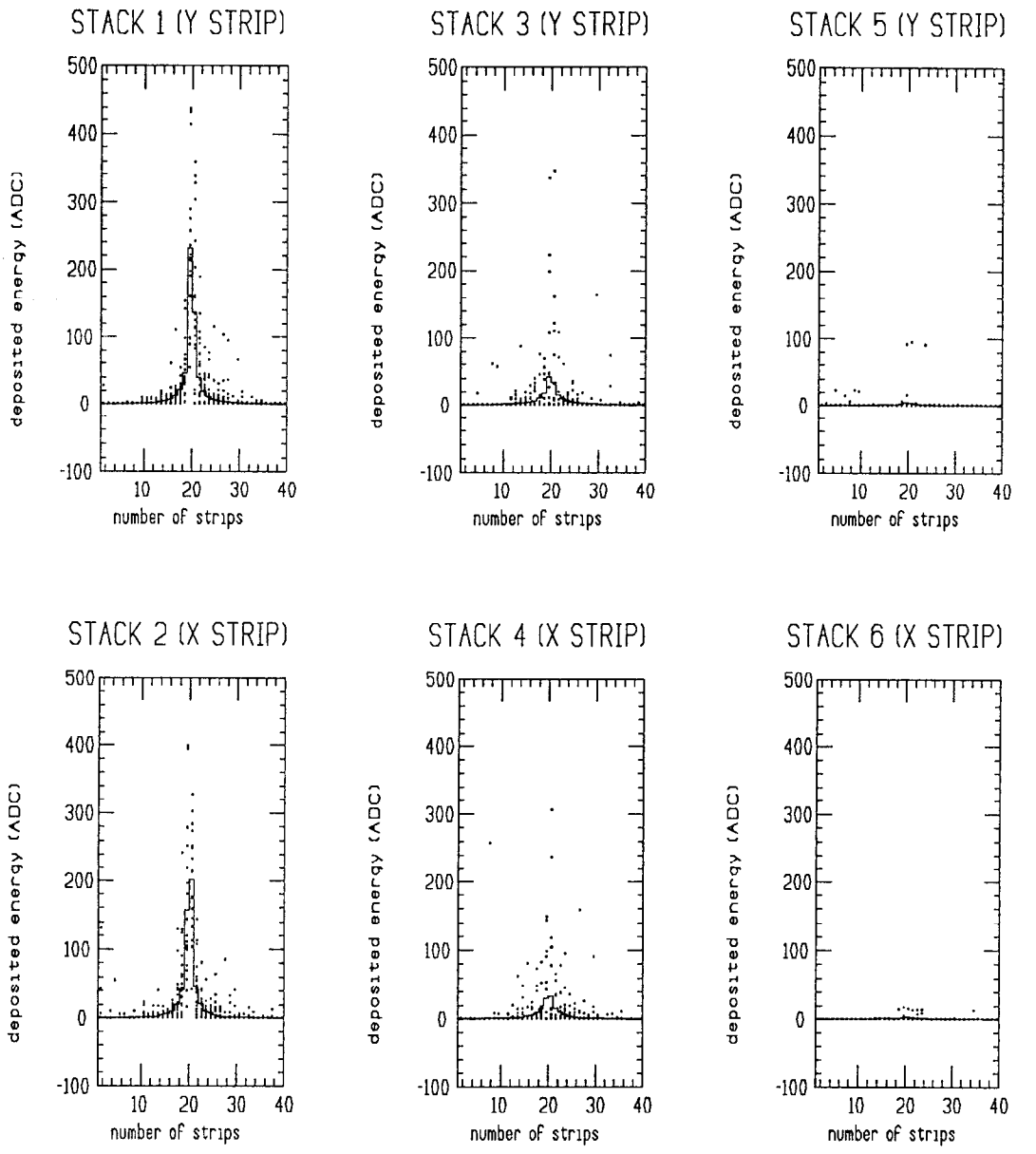

Figure 8.12: The simulated (signal) energies versus strips in each stack for arbitrary events (MC simulation for 10 GeV π^-: The dot points represent MC values for each of 100 events. The solid line histograms show average values of calculated MC values for 100 events).

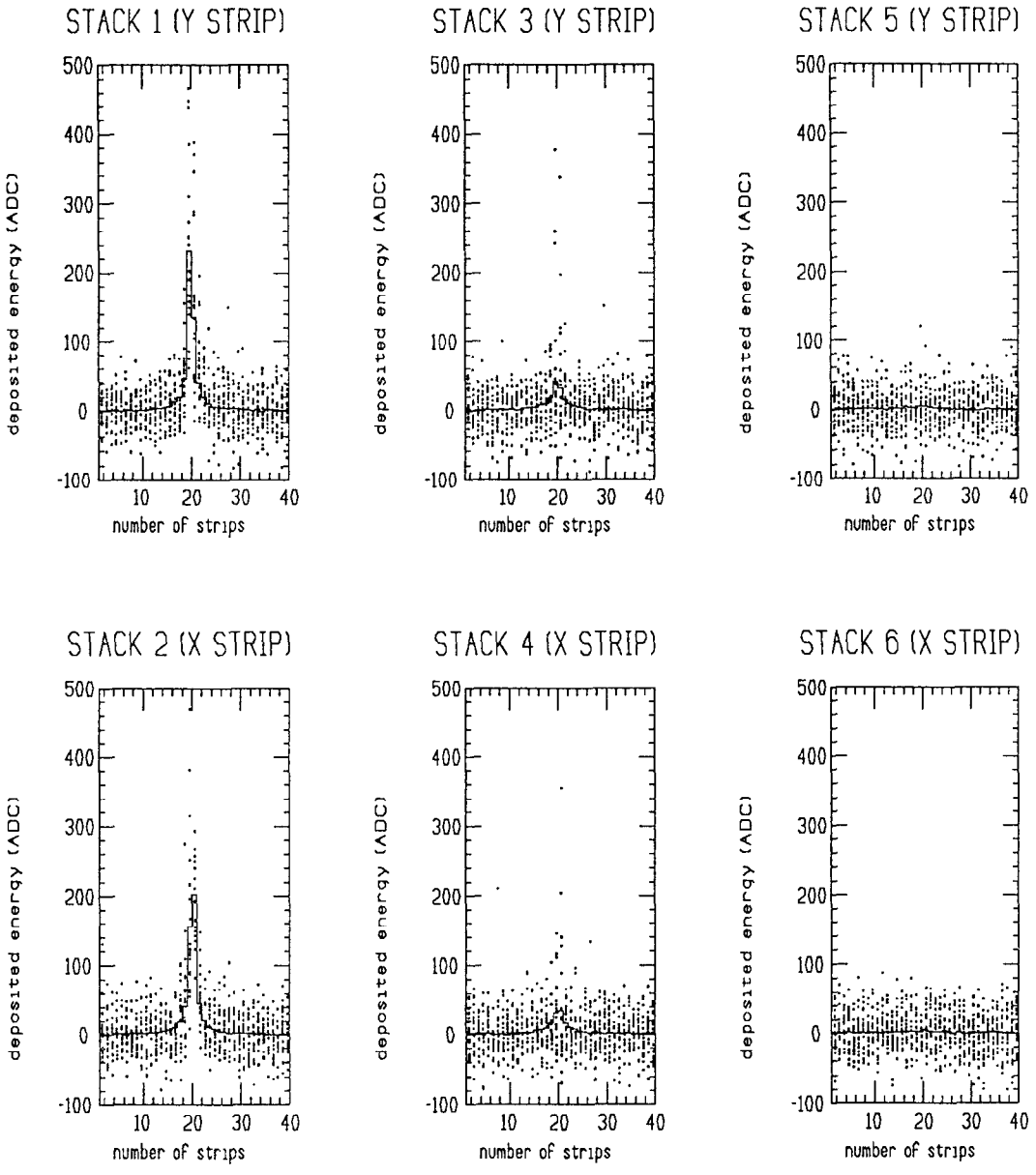

Figure 8.13: The simulated (signal) energies versus strips in each stack for arbitrary events (MC simulation for 10 GeV π^-: The dot points represent MC values for each of 100 events. The solid line histograms show average values of calculated MC values for 100 events).

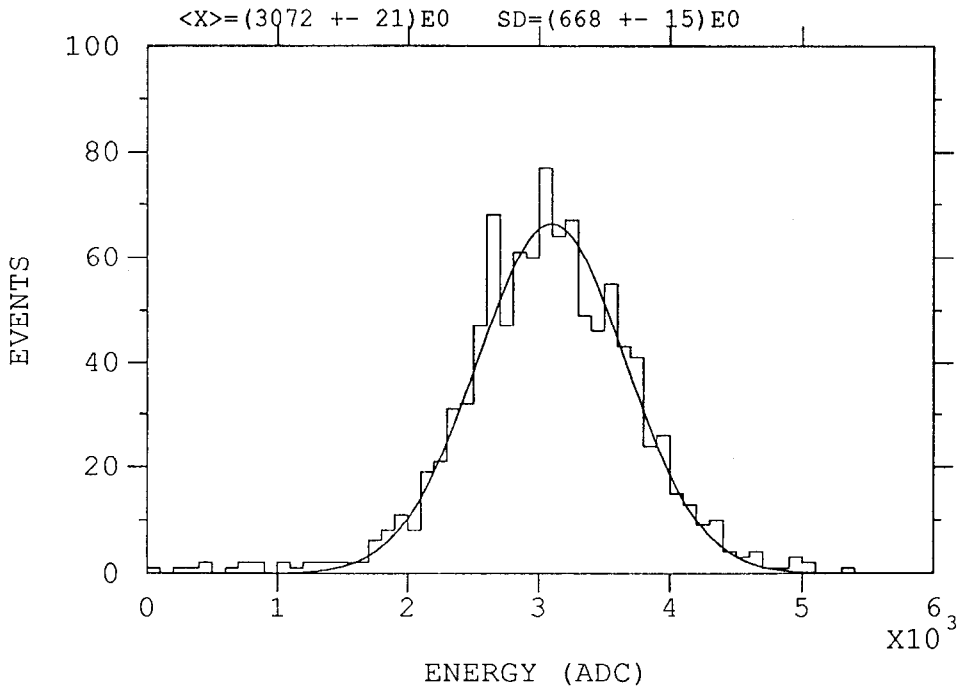

Figure 8.14: The distribution of the 20 GeV π^- energies of BNL data without cut threshold for 1,000 events with the overlaid gaussian.

8.3.2 BNL Data and MC Simulation for Arbitrary Events

Figures 8.7 and 8.8 show the deposited (signal+pedestal) and pedestal energies versus strips. Measurements were obtained at BNL for 10 GeV π^- particle in each stack for an arbitrary event. Figure 8.9 shows the deposited energy versus strips which were simulated with CALOR 89 for an arbitrary event. Figure 8.10 shows the MC deposited energy of figure 8.10 plus MC simulated noise.

8.3.3 BNL Data and MC Simulation For 100 Events

Figure 8.11 shows the deposited energies versus strips which were measured at BNL in each stack. The dots represent data values at each of 100 events. The solid line histograms show the average values of calculated data values for 100 events. Figure 8.12 shows MC signal from each stack. Figure 8.13 shows MC signal plus MC noise from each stack. Also, solid line histograms of MC simulation were calculated with the same method as for the data in figure 8.11.

There were the differences between BNL data and MC results for the third and the fourth stack at the central region of calorimeter as seen in figures 8.11 and 8.13. That is, the shape of BNL data was broader than that of MC result. The reason for the differences was suspected to come from the multiple scattering process which the CALOR 89 program did not include.

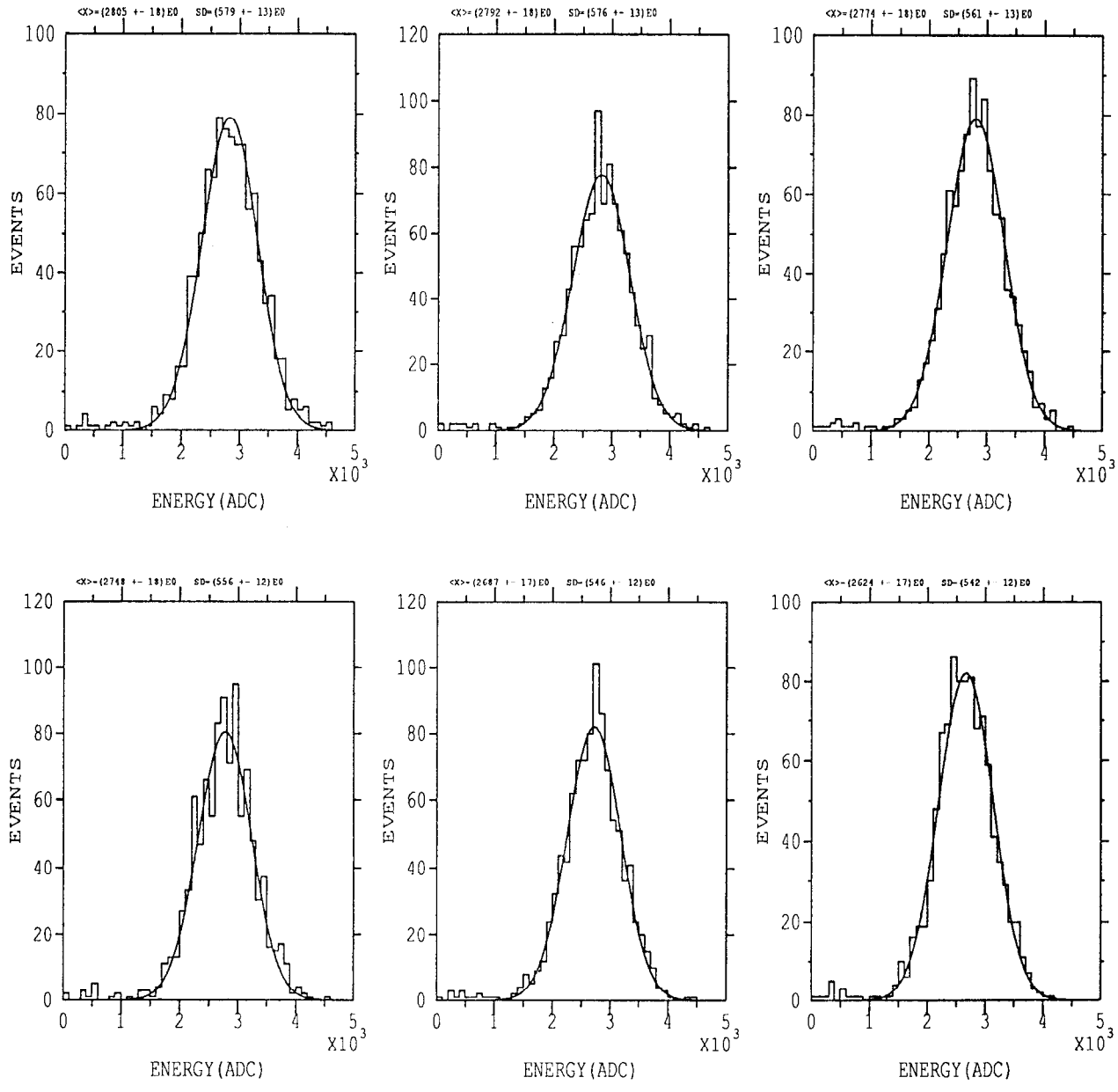

Figure 8.15: Energy distributions for constant cut thresholds of 30, 40, 50, 60, 70 and 80 ADC counts for 1,000 events in BNL data of 20 GeV π^-.

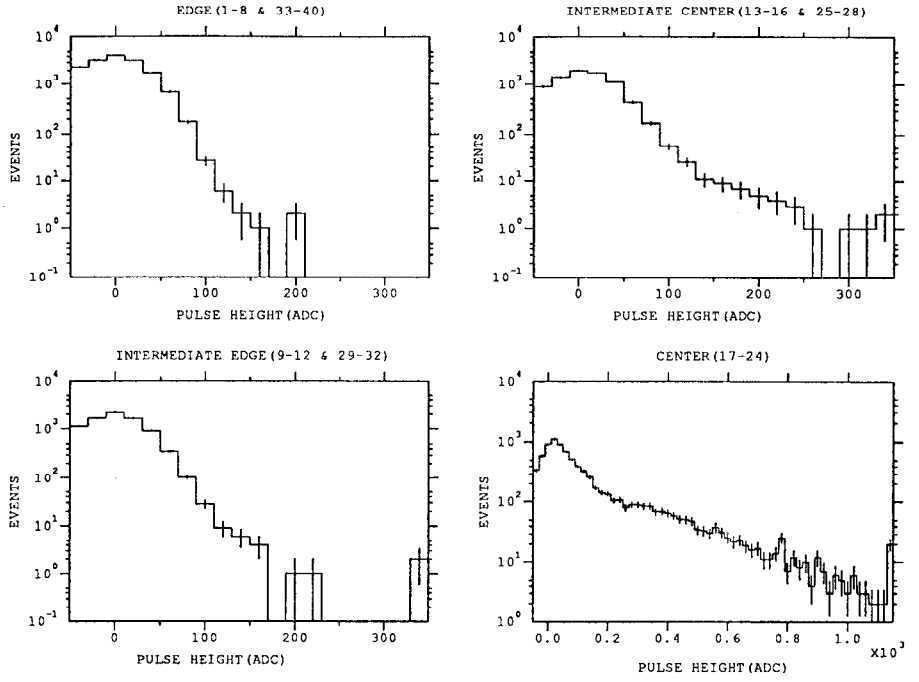

Figure 8.16: Signal energy distribution for four different regions of the first stack: Upper-Left is Edge, Upper-Right is Intermediate Center, Lower-Left is Intermediate Edge and Lower Right is Center.

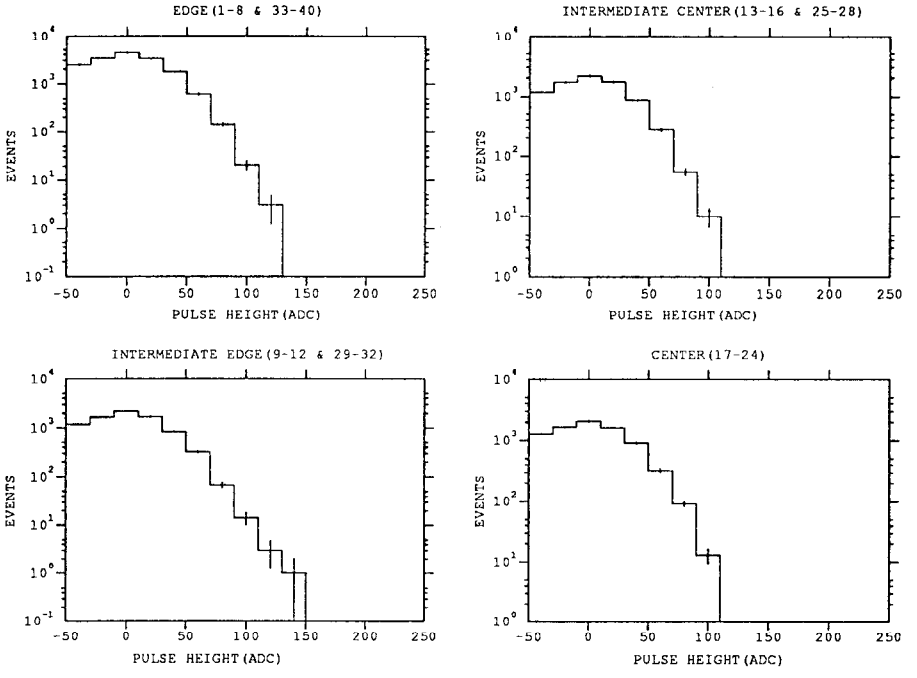

Figure 8.17: Noise distribution for four different regions of the first stack: Upper-Left is Edge, Upper-Right is Intermediate Center, Lower-Left is Intermediate Edge and Lower Right is Center.

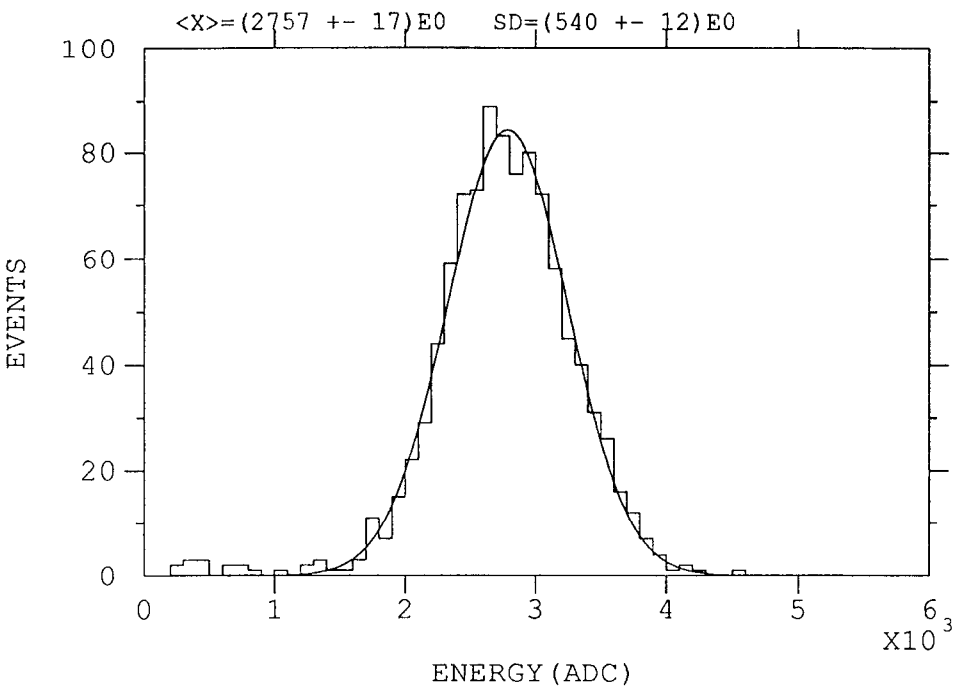

Figure 8.18: Energy distribution of BNL data of 20 GeV π^- with channel dependent cut thresholds for 1,000 events.

8.4 Energy Resolution

The energy resolutions of BNL data were analyzed at 10 and 20 GeV π^- energies for three different ways:

- All pulse heights were summed (no cut sum)
- All pulse heights above a certain threshold were summed (constant cut sum)
- All pulse heights above a channel dependent threshold were summed (channel dependent cut sum).

As an example, 20 GeV π^- case will be explained.

8.4.1 Energy Resolution without the Cut Thresholds

Figure 8.14 shows the average of 3072 ADC counts and standard deviation of 668 ADC counts of the histogram, and the average of 3095 ADC counts and deviation of 566 ADC counts of the overlaid gaussian at the 20 GeV negative pion energy of BNL data with 1,000 events. As is seen in figure 8.14, the main difference between the gaussian and the histogram comes from the long tail distribution. Table 8.1 shows averages, standard deviations, and resolutions of the 10 and 20 GeV π^- energies

		Noise		Mean and RMS				Gaussian Fit			
Data Type	E_{in}	N	RMS	E	RMS	RMS/E	RMS/E× $\sqrt{E_{in}}$(%)	E	RMS	RMS/E	RMS/E× $\sqrt{E_{in}}$(%)
BNL data	10	46	428	1540	565	0.3609	116.0	1549	556	0.3589	113.5
MC signal	GeV			1550	225	0.1452	45.92	1534	206	0.1342	42.47
MC signal + MC noise	π^-	37	432	1587	480	0.3025	95.66	1579	460	0.2913	92.12
MC signal + data pedestal				1622	512	0.3157	99.83	1616	507	0.3137	99.21
BNL data	20	72	443	3072	668	0.2174	97.24	3095	566	0.1829	81.78
MC signal	GeV			3044	349	0.1147	51.27	3055	292	0.0956	42.74
MC signal + MC noise	π^-	55	432	3099	538	0.1736	77.64	3104	520	0.1675	74.92
MC signal + data pedestal				3116	566	0.1816	81.23	3127	498	0.1593	71.22

Table 8.1: Energy resolution without cut threshold.

		Noise		Mean and RMS				Gaussian Fit			
Data Type	E_{in}	N	RMS	E	RMS	RMS/E	RMS/E× $\sqrt{E_{in}}$(%)	E	RMS	RMS/E	RMS/E× $\sqrt{E_{in}}$(%)
BNL data	10	46	428	1303	390	0.2993	94.65	1299	352	0.2710	85.78
MC signal + MC noise	π^-	37	432	1321	305	0.2309	73.01	1309	299	0.2284	72.23
MC signal + data pedestal				1318	319	0.2420	76.54	1306	303	0.2320	73.42
BNL data	20	72	443	2748	556	0.2023	90.48	2770	460	0.1660	74.27
MC signal + MC noise	π^-	55	432	2732	422	0.1545	69.07	2739	392	0.1430	64.00
MC signal + data pedestal				2719	423	0.1556	69.57	2724	388	0.1424	63.70

Table 8.2: Energy resolution with constant cut thresholds: cut threshold (60 ADC counts).

	Channel Regions			
Stack Number	1-8 and 33-40 (Edge)	9-12 and 29-32 (Intermediate Edge)	13-16 and 25-28 (Intermediate Center)	17-24 (Center)
1	90	90	50	0
2	90	90	50	0
3	90	90	50	30
4	90	90	50	30
5	90	90	90	50
6	90	90	90	50

Table 8.3: Channel dependent cut thresholds (Unit: ADC counts).

		Noise		Mean and RMS				Gaussian Fit			
Data Type	E_{in}	N	RMS	E	RMS	RMS/E	RMS/E× $\sqrt{E_{in}}$(%)	E	RMS	RMS/E	RMS/E× $\sqrt{E_{in}}$(%)
BNL data	10	46	428	1344	374	0.2783	87.99	1346	323	0.2399	75.89
MC signal + MC noise	π^-	37	432	1353	285	0.2106	66.61	1339	274	0.2046	64.70
MC signal + data pedestal				1355	291	0.2148	67.91	1334	282	0.2114	66.85
BNL data	20	72	443	2757	540	0.1959	87.59	2785	462	0.1659	74.21
MC signal + MC noise	π^-	55	432	2745	399	0.1454	65.00	2758	383	0.1389	62.06
MC signal + data pedestal				2744	399	0.1454	65.02	2761	372	0.1347	60.28

Table 8.4: Energy resolution with channel dependent cut thresholds.

displayed by four data combinations: BNL data, MC signal, MC signal plus MC noise and MC signal plus BNL pedestal data.

8.4.2 Energy Resolution with the Constant Cut Thresholds

Let the deposited (signal+pedestal) energy at the i-th channel be E_i and the deposited energies at the nearest side channels of the i-th channel be E_{i-1} and E_{i+1}. The deposited energies were selected if E_i, E_{i-1}, or E_{i+1} energies surpass the cut threshold. The selected deposited energies were summed for all channels passing the cut from the first to the 240th channel at each event. The pedestal energies were done by the same method, but, the pedestal energies were averaged for all events. The average pedestal energy was constant for all events.

The energy distributions were calculated by subtracting the average pedestal energy from the deposited energy at each event. For example, figure 8.15 shows energy distributions calculated with the above described method and the constant cut thresholds of 30, 40, 50, 60, 70, and 80 ADC counts for 1,000 events in BNL data of 20 GeV. Table 8.2 shows results in the same cases as table 8.1 at the constant cut threshold with 60 ADC counts.

8.4.3 Energy Resolution with the Channel Dependent Cut Thresholds

Since the deposited energies are changed according to channel, energy resolutions by the channel dependent cut thresholds were expected to be better than those by the constant cut thresholds. The regions of channels were classified as four regions for each stack: center (17-24), intermediate center (13-16 and 25-28), intermediate edge (9-12 and 29-32) and edge (1-8 and 33-40). The number in the parenthesis denotes the channel order number from left edge of each stack , see figure 8.2.

Figure 8.16 shows the signal energy distribution at four regions of the first stack; the upper left side is the edge, the upper right side is the intermediate center, the lower left side is the intermediate edge and the lower right side is the center. Figure 8.17 shows the noise distribution. By comparing figures 8.16 and 8.17, the channel dependent cut thresholds are assigned and shown in table 8.3. Figure 8.18 shows energy distribution for 1,000 events in BNL data of 20 GeV π^- calculated with channel dependent cut thresholds like a table 8.3. Table 8.4 shows the results of energy resolutions with the channel dependent cut thresholds.

8.4.4 Comments

Since the histogram data profile displayed the long tail distribution, it was decided to use the gaussian profile for our calculations.

We express energy resolution as RMS/$\sqrt{E}$ in units of $\sqrt{GeV}$. Table 8.1 shows the energy resolutions of BNL data were 113.5% (10 GeV) and 81.78% (20 GeV),

those of BNL pedestal data plus MC signal were 99.21% (10 GeV) and 71.22% (20 GeV). Even if the energy increased from 10 to 20 GeV, the deviation of the pedestal was constant, therefore, resolution was improved with the energy increase.

The MC signal was assumed to be correct, then, the two energy resolutions described above should be same. However, those were differences of 81.78 % and 71.22% at 20 GeV, 113.5% and 99.21% at 10 GeV. The reason for the difference was suspected to come from multiple scattering as mentioned in the section 8.3.3, spurious pion particles during data taking, and possibly, other unknown factors.

By using the constant cut thresholds in table 8.2, energy resolutions of BNL data were improved from 113.5% to 85.78% at 10 GeV and from 81.78% to 74.27% at 20 GeV, respectively. Energy resolutions of BNL pedestal data plus MC signal improved from 99.21% to 71.22% at 10 GeV and from 71.22% to 63.70% at 20 GeV. Since the standard deviation of pedestal was constant regardless of energy increase, resolution at 20 GeV was much better than that at 10 GeV.

With the channel dependent cut thresholds in table 8.4, energy resolutions of BNL data were improved from 113.5% to 75.89% at 10 GeV and from 81.78% to 74.21% at 20 GeV. Also, resolutions of BNL pedestal data plus MC signal improved from 99.21% to 66.85% at 10 GeV and from 71.22% to 60.28% at 20 GeV.

While the improvement of energy resolution was almost same with two cut methods, constant and channel dependent cut thresholds, at 20 GeV, resolution was better in the channel dependent cut thresholds than in the constant different thresholds at 10 GeV. Therefore, the method using the channel dependent cut thresholds showed better resolution in the low pion energies than in the high pion energies.

8.5 Noise Correlation of BNL Data between Channels

To obtain noise correlation between channels, the pedestal energy of each channel was multiplied by the pedestal energy of a different channel, then summed for all events (pedestal energy of 20 GeV and events are 403). For example, figure 8.19 shows noise correlation of each channel for six channels from the first (upper-left) to the sixth channel (lower-right). We did not find any significant noise correlation in the BNL data.

8.6 The Pion Rejection Studies

In an experiment aimed at identifying isolated electromagnetic showers (eq. a search for $H^0 \rightarrow \gamma\gamma$ where there is a large background from non-isolated electromagnetic showers) it is necessary to reject non-isolated showers with the smallest possible associated hadronic energy. Keeping in mind that this calorimeter has relatively coarse sampling we have attempted to reject each event with the slightest indication of energy. If any channel of the 240 is above a set threshold, we assume we can reject

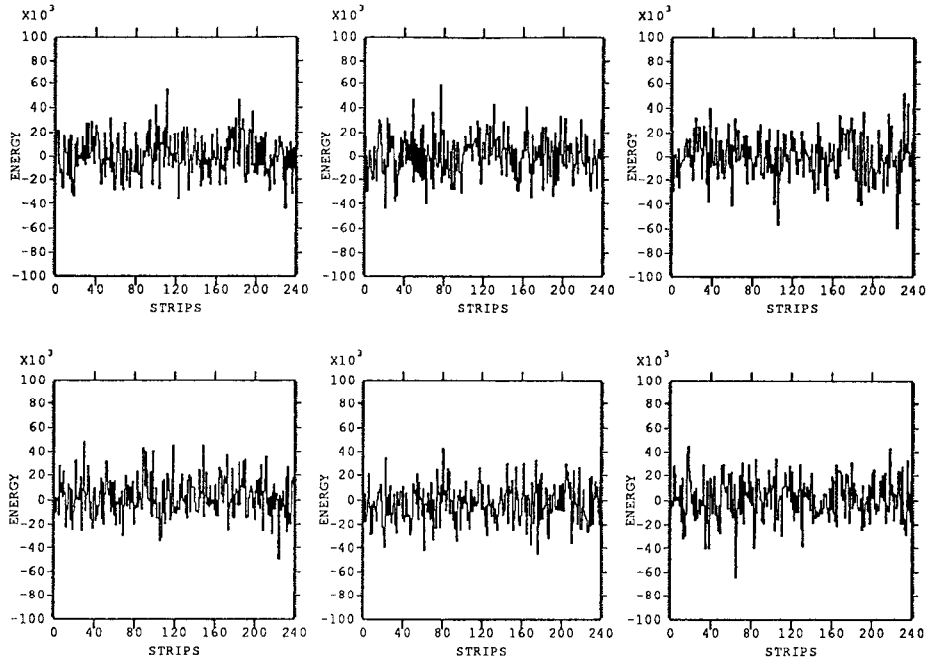

Figure 8.19: Noise correlation between channels for six channels from the first (upper-left) to the sixth channel (lower-right).

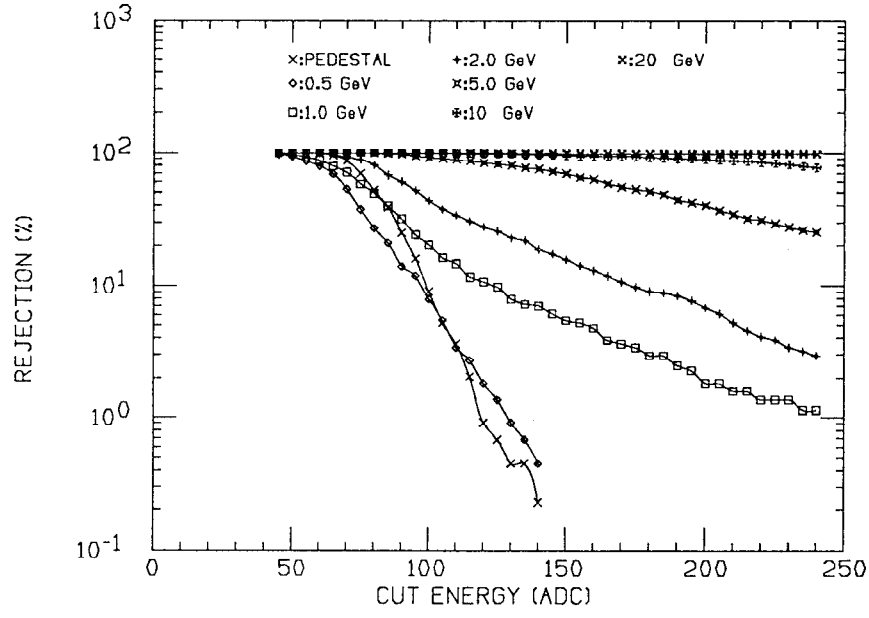

Figure 8.20: Rejection factor versus cut energy (ADC counts).

this event. Figure 8.20 shows the rejection % as a function of the cut energy for the six beam energies with data. 135 ADC counts corresponds to 1 GeV of hadronic energy. Also shown is the rejection of pedestal events. From this figure we can see that if we require only a 1% rejection for pedestal events, we can obtain nearly 90% rejection for 5 GeV and much better for 10 and 20 GeV. For a finer calorimeter we would expect somewhat better performance.

8.7 Conclusion

We calculated averages, standard deviations, and resolutions of the 10 and 20 GeV π^- energies displayed by four data combinations: BNL data, MC signal, MC signal plus MC noise and MC signal plus BNL pedestal data. The energy resolutions of three data types except MC signal were analyzed at the 10 and 20 GeV π^- energies for three different ways: no cut threshold, the constant cut thresholds, and the channel dependent cut thresholds.

While the improvement of energy resolution was almost same with two cut methods at 20 GeV (the constant and the channel dependent cut thresholds), resolution was better in the channel dependent cut thresholds than in the constant thresholds at 10 GeV. That is, energy resolutions of BNL data (MC) were improved from 113.5% (99.21%) to 75.89% (66.85%) at 10 GeV and from 81.78% (71.22%) to 74.21% (60.28%) at 20 GeV

Also, energy resolutions of BNL data (MC) were improved from 113.5% (99.21%) to 85.78% (73.42%) at 10 GeV and from 81.78% (71.22%) to 74.27% (63.70%) at 20 GeV with the constant cut thresholds. Therefore, the method using the channel dependent cut thresholds showed better resolution in the low pion energies than in the high pion energies. The difference of energy resolution between BNL data and MC was suspected to come from multiple scattering as mentioned in the section 8.3.3, spurious pion particles during data taking, and possibly, other unknown factors.

We did not find any noise correlation of BNL data. In the pion rejection studies, if we require only a 1% rejection for pedestal events, we can obtain nearly 90% rejection for 5 GeV and much better for 10 and 20 GeV. For a finer calorimeter we would expect somewhat better performance.

CHAPTER IX

CONCLUSION

The distributions of three-jet events have been measured to check the spin of the gluon with $\approx$ 50,000 Z^0 93 hadronic events accumulated in the SLD liquid argon calorimeter (LAC). The correction factor was obtained with comparisons to HERWIG5.7 simulations in order to compensate the endcap LAC energy response inefficiency due to the electronics and materials in front of the LAC. The hadronic data events after correction give good direction and the energy resolution improves from 21% to 17%. They were reconstructed to three-jet events. The three-jet events reconstructed with the YCLUS algorithm and $y_c = 0.02$ are rescaled by momentum conservation. We have a tremendous improvement after momentum conservation. Good agreement is found between data and the vector QCD model for the distributions of x_1, x_2, x_3 and $cos\theta_{EK}$. We have three parameters $(\alpha, \alpha_N, \beta)$ associated with the angles ($cos\theta$, $cos\theta_N$, χ) of event plane orientation depending on the most energetic jet ($T = x_1$). The data favors the vector gluon model, particularly in the parameter (α_N). The signature of T violation, depending on right or left helicities with an electron beam polarization of 63% during 1993 run, has not been found.

The silicon-tungsten preradiator was designed to distinguish between single photons from Higgs decay and background photon pairs from π^0 decay. The test results on spatial distributions and energy resolution, including correction for the energy deposited in the preradiator have reasonably a good agreement with comparisons to EGS simulation. Data from a beam test of the liquid argon prototype was analyzed and compared to CALOR89 simulation. The studies concentrated on energy resolution optimization through electronic noise suppression with different thresholds. The pion rejection studies have been done with the purpose of identifying isolated electromagnetic shower.

APPENDIX A

THE SLD COLLABORATION

K. Abe,[18] I. Abt,[25] W.W. Ash,[17] D. Aston,[17] N. Bacchetta,[9]
K.G. Baird,[15] C. Baltay,[34] H.R. Band,[32] M.B. Barakat,[34]
G. Baranko,[23] O. Bardon,[13] R. Battiston,[10] A.O. Bazarko,[5]
A. Bean,[20] R.J. Belcinski,[26] R. Ben-David,[34] A.C. Benvenuti,[7]
M. Biasini,[10] T. Bienz,[17] G.M. Bilei,[10] D. Bisello,[9] G. Blaylock,[21]
J. R. Bogart,[17] T. Bolton,[5] G.R. Bower,[17] J. E. Brau,[27]
M. Breidenbach,[17] W.M. Bugg,[29] D. Burke,[17] T.H. Burnett,[31]
P.N. Burrows,[13] W. Busza,[13] A. Calcaterra,[6] D.O. Caldwell,[20]
D. Calloway,[17] B. Camanzi,[8] M. Carpinelli,[11] J. Carr,[23] R. Cassell,[17]
R. Castaldi,[11] [24] A. Castro,[9] M. Cavalli-Sforza,[21] G.B. Chadwick,[17]
L. Chen,[33] E. Church,[31] R. Claus,[17] H.O. Cohn,[29] J.A. Coller,[2]
V. Cook,[31] R. Cotton,[3] R.F. Cowan,[13] P.A. Coyle,[21] D.G. Coyne,[21]
A. D'Oliveira,[22] C.J.S. Damerell,[16] S. Dasu,[17] R. De Sangro,[6]
P. De Simone,[6] S. De Simone,[6] R. Dell'Orso,[11] P.Y.C. Du,[29]
R. Dubois,[17] J.E. Duboscq,[20] B.I. Eisenstein,[25] R. Elia,[17] E. Erdos,[23]
C. Fan,[23] B. Farhat,[13] M.J. Fero,[13] R. Frey,[27] J.I. Friedman,[13]
K. Furuno,[27] M. Gallinaro,[6] A. Gillman,[16] G. Gladding,[25]
S. Gonzalez,[13] G.D. Hallewell,[17] T. Hansl-Kozanecka,[13] E.L. Hart,[29]
K. Hasegawa,[18] Y. Hasegawa,[18] S. Hedges,[3] S.S. Hertzbach,[26]
M.D. Hildreth,[17] D.G. Hitlin,[4] A. Honma,[30] J. Huber,[27] M.E. Huffer,[17]
E.W. Hughes,[17] H. Hwang,[27] Y. Iwasaki,[18] J.M. Izen,[25] P. Jacques,[15]
A.S. Johnson,[2] J.R. Johnson,[32] R.A. Johnson,[22] T. Junk,[17]
R. Kajikawa,[14] M. Kalelkar,[15] I. Karliner,[25] H. Kawahara,[17]
M.H. Kelsey,[4] H.W. Kendall,[13] H.Y. Kim,[31] M.E. King,[17] R. King,[17]
R.R. Kofler,[26] N.M. Krishna,[23] R.S. Kroeger,[29] Y. Kwon,[17]
J.F. Labs,[17] M. Langston,[27] A. Lath,[13] J.A. Lauber,[23] D.W.G. Leith,[17]
X. Liu,[21] M. Loreti,[9] A. Lu,[20] H.L. Lynch,[17] J. Ma,[31] W.A. Majid,[25]
G. Mancinelli,[10] S. Manly,[34] G. Mantovani,[10] T.W. Markiewicz,[17]
T. Maruyama,[17] H. Masuda,[17] E. Mazzucato,[8] J.F. McGowan,[25]
S. McHugh,[20] A.K. McKemey,[3] B.T. Meadows,[22] D.J. Mellor,[25]
R. Messner,[17] P.M. Mockett,[31] K.C. Moffeit,[17] B. Mours,[17]

G. Müller,[17] D. Muller,[17] T. Nagamine,[17] U. Nauenberg,[23] H. Neal,[17]
M. Nussbaum,[22] L.S. Osborne,[13] R.S. Panvini,[33] H. Park,[27]
M. Pauluzzi,[10] T.J. Pavel,[17] F. Perrier,[17] I. Peruzzi,[6] [28] L. Pescara,[9]
M. Petradza,[17] M. Piccolo,[6] L. Piemontese,[8] E. Pieroni,[11] K.T. Pitts,[27]
R.J. Plano,[15] R. Prepost,[32] C.Y. Prescott,[17] G.D. Punkar,[17]
J. Quigley,[13] B.N. Ratcliff,[17] T.W. Reeves,[33] P.E. Rensing,[17]
J.D. Richman,[20] L.S. Rochester,[17] L. Rosenson,[13] J.E. Rothberg,[31]
S. Rousakov,[33] P.C. Rowson,[5] J.J. Russell,[17] P. Saez,[17]
O.H. Saxton,[17] T. Schalk,[21] R.H. Schindler,[17] U. Schneekloth,[13]
D. Schultz,[17] B.A. Schumm,[12] A. Seiden,[21] S. Sen,[34] L. Servoli,[10]
M.H. Shaevitz,[5] J.T. Shank,[2] G. Shapiro,[12] S.L. Shapiro,[17]
D.J. Sherden,[17] R.L. Shypit,[19] C. Simopoulos,[17] S.R. Smith,[17]
J.A. Snyder,[34] M.D. Sokoloff,[22] P. Stamer,[15] H. Steiner,[12] R. Steiner,[1]
I.E. Stockdale,[22] M.G. Strauss,[26] D. Su,[16] F. Suekane,[18] A. Sugiyama,[14]
S. Suzuki,[14] M. Swartz,[17] A. Szumilo,[31] T. Takahashi,[17] F.E. Taylor,[13]
J.J. Thaler,[25] N. Toge,[17] E. Torrence,[13] M. Turcotte,[30] J.D. Turk,[34]
T. Usher,[17] J. Va'vra,[17] C. Vannini,[11] E. Vella,[17] J.P. Venuti,[33]
R. Verdier,[13] P.G. Verdini,[11] S. Wagner,[17] A.P. Waite,[17] S.J. Watts,[3]
A.W. Weidemann,[29] J.S. Whitaker,[2] S.L. White,[29] F.J. Wickens,[16]
D.A. Williams,[21] D.C. Williams,[13] S.H. Williams,[17] S. Willocq,[34]
R.J. Wilson,[2] W.J. Wisniewski,[4] M.S. Witherell,[20] M. Woods,[17]
G.B. Word,[15] J. Wyss,[9] R.K. Yamamoto,[13] J.M. Yamartino,[13]
S.J. Yellin,[20] C.C. Young,[17] H. Yuta,[18] G. Zapalac,[32] R.W. Zdarko,[17]
C. Zeitlin,[27] J. Zhou,[27] M. Zolotorev,[17] and P. Zucchelli[8]

[1] Adelphi University
[2] Boston University
[3] Brunel University
[4] California Institute of Technology
[5] Columbia University
[6] INFN Lab. Nazionali di Frascati
[7] INFN Sezione di Bologna
[8] INFN Sezione di Ferrara and Universitá di Ferrara
[9] INFN Sezione di Padova and Universitá di Padova
[10] INFN Sezione di Perugia and Universitá Perugia
[11] INFN Sezione di Pisa and Universitá di Pisa
[12] Lawrence Berkeley Laboratory, University of California
[13] Massachusetts Institute of Technology
[14] Nagoya University
[15] Rutgers University
[16] Rutherford Appleton Laboratory
[17] Stanford Linear Accelerator Center

[18] Tohoku University
[19] University of British Columbia
[20] University of California, Santa Barbara
[21] University of California, Santa Cruz
[22] University of Cincinnati
[23] University of Colorado
[24] Universitá di Genova
[25] University of Illinois
[26] University of Massachusetts
[27] University of Oregon
[28] Universitá di Perugia
[29] University of Tennessee
[30] University of Victoria
[31] University of Washington
[32] University of Wisconsin
[33] Vanderbilt University
[34] Yale University

Bibliography

[1] TASSO Collaboration, R. Brandelik *et al.,* Phys. Lett. **97B** (1980) 453.

[2] CELLO Collaboration, H.J. Behrend *et al.,* Phys. Lett. **110B** (1982) 329.

[3] PLUTO Collaboration, Ch. Berger *et al.,* Phys. Lett. **97B** (1980) 459.

[4] L3 Collaboration, B. Adeva *et al.,* Phys. Lett. **263B** (1991) 551.

[5] OPAL Collaboration, G. Alexander, *et al.,* Z. PHYS. **C52** (1991) 543.

[6] DELPHI Collab., P. Abreu *et al.,* Phys. Lett. **B274** (1992) 498.

[7] H.A. Olsen, P. Osland and I. Øverbø, Nucl. Phys. **B171** (1980) 209.

[8] M. Gell-Mann. A schematic model of baryons and mesons, Physics Letters, 8(3):214, 1964.

[9] J.I. Friedman and H.W. Kendall. Annual Review of Nuclear Science, **22** (1972) 203.

[10] TASSO Collb., M. Althoff *et al.,* Z. Phys. **C22** (1984) 307.

[11] See eg. R.J. Cashmore, Sci. Prog., Oxf. **71** (1987) 305.

[12] E. Laermann, K.H. Streng, P.M. Zerwas, Z. Phys. **C3** (1980) 209.

[13] P.N. Burrows, SLAC-PUB-6004 (1992).

[14] K. Koller, H.G. Sander, T.F. Walsh and P.M. Zerwas, Z. Phys. **C6** (1980) 131.

[15] G. Kramer, G. Schierholz and J. Willrodt, Phys. Lett. **B79** (1978) 249.

[16] J.G. Körner, G.A. Schuler and F. Barreiro, Phys. Lett. **B188** (1987) 272.

[17] C.G. Fan, SLAC-REP 424 (November 1993).

[18] J.A. Lauber, SLAC-REP 413 (February 1993).

[19] B. Bambah *et al.,* QCD generators. In G. Altarelli *et al.,* editor, Z physics at LEP, volume 3, pages 143-340. CERN, 1989.

[20] G. Altarelli and G. Parisi. Asymptotic freedom in parton language. Nuclear Physics B, **126** (1977) 298.

[21] X. Artru, Phys. Rept. **97** (1983) 147.

[22] T. Sjöstrand, Phys. Lett. **B185** (1987) 810. 453.

[23] P. Holly *et al.*, Nucl. Phys. **B161** (1979) 349.

[24] A. Ali *et al.*, Nucl. Phys. **B168** (1980) 409.

[25] T. Söstrand, M. Bengtsson, Computer Phys. Comm. **39** (1986) 347.

[26] G. Marchesini *et al.*, Cambridge preprint Carvendish-HEP-90/26 (DESY preprint DESY-01-048).

[27] B.R. Webber, Nucl. Phys. **B228** (1984) 492.

[28] JADE collaboration, S. Bethke *et al.*, Phys. Lett. **213B** 235 (1988).

[29] T. Sjöstrand, Computer Phys. Commun. **28** (1983) 229.

[30] N. Brown, W.J. Stirling, Finding Jets and summing soft gluons: a new algorithm, RAL-91-049 DTP/91/30 (1991).

[31] S. Bethke *et al.*, New Jet Cluster Algorithms, CERN-TH.6222/91.

[32] The SLC Design Report, SLAC Report 229, 1980.

[33] M.L. Swartz, Polarization at SLC. SLAC-PUB-4656 (1988).

[34] T. Maruyama *et al.*, Phys. Rev. Lett. **66**, 2351 (1991).

[35] SLD Design Report, SLAC-273, UC-34D (1984).

[36] C. Damerell, Nucl. Inst. and Meth. **A253**, 478 (1987).

[37] M. Cavalli-Sforza *et al.*, IEEE Trans. Nucl. Sci. **37**, 1132 (1990); K. Abe *et al.*, Report No. SLAC-PUB-6399, November 1993.

[38] D. Axen *et al.*, Nucl. Inst. Meth. **A328**, 472 (1993).

[39] J.E. Brau and T.A. Gabriel, Nucl. Instr. Meth. **A279**, 40 (1989).

[40] S.C. Berridge. Beam test of the SLD silicon-tungsten luminosity monitor. IEEE Trans. Nucl. Sci. **37**, 1191-1198, 1990.

[41] K.T. Pitts. Luminosity measurement for the 1992 run. SLD Physics Note # 20, U. of Oregon, 1993.

[42] A.C. Benvenuti *et al.,* Nucl. Instr. Meth. **A290** (1990) 353.

[43] M. Breidenbach *et al.,* IEEE Trans. Nucl. Sci. **36**, 23 (1989).

[44] J.M.Yamartino, SLD Physics Note # 14 (November 1992).

[45] K.T. Pitts, University of Oregon Ph.D Thesis, March 1994.

[46] E.Vella, J.M.Yamartino, SLD Note # 213 (February 1992).

[47] S. Youssef, Comput.Phys.Commun. **45**, 423 (1987).

[48] J.M. Yamartino, Massachusetts Institute of Technology Ph.D. Thesis, February 1994.

[49] S. González, SLD Note # 24 (October 1993).

[50] R. Brun *et al.,* CERN-DD/78/2 (1978).

[51] G. Grindhammer *et al.,* Nucl. Inst. Meth. **A290**, 469 (1990).

[52] D. Axen *et al.,* SLAC-PUB-5354 (September 1992).

[53] K.T. Pitts, private communication.

[54] M. Kamionkowski, Phys. Rev. D **41**, 1672 (1990).

[55] Morris L. Swartz, lepton and photon interactions, AIP conference proceedings 302, (1993) 381. 259-269.

[56] C. Barter *et al.,* Proceedings of the Summer Study on High Energy Physics in the 1990's, Snowmass, June (1988), S. Jensen, Ed.

[57] Ren Yuan Zhu, Physics Requirements to the Precisions of EM Calorimeter at SSC. GEM Calorimeter Work Shop SSCL, August 8, 1991.

[58] E. Eichten, I. Hinchliffe, K. Lane and C. Quigg Rev. Mod. Phys. **56** (1984) 579.

[59] R. Kless, Z. Kunszt, W.J. Stirling, Physics Letters B, **253**, (1991) 269.

[60] Duane A. Dicus, Scott S.D. Willenbrock, Physical Review D, **37** (1988) 1801.

[61] E.C. Berger, E. Braaten and R.D. Field, Nuclear Physics, **B239** (1984) 52.

[62] Chapter 2: Physics Goals and Detector Performance, GEM Calorimeter Workshop, Summer Study.

[63] A. Arodzero *et al.,* IEEE Transactions on Nuclear Science, Vol.40, No.4, August 1993.

[64] G. Lindstroem *et al.,* "MC Simulations with EGS4 for Calorimeters with Thin Silicon Detectors", in *Proc. of the Workshop on Calorimetry for the Supercollider,* Tuscaloosa, Alabama, March 1989, p. 215.

[65] Scott J. DeBoer, "Results from a SSC ligid argon calorimeter test at Brookhaven National Laboratory", Master of Science Thesis, Iowa State Univ.

[66] T.A. Gabriel *et al.,* CALOR 89.

[67] Technical Design Report, GEM-TN-93-262, SSCL-SR-1219, April 30, 1993.